Coupling electronic properties of molecules and materials to cavity optical modes: a road towards optical and chemical complexity

Rémi Avriller

Université de Bordeaux

École doctorale Sciences Physiques et de l'Ingénieur (SPI)
Laboratoire Ondes et Matière d'Aquitaine, CNRS, UMR 5798
Equipe Théorie de la Matière Condensée

Coupling electronic properties of molecules and materials to cavity optical modes: a road towards optical and chemical complexity

Par Rémi AVRILLER

Thèse d'Habilitation à diriger des recherches en Lasers, matière et nanosciences
Présentée et soutenue à l'Université de Bordeaux, le 23/05/2025

Devant un jury composé de :

Guillaume Schull, DR CNRS	Université de Strasbourg	Rapporteur
Markus Kowalewski, Associate Prof.	Stockholm University	Rapporteur
Dario Bassani, DR CNRS	Université de Bordeaux	Rapporteur
Fabio Pistolesi, DR CNRS	Université de Bordeaux	Garant
Gediminas Jonusauskas, DR CNRS	Université de Bordeaux	Membre du jury
Cyriaque Genet, DR CNRS	Université de Strasbourg	Membre du jury

Summary

Title: Coupling electronic properties of molecules and materials to cavity optical modes: a road towards optical and chemical complexity.

Keywords: Electronic transport; STM plasmonic cavities; Photon emission statistics; Stochastic dynamics; Energy-transfer; Chemical reaction networks; Optical Fabry-Pérot cavities; Electronic strong coupling; Polaritons; Polaritonic chemistry; Chirality

Abstract: We investigate from the point of view of theory spectral and transport properties of open systems in interaction with electronic baths and photonic electromagnetic environments. We focus on three recent research fields for which this investigation is relevant and deal with the following questions of i) understanding how electronic transport properties (current and current-current fluctuations) of STM plasmonic nanojunctions correlate to their light-emission properties (luminescence spectra, $g^{(2)}(\tau)$-measurements), ii) grasping how collective effects related to the intertwined dynamics between molecular aggregates and Fabry-Pérot cavity modes might be responsible for a modification of the embedded material chemical reactivity or chiroptical properties, and iii) how to model and characterize the stochastic dynamics of chemical reaction networks in concentrated molecular aggregates for ultrafast pump-probe experiments.

In all those research directions our objective is to propose and develop some theoretical tools and methods that enable both analytical and numerical calculation of transport properties, spectroscopic signatures and characterization of physico-chemical properties of molecular ensembles going from the single-molecule limit to the mesoscopic aggregate in presence of interactions with a dynamical electromagnetic bath. We aim at initiating a discussion on how to incorporate in the modeling the necessary level of electronic, electromagnetic or chemical complexity found in the related experiments.

This HDR thesis is an attempt to describe some interesting physical mechanisms I had the luck to find or think about during this research journey and to enlighten open questions in systems where the chemical and optical complexity is a relevant or key issue.

To be read before reading

This manuscript covers a period of my own research activities from 2017 to 2024. It is structured in three different parts that are independent and reflect my research interests as well as the related future research perspectives I will follow in the next years. Each part contains an introduction, a core text taken and reformulated from my recent publications containing some unpublished material, and additional derivations that I found useful to add for a better understanding of the main text. I tried to provide a pedagogical introduction to the concepts and theoretical calculations developed in each of those parts. The conclusion and a middle- to long-term research perspective are presented at the end of each section.

Penser n'est pas sortir de la caverne, ni remplacer l'incertitude des ombres par les contours tranchés des choses mêmes, la lueur vacillante d'une flamme par la lumière du vrai Soleil. C'est entrer dans le Labyrinthe, plus exactement faire être et apparaître un Labyrinthe alors que l'on aurait pu rester «étendu parmi les fleurs, faisant face au ciel».

Les Carrefours du labyrinthe I. **Cornélius Castoriadis**.

Remerciements

Je tiens à remercier Gediminas Jonusauskas pour m'avoir initié à la spectroscopie par fluorescence ultra-rapide ainsi qu'à la physico-chimie du RET dont la complexité et la beauté sont encore une source d'intérêt pour mes recherches actuelles. Je remercie également Fabio Pistolesi pour avoir accompagné mes débuts de chercheur CNRS au sein du LOMA en 2011, ainsi que pour une longue collaboration scientifique au cours de laquelle j'ai beaucoup appris concernant les domaines de recherche que sont la nanomécanique, l'optomécanique et le transport électronique. Enfin, mes remerciements à Cyriaque Genet qui m'a fait confiance et m'a accueilli une année à temps plein (2023-2024) au sein de son équipe, et auprès duquel j'ai pu découvrir la richesse des problèmes actuels posée par la chiralité et les interactions chiroptiques en présence de couplage fort lumière-matière en cavité.

Les résultats présentés dans cette thèse d'habilitation n'auraient pu voir le jour sous cette forme sans le travail des chercheurs et chercheuses avec lesquels j'ai eu la chance de pouvoir collaborer, discuter et échanger scientifiquement et humainement au cours de ces années, qu'ils soient professeurs ou chercheurs permanents, postdoctorants, thésards ou stagiaires. Ceci constitue l'essence humaine de la recherche scientifique où les idées et leurs réalisations se mettent en place sur le temps long, parfois dans le doute le plus profond, parfois dans la clarté et la joie d'avoir pu enfin comprendre un petit mieux ce que l'on doit chercher ainsi que ce que l'on cherche. Je remercie donc parmi tant d'autres: Thomas Frederiksen, Thomas Guérin, Clément Dutreix, Ludovic Jaubert, Thomas Ebbesen, Michael Ruggenthaler, Johannes Feist, Lorenzo Mauro, Quentin Schaeverbeke, Andrés Bejarano, Alice Marché, Karen Caicedo, Jacopo Fregoni, Moritz Frankerl, ainsi que tous les chercheurs et membres des services IT du LOMA qui permettent de créer au laboratoire un environnement de recherche bienveillant, dynamique et ouvert. Je remercie aussi les rapporteurs et membres du jury d'avoir accepté d'être dans le jury de ma thèse de HDR et de me transmettre ainsi leurs commentaires et questions scientifiques ayant permis d'en améliorer la rédaction.

Pour finir, je remercie les membres de ma famille: mes parents pour m'avoir inculqué la valeur intrinsèque du savoir, mes sœurs Anne et Cathie pour leur soutien et affection dans les moments difficiles, ainsi que mes enfants Léandre, Octave et Elisabeth qui m'ont appris à devenir père. Et une mention spéciale pour Marie: nos lignes d'univers se sont rencontrées de manière inattendue. Puissent-elles poursuivre leur chemin ensemble, à l'intérieur d'un seul et même cône de lumière...

Contents

Summary i

To read before reading iii

Remerciements v

1 Photon-Emission Statistics induced by Electron Tunneling in Plasmonic Nanojunctions 1

1.1 Introduction . . . 1
1.2 An introduction to photon emission statistics . . . 4
1.2.1 Photon antibunching in the two-level system model . . . 4
1.2.2 Waiting time distribution between successive photon emission events 8
1.2.3 Role of a non-perfect photon detection yield . . . 11
1.3 Inelastic electronic transport properties of a STM plasmonic nanojunction 13
1.3.1 Problematic . . . 13
1.3.2 The single-level model of a STM nanojunction . . . 14
1.3.3 Fermi Golden Rule and its consequences . . . 18
1.3.4 The rate equation dynamics of plasmon-molecule interactions . . . 21
1.3.5 Computing the current-voltage characteristics . . . 23
1.4 Bunching and antibunching in a single level plasmonic nanojunction . . . 25
1.4.1 Expression of the second order correlation function . . . 25
1.4.2 Statistics of photon emission in the single level model . . . 28
1.5 Conclusion and future research perspectives . . . 32

2 Stochastic Dynamics of Resonance Electronic Energy Transfer in Molecular Aggregates 37

2.1 Introduction . . . 37
2.2 Stochastic description of fluorescence in molecular aggregates . . . 40
2.2.1 Position of the problem . . . 41
2.2.2 Statistical description of fluorescence in molecular ensembles . . . 41
2.2.3 Solving the chemical master equation . . . 42
2.2.4 Derivation of exact kinetic equations . . . 45
2.2.5 Towards a description of transient fluorescence experiments . . . 46
2.3 Stochastic description of RET in molecular aggregates . . . 48
2.3.1 Position of the problem . . . 49
2.3.2 Statistical description of RET in molecular ensembles . . . 50
2.3.3 Hierarchy of exact kinetic equations . . . 54

2.3.4 The mean-field approximation . . . 57
2.4 Mesoscopic fluctuations and collective aspects of RET . . . 61
2.4.1 Position of the problem . . . 61
2.4.2 Chemical master equation for the homogeneous RET process . . . 62
2.4.3 Derivation of the Fokker–Planck equation for RET . . . 64
2.4.4 Analysis of mesoscopic fluctuations in the RET process . . . 66
2.5 Conclusion and future research perspectives. . . . 68

3 Chirality and dimensionality in the ultrastrong light-matter coupling regime 71
3.1 Introduction . . . 71
3.2 Canonical model of polariton formation . . . 74
3.2.1 Position of the problem . . . 75
3.2.2 Microscopic Hamiltonian of the Fabry-Pérot cavity . . . 76
3.2.3 Projected Hamiltonian in the single-photon excitation sector . . . 77
3.2.4 Effect of disorder on the polariton spectra . . . 80
3.3 A jump into the ultrastrong coupling regime . . . 86
3.3.1 A variational approach to the polariton problem . . . 86
3.3.2 A bosonization of the polariton problem . . . 88
3.3.3 Classical analog and exact solution to the Hopfield problem . . . 91
3.3.4 Polariton spectra in the electronic ultrastrong coupling regime . . . 93
3.4 Chiral light-matter interactions in optical cavities . . . 96
3.4.1 Position of the problem . . . 96
3.4.2 Microscopic model of a 2D-layer inside an optical cavity . . . 97
3.4.3 Hopfield polaritonic spectra in the 2D-layer configuration . . . 101
3.4.4 Analogous classical model in dimension 2+1 . . . 106
3.4.5 Analysis of the analogous classical trajectories . . . 108
3.5 Conclusion and future research perspectives . . . 113

Bibliography 129

Chapter 1

Photon-Emission Statistics induced by Electron Tunneling in Plasmonic Nanojunctions

1.1 Introduction

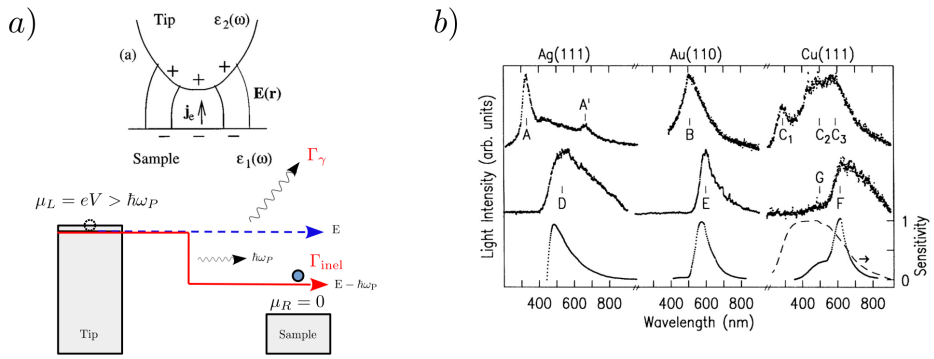

Figure 1.1: a) Schematics of current-induced light emission by a STM tunneling junction. Inelastic tunneling of electrons is at the origin of the photon emission process. b) Observed light emission spectra in a STM plasmonic nanojunction. Adapted from Ref. [16].

A brief introduction to STM light-emission. The scanning tunneling microscops (STM) is a powerful tool in nanotechnology that enables to image atoms and molecules deposited onto surfaces. *Not only such device enables to explore and image the complex physical and chemical properties of molecules with atomic resolution, but also it can be used to emit light, thus playing the role of a new current-induced source of photons at the nanoscale.* The understanding and control of the light emission process is of crucial importance in this field of research, but is still incompletely understood. The simplest mechanism for light emission is presented in Fig. 1.1-a): it involves inelastic tunneling of electrons across the tunneling gap which couples to and excites the localized plasmon mode between tip and substrate

when the bias voltage exceeds an inelastic threshold [73, 93]. The light emitted out of this plasmonic cavity is further collected by a far-field detector: *this gives rises to broad band and high frequency plasmonic resonances [16] (due to losses in the metal) in the optical frequency range (see Fig. 1.1-b)).* A description of the light emission power spectrum can be obtained by the following approach [60]: the electronic tunneling current is seen as a current source in Maxwell equations and thus generates an output electromagnetic field which depends on the peculiarities of the source and on the electromagnetic Green function of the STM nanojunction that is function of its geometry and dielectric properties.

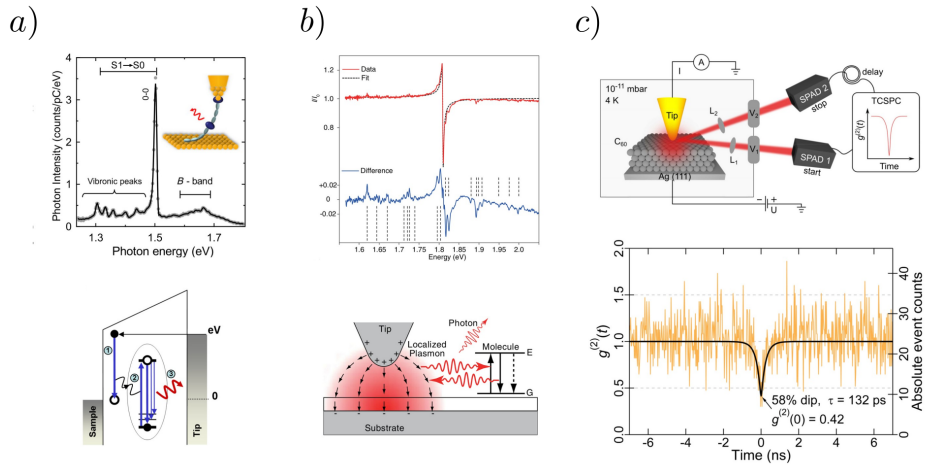

Figure 1.2: a) Photon emission spectrum of a molecular wire contacting the tip to the sample of a STM plasmonic junction. The emission mechanism involves a narrow 0-0 transition and vibrational sidebands due to the formation of a molecular exciton. Adapted from Ref.[23]. b) Observed light emission spectra in a plasmonic STM nanojunction in proximity of a molecule deposit on an insulating substrate. Fano resonances are seen which are a signatures of molecular fingerprints on the emitted signal. Adapted from Ref. [65]. c) Measured second order correlation function of the emitted light field presenting an anti-bunching behavior. Light is emitted from single levels out of the band of C60 molecular layer between the STM tip and substrate. Adapted from Ref. [81].

Molecular fingerprints in STM light emission. The actual mechanism at the origin of light-emission in current-driven STM nanojunctions is however still not completely well understood and is actually quite complex. In presence of a molecule inside or close to the localized cavity plasmon, current injection excites the molecule to an electronic excited-state that further decays back to ground state by emitting a photon. Several mechanisms (see Fig. 1.2) were proposed for describing this molecular excitation, including elastic tunneling of an electron and a hole from the metallic electrodes to the molecule [40], inelastic tunneling of an electron across the junction at the origin of emission of a localized plasmon that is further absorbed by the molecule [40, 39], and a more complex energy-transfer mechanism in which the absorption and emission processes of the localized plasmon by the molecule interfere one with each other [65]. *We note that the deposition of a single molecule on an insulating substrate enables to block fluorescence quenching usually due to*

fast charge-transfer from the molecule to the metallic substrate. This allowed to report signatures of molecular fingerprints like molecular vibrations [96] that impact the luminescence spectra on top of the broad plasmonic feature. The relative isolation from the metallic substrate of the deposited molecule is a nice playground for unveiling complex Coulombian effects due to charging and discharging of the molecule upon passing an electronic current from the STM apex: *this signals the necessity to keep a manybody description of the molecular electronic structure for computing light-emission in such structured plasmonic electromagnetic environments [72].* While most of the works in STM tunneling junctions deal with such a complex molecular structure and its impact on photon emission, we recently predicted that upon proper tuning of the external electrode potentials *a single electronic level was sufficient to generate electrically-driven single-photon emission* [107]. Recent experiments with STM on C_{60} molecular films go in that direction and reported *a Coulomb-blockade mechanism resulting from tip-induced split-off single-level states* [81]. The resulting single level model of a STM plasmonic junction is interesting and simpler than the complex molecular effects above mentioned and are thus the topic of the present section of this study. This model was even reported to lead to *a photon antibunching mechanism both theoretically [107] and experimentally [81] (see 1.2-c)), which is the hallmark of single photon emission by the STM junction.*

Problematic of the present study. The main problematic of the present study in relation to the light emission mechanism in STM junctions is related to the following questions

1. What is the mechanism describing plasmon-molecule interactions and it role on light emission ? What is *the interplay between tunneling electrons charging or discharging the molecule and the plasmonic electromagnetic environment* ?

2. Is it possible *to design innovative current-induced single photon sources of interest from such STM junctions* that would be tunable with external electrical parameters ?

3. *How to characterize and model the statistics of light emission out of such junction ?*

4. When and how is there single photon emission in such plasmonic devices ? *What controls the timescales of the related antibunching mechanism ?*

In this section, we present a theoretical investigation of the statistics of photon emission in a single-level plasmonic nanojunction in order to deal at least partially with the above open questions. In Sec. 1.2, we introduce the notion of photon emission statistics in the framework of the paradigmatic model of two-level system. We show how to characterize this statistics by defining and computing the second order correlation function of the emitted light field $g^{(2)}(\tau)$ and the waiting-time distribution $w(\tau)$ between successive photon-emission events [99, 20, 26]. In Sec. 1.3.1, we formulate a microscopic model of single level STM plasmonic nanojunction from which we compute the current-voltage characteristics at the origin of plasmon excitation. In Sec. 1.4, we compute explicitly the second correlation function of light emitted out of this junction and show the existence of a crossover from bunching to antibunching upon fine tuning the molecular junction to a "sweet spot" of high symmetry. The departure from this "sweet spot" and the related open perspectives

of research in this field are sketched in the last Sec. 1.5. This work is the outcome of a collaboration with Fabio Pistolesi (LOMA) and Thomas Frederiksen (San Sebastian). Most of the presented results are part of the PhD thesis of Quentin Schaeverbeke [108]. I tried to reformulate those results and rederive them in a way that is generalizable to more complex situations.

1.2 An introduction to photon emission statistics

In this section, we provide *an introduction to the notion of photon emission statistics*. We found simpler to introduce this notion through the paradigmatic model of a two-level system (TLS) which, after being excited, can emit single photons in the far-field electromagnetic environment. The emitted photons are then collected by a single photon detector. We characterize *the statistics of random clicks measured by the photon detector* in Sec. 1.2.1 and explain how to define and compute exactly *the second-order correlation function $g^{(2)}(\tau)$ of the emitted field in the TLS model.* We show that the emitted photons are antibunched, namely they present a lower probability of being emitted close in time one from each other. *The signature of antibunching is obtained as a vanishing of $g^{(2)}(\tau)$ at zero delay time $\tau = 0$.* In order to understand better this antibunching mechanism, we introduce and compute exactly in Sec. 1.2.2 *the waiting time distribution (WTD) between pairs of successive emitted photons in the TLS model.* We show that the WTD is a statistical indicator that is complementary to the second order correlation function and that it provides additional information about the typical timescales involved in the photon emission process. We close this analysis by considering in Sec. 1.2.3 the role of having *a non perfect photon detector with finite detection yield.* To write this whole section, we used part of the material that we published in our recent Ref. [9]. *This material follows directly from the PhD research work done by Quentin Schaeverbeke [108], in collaboration between LOMA and San Sebastian.* The derivation that we propose here is inspired by the reading of the section devoted to photon emission statistics in the book of van Kampen [117] and by the seminal paper of Serge Reynaud [99] devoted to fluorescence of atoms in the "dressed atom" picture. *The former reference was and is still to me the source and origin of most of the understanding I could developed in this research topic.*

1.2.1 Photon antibunching in the two-level system model

A first glimpse to the photon correlation functions. In this paragraph, we provide a first glimpse at the description of the statistics of photons emitted by a simple two-level system (TLS). This model is shown in Fig. 1.3-b). It is made of two levels labeled 0 and 1 connected by an upward rate Γ_{10} for exciting the TLS and a downward rate κ for de-exciting it and emitting a single photon in the electromagnetic environment. The emitted photon is then collected by a single-photon detector, leading to a temporal trace of the photon "clicks" (see Fig. 1.4-upper panel). *The study of photon emission statistics aims at characterizing the correlation functions of the stochastic temporal trace of the photon "clicks" provided by the detector.* In this context, following the seminal paper of Glauber [53], it is natural to define

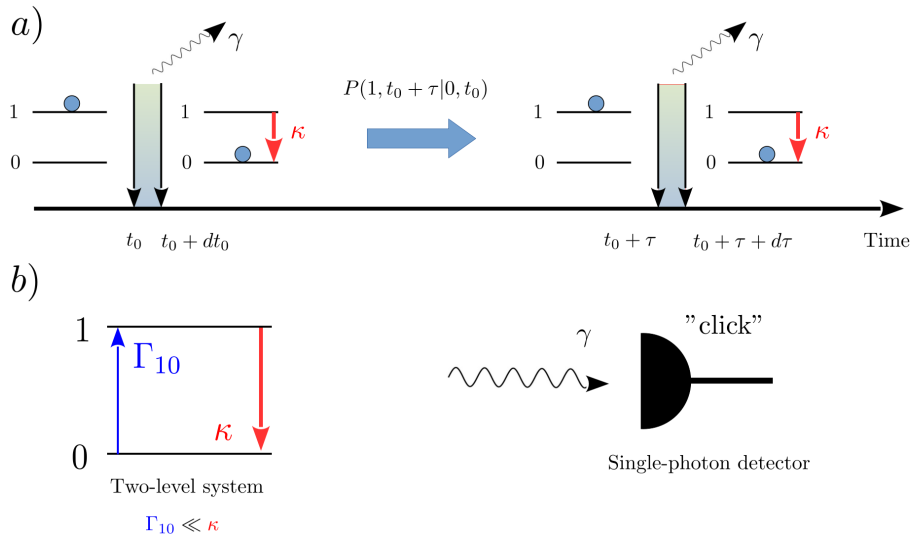

Figure 1.3: Scheme of a simple two-level system at the origin of photon emission. The states 0 and 1 are connected by an upward rate Γ_{10} for exciting the TLS and a downward rate κ for de-exciting it by emitting a photon in the electromagnetic environment. The emitted photon is collected by a single-photon detector. This leads to a temporal stochastic sequence of photon detection events or "clicks" given by the detector. Unpublished Fig.

the correlation functions of the emitted photon output field as

1. $G_1(t_0)dt_0$ the probability to *"emit a photon"* in the time interval $[t_0, t_0 + dt_0]$,

2. $G_2(t_0, t_0 + \tau)dt_0 d\tau$ the joint probability to *"emit a first photon"* in the time interval $[t_0, t_0 + dt_0]$ AND to *"emit a second photon"* in the time interval $[t_0 + \tau, t_0 + \tau + d\tau]$.

The normalized second-order correlation function (SCF) of the emitted photons is defined from the above correlation functions as

$$g^{(2)}(t_0, t_0 + \tau) = \frac{G_2(t_0, t_0 + \tau)}{G_1(t_0)G_1(t_0 + \tau)}\,. \tag{1.1}$$

In the stationary regime, the stochastic process is independent of time thus leading to $G_1(t_0) \equiv G_1^{\text{st}}$ and $G_2(t_0, t_0 + \tau) \equiv G_2^{\text{st}}(\tau = \tau)$. The stationary $g^{(2)}(\tau)$ correlation function is thus given by

$$g^{(2)}(\tau) = \frac{G_2^{\text{st}}(\tau)}{(G_1^{\text{st}})^2}\,. \tag{1.2}$$

While the first correlation function G_1^{st} characterizes the average intensity of emitted light by the TLS, the second correlation function $g^{(2)}(\tau)$ is a signature of the correlations between two photon emission events obtained at a delay time τ. The computation and characterization of $g^{(2)}(\tau)$ is the main goal of this section.

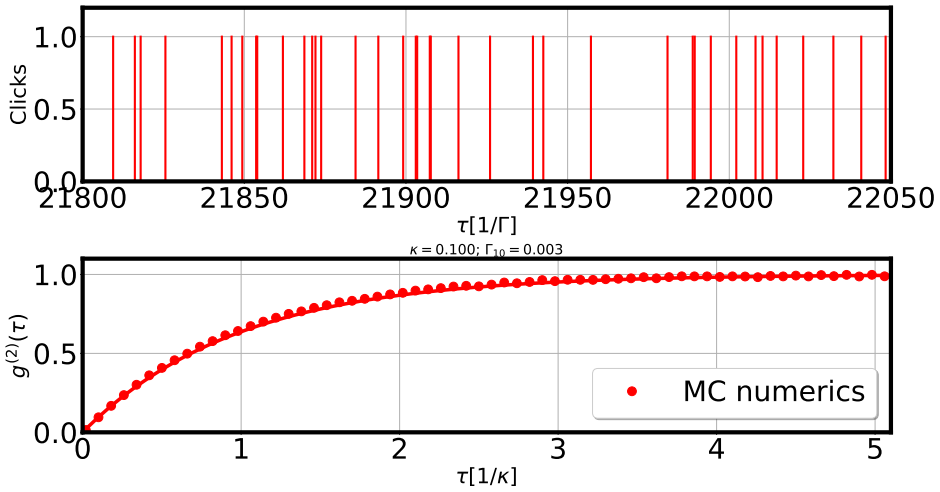

Figure 1.4: Upper panel: Time-trace of the history of "clicks" for a photodetector detecting the emission of photons by a TLS with upward rate $\Gamma_{10} = 0.03$ and downward rate $\kappa = 0.1$. This stochastic process is computed using a Monte Carlo simulation. Lower panel: Corresponding $g^{(2)}(\tau)$ signal obtain from the Monte Carlo simulation (red points) compared to the exact analytical solution in Eq. 1.10 that exhibits antibunching behavior. Generated using the Monte Carlo code implemented in our Ref. [9]. Unpublished Fig.

Expression of $g^{(2)}(\tau)$ in terms of occupation probabilities. We now consider the time-dependent process at the origin of the measurement of the correlation functions by a single-photon detector, as exemplified in panel a) of Fig. 1.3. The first order correlation $G_1(t_0)$ provides the probability of emitting a single photon between t_0 and $t_0 + dt_0$. It is given by

$$G_1(t_0)dt_0 = \kappa dt_0 \pi_1(t_0)\,, \tag{1.3}$$

namely it is proportional to *the probability of having the TLS in the excited state* $\pi_1(t_0)$ *at time* t_0 *times the probability* κdt_0 *of emitting a photon through the radiative transition* $1 \to 0$ *in the time interval* $[t_0+\tau, t_0+\tau+d\tau]$ *with rate* κ. Similarly, the unnormalized second-order correlation function $G_2(t_0, t_0+\tau)$ is provided by the expression

$$G_2(t_0, t_0+\tau)dt_0 d\tau \;\; = \;\; \kappa d\tau P\left(1t_0+\tau|0t_0\right)\kappa dt_0 \pi_1(t_0)\,, \tag{1.4}$$

namely it is proportional to *the probability* $\kappa dt_0\pi_1(t_0)$ *of emitting a photon in the time interval* $[t_0, t_0+dt_0]$, *times the conditional probability* $P\left(1t_0+\tau|0t_0\right)$ *of having the TLS in excited state* 1 *at a later time* $t_0+\tau$ *KNOWING it was in the ground state* 0 *at time* t_0 *after the first measurement, times the probability* $\kappa d\tau$ *of emitting another photon in the time interval* $[t_0+\tau, t_0+\tau+d\tau]$. We note the crucial role played in this expression by the collapse of the wavefunction in the photon measurement process that imposes the TLS to be in the ground state 0 after each photon emission process: this was noticed explicitly for the first time by Claude Cohen Tannoudji and Serge Reynaud in Ref. [26]. Using Eq. 1.2, we obtain the expression for the normalized second-order correlation function $g^{(2)}(\tau)$ in the stationary state

$$g^{(2)}(\tau) = \frac{P\left(1\tau|00\right)}{\pi_1^{\rm st}}\,. \tag{1.5}$$

Explicit expression of $g^{(2)}(\tau)$ for the TLS system. We compute in this paragraph the explicit expression of $g^{(2)}(\tau)$ as written in Eq. 1.5. For that purpose, we need to find the conditional probability $P\left(1\tau|00\right)$, which is nothing but the $\pi_1(\tau)$ probability for the TLS to be in the excited state 1 at time τ provided the choice of initial condition $\pi_0(0) = 1$ at time 0 is adopted. The former population is obtained from the rate equation (see also Fig. 1.3-b))

$$\dot{\pi}_1(\tau) = \Gamma_{10}\pi_0(\tau) - \kappa\pi_1(\tau)\,, \tag{1.6}$$
$$\pi_0(t) = 1 - \pi_1(t)\,. \tag{1.7}$$

Its solution for the initial condition $\pi_1(0) = 0$ is given by

$$\pi_1(\tau) = \pi_1^{\rm st}\left\{1 - e^{-\kappa_t\tau}\right\}\,, \tag{1.8}$$
$$\pi_1^{\rm st} = \frac{\Gamma_{10}}{\kappa}\,, \tag{1.9}$$

with $\kappa_t = \kappa + \Gamma_{10}$ the total relaxation rate. From the previous Eqs. 1.8,1.9, the explicit expression of the second-order correlation function follows

$$g^{(2)}(\tau) = 1 - e^{-\kappa_t\tau}\,. \tag{1.10}$$

This is the main result of this section. The SCF is shown in Fig. 1.4-lower panel by comparing the outcome of a Monte Carlo calculation (red points) to the analytical formula of Eq. 1.10 (plain red curve). In the case of the TLS model, the second-order correlation function thus goes to zero at zero time-delay ($g^{(2)}(0) = 0$) and increases exponentially towards unity on a time scale $\tau_{g^{(2)}}$ given by

$$\tau_{g^{(2)}} = \frac{1}{\kappa_t} \equiv \frac{1}{\kappa + \Gamma_{10}}\,. \tag{1.11}$$

It also fulfills at all times the inequality $g^{(2)}(\tau) \leq 1$ which is the hallmark of a sub-Poisonian statistics. *The fact that $g^{(2)}(\tau) \geq g^{(2)}(0)$ with $g^{(2)}(0) = 0$ is a clear signature of antibunching [125], namely the property for the TLS to have a lower probability to emit a photon at short delay-times $\tau \ll \frac{1}{\kappa_t}$, after a first photon has been emitted at time 0.* At large times $\tau \gg \frac{1}{\kappa_t}$ we find $g^{(2)}(\tau) \to 1$ and the photon emission statistics recovers the Poisonian statistics of uncorrelated photon emission events.

Open question. We have shown that the light emitted by a TLS exhibits antibunching in its $g^{(2)}(\tau)$ correlation function and thus vanishes at zero delay time. The interpretation of this antibunching mechanism is related to the interpretation of the second order correlation function in terms of a two-probe measurement process: *once the first photon has been detected, the TLS is projected onto its ground state 0 and one has thus to wait during a given delay time $\langle\tau\rangle$ before the next photon will be emitted.* At this stage, the $g^{(2)}(\tau)$ correlation function contains only one time scale given by $\tau_{g^{(2)}}$ in Eq. 1.11. *The question we ask is thus the following: do we have that $\tau_{g^{(2)}} = \langle\tau\rangle$?*

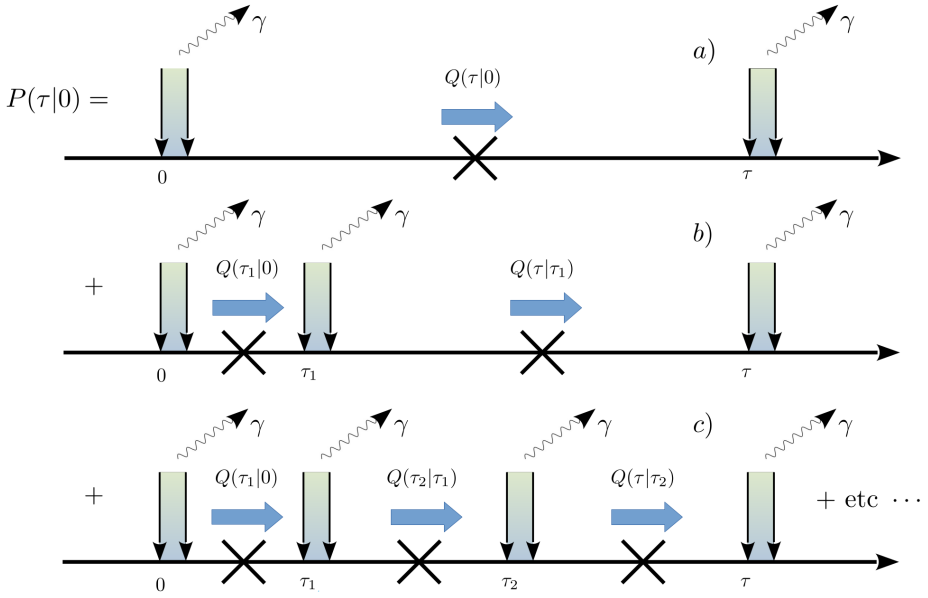

Figure 1.5: Illustration of Eq. 1.15 giving the conditional probability distribution $P(\tau|0)$ to emit one photon at time τ knowing that a photon was emitted at time 0 as a series in terms of the corresponding "exclusive" probability distribution $Q(\tau|0)$. A cross in a time interval means that no photon has been emitted in that interval, while curly arrows stand for elementary single photon emission events. Unpublished Fig.

1.2.2 Waiting time distribution between successive photon emission events

Definition and expression of the WTD. To answer the question of the previous section, we introduce here another indicator characterizing the statistics of emitted light by a given emitter which is *the delay-time distribution or waiting-time distribution (WTD)* $w(\tau)$ *between two successive photon emission events.* In order to compute the WTD, we need to introduce the following additional distribution functions [117, 99]

1. $P(\tau_2|\tau_1)$ the conditional probability distribution to emit a photon at time τ_2 KNOWING that a photon has been previously emitted at time τ_1.

2. $Q(\tau_2|\tau_1)$ the "exclusive" conditional probability distribution to emit a photon at time τ_2 KNOWING that a photon has been previously emitted at time τ_1 but with THE CONSTRAINT that no photon has been emitted in the time-interval $]\tau_1, \tau_2[$.

Both P and Q are obtained from the time-trace or history of "clicks" provided by the single photon detector (see Fig. 1.5) from which both the SCF and WTD can be expressed

$$g^{(2)}(\tau) = \frac{S(\tau)}{G_1^{(\mathrm{st})}}, \tag{1.12}$$

$$w(\tau) = Q(\tau|0), \tag{1.13}$$

with $S(\tau) \equiv P(\tau|0)$. However, we remark that in general $P \neq Q$. Indeed, as shown in Fig. 1.5, Q involves to *the statistics of "exclusive" histories in which no photon-emission event is observed in between two successive photon-emission events* (see the a) history), while P includes *the statistics of the "complete" history of emission events including "*0*-photon" emission event plus "*1*-photon" emission events* (see the b) history) *plus "*2*-photon" emission events* (see the c) history) *plus etc* $\cdots$ *in between two photon-emission events.* This can be written mathematically as the following series

$$P(\tau|0) \;=\; Q(\tau|0) + \int_0^\tau d\tau_1 Q(\tau,\tau_1|0) + \int_0^\tau d\tau_1 \int_{\tau_1}^\tau d\tau_2 Q(\tau,\tau_2,\tau_1|0) + \cdots \,, \tag{1.14}$$

with $Q(\tau,\tau_1|0)$ the exclusive probability distribution that one photon is emitted at time τ_1 and another one is emitted at later time τ, knowing that one photon-emission event occurred at time 0. A similar definition holds for $Q(\tau,\tau_2,\tau_1|0)$ that contains an additional photon-emission event at a time τ_2 in the interval $]\tau_1,\tau[$. If the stochastic process of photon emission events is Markovian then $Q(\tau,\tau_1|0) \equiv Q(\tau|\tau_1)Q(\tau_1|0)$ and $Q(\tau,\tau_2,\tau_1|0) \equiv Q(\tau|\tau_2)Q(\tau_2|\tau_1)Q(\tau_1|0)$ such that Eq. 1.14 can be simplified to

$$P(\tau|0) \;=\; Q(\tau|0) + \int_0^\tau d\tau_1 Q(\tau|\tau_1)Q(\tau_1|0) + \int_0^\tau d\tau_1 \int_{\tau_1}^\tau d\tau_2 Q(\tau|\tau_2)Q(\tau_2|\tau_1)Q(\tau_1|0) + \cdots \tag{1.15}$$

This series is illustrated in Fig. 1.5 and can be resummated into an integral equation connecting the P and Q distributions

$$P(\tau|0) \;=\; Q(\tau|0) + \int_0^\tau d\tau_1 P(\tau|\tau_1)Q(\tau_1|0)\,. \tag{1.16}$$

Using the definition of $w(\tau)$ in Eq. 1.13, we finally obtain *for a stochastic photon emission process that is both Markovian and stationary*

$$S(\tau) \;=\; w(\tau) + (S * w)(\tau)\,, \tag{1.17}$$

with $*$ meaning the convolution product as in Eq. 1.16. *This integral equation can be solved by Laplace-transform thus providing a simple algebraic link between* $\tilde{S}(z)$ *and* $\tilde{w}(z)$*, the respective Laplace transforms of* $S(\tau) = G_1^{(\mathrm{st})} g^{(2)}(\tau)$ *and* $w(\tau)$

$$\tilde{w}(z) \;=\; \frac{1}{1+\tilde{S}^{-1}(z)}\,. \tag{1.18}$$

This is the main result of this paragraph devoted to the WTD.

Explicit expression of $w(\tau)$ for the TLS model. We now compute $w(\tau)$ analytically for the TLS model of Sec. 1.2.1. We find a one to one mapping between $P(\tau|0)$ and conditional probability $P(1\tau|00)$ in Eq. 1.5, leading to $S(\tau) = P(\tau|0) \equiv \kappa P(1\tau|00)$. This implies that for the TLS emitter, the photon emission process is indeed Markovian and that we can use

the relation connecting the WTD to the SCF written in Eq. 1.18. We find for $S(\tau)$ and its Laplace transform $\tilde{S}(z)$ the values

$$S(\tau) = \frac{\kappa\Gamma_{10}}{\kappa_t}\left\{1 - e^{-\kappa_t\tau}\right\}, \tag{1.19}$$

$$\tilde{S}(z) = \frac{\kappa\Gamma_{10}}{z\,(z+\kappa_t)}. \tag{1.20}$$

Incorporating Eq. 1.20 into the expression of $\tilde{w}(z)$ in terms of $\tilde{S}(z)$ written in Eq.1.18, we find after inverse Laplace transform

$$w(\tau) = \frac{\kappa\Gamma_{10}}{\kappa - \Gamma_{10}}\left\{e^{-\Gamma_{10}\tau} - e^{-\kappa\tau}\right\}, \tag{1.21}$$

$$\approx \kappa\Gamma_{10}\tau \xrightarrow[\tau\to 0^+]{} 0^+, \tag{1.22}$$

$$\approx \Gamma_{10}e^{-\Gamma_{10}\tau} \xrightarrow[\tau\to+\infty]{} 0^+. \tag{1.23}$$

This expression is the main result of this section. It shows that $w(\tau)$ *is the sum of two exponential functions, one with relaxation rate* Γ_{10} *and the other with relaxation rate* κ. The WTD is shown in Fig. 1.6. At "short" times ($\tau \ll$ min $(\frac{1}{\kappa}, \frac{1}{\Gamma_{10}})$), $w(\tau)$ vanishes linearly with τ and is proportional to the product of both upward rate Γ_{10} and downward rate κ at which photons are emitted out of the TLS. *The vanishing of* $w(\tau)$ *at zero delay-time* $\tau = 0$ *is a signature of antibunching of emitted photons, while the proportionality of the slope with* Γ_{10} *translates the fact that after one photon has been emitted, one needs to wait some delay time for re-exciting the TLS and have another photon to be emitted.* In the opposite limit of "long" times ($\tau \gg$ min $(\frac{1}{\kappa}, \frac{1}{\Gamma_{10}})$), the WTD vanishes exponentially in time with the upward rate Γ_{10} (for $\kappa > \Gamma_{10}$). This reflects both facts that the WTD is a normalized distribution function $\left[\int_0^{+\infty} d\tau w(\tau) = 1\right]$ and that it becomes very unlikely that after one photon has been emitted initially, another photon is not emitted after a delay-time much larger than the TLS typical relaxation time. *It is interesting to notice that* $w(\tau)$ *is a non-monotonous function of time*, reaching a maximum at time $\tau_{\rm m}$ given by

$$\tau_{\rm m} = \frac{1}{\kappa - \Gamma_{10}} \ln\left(\frac{\kappa}{\Gamma_{10}}\right). \tag{1.24}$$

Finally, we obtain from Eq. 1.21 an analytical expression for *the average delay-time* $\langle\tau\rangle$ *between two photon emission events*

$$\langle\tau\rangle = \int_0^{+\infty} d\tau\tau w(\tau) = \frac{1}{\Gamma_{10}} + \frac{1}{\kappa}. \tag{1.25}$$

Conclusion regarding the TLS model. We conclude this introductory exploration of the statistics of photons emitted by a TLS with the following summary

1. The normalized second-order correlation function of the emitted photons $g^{(2)}(\tau)$ *decays exponentially in time with time scale given by the total dissipation time of the TLS* $\tau_{g^{(2)}} = \frac{1}{\kappa+\Gamma_{10}}$ in Eq. 1.11.

2. In contrast, the WTD of delay times between photon emission events $w(\tau)$ exhibits a non-monotonous behavior with time. The corresponding average delay-time between two photon emission events $\langle\tau\rangle = \frac{1}{\Gamma_{10}} + \frac{1}{\kappa}$ in Eq. 1.25 is given by *the sum of the inverse upward excitation time of the TLS* $1/\Gamma_{10}$ *plus the inverse relaxation time* $1/\kappa$ *by photon emission from the TLS.*

Surprisingly, we thus find that in general $\tau_{g^{(2)}} \neq \langle\tau\rangle$. This is due to the fact that the SCF $g^{(2)}(\tau)$ and WTD $w(\tau)$ do not contain the same statistical information, each exhibiting different characteristic time-scales characterizing a different aspect of the photon-emission statistics. *The first timescale* $\tau_{g^{(2)}}$ *provides information about the speed at which the correlations in the detection of photons pairs decay in time, while* $\langle\tau\rangle$ *provides information on how long one has to wait between two successive photon emission events, hence the speed at which the TLS is re-excited from the TLS ground state.* Those two time-scales are thus not inconsistent one with each other but constitute complementary statistical indicators of the photon emission statistics [19]. Only in the short-time regime $\tau \ll \tau_{\mathrm{m}}$, the behavior in time of $w(\tau)$ and $S(\tau) = G_1^{(\mathrm{st})} g^{(2)}(\tau)$ do coincide since they are related to the same antibunching mechanism, while at larger time $\tau \gg \tau_{\mathrm{m}}$ they differ in a significant manner since $w(\tau)$ goes exponentially to zero while $S(\tau)$ converges to the constant value Γ_{10}.

1.2.3 Role of a non-perfect photon detection yield

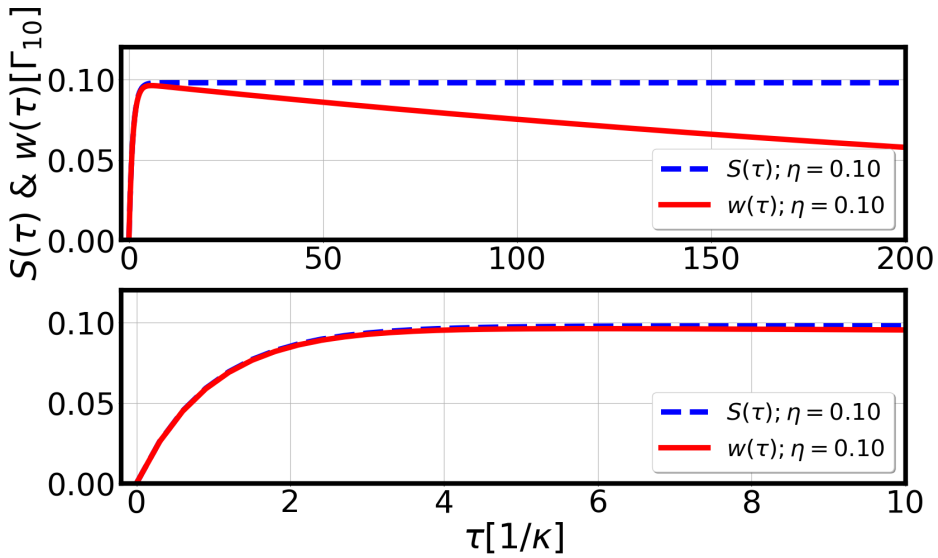

Figure 1.6: Upper panel: SCF $S(\tau) = G_1^{(\mathrm{st})} g^{(2)}(\tau)$ and WTD $w(\tau)$ of the photon emitted by a TLS as function of time τ. The detector has a non-perfect detection yield $\eta = 0.1$. Lower panel: same curve but zoomed in the short time range. Parameters are those of Fig. 1.4. Adapted from our recent Ref. [9].

In this last section, we model the non-perfect detection efficiency of the photodetector collecting the photons emitted out of the emitter. For that purpose, *we assign a probability* $\eta \in [0, 1]$ *for a photon to be detected by the photodetector, namely* η *is the experimental*

detection-yield. A perfect detector efficiency means $\eta = 1$. For computing how the SCF $g^{(2)}(\tau)$ and WTD $w(\tau)$ are impacted by this detector efficiency, we need to generalize the definitions of the previous probability distributions written in Sec. 1.2.1 and Sec. 1.2.2. We thus redefine (see Fig. 1.3)

1. $G_1(t_0)dt_0$ the probability to *"emit a photon AND detect it by the apparatus"* in the time-interval $[t_0, t_0 + dt_0]$.
2. $P\left(t_0, t_0 + \tau\right) dt_0 d\tau$ the joint-probability that *"a first photon is emitted AND detected by the apparatus"* in the time interval $[t_0, t_0 + dt_0]$ AND that a *"another photon is emitted AND detected by the apparatus"* in the time interval $[t_0 + \tau, t_0 + \tau + d\tau]$.
3. $Q\left(t_0, t_0 + \tau\right) dt_0 d\tau$ the exclusive joint-probability that *"a first photon is emitted AND detected by the apparatus"* in the time interval $[t_0, t_0 + dt_0]$ AND that a *"second photon is emitted AND detected by the apparatus"* in the time interval $[t_0 + \tau, t_0 + d\tau]$, with THE CONSTRAINT that *"no photon is emitted in the time interval* $]t_0 + dt_0, \tau[$*"*.

The role of a non-perfect detection-yield is taken into account by *adding an additional random process with probability* η *to detect the photon arriving on the detector that is independent of the photon-emission event itself.* Due to the above mentioned statistical independence between the photon-emission and photon-detection events, the previously defined probability distributions do factorize

$$G_1(t_0) = \eta \underline{G}_1(t_0)\,, \tag{1.26}$$
$$P(t_0, t_0 + \tau) = \eta^2 \underline{P}(t_0, t_0 + \tau)\,, \tag{1.27}$$

with the underline symbols corresponding to quantities evaluated at a perfect detection efficiency ($\eta = 1$). Those equations imply a modification of the expression of the SCF and WTD as

$$S(\tau) = P(\tau|0) = \eta \underline{S}(\tau)\,, \tag{1.28}$$
$$G_2^{\rm st}(\tau) = P(\tau, 0) = \eta^2 \underline{G}_2^{\rm st}(\tau)\,, \tag{1.29}$$
$$g^{(2)}(\tau) = \frac{P(\tau|0)}{G_1^{\rm st}(0)} = \frac{\eta \underline{S}(\tau)}{\eta \underline{G}_1^{\rm st}} = \underline{g}_2(\tau)\,, \tag{1.30}$$

so that the unnormalized SCF $G_2^{\rm st}(\tau)$ is modified by the non-perfect photon-detection quantum yield: this is expected since the lower the detection yield, the lower the number of collected photons per unit time by the detector. However, *the normalized SCF* $g^{(2)}(\tau)$ *is not modified by decreasing* η *since the* η^2 *factors simplify in the numerator and denominator: the only effect being now that one has to wait longer in order to achieve the proper statistics of photon "clicks" !* Using the definition of $w(\tau) = Q(\tau|0)$ in Eq. 1.17, we find that the modified relation between the SCF and WTD

$$\eta \underline{S}(\tau) = w(\tau) + \eta \left(w * \underline{S}\right)(\tau)\,, \tag{1.31}$$

which provides after Laplace transform

$$\tilde{w}(z) = \frac{1}{1 + \left\{\eta \tilde{\underline{S}}(z)\right\}^{-1}}\,. \tag{1.32}$$

This expression generalizes Eq. 1.18 and shows that the WTD is modified by a non-perfect detection yield. It recovers the results of Ref. [118]. The final expression of the WTD is obtained after inverse Laplace transform of Eq. 1.32 providing

$$w(\tau) \;=\; \frac{\eta\kappa\Gamma_{10}}{\kappa_d}\left\{e^{-\frac{(\kappa_t-\kappa_d)\tau}{2}} - e^{-\frac{(\kappa_t+\kappa_d)\tau}{2}}\right\}, \tag{1.33}$$

with $\kappa_d = \sqrt{\kappa_t^2 - 4\eta\kappa\Gamma_{10}}$. The resulting WTD is shown in Fig. 1.6. *The corresponding average delay-time $\langle\tau\rangle$ between two photon emission events is also modified to*

$$\langle\tau\rangle \;=\; \frac{1}{\eta}\left\{\frac{1}{\Gamma_{10}} + \frac{1}{\kappa}\right\}. \tag{1.34}$$

It is interesting to notice that, in contrast to the SCF, the WTD and the average delay time between successive photon emission events $\langle\tau\rangle$ depends significantly on the non-perfect detector efficiency η. In the case of $\langle\tau\rangle$, this is understood because due to a lower detection yield η, a fraction of the emitted photons arriving to the detector are not detected by it (false negative) thus leading to a larger time to wait in average for a next photon to come after a first photon has been detected.

1.3 Inelastic electronic transport properties of a STM plasmonic nanojunction

1.3.1 Problematic

The TLS model for photon emission presented in the previous Sec. 1.2 was a very simple one. However it seems to be insufficient to take into account the complexity of actual experiments performed in STM plasmonic nanojunctions. The following points making the mechanism of light emission quite a complex one are listed below:

1. Molecules have *complex electronic and vibrational strutures* that are beyond the description by only two levels.

2. A plasmon mode is actually localized in the tunneling gap between the STM tip apex and the substrate. This plasmon mode is characterized by *a high frequency (here optical frequency), a broad-band plasmonic spectrum and an inhomogeneous spatial structure of the electromagnetic field.*

3. The interaction mechanism at the origin of light emission involves either *inelastic tunneling of charges through the tunneling gap* or *direct tunneling through the molecule*, or even *interference between the plasmon field and the fluorescence spectrum of the molecule.*

4. The low mode volume of the plasmonic cavity in the STM gap might enable to reach enhanced and thus *stronger molecule-plasmon interaction strength.*

We do not aim in describing *ab initio* the mechanism of current-induced molecule-plasmon interaction, but are willing to find a minimal model that would incorporate some of the features listed previously. To the best of our knowledge, a complete theoretical understanding of light-emission in STM is still missing.

Open question. *Can we formulate a minimal microscopic model that could be solved with a sufficient level of accuracy and would enable to explore some of the characteristics of current-induced light emission in STM plasmonic nanojunctions ?*

For that purpose, we introduce in Sec. 1.3.2 a theoretical microscopic model of single-level plasmonic nanojunction from which we characterize the statistics of photon emission. This model is derived from a formalism developed by Audrey Cottet *et al.* in Ref. [29] and was adapted by us to describe a current-driven plasmonic nanojunction in our Ref. [107]. We then describe in Sec. 1.3.3 the plasmon-molecule interaction mechanism in this junction. For that purpose *we write and solve formally a rate equation ruling the dynamics of the junction manybody states mixing charge and plasmon occupancies, with incoherent rates computed using Fermi Golden Rule.* This approach was developed in our recent Ref. [9]. We present in Sec. 1.3.5 the current-voltage characteristics of this junction obtained from the solution of the rate equation. The computed $I(V)$ curves present inelastic channels corresponding to the onset of single or many plasmon emission in the plasmonic gap that is induced by single electron tunneling events: this is a signature of the conversion of the electron kinetic energy provided by the bias voltage into plasmon excitation inside the STM cavity. *This current-driving mechanism is at the origin of light-emission is this simple model of STM plasmonic nanojunction. Most of the results presented here in a compact way, where derived and expressed for the first time in the PhD work of Quentin Schaeverbeke [108].* For the sake of clarity and simplicity, I chose to present here those results using only the plasmon-molecule bi-partite rate equation, with the philosophy that most of the physics we discuss can be understood using properly the Fermi Golden Rule.

1.3.2 The single-level model of a STM nanojunction

Hamiltonian description of the single-level nanojunction. In order to deal with the open questions of the previous section, we proposed and study in our previous Refs. [9],[108] a model of STM plasmonic nanojunction where the molecule is described by a single (HOMO or LUMO) electronic level (see Fig. 1.7). That single level is coupled to two electronic leads at the origin of current injection and to a composite electromagnetic environment made one plasmonic mode that decays to an external electromagnetic bath. In this way, we take into account *the presence of a high optical frequency and damped plasmonic mode with its proper dynamics that is coupled to the slower dynamics of current tunneling across the junction.* Off course, the complex electronic and vibrational structure of the molecule is not taken into account in this model. Such models describing electron-photon coupling in mesoscopic devices has been proposed in the context of circuit quantum electrodynamics in Ref. [29], which led to *a theoretical framework taking into account spatial inhomogeneities of the electromagnetic field at the scale of the molecular orbitals describing the junction.* We use this formalism and propose the following microscopic Hamiltonian describing the single-level

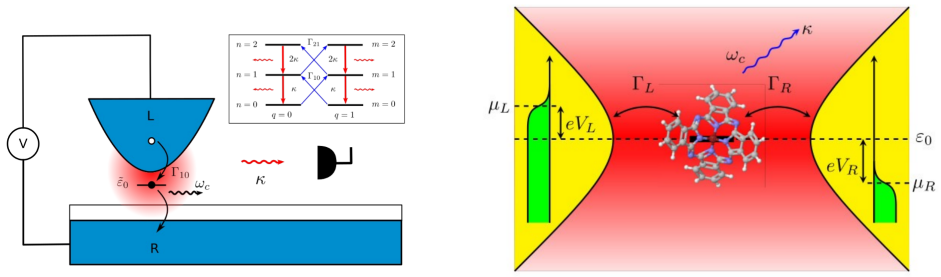

Figure 1.7: Representation of a current-driven STM plasmonic nanojunction. The molecule is shown as a single electronic level of energy $\tilde{\varepsilon}_0$. In presence of a bias-voltage V, electrons from the STM apex (L) or from the substrate (R) can tunnel to the electronic level, emitting a cavity plasmon of frequency ω_c. The former decays with rate κ, and a photon is emitted (red wavy arrow) that is finally collected by a detector (in black) with detection-yield η. Adapted from our recent Refs. [9],[107].

molecular junction (SLM) presented in Fig. 1.7

$$H \quad = \quad H_{\rm S} + H_{\rm B} + H_{\rm I}\,, \tag{1.35}$$

with $H_{\rm S}$ the Hamiltonian describing *the "molecule + plasmon mode" system as a whole*, $H_{\rm B}$ the bath Hamiltonian containing *the electronic and electromagnetic environments* and $H_{\rm I}$ the tunneling Hamiltonian at the origin of system-environment coupling and *tunneling of electrons (photons) at the origin of the electronic (photonic) current*. The "system" Hamiltonian is written as

$$H_{\rm S} \quad = \quad \varepsilon_0 d^\dagger d \;+ \omega_c a^\dagger a + \left(a + a^\dagger\right)\left(\Lambda_{\rm m} d^\dagger d + \cdots\right)\,, \tag{1.36}$$

with $d^\dagger$ the creation operator for an electron on the single level of energy ε_0 and $a^\dagger$ the creation operator for the plasmon mode of frequency ω_c. The last term contains the molecule-plasmon coupling operator that couples the dot charge fluctuations to the plasmonic electric field, with a coupling strength $\Lambda_{\rm m} = \lambda\omega_c$ with λ the dimensionless coupling strength. The corresponding coupling strength is given by the matrix element

$$\Lambda_{\rm m} = -e\int d^3r |\phi_d\left(\vec{r}\right)|^2 V_\perp\left(\vec{r}\right)\,, \tag{1.37}$$

with $\phi_d\left(\vec{r}\right)$ the dot electronic wave function and $V_\perp\left(\vec{r}\right) = -i\omega_c\int_{\mathcal{C}(\vec{r}_0,\vec{r})}\vec{A}(\vec{l})\cdot d\vec{l}$ the photonic pseudo-potential [29] obtained as the integral of the cavity electrical field $-i\omega_c\vec{A}(\vec{l})$ ($\vec{A}$ is the vector potential) on a path $\mathcal{C}\left(\vec{r}_0,\vec{r}\right)$ connecting any reference point $\vec{r}_0$ to the point $\vec{r}$. The coupling term $\Lambda_{\rm m}$ has a simple physical interpretation: *it stands for the work a tunneling electron has to perform against quantum vacuum fluctuations of the plasmonic field in the STM gap along the path it follows in an elementary tunneling event from one lead to the molecule.* We estimated in our Ref. [107] that, *due to the small cavity mode volume of the plasmonic cavity, this monopolar coupling strength can be actually quite large*, reaching upper values $\Lambda_{\rm m} \approx 0.1 - 2\omega_c$. This mechanism of coupling the plasmon mode to the charge fluctuations of the dot level should be differentiated from the different mechanism of direct coupling

of the plasmon mode to the electronic tunneling current across the tunneling gap which is usually much weaker in the experiments and provides a low quantum yield for photon emission of order 10^{-4} [93]. We note in Eq. 1.36 the presence of dots "$\cdots$" standing for additional terms in the interaction Hamiltonian describing *a modulation of the electronic tunneling from the leads to the dot induced by the photonic potential* as well as *a direct coupling between the electrons in the leads and the cavity plasmon mode.* The former terms of weaker amplitude are discussed in our Ref. [107] and will be neglected in our model. *The electronic and photonic environments are described by the bath Hamiltonian* $H_{\rm B}$ in Eq. 1.35 which is given by

$$H_{\rm B} = \sum_{\alpha k} \varepsilon_{\alpha k} c^\dagger_{\alpha k} c_{\alpha k} + \sum_q \omega_q b^\dagger_q b_q \,, \tag{1.38}$$

with $c^\dagger_{\alpha k}$ and $b^\dagger_q$ the creation operators for the electrons on the leads $\alpha = L, R$ with energy $\varepsilon_{\alpha k}$ and for the propagating photons of energy ω_q, respectively. Finally, the last term $H_{\rm I}$ in Eq. 1.35 is the system-environment tunneling term given by

$$H_{\rm I} = \sum_{\alpha k} \left[t_{\alpha k} c^\dagger_{\alpha k} d + t^*_{\alpha k} d^\dagger c_{\alpha k} \right] + \sum_q \left[l_q a^\dagger b_q + l^*_q b^\dagger_q a \right] , \tag{1.39}$$

with $t_{\alpha k}$ and l_q the electronic and photonic tunneling amplitudes respectively. As usual in quantum transport, we suppose that *the electrons in the leads are at thermal equilibrium with a population given by the Fermi distribution function* $f(\omega - \mu_\alpha)$ *at temperature* T *and chemical potential* μ_α *for the lead* α*. The photons in the electromagnetic environment are also supposed to be at thermal equilibrium at the same temperature* T which, being much smaller than the optical frequency, makes as if the electromagnetic environment was at zero temperature (corrections due to finite Bose distribution at temperature T are negligible).

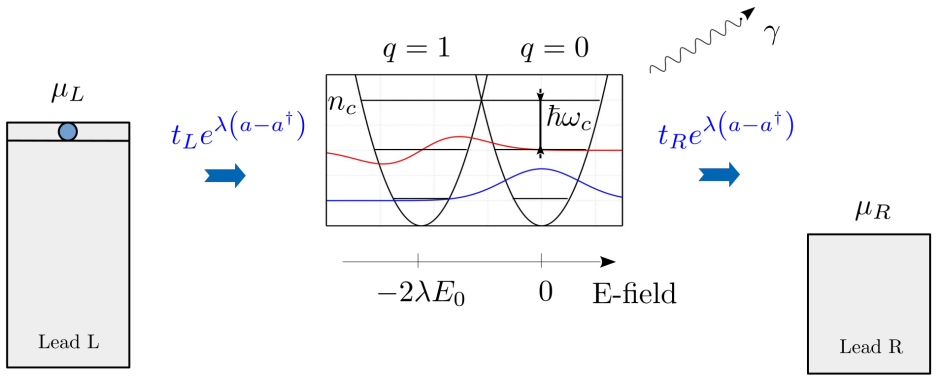

Figure 1.8: Representation of the eigenstates of the system Hamiltonian after Lang-Firsov transformation in Eq. 1.43. The eigenstates are the (q, n) manybody states corresponding to the dot charge states $q = 0, 1$ and plasmon mode occupancies $n \in \mathbb{N}$. There are two displaced harmonic ladders for the shifted plasmon mode written in Eq. 1.41 and the electronic tunneling terms are dressed by the plasmon mode as written in Eq. 1.42.

Lang-Firsov unitary transformation. The Hamiltonian written in the previous section shares similarities with the well known Holstein model describing electron-phonon inter-

actions in molecular junctions [61, 7, 79]. As in the former case, the spectrum of the Hamiltonian Eq. 1.35 is not known for arbitrary values of the junction parameters, especially in out of equilibrium situations where a bias voltage is applied between the leads that is at the origin of an electronic current. In this paragraph, we perform a Lang-Firsov unitary transformation on the Hamiltonian H. *This transformation enables to remove the explicit electron-photon interaction term from the system Hamiltonian* $H_{\rm S}$. This unitary transformation is defined as

$$U = e^{\lambda d^\dagger d(a-a^\dagger)}\,, \tag{1.40}$$

which acts by shifting the cavity plasmon mode operator $\tilde{a} = UaU^\dagger$ to the displaced operator depending on the dot charge

$$\tilde{a} = a - \lambda d^\dagger d\,, \tag{1.41}$$

and dresses the electronic dot operator $\tilde{D} = UdU^\dagger$ by a photon cloud operator coupling exponentially to the plasmonic electromagnetic environment

$$D = de^{\lambda(a-a^\dagger)}\,. \tag{1.42}$$

The new Hamiltonian $\tilde{H} = UHU^\dagger$ thus gets modified in the following way: *first the system Hamiltonian gets to a form that is diagonal in the charge and plasmon occupancy degrees of freedom*

$$\tilde{H}_{\rm S} \;=\; \tilde{\varepsilon}_0 d^\dagger d + \omega_c a^\dagger a\,, \tag{1.43}$$

with the shifted dot level position $\tilde{\varepsilon}_0 = \varepsilon_0 - \lambda^2\omega_c$. The eigenstates of $\tilde{H}_{\rm S}$ are the manybody states $|q,n\rangle$ corresponding to the charged (uncharged) state of the dot $q = 1(0)$ and to the number $n \in \mathbb{N}$ of quanta occupying the harmonic oscillator corresponding to the plasmon mode of frequency ω_c. They have eigenenergies $q\tilde{\varepsilon}_0 + n\omega_c$. *Both eigenstates and eigenenergies can be represented as two displaced harmonic ladders shown schematically in Fig. 1.8.* Finally, the Hamiltonian $H_{\rm I}$ coupling the system to the environment gets modified by the unitary transformation to

$$\tilde{H}_{\rm I} \;=\; \sum_{\alpha k}\left[t_{\alpha k}c^\dagger_{\alpha k}D + t^*_{\alpha k}D^\dagger c_{\alpha k}\right] + \sum_q\left[l_q\tilde{a}^\dagger b_q + l^*_q b^\dagger_q\tilde{a}\right]. \tag{1.44}$$

The electronic tunneling term is dressed by the plasmonic environment as written in Eq. 1.42: this is *a similar phenomenon to the dynamical Coulomb blockade theory describing the coupling of electrons tunneling to the electromagnetic environment in ultrasmall tunnel junctions [66].* Then the photon tunneling term couples to the displaced plasmonic field: this is a signature of *the possibility for slow charges fluctuations to couple to the high frequency plasmonic electromagnetic field.*

A comment about this transformed Hamiltonian. The transformed Hamiltonian $\tilde{H}$ removes the explicit plasmon-molecule coupling from the system Hamiltonian and displaced it into the tunneling Hamiltonian coupling the system to the environment. *This is well suited to perform an expansion into a weak sytem-bath interaction, while keeping the nonpertubative nature of the plasmon-molecule interactions given by the coupling strength* λ. We

also note that $\tilde{H}$ is the same Hamiltonian as the one describing the Franck-Condon physics induced by electron-phonon interactions that was studied in depth in molecular electronics [77, 78], expect that now the energy scales are quite different (the plasmon mode is in the high-frequency optical range).

1.3.3 Fermi Golden Rule and its consequences

Problematic. We want in this section to compute *the typical timescales associated to inelastic electronic tunneling of electrons and by photon emission out of the STM plasmonic junction*, as described by the microscopic Hamiltonian in the previous Sec. 1.3.2. The electronic and photonic environments will provide the necessary energy costs to induce incoherent transitions between the manybody states (q, n) of the system "plasmon + molecule" through the perturbation Hamiltonian $\tilde{H}_{\rm I}$ in Eq. 1.44. *We will compute the rates associated to those incoherent transitions using Fermi Golden Rule.*

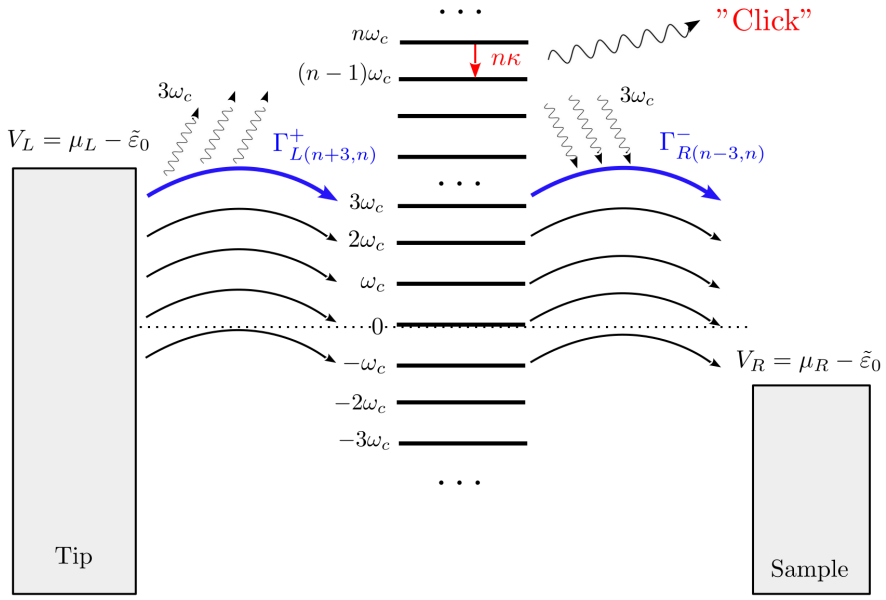

Figure 1.9: Representation of the incoherent transitions associated to inelastic electronic tunneling and photon emission out of the STM plasmonic cavity. The rate $\Gamma^+_L(n+3, n)$ in blue is the rate of tunneling of a single electron from left lead thus charging the dot and emitting three quanta in the plasmon mode. The rate $\Gamma^-_R(n-3, n)$ in blue is the rate of tunneling of a single electron from the dot to the right lead thus discharging the dot and absorbing three quanta in the plasmon mode. The rate κ is the rate at which single photons are emitted out of the cavity from the decay of the plasmon mode occupation by one quantum. Unpublished Fig.

Inelastic electronic tunneling rates. We first consider the incoherent electronic tunneling events coming from the photon-dressed electronic tunneling Hamiltonian in $\tilde{H}_{\rm I}$ (see

Eq. 1.44). The former Hamiltonian induces transitions of the form $(q,n) \to (\bar{q}=1-q,m)$ among the system manybody states with $\bar{q}=1-q$. *In such a transition, the charge-state of the dot is modified from $q=0$ to $q=1$ or from $q=1$ to $q=0$ for a charging or discharging event of the dot level respectively.* Moreover, it is accompanied by a modification of $m-n$ additional or lower number of quanta populating the cavity-plasmon mode. *If $m-n>0$ the corresponding transition is an inelastic tunneling event of a single electron mediated by the emission of $m-n$ quanta into the plasmon mode. On the other hand, if $m-n<0$ the inelastic tunneling event is mediated by absorption of $n-m$ quanta from the plasmon mode.* The specific case $m=n$ is an elastic tunneling event of a single electron in the molecular junction. We write $\Gamma^{+}_{\alpha(m,n)}$ the inelastic tunneling rate of a single electron emitted from lead $\alpha=L,R$ that charges the dot in the transition $(0,n)\to(1,m)$. The other rate associated to discharging of the dot is written $\Gamma^{-}_{\alpha(m,n)}$. Using Fermi Golden Rule, we obtain for those incoherent rates

$$\Gamma^{+}_{\alpha(m,n)} = \Gamma_\alpha |X_{n,m}|^2 f\left((m-n)\,\omega_c - V_\alpha\right) , \tag{1.45}$$

$$\Gamma^{-}_{\alpha(m,n)} = \Gamma_\alpha |X_{m,n}|^2 \left[1-f\left((n-m)\,\omega_c - V_\alpha\right)\right] , \tag{1.46}$$

with $\Gamma_\alpha \equiv 2\pi\sum_k |t_{\alpha k}|^2 \delta(E_F-\varepsilon_{\alpha k})$ the tunneling rate of electrons from the lead α to the dot level evaluated at Fermi energy. We note that we made *the wide band approximation which neglects the energy dependence of* Γ_α on the scale provided by the voltage around Fermi energy. The factor $X_{n,m}\equiv\langle n|\tilde{m}\rangle$ is the Franck-Condon overlap [78] between the state $|n\rangle$ of the cavity with empty dot and the displaced-state $|\tilde{m}\rangle$ of the cavity with occupied dot. Finally we introduced the lead voltage $V_\alpha=\mu_\alpha-\tilde{\varepsilon}_0$ which provides the relative distance in energy between the chemical potential of the lead and the position of the renormalized single level of the molecule. The expression of the rates $\Gamma^{\pm}_{\alpha(mn)}$ are dependent on temperature T, on the voltage drop V_α and on the tunneling rate Γ_α. *Upon modifying those electronic parameters of the junctions, it becomes possible to excite the plasmon mode by injecting an electronic current across the STM junction.* We illustrate in Fig. 1.9 the transition $\Gamma^{+}_{L(n+3,n)}$ (blue arrow) in which *an electron from the left lead charges the dot level and emits three plasmons in the junction.* Another transition rate $\Gamma^{-}_{R(n-3,n)}$ (blue arrow) is shown for which *an electron discharges the dot level to the right lead and absorbs three plasmons in the junction.*

Photon emission rate. The second type of transitions is induced by the photon tunneling Hamiltonian in $\tilde{H}_{\rm I}$ (see Eq. 1.44). *Those are transitions of the form $(q,n)\to(q,n-1)$ which do not change the charge state of the dot but decrease by one the number of cavity-plasmons. Those incoherent transitions are associated to the cavity losses through which single photons are emitted in the far field and later detected by a photon detector.* We write $\kappa_{(n-1,n)}$ the incoherent rate associated to such a transition the expression of which is given by

$$\kappa_{(n-1,n)} = n\kappa\,, \tag{1.47}$$

with $\kappa\equiv 2\pi\sum_q |l_q|^2\delta(\omega_c-\omega_q)$ the cavity damping rate. Here also we made a wide band approximation, evaluating this rate at the cavity optical frequency ω_c. One transition $\kappa_{(n-1,n)}$ is shown as a red arrow in Fig. 1.9. *In this transition a photon of frequency ω_c is emitted out of the STM plasmonic cavity and induces a "click" of the photon detector.* Finally, we make

a remark that the photon dressed tunneling Hamiltonian couples the displaced plasmonic field (see Eq. 1.41) to the electromagnetic far field. Thus, strictly speaking, the electromagnetic far field of the bath couples not only to the high frequency optical plasmon mode of the STM cavity, but also to lower frequency charge fluctuations of the single dot level occurring on a timescale $1/\Gamma_\alpha$. *It is clear physically that low frequency electronic current fluctuations always induce photon emission. The possibility to detect or not those additional lower frequency (MW) photons out of the plasmonic junction is a property of the photon detector that is used.* This question will be discussed in a new preprint in preparation [13] that is part of the PhD thesis of Andres Bejarano. In what follows, we will suppose that we have a photon detector with a bandwitdh centered on optical frequencies so that only optical photons at frequency ω_c are detected out of the STM plasmonic nanojunction.

Hierarchy of energy scales. In this paragraph we evaluate the typical energy scales associated to the previously derived incoherent transition rates. We estimate from experiments performed on current-induced STM tunnel junctions [73, 93] and STM molecular junctions [72] typical values of the parameters

1. The typical tunneling current $I \approx e\Gamma \approx 5 - 500$ pA.
2. The plasmon mode frequency $\omega_c \approx 2\frac{\text{eV}}{\hbar}$.
3. The cavity losses $\kappa = \frac{\omega_c}{Q} \approx 0.1\omega_c$ related to a quality factor $Q \approx 10$ of the STM cavity.
4. A temperature $T \approx 4 - 10$ K.

We thus end up with *a hierarchy of typical frequencies characterizing the physical problem* given by

$$\Gamma_\alpha \approx 10^{-5} - 10^{-4}\omega_c < T \approx 10^{-3}\omega_c < \kappa \approx 10^{-1}\omega_c < \omega_c\,. \tag{1.48}$$

In the previous inequality, the condition $\Gamma_\alpha < T$ plus the fact that the molecules are deposited on an insulated substrate thus preventing charge transfer and fluorescence quenching due to the underlying metallic substrate enables to consider that *electronic tunneling is a sequential process, namely the electrons that tunnel from one lead to the dot loose their phase coherence fast enough on timescale $1/T$ before the next coming electron enters the dot on the slower timescale $1/\Gamma_\alpha$.* In parallel, the condition $\kappa < \omega_c$ corresponds to an electromagnetic bath that decays to equilibrium on the fast timescale $1/\omega_c$ compared to the slower plasmon mode that relaxes with the cavity damping time $1/\kappa$. *In both cases of electronic and electromagnetic environments, one can thus treat perturbatively the coupling between the system and such environments, making use of a Born-Markov approximation for describing the plasmon-molecule dynamics.* We derived the corresponding generalized master equation describing the dynamics of the system reduced density matrix in our Ref. [107]. In our more recent preprint in preparation [14] we extended this approach to a two level model of the plasmonic nanojunction. We solved and computed the electronic currents, the power emission spectra and second order correlation spectra characterizing the emitted light field by such STM nanojunctions. *In this section, however, we choose another approach and decide*

to present all computations of physically relevant observables within a rate equation approach (when possible) where the rates are computed using Fermi Golden Rule. This is so not only because of the simplicity of this way of presenting, but also because most of the physics we discuss can be understood with Fermi Golden Rule. The eventual limitations of such an approach will be enlightened and the way to eventually cure it will be briefly given.

1.3.4 The rate equation dynamics of plasmon-molecule interactions

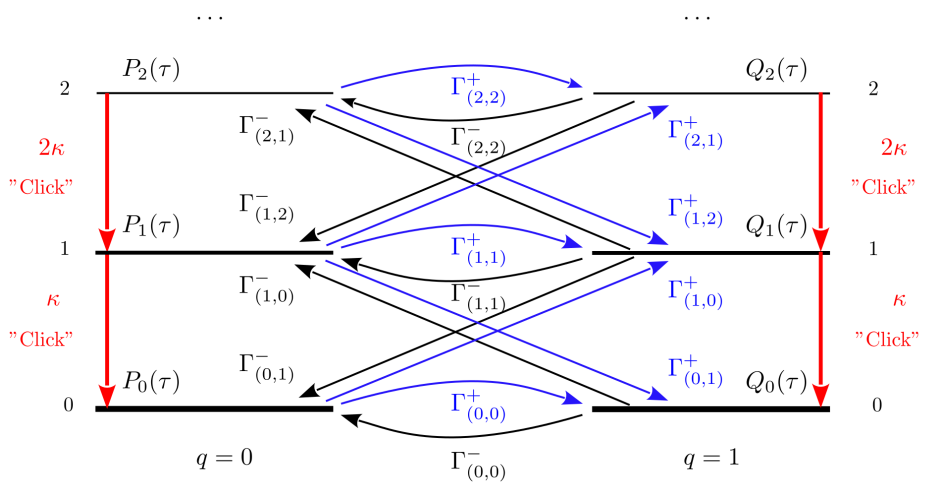

Figure 1.10: Representation of the rate equation connecting the manybody states of the plasmon-molecule system in the case $|V_L|, |V_R| < 2\omega_c$. The rates $\Gamma^+_{m,n}$ corresponding to inelastic tunneling of electrons and charging of the single level are shown as blue arrows while the rates $\Gamma^-_{m,n}$ corresponding to discharging of the single level are represented by black arrows. The rates $\kappa_{(m,n)}$ associated to photon emission out of the STM cavity are shown as red arrows.

Writing of the rate equation. We investigate the dynamics of the manybody states (q,n) describing the molecule-plasmon system. We define $P_n(t) \equiv P_{(0,n)}(t)$ the probabilities of occupying the state $(0,n)$ of the ladder of states with uncharged dot $q=0$ and $Q_n(t) \equiv P_{(1,n)}(t)$ the probabilities of occupying the state $(1,n)$ of the ladder of states with charged dot $q=1$. *Those time-dependent probabilities are solution of a bi-partite rate-equation (RE) with incoherent rates computed in Sec. 1.3.3.* We obtain

$$\dot{P}_n(t) = \sum_{m=0}^{+\infty} \left\{ \Gamma^-_{(n,m)} Q_m(t) - \Gamma^+_{(m,n)} P_n(t) \right\} + \kappa \left\{ (n+1) P_{n+1}(t) - n P_n(t) \right\} , \quad (1.49)$$

$$\dot{Q}_n(t) = \sum_{m=0}^{+\infty} \left\{ \Gamma^+_{(n,m)} P_m(t) - \Gamma^-_{(m,n)} Q_n(t) \right\} + \kappa \left\{ (n+1) Q_{n+1}(t) - n Q_n(t) \right\} , \quad (1.50)$$

with given initial conditions $(P_n(0), Q_n(0))$ and with the rates $\Gamma^\pm_{(m,n)} \equiv \Gamma^\pm_{L(m,n)} + \Gamma^\pm_{R(m,n)}$ obtain as the contribution of both leads. This a bi-partite RE with two harmonic ladders

that are coupled by inelastic tunneling events changing the charge state of the single level. The RE in Eqs. 1.49,1.50 is shown schematically in Fig. 1.10 for the case $|V_L|, |V_R| < 2\omega_c$. *At the "sweet spot" corresponding to an electron-hole symmetric junction for which* $\Gamma_L = \Gamma_R = \Gamma$ *and* $V_L = -V_R$ *the RE takes a simpler form.* Indeed in this regime, the tunneling rates get independent of the charge-state of the dot

$$\Gamma^{+}_{(m,n)} \;=\; \Gamma^{-}_{(m,n)} \equiv \Gamma_{(m,n)}\,, \tag{1.51}$$

thus the occupation probabilities of the cavity-mode in each ladder are equal $P_n(t) = Q_n(t)$. Introducing $\pi_n(t) = P_n(t) + Q_n(t)$ after integrating-out the dot charge states, we obtain the simpler RE at the "sweet spot"

$$\dot{\pi}_n(t) \;=\; \sum_{m=0}^{+\infty} \left\{\Gamma_(n,m)\pi_m(t) - \Gamma_{(m,n)}\pi_n(t)\right\} + \kappa\left\{(n+1)\pi_{n+1}(t) - n\pi_n(t)\right\}\,, \tag{1.52}$$

with initial conditions $\pi_n(0)$.

Formal solution of the rate equation. The RE in Eqs. 1.49,1.50 are in general not solvable analytically, especially in the case shown in Fig. 1.10 where two infinite ladders of states are coupled one to each other. *The stationary out of equilibrium population thus results from a delicate balance between the incoherent drive of the plasmonic cavity induced by inelastic tunneling of electrons and the damping of the cavity that tends to relax the cavity population to its ground state.* We can however solve formally the RE and grasp the behavior of its time-dependent solution since the RE is a system of linear equations. For that purpose, *we first eliminate the redundant degree of freedom contained into the normalization condition of the probability of the manybody states*, namely we substitute in the RE the population $P_0(t) = 1 - Q_0(t) - \sum_{n=1}^{+\infty}\left(P_n(t) + Q_n(t)\right)$ by its expression in terms of all the other ones. The resulting system of linear equation then becomes invertible. For solving generally the RE, we first define $\underline{\pi}(t) \equiv [Q_0(t), P_1(t), Q_1(t), \cdots, P_n(t), Q_n(t), \cdots]$ the vector of which components are given by the population of the manybody states. We then rewrite the RE that connects those populations among themselves in the following algebraic form

$$\dot{\underline{\pi}}(t) = \hat{\Gamma}\underline{\pi}(t) + \underline{q}\,, \tag{1.53}$$

with $\hat{\Gamma}$ the invertible rate-matrix and $\underline{q}$ a constant vector due to the substitution of $P_0(t)$ in terms of the all the other populations. The RE is complemented with an initial condition $\underline{\pi}(0)$. Its solution is formally obtained as

$$\underline{\pi}(t) = e^{\hat{\Gamma}t}\underline{\pi}(0) + \left(\hat{\mathrm{Id}} - e^{\hat{\Gamma}t}\right)\underline{\pi}^{(\mathrm{st})}\,, \tag{1.54}$$

with $\underline{\pi}^{(\mathrm{st})}$ the stationary population given by

$$\underline{\pi}^{(\mathrm{st})} \;=\; -\hat{\Gamma}^{-1}\underline{q}\,. \tag{1.55}$$

We can further analyse the behavior of Eq. 1.54 by expanding it in terms of eigenmodes of the RE. For this purpose, we define the right and left eigenvectors $\underline{v}_\lambda$ and $\underline{w}_\lambda$ associated to the λ (real and strictly negative) eigenvalue of the $\hat{\Gamma}$-matrix, such that

$$\hat{\Gamma}\underline{v}_\lambda \;=\; \lambda\underline{v}_\lambda\,, \tag{1.56}$$

$$\underline{w}^t_\lambda\hat{\Gamma} \;=\; \lambda\underline{w}^t_\lambda\,. \tag{1.57}$$

The solution of the RE given in Eq. 1.54 can thus be expressed as a linear superposition of eigenmodes with coefficients given by the initial condition

$$\underline{\pi}(t) \;=\; \sum_{\lambda} \left(1-e^{\lambda t}\right) \left[\underline{w}_{\lambda}^{t} \cdot \left(\underline{\pi}^{(\mathrm{st})} - \underline{\pi}(0)\right)\right] \underline{v}_{\lambda} + \underline{\pi}(0)\,. \tag{1.58}$$

This expression is exact and shows that $\underline{\pi}(t)$ is the superposition of damped exponential functions $(\lambda < 0)$ towards the stationary state, with damping rate given by the eigenvalues λ of the rate-matrix. In particular, for times $t \geq \frac{1}{\lambda_m}$ larger than the inverse of the eigenvalue $\lambda_m = \max_{\lambda}(\lambda)$ that is closer to zero, the time-dependent population dynamics takes the following simple asymptotic form

$$\underline{\pi}(t) \;\approx\; \left(1-e^{\lambda_m t}\right) \left[\underline{w}_{\lambda_m}^{t} \cdot \left(\underline{\pi}^{(\mathrm{st})} - \underline{\pi}(0)\right)\right] \underline{v}_{\lambda_m} + \underline{\pi}(0)\,. \tag{1.59}$$

Open question. The formal solution of the RE written in Eq. 1.58 generalizes the analytical expressions written for the TLS system in Sec. 1.2.1 to the case of a bi-partite ladder of states describing light emission in a single-level plasmonic nanojunction. *However, we still do not have written explicitly the connection of those populations to the actually measured observables.*

1.3.5 Computing the current-voltage characteristics

Analytical expression for the electronic current. We close this section by computing and showing briefly the current-voltage characteristic in the single level model. For that purpose, we first express the tunneling current in terms of the stationary occupation probabilities of the manybody states of the junction obtained in the previous Sec. 1.3.4. We note that since we look for dc currents, the electronic currents computed at left electrode $< I_L >$ or at right electrode $< I_R >$ do coincide, thus expressing that no charge is accumulated in average on the dot in stationary state. Within Fermi Golden Rule and RE approximations, a simple balance or charge conservation at the left electrode enables to express the $< I_L >$ current as

$$< I_L > \;=\; -e \sum_{n=0}^{+\infty} \sum_{m=0}^{+\infty} \left\{ \Gamma^{+}_{L(m,n)} P_n^{(\mathrm{st})} - \Gamma^{-}_{L(m,n)} Q_n^{(\mathrm{st})} \right\}\,. \tag{1.60}$$

This expression has a simple physical interpretation: the first term gives *the contribution to current of tunneling events starting from the left electrode and charging the dot with emission of $m-n$ plasmons (when this quantity is positive) or absorption of $n-m$ plasmons (when this quantity is positive) inside cavity.* The second term has a similar interpretation is terms of discharging events of the dot. Following the discussion of energy scales in Sec. 1.3.3, we suppose that $\Gamma < T < \kappa < \omega_c$. In this limit where $\kappa \gg \Gamma$ is the fastest relaxation rate, the cavity damping is so large that we anticipate the cavity states to be nearly not populated in stationary states (see also Fig. 1.10), namely that

$$P_n^{(\mathrm{st})} \;\approx\; \delta_{n,0} P_0^{(\mathrm{st})}\,, \tag{1.61}$$

$$Q_n^{(\mathrm{st})} \;\approx\; \delta_{n,0} Q_0^{(\mathrm{st})}\,. \tag{1.62}$$

Placing ourselves at the "sweet spot" with symmetric tunneling $\Gamma_L = \Gamma_R = \Gamma$ and bias voltage $V_L = -V_R = \frac{V}{2}$, we have that $P_0^{(\mathrm{st})} = Q_0^{(\mathrm{st})} \approx \frac{1}{2}$ and using the expression of the rates written in Eqs. 1.45,1.46, we obtain for the expression of the current within this large-κ approximation

$$< I_L > \approx -e\frac{\Gamma}{2}\sum_{m=0}^{+\infty} e^{-\lambda^2}\frac{\lambda^{2n}}{n!}\left\{f\left(m\omega_c - \frac{V}{2}\right) - f\left(m\omega_c + \frac{V}{2}\right)\right\}. \qquad (1.63)$$

This expression means that each time the voltage crosses a plasmonic sideband, one or several plasmons might be emitted in the junction due to inelastic tunneling of single electrons. The linewidth of those jumps in the current is given by the temperature in this model. The sidebands are populated with a Poissonian distribution depending on the plasmon-molecule coupling strength λ. The typical scale for electron tunneling is $e\Gamma$ as expected in the sequential tunneling regime.

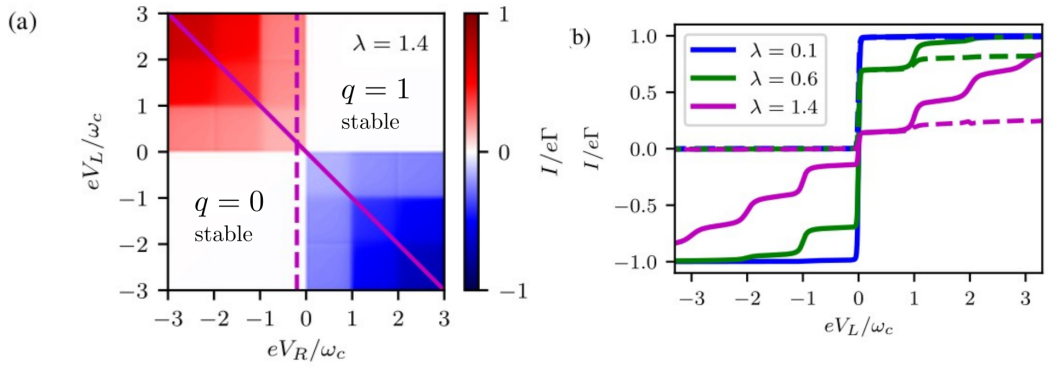

Figure 1.11: a) Stability diagram as a function of (V_L, V_R) of the single level model for $\lambda = \sqrt{2}$. The charge states $q = 0$ and $q = 1$ are stable in the white sectors while the colored sectors correspond to the bias window where electronic tunneling occurs. b) Cuts of the electronic current-voltage $I(V_L)$ characteristics along the symmetric voltage drop (plain curves) and asymmetric ones (dashed curves) upon varying both the voltage V_L and the plasmon-molecule coupling strength λ. Jumps occur each time the voltage crosses an inelastic threshold for emitting one or several plasmons in the junction. Adapted from our Ref. [107].

Numerical calculation of the electronic current. For completeness, we show in Fig. 1.11 the $I - V$ characteristics as a function of (V_L, V_R) computed in our Ref. [107] for various values of the plasmon-molecule coupling strength, in the regime of symmetric tunneling rates $\Gamma_L = \Gamma_R$. The panel a) exemplifies the stability diagram of the dot level coupled to the plasmon mode, with the white sectors corresponding to the region of parameters where the charge states $q = 0$ and $q = 1$ of the dot are stable. Single electron tunneling occurs in the colored sectors. We show in panel b) a cut of the $I(V)$ along either the symmetric bias situation (plain curves) or asymmetric bias (dashed ones). *The inelastic thresholds (position and height) are well reproduced at the "sweet spot" (plain curves) by the approximate output of the RE given in Eq. 1.63.* However, their linewidth is not given by temperature but rather

by the damping rate κ of the cavity. Indeed, since $\kappa > T$, in Ref. [107] we had to take into account the finite lifetime of the plasmon mode which necessitates to resummate the perturbation expansion in the photon tunneling Hamiltonian to all orders. *This resummation goes beyond the RE and Fermi Golden Rule approximation we made in this section.*

1.4 Bunching and antibunching in a single level plasmonic nanojunction

In this section, we would like to investigate the photon emission statistics of the single level plasmonic nanojunction presented in Sec. 1.3, generalizing the approach presented for the paradigmatic two-level system in Sec. 1.2. For that purpose, we provide in Sec. 1.4.1 a theoretical framework based on the rate equation to compute the second order correlation function characterizing the statistics of light emitted by this single level junction. Exact analytical expressions are given for it at the junction symmetric "sweet spot". The related $g^{(2)}(\tau)$ signals are computed and shown in Sec. 1.4.2. A crossover from bunching to antibunching of the photon statistics is predicted and analyzed at the "sweet spot".

1.4.1 Expression of the second order correlation function

General formulation. We derive in this section the relation between the second order correlation function $g^{(2)}(\tau)$ and the conditional probabilities that are solution of the rate equation written in Eqs. 1.49,1.50 with given initial conditions. This is the direct generalization of Eq. 1.5 that is only valid for the two-level system. *We target the regime in which $\kappa \gg \Gamma$ is the largest relaxation rate, following in that the hierarchy of energy scales written in Eq. 1.48.* In this range of parameters, we expect that the populations of the manybody states of the system formed by the single molecular level coupled to the plasmon mode fulfill the following hierarchy in the stationary state occupancies (see also Fig. 1.10)

$$P_0^{(\mathrm{st})}, Q_0^{(\mathrm{st})} \gg P_1^{(\mathrm{st})}, Q_1^{(\mathrm{st})} \gg P_2^{(\mathrm{st})}, Q_2^{(\mathrm{st})} \gg \cdots . \tag{1.64}$$

This hierarchy is also reminiscent of the approximation we used for computing the electronic tunneling current in Eqs. 1.61,1.62. *It basically amounts to perform an asymptotic expansion of the rate equation in the small parameter Γ/κ: the higher the excitation energy of a state, the lower its probability.* We also restrict ourselves to the range of voltage bias $|V_L|, |V_R| < 2\omega_c$. *Those restrictions enable to simplify the problem of the bi-partite infinite ladder of manybody states due to the only remaining possibility in this regime to excite single photons in the junction and thus the possibility to truncate the RE to at most $n = 2$ plasmon excitations.* The truncated rate equation is shown in Fig. 1.10 with the probabilities that remain to be computed $(P_0(t), Q_0(t), P_1(t), Q_1(t), P_2(t), Q_2(t))$. The first Glauber correlation generalizing Eq. 1.3 is provided by

$$G_1^{\mathrm{st}} = \kappa \left\{ P_1^{(\mathrm{st})} + Q_1^{(\mathrm{st})} + 2 \left[P_2^{(\mathrm{st})} + Q_2^{(\mathrm{st})} \right] \right\} , \tag{1.65}$$

and is then expressed as *the rate κ of photon emission out of the STM gap times the contribution of each populated excited state of the cavity with charge or uncharged dot.* We note that the contribution to the decay rate of the states with two plasmons $n = 2$ inside cavity is multiplied by two compared to the one of the state with only one plasmon. The non-normalized second order Glauber correlation function generalizing Eq. 1.10 then becomes

$$\begin{aligned} G_2(\tau) &= \kappa^2 \Bigg\{ P_1^{(\mathrm{st})} \left[P_1(\tau)\Big|_{(P_0,0)} + Q_1(\tau)\Big|_{(P_0,0)} + 2\left(P_2(\tau)\Big|_{(P_0,0)} + Q_2(\tau)\Big|_{(P_0,0)} \right) \right] \\ &+ Q_1^{(\mathrm{st})} \left[P_1(\tau)\Big|_{(Q_0,0)} + Q_1(\tau)\Big|_{(Q_0,0)} + 2\left(P_2(\tau)\Big|_{(Q_0,0)} + Q_2(\tau)\Big|_{(Q_0,0)} \right) \right] \\ &+ 2P_2^{(\mathrm{st})} \left[P_1(\tau)\Big|_{(P_1,0)} + Q_1(\tau)\Big|_{(P_1,0)} + 2\left(P_2(\tau)\Big|_{(P_1,0)} + Q_2(\tau)\Big|_{(P_1,0)} \right) \right] \\ &+ 2Q_2^{(\mathrm{st})} \left[P_1(\tau)\Big|_{(Q_1,0)} + Q_1(\tau)\Big|_{(Q_1,0)} + 2\left(P_2(\tau)\Big|_{(Q_1,0)} + Q_2(\tau)\Big|_{(Q_1,0)} \right) \right] \Bigg\} \\ &, \end{aligned} \tag{1.66}$$

where we introduced the conditional probabilities like $P_1(\tau)\Big|_{(P_0,0)}$ to be in state $(q = 0, n = 1)$ at time τ knowing the system was in state $(q = 0, n = 0)$ at time 0. *This expression corresponds to the sum of all possible ways, starting from a state of the system just after a first photon emission event, to excite the plasmonic nanojunction again at time τ and emit a second photon.* At zero time delay, this correlation function becomes

$$G_2(0) = 2\kappa^2 \left\{ P_2^{(\mathrm{st})} + Q_2^{(\mathrm{st})} \right\} . \tag{1.67}$$

From Eq. 1.65,1.66,1.67, we can express formally the normalized second order correlation function as

$$g^{(2)}(\tau) = \frac{G_2(\tau)}{\left(G_1^{\mathrm{st}}\right)^2} , \tag{1.68}$$

$$g^{(2)}(0) = \frac{2\left\{ P_2^{(\mathrm{st})} + Q_2^{(\mathrm{st})} \right\}}{\left\{ P_1^{(\mathrm{st})} + Q_1^{(\mathrm{st})} + 2\left[P_2^{(\mathrm{st})} + Q_2^{(\mathrm{st})} \right] \right\}^2} . \tag{1.69}$$

In general, the conditional probabilities and stationary probabilities entering into the expression of $g^{(2)}(\tau)$ cannot be found analytically and have to be computed analytically. Looking at the rate equation in Eqs. 1.49,1.50, we see that *the population dynamics is in general a multiscale dynamics involving both the energy scale κ associated to photon damping out of the plasmonic cavity, the electronic tunneling rates Γ_L, Γ_R and the inelastic tunneling rates $\Gamma^{\pm}_{(m,n)}$.* We thus anticipate a rich stochastic dynamics describing the photon emission statistics even in the simpler model of single level molecular junction.

Particular case: populations at the symmetric "sweet spot". We consider now the specific "sweet spot" case described in Sec. 1.3.4 for which the tunneling to the leads and voltage bias are symmetric and close to the first inelastic threshold for photon emission.

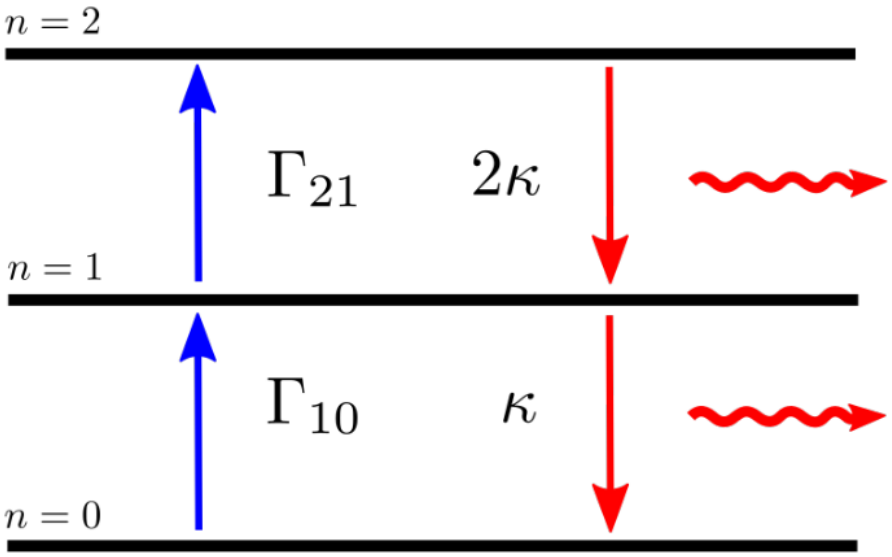

Figure 1.12: Graphical representation of the truncated rate equation giving the cavity-mode populations $\pi_n(t)$ in the case of a symmetric junction at the "sweet spot" and close to the first inelastic threshold for photon emission. Red (blue) downward (upward) arrows stand for dominant (subdominant) transition rates induced by cavity-damping (inelastic tunneling of electrons) . Adapted from our recent Ref. [9].

The rate equation has a simpler form derived in Eq. 1.52 that involves only the occupation probability $\pi_n(t)$ of the plasmon mode (the two ladder with different charge states having the same probability of occupancy). The truncated RE is shown in Fig. 1.12, which is a specific case of Fig. 1.10. In this regime, the dominant transition rates are represented in Fig. 1.12 as red downward arrows for cavity-damping rates (κ and 2κ) and blue upward arrows for inelastic tunneling rates of single electrons across the STM junction (Γ_{10} and Γ_{21}). After eliminating $\pi_0(t)$, one obtains the reduced RE written in Eq. 1.53 for the vector of populations $\underline{\pi}(t) = [\pi_1(t), \pi_2(t)]$ with a reduced matrix of rate $\hat{\Gamma}$ given by

$$\hat{\Gamma} = \begin{bmatrix} -(\kappa + \Gamma_{10} + \Gamma_{21}) & 2\kappa - \Gamma_{10} \\ \Gamma_{21} & -2\kappa \end{bmatrix} . \tag{1.70}$$

In the limit of large $\kappa \gg \Gamma$ discussed in the previous paragraph, using the hierarchy of probabilities written in Eq. 1.64, we find the following asymptotic expressions for the eigenvalues $\lambda_\pm$ of the reduced rate matrix $\hat{\Gamma}$ in Eq. 1.70 as

$$\lambda_+ \approx -(\kappa + \Gamma_{10} - \Gamma_{21}) \approx -\kappa , \tag{1.71}$$
$$\lambda_- \approx -2(\kappa + \Gamma_{21}) \approx -2\kappa , \tag{1.72}$$

as well as the stationary populations of the STM cavity plasmon-mode

$$\pi_1^{\rm st} \approx \frac{\Gamma_{10}}{\kappa}\pi_0^{\rm st} , \tag{1.73}$$
$$\pi_2^{\rm st} \approx \frac{\Gamma_{21}}{2\kappa}\pi_1^{\rm st} , \tag{1.74}$$
$$\pi_0^{\rm st} = 1 - \pi_1^{\rm st} - \pi_2^{\rm st} \approx 1 . \tag{1.75}$$

The corresponding approximate solution for the time-dependent populations $\underline{\pi}(t)$ with arbitrary initial condition $\underline{\pi}(0) = [\pi_1(0), \pi_2(0)]$ follows as

$$\pi_1(t) \approx \pi_1^{\rm st} + \left\{\pi_1(0) + 2\pi_2(0) - \left[\pi_1^{\rm st} + 2\pi_2^{\rm st}\right]\right\} e^{-\kappa t} + 2\left\{\pi_2^{\rm st} - \pi_2(0)\right\} e^{-2\kappa t}\,, \quad (1.76)$$

$$\pi_2(t) \approx \pi_2^{\rm st} + \left\{\pi_2(0) - \pi_2^{\rm st}\right\} e^{-2\kappa t}\,, \quad (1.77)$$

$$\pi_0(t) = 1 - \pi_1(t) - \pi_2(t)\,. \quad (1.78)$$

Exact asymptotic solution for $g^{(2)}(\tau)$ at the "sweet spot". Using the previous results for the populations of the plasmon mode at "sweet spot" and the expressions of the two Glauder correlation functions of the emitted field out of the plasmonic cavity written in Eqs. 1.65,1.66, we find the asymptotic analytical expressions

$$G_1^{\rm st} \approx \kappa\left(\pi_1^{\rm st} + 2\pi_2^{\rm st}\right) = \frac{\Gamma_{10}(\kappa + \Gamma_{21})}{\kappa} \approx \Gamma_{10}\,, \quad (1.79)$$

$$G_2^{\rm st}(\tau) \approx \kappa^2\left\{\left(\pi_1^{\rm st} + 2\pi_2^{\rm st}\right)^2\left(1 - e^{-\kappa\tau}\right) + 2\pi_2^{\rm st} e^{-\kappa\tau}\right\}\,, \quad (1.80)$$

from which the normalized $g^{(2)}(\tau)$ correlation function of emitted photons is obtained

$$g^{(2)}(\tau) \approx 1 + e^{-\kappa\tau}\left(g^{(2)}(0) - 1\right)\,, \quad (1.81)$$

$$g^{(2)}(0) = \frac{2\pi_2^{\rm st}}{\left(\pi_1^{\rm st} + 2\pi_2^{\rm st}\right)^2} \approx \frac{\Gamma_{21}}{\Gamma_{10}} = \frac{\left(2 - \lambda^2\right)^2}{2}\,. \quad (1.82)$$

Those expression for the second order correlation function of the light emitted by a single level plasmonic nanojunction recover the ones we obtained in our Refs. [107, 9]. They are only valid at the high symmetry "sweet spot" of the junction.

1.4.2 Statistics of photon emission in the single level model

Analysis of the second order correlation function. We show in Fig. 1.13 the normalized second order correlation function $g^{(2)}(\tau)$ of the emitted photon field as a function of time τ. This curve is computed at the symmetric "sweet spot" and is obtained numerically from a Monte Carlo simulations (dot and triangle curves) which is equivalent to solve the RE written in Eq. 1.49,1.50. The voltage-bias is fixed at the first inelastic threshold for photon-emission ($eV = 2\hbar\omega_c$) and the photon detection is perfect ($\eta = 1$). The outcome of the analytical formula written in Eq. 1.81 are shown as plain curves for comparison. A very good agreement between the Monte Carlo and analytical calculation is obtained in the whole range of plasmon-molecule coupling strenght. *We thus find that, at the "sweet spot" and in the large κ limit, the $g^{(2)}(\tau)$ correlation function evolves exponentially in time from $g^{(2)}(0)$ with the cavity-damping rate κ.* The convergence of $g^{(2)}(\tau)$ to 1 is due to the fact that two distinct photon emission events separated by a time-interval $\tau \gg 1/\kappa$ become independent. We find however that, depending on the plasmon-molecule coupling strength λ, the behavior of the second order correlation function is predicted to be quite different (increasing or decreasing function), namely that

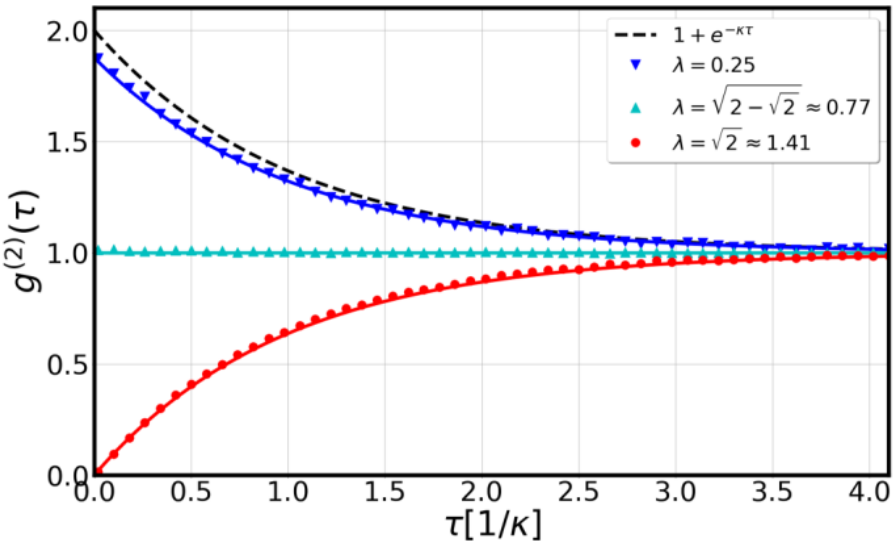

Figure 1.13: Second-order correlation function $g^{(2)}(\tau)$ for the emitted photons as a function of time τ, obtained from a Monte Carlo simulations (averaged over 40 runs) that is equivalent to solve numerically exactly the RE written in Eq. 1.49,1.50. Blue lower triangles are obtained for a plasmon-molecule coupling strength $\lambda = 0.25$, cyan upper triangles for $\lambda = \sqrt{2-\sqrt{2}} \approx 0.77$ and red dots for $\lambda = \sqrt{2} \approx 1.41$. Plain curves are the analytical results from Eq. 1.81. Parameters corresponding to the symmetric "sweet spot": $\eta = 1$, $\kappa = k_B T/\hbar = 0.1\omega_c$, $\Gamma_L = \Gamma_R = \Gamma = 0.01\omega_c$, and $V_L = -V_R = V/2 = \hbar\omega_c$. Adapted from Ref. [9].

1. For weak coupling $\lambda \ll 1$, the second order correlation function exhibits a behavior $g^{(2)}(\tau) \leq g^{(2)}(0)$ on the whole time-range with $g^{(2)}(0) \approx 2 > 1$. *Those conditions are a signature of a bunching behavior of the photon emission statistics, for which the emitted photons tend to be emitted by packets at short delay times.*

2. *The opposite antibunching behavior is obtained for* $\lambda = \sqrt{2} \approx 1.41$ *which is characterized by* $g^{(2)}(\tau) \geq g^{(2)}(0)$ *on the whole time range with* $g^{(2)}(0) \approx 0 < 1$. The photons tend to be emitted one by one at short delay times, like in a single photon emitter.

3. At the critical point $\lambda = \sqrt{2-\sqrt{2}} \approx 0.77$, we find that $g^{(2)}(\tau) = g^{(2)}(0) = 1$, namely *the photon emission events are uncorrelated and the statistics of photon emission is Poissonian in this regime.*

Upon increasing the plasmon-molecule coupling strength λ we find a crossover from photon-bunching to photon-antibunching in the second order correlation function. This result was derived for the first time in our recent Refs. [107, 9].

Analysis of the bunching regime. We interpret the results of the previous paragraph first in the case of weak plasmon molecule coupling $\lambda \ll 1$. While this case is described approximately well by Eq. 1.82 which predicts $g^{(2)}(0) \approx 2$ in the low coupling limit, the

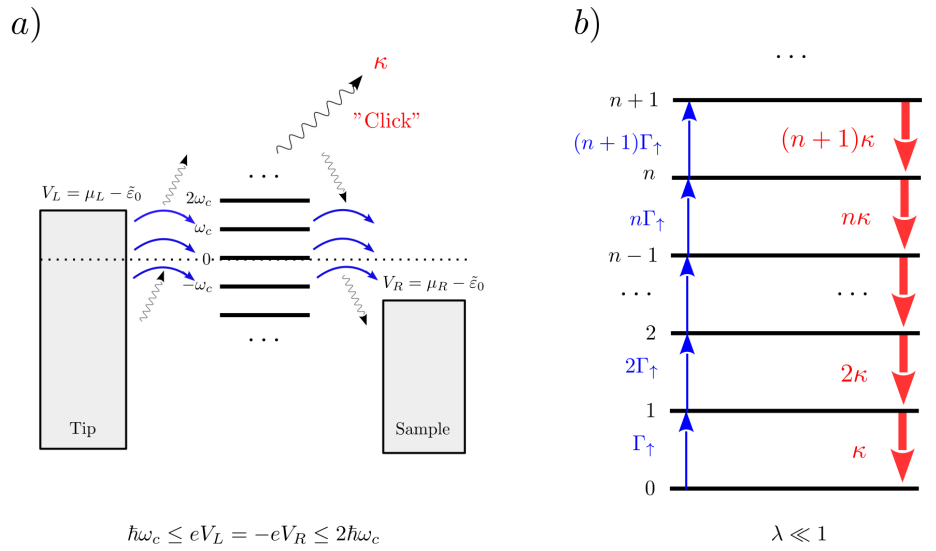

Figure 1.14: a) Representation of the incoherent transitions associated to inelastic electronic tunneling and photon emission out of the STM plasmonic cavity at the "sweet spot", close to the first inelastic threshold $2\omega_c > V_L = -V_R \geq \omega_c$, and with low plasmon-molecule coupling strength $\lambda \ll 1$. The main inelastic tunneling rate for plasmon emission available in this bias window are $\Gamma_{(n+1,n)} \equiv (n+1)\Gamma_\uparrow$. b) Infinite ladder of the states of plasmonic occupation in this regime. Unpublished Fig.

understanding of the physical mechanism at the origin of this value necessitates to take into account the whole ladder of states that might be reached in this regime (see Fig. 1.14-b)). Indeed, at the "sweet spot", close to the first inelastic threshold ($V_L = -V_R \geq \omega_c$), *the only inelastic tunneling rates at the origin of plasmon emission involve the emission of a single plasmon* (see Fig. 1.14-a)) and are obtained in the limit $\lambda \to 0$ from the expression of the Franck Condon rates in Eq. 1.51 as

$$\Gamma_{(n+1,n)} \approx (n+1)\Gamma_\uparrow\,, \tag{1.83}$$

$$\Gamma_\uparrow = \Gamma\lambda^2\,. \tag{1.84}$$

From those expressions, the RE of Eq. 1.52 becomes the simpler one in this regime

$$\dot{\pi}_n(t) \approx (n+1)\kappa\pi_{n+1}(t) + n\Gamma_\uparrow\pi_{n-1}(t) - \{n\kappa + (n+1)\Gamma_\uparrow\}\,\pi_n(t)\,, \tag{1.85}$$

The stationary solution $\pi_n^{(\mathrm{st})}$ of Eq. 1.85 is the balance between inelastic tunneling current that tend to increase the population of the plasmon mode and the damping of the cavity that tend to decrease it. This balance leads to an out of equilibrium distribution which is thermal-like with effective temperature T_{eff} given by

$$\pi_n^{(\mathrm{st})} = \left(1 - e^{-\frac{\omega_c}{T_{\mathrm{eff}}}}\right) e^{-\frac{n\omega_c}{T_{\mathrm{eff}}}}\,, \tag{1.86}$$

$$\frac{1}{T_{\mathrm{eff}}} = \frac{1}{\omega_c}\ln\left(\frac{\kappa}{\Gamma_\uparrow}\right)\,. \tag{1.87}$$

The average number $< n >$ and second moment $< n^2 >$ of the plasmon disctribution in the cavity follow immediately and are written as a function of the Bose distribution $n_{\rm B}(\omega_c)$

$$< n > \;=\; n_{\rm B}(\omega_c) = \frac{1}{e^{-\frac{\omega_c}{T_{\rm eff}}} - 1}\,, \tag{1.88}$$

$$< n^2 > \;=\; n_{\rm B}(\omega_c)\left[1 + n_{\rm B}(\omega_c)\right]\,. \tag{1.89}$$

From those expressions, the zero time delay second order correlation function becomes

$$g^{(2)}(0) \;=\; \frac{< n(n-1) >}{< n >^2} = 2\,. \tag{1.90}$$

The result $g^{(2)}(0) = 2$ in Eq. 1.90 is consistent with the outcome of the approximation Eq. 1.82 in the limit $\lambda \to 0$. Hence *the bunching behavior obtained for $\lambda \ll 1$ in Fig. 1.13 (blue curve) is due to the establishment of a thermal-like out of equilibrium state in the junction with effective temperature provided by Eq. 1.87.*

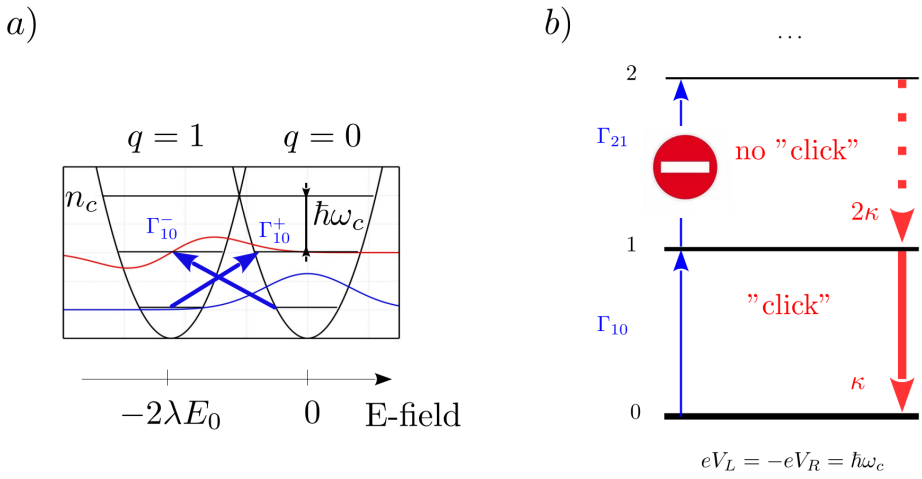

Figure 1.15: a) Representation of the bi-partite harmonic ladder of plasmonic states of the STM cavity. Case of the Franck-Condon overlaps at the origin of the inelastic tunneling rates $\Gamma_{10}^{\pm}$ at the symmetric "sweet spot". b) Scheme of the ladder of states that remain from Fig. 1.12 at the specific value of the coupling $\lambda = \sqrt{2}$. The transition Γ_{21} vanishes at this value of λ forbidding to climb up further the ladder of states. Unpublished Fig.

Analysis of the antibunching regime. We now interpret the occurrence of photon antibunching at the specific point $\lambda = \sqrt{2}$ in Fig. 1.13. For this, we consider the ladder of states in the RE shown in Fig. 1.15. We remark first that the Franck-Condon matrix element at the origin of the rate Γ_{21} vanishes when $\lambda = \sqrt{2}$, which induces $g^{(2)}(0) = 0$ in Fig. 1.13. This implies the impossibility to reach excited states of the ladder for which $n \geq 2$ (see Fig. 1.15-b)). *Hence, the stochastic dynamics of photon emission in single level plasmonic nanojunctions at this specific point is ruled by the effective two-level system made of the two states $n = 0$ and $n = 1$ shown in Fig. 1.15-b), which are connected by the incoherent rates Γ_{10} and κ.* The mechanism of antibunching is thus completely mapped to the one explained

in detail in the introduction given by Sec. 1.2.1 for the paradigmatic TLS coupled to an electromagnetic environment. As in this TLS case (for the regime $\kappa \gg \Gamma_{10}$), we find that antibunching occurs with a typical timescale $1/\kappa$ given by the cavity relaxation time (see Eq. 1.11) while the average delay time between two photon emission events is provided by $1/\Gamma_{10}$ the inelastic tunneling time of single electrons in the junction (see Eq. 1.25). A similar effect has been reported in dc-biased Josephson junctions coupled to microwave resonators [102, 55]. *We note that the fact that $\Gamma_{21} = 0$ for $\lambda = \sqrt{2}$ is a kind of additional selection rule due to Franck-Condon blockade of photon emission occurring in the strong coupling regime between the molecular single level and the STM plasmonic mode.*

Open question. *In the case of a single level model molecular junction finely tuned at the symmetric "sweet spot", we have shown the existence of a crossover between bunching and antibunching for photon emission out of the cavity upon increasing the plasmon-molecule coupling strength.* However, the question remains about what is happening of this phenomenon out of the "sweet spot" which might be hard to reach experimentally. We also ask whether or not such signatures of antibunching are measurable depending on the time-resolution of state-of-the-art photodetectors used in experiments to measure the $g^{(2)}(\tau)$ signals.

1.5 Conclusion and future research perspectives

Conclusion. In this section, we have explored the statistics of photon emission out of a single level STM plasmonic nanojunction. We characterized the related stochastic process of photon emission by introducing, computing and investigating the time-dependence of the second-order correlation function $g^{(2)}(\tau)$ and the waiting-time distribution $w(\tau)$ between emitted photons. By mixing numerical calculations based on Monte Carlo simulations and analytical results derived from the rate equation ruling the dynamics of the molecule-plasmon interaction in presence of decay or excitation to the electronic and electromagnetic environments, *we have shown that the two above mentioned quantities provide complementary but not equivalent information about the statistics of emitted photons by the nanojunction.* In particular, we focused on the highly symmetric "sweet spot" for which tunneling rates to the leads and voltage drops are symmetric. In this regime, for which additionally the damping rate of the cavity κ is much larger than the inelastic tunneling rate Γ_{10} of single plasmons in the junction ($\kappa \gg \Gamma_{10}$), *we have predicted the existence of a crossover from bunching to antibunching that occurs upon increasing the plasmon-molecule coupling strength λ.* The bunching regime at weak coupling strength ($\lambda \ll 1$) is associated to *the build up of an out-of-equilibrium thermal-like distribution in the plasmonic junction with an effective temperature that reflects the balance between inelastic current-injection and plasmon relaxation due to cavity damping and photon emission out of the STM gap.* We analyzed in depth the regime of photon-antibunching occurring at a specific value of the coupling strength $\lambda = \sqrt{2}$. We have shown that, in this case, the normalized second order correlation function $g^{(2)}(\tau)$ relaxes in time towards unity with the cavity damping-time $1/\kappa$, while the average delay-time $\langle\tau\rangle$ between successive photon emission and detection events is proportional to the inelastic tunneling time of single-electrons across the nanojunction $1/\Gamma_{10}$. We interpreted this phenomenon as resulting from *a photon blockade mechanism mediated*

by an additional selection rule for which the Franck-Condon overlap between the bi-partite plasmonic states of the cavity vanishes. This is at the origin of a highly non-linear behavior of the plasmonic junction: everything happens as if there were an effective two-level system dynamics between the two lowest energy states of the plasmonic cavity.

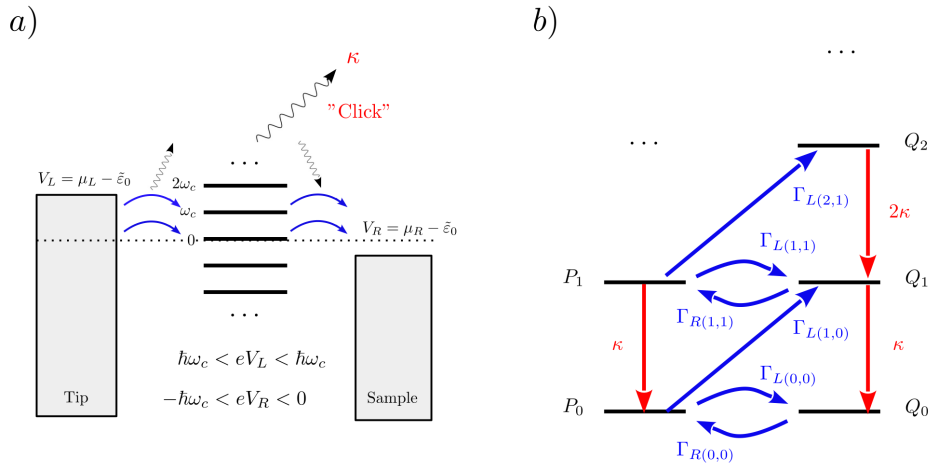

Figure 1.16: a) Representation of the incoherent transitions associated to inelastic electronic tunneling and photon emission out of the STM plasmonic cavity in an asymmetric configuration for which $\Gamma_L \neq \Gamma_R$, $\omega_c < V_L < 2\omega_c$ and $-\omega_c < V_L < 0$. b) Asymmetric ladder of states connecting $P_n(t)$ to $Q_n(t) \neq P_n(t)$. Unpublished Fig.

Future research perspectives. The work presented in this section leads the following natural question: *are the timescale measured in $g^{(2)}(\tau)$ experiments due to the finite detector time resolution or are they due to the intrinsic plasmon-molecule interaction mechanism developing in current-induced STM photon sources ?* The answer to this question is not trivial and contains both experimental and theoretical aspects that necessitate further investigations. We identify the following open questions as natural a perspective and continuation to our work:

1. *What is the issue of having a finite time-resolution of the photodetector* in measuring the power spectra and second order correlation function of the emitted light out of plasmonic cavity ?

2. *How robust is the mechanism of crossover from bunching to antibunching that we investigated to asymmetries in the configuration of the nanojunction* like asymmetric tunneling rates and voltage drops (see for instance the case of Fig. 1.16-a)) ? What are the timescales characterizing the photon emission statistics in those regimes that are closer to the ones of experiments (like in Ref. [81]) ?

3. *What is the effect on photon emission statistics of the inherently complex molecular structure* which contains more than one electronic levels, molecular vibrations, Coulomb repulsion and spin degrees of freedom ?

4. The plasmonic cavity having a low cavity mode volume, one expects increased light-matter interactions in this cavity. The question is thus *to characterize the signatures of entering the moderate to strong coupling regime for such plasmonic STM nanodevices.* Do we expect striking coherent signatures like a vacuum Rabi splitting of the measured emission spectra or simply an impact of the larger coupling between molecule and plasmon on the timescales extracted from the measured optical signals ? We started recently to investigate such questions in a manuscript in preparation [14], but many aspects related to a consistent description of strong plasmon-molecule interactions like the interplay between monopolar, dipolar and quadrupolar couplings in such plasmonic cavities remain largely open.

Recently, we started to investigate some of those points within the single level model of a plasmonic nanojunction. In particular, in a work in preparation [13], we anticipate the role of the photon detector time resolution on optically measured spectra. For instance, the photon emission spectrum as measured by a perfect photodetector that is able to measure all emitted photons out of the STM cavity is the Fourier transform of the output field correlation function $S(\tau) \equiv < E^-_{\rm out}(\tau) E^+_{\rm out}(0) >$ [53]. The former is given by the expression

$$\begin{aligned} S(\tau) &\approx \kappa < \tilde{a}^\dagger(\tau)\tilde{a}(0) > \\ &= \kappa \left\{ < a^\dagger(\tau)a(0) > -2\lambda \,\mathrm{Re}\, < a^\dagger(\tau) n_d(0) > + \lambda^2 < n_d(\tau) n_d(0) > \right\} , \end{aligned} \tag{1.91}$$

with $n_d = d^\dagger d$ the occupation operator of the single level. Thus *the high frequency (optical) spectrum of photon emission is accompanied by a lower frequency contribution to the emission spectrum due to charge fluctuations of the dot level, as well as with mixed terms.* The question of the possibility to observe this low frequency (typically in the microwave-range) signal completely depends on the detector resolution. We also anticipate on the robustness of the mechanism of crossover to antibunching developed in this section. For instance, in the asymmetric regime for which $\Gamma_L \neq \Gamma_R$, $\omega_c < V_L < 2\omega_c$ and $-\omega_c < V_L < 0$ (see Fig. 1.92-b)), the bi-partite ladder of manybody state between the dot and plasmonic mode get populated in a very asymmetric way, namely in this case $P_n^{(\rm st)} \neq Q_n^{(\rm st)}$. We predict a modified zero time-delay of the second order correlation function in this regime as a result of the asymmetric way of reaching the excited state $n = 2$ of the plasmon mode from $P_0^{(\rm st)}$ but not from $Q_0^{(\rm st)}$

$$g^{(2)}(0) \approx \frac{\Gamma_{L(21)}\Gamma_{R(11)}}{\kappa \Gamma_{L(10)} P_0^{(\rm st)}} . \tag{1.92}$$

In the limit $\kappa \gg \Gamma$, one can thus get antibunching signals in this asymmetric single level junction, even at low plasmon molecule coupling strengths, with a slow relaxation time provided by the electronic inelastic tunneling time. We anticipate also more complex time dependencies of the $g^{(2)}(\tau)$ correlation function that is intrinsically a multiscale process: *the computed signals involve the cavity damping time $1/\kappa$ and inelastic tunneling times $1/\Gamma_{\alpha,(m,n)}$ depending on the electronic configuration of the junction.* Here also the possibility to measure the short-time dynamics depends crucially on the detector time resolution.

A final remark. The investigation of photon emission statistics by STM junctions thus promises new and dynamic developments from both theory and experiments. On a more

fundamental point of view, a missing link up to day is *to connect the electronic current noise at the origin of photon emission to the actually measured correlation functions of the photon field emitted out of the STM cavity*: this relation involves to deal non-perturbatively with the plasmon-molecule coupling mechanism and to perform the joint calculation or measurement of the electronic current fluctuations and of the photonic ones. The interplay and feedback between those fluctuation signals promises a rich new playground for molecular technologies and fundamental physics.

Chapter 2

Stochastic Dynamics of Resonance Electronic Energy Transfer in Molecular Aggregates

2.1 Introduction

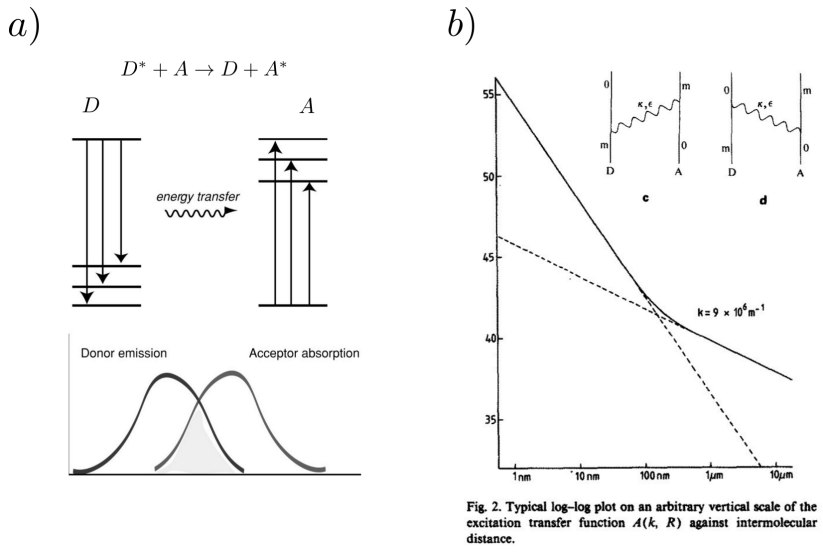

Figure 2.1: a) Scheme of a RET process where a donor D molecule transfers energy to an acceptor A molecule. The rate of RET is proportional to the overlap between the donor emission spectrum and the acceptor absorption spectrum. Adapted from Ref. [110]. b) Scheme of the dependence of the rate of RET as a function of the intermolecular distance in log scale, computed with the perturbative quantum electrodynamic calculation of Ref. [3]. Inset: the two diagrams used in the perturbative calculation corresponding to a virtual photon of the vacuum exchanged between the two interacting molecules. Adapted from Ref. [3].

A brief introduction to RET. We investigate in this chapter how energy dissipates and migrates from one place to another in complex molecular aggregates. In this context a key role is played by resonance electronic energy transfer (RET) processes through which an excitation (labeled *) initially stored onto a donor molecule (D) can be transferred to an acceptor molecule (A), resulting into the RET process $D^* + A \rightarrow D + A^*$ (see Fig.2.1-a)). This topic is of paradigmatic importance in understanding various physical, chemical and biological processes [22, 10]. The mechanism of RET is usually described by Förster resonance energy transfer (FRET) theory [46, 76]. *It involves the coupling mediated by fluctuating dipole-dipole interactions between the involved donor and acceptor molecules.* The rate of FRET $k_{\mathrm{D-A}}$ is obtained from quantum mechanics using Fermi Golden Rule [68]

$$k_{\mathrm{D-A}} \;=\; |V_{\mathrm{D-A}}|^2 J_{\mathrm{D-A}}/2\pi\hbar^2 = \Gamma_D \left(R_0/R_{\mathrm{D-A}}\right)^6 , \tag{2.1}$$

with $V_{\mathrm{D-A}}$ the matrix-element corresponding to the dipole-dipole interaction Hamiltonian, $J_{\mathrm{D-A}}$ the overlap integral between the donor emission spectrum and acceptor absorption spectrum (see Fig.2.1-a)), and $\hbar$ the Planck constant. This expression can be rewritten in the standard form [46, 15] in the second equality of Eq. 2.1. We introduced Γ_D the rate of spontaneous photon emission of the donors, $R_{\mathrm{D-A}}$ the distance between the D-A molecules, and R_0 the Förster radius that quantifies the typical range of the RET process of order $1 - 10$ nm. *The rate of RET thus has a scaling with intermolecular distances $k_{\mathrm{D-A}} \propto R_{\mathrm{D-A}}^{-6}$ that is reminiscent of the dipole-dipole interactions between the donor and acceptor molecules.*

Recent issues related to the RET mechanism. Despite its long history, the mechanism of FRET is still the object of intense research activities and fruitful debates. For instance, some recent theoretical investigations in molecules made of multiple chromophores, emphasized the central role of non-equilibrium effects and molecular vibrations in FRET [15, 68, 59, 37, 70]. *The latter were shown to be responsible for a vibration-assisted long-range energy-transfer mechanism beyond standard Förster theory.* Other studies focused on deriving $k_{\mathrm{D-A}}$ rigorously from a microscopic model using a non-relativistic quantum-electrodynamics framework. *In the former case, the interaction between two molecules is mediated by coupling to virtual photons of the electromagnetic reservoir [71, 33, 3, 31, 30, 105] (see inset of the right panel in Fig. 2.1). Those studies predict the existence of a crossover from the standard Förster static-regime at short-distances scaling with $k_{\mathrm{D-A}} \propto R_{\mathrm{D-A}}^{-6}$ to a long-range retarded radiation-regime mediated by the emission and propagation of real photons scaling with $k_{\mathrm{D-A}} \propto R_{\mathrm{D-A}}^{-2}$ (see the right panel in Fig. 2.1).* The question of understanding the effective range of RET processes beyond the two-molecule process is actually a very important one, *in particular for biological complexes or molecular aggregates, where disorder-induced [83, 110, 1, 24], and coherent long-range mechanisms in the mechanism of FRET at the mesoscale are supposed to play a key-role in the mechanism of photosynthesis [111, 69, 114, 49, 89].*

RET mechanism in optical cavities. A revival of those issues occurred recently in a different context for which the RET processes are modified by an alteration of the electromagnetic environment mediating the interaction between the D and A molecules. This is the case for molecules deposited close to a mirror [120] in which case the electromagnetic vacuum is modified close to the mirror interface. This is also the case when embedding the

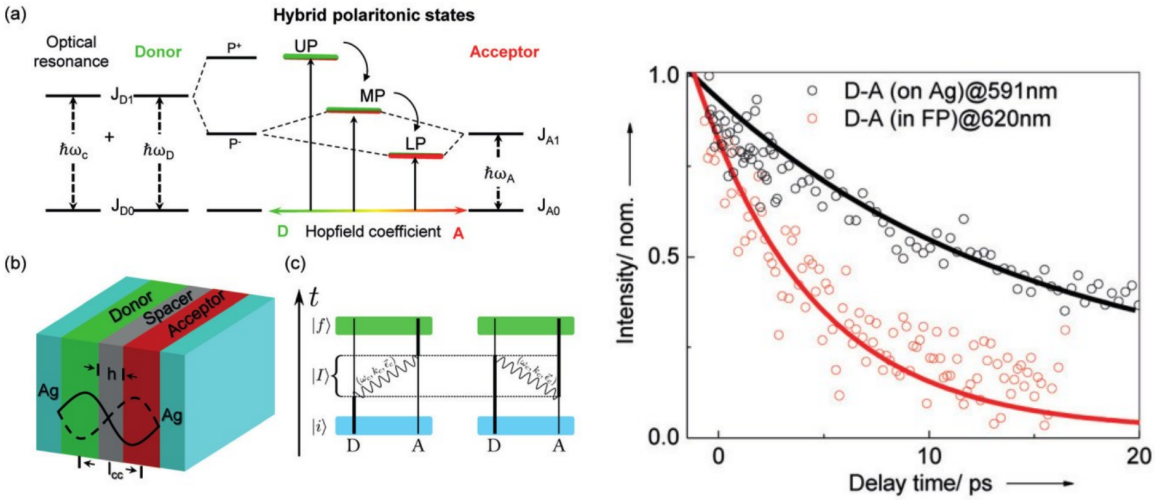

Figure 2.2: Left panel: Scheme of an optical Fabry-Pérot cavity in which a layer of donor D molecules and one of acceptor A molecules have been inserted. The D molecules are resonant with one optical cavity mode frequency leading to the formation of polaritonic excitations. The former hybridate with the A electronic states leading to a long-range energy transfer mechanism. Right panel: resulting kinetics of the RET relaxation process measured as a function of time inside cavity (red curve) that is faster compared to the one outside cavity (black curve). Adapted from Ref. [123].

donor and acceptor molecules inside electromagnetic cavities (see left panel of Fig. 2.2) for which one electromagnetic cavity mode couples resonantly and strongly to one molecular species [123, 104, 51, 41, 98]. *This results into a new kind of long-range resonance energy transfer mechanism [123, 104, 51, 41, 98] mediated by the collective polariton excitations resulting from the coupling between the molecules and the resonant electromagnetic cavity mode.* For instance, in the seminal paper of T. Ebbesen in Ref. [123], was reported a modification of the rate of RET by a factor seven as a consequence of this mechanism (see right panel of Fig. 2.2).

Problematic of the present study of RET. The question of *understanding collective and non-equilibrium effects in RET processes occurring in molecular ensembles or aggregates* beyond the standard description in terms of single donor and acceptor molecules is thus still a lively and open important question in molecular sciences. In this chapter, we will develop a theoretical modeling and understanding of one aspect of RET in molecular aggregates, namely *how to describe the incoherent but collective RET process occurring between many molecules in the aggregate.* We will deal with the following questions

1. How to define and compute a mean-field rate of RET, given a specific aggregate with donor and acceptor molecules ? What is the scaling the computed rate with the average intermolecular distances ?

2. How to describe more generally the full stochastic dynamics of an incoherent RET

process ? How to recover the mean-field solution in the macroscopic limit ? What are the effects of spatial frustrations and correlations due to interactions between more than two molecules ?

3. How to quantify deviations from the mean-field approximation due to mesoscopic fluctuations in a finite but large aggregate ?

We will formalize those problems in three steps: we provide first in Sec. 2.2 *a pedagogical introduction to the description of the stochastic dynamics for the simpler process of fluorescence.* We will introduce the necessary concepts and theoretical tools in the context of this example, leading in the next section to the more complex study of RET. Then, we apply those tools in Sec. 2.2 to *the description of stochastic processes involving RET between many D and A molecules dispersed in a mesocopic aggregate.* Finally, in Sec. 2.4, we will compute quantitatively *the impact of mesoscopic fluctuations at the origin of deviations with respect to the mean-field description of RET.* This chapter is an extended version of the work we published in Ref. [8]. *We took the opportunity of this HDR thesis to provide additional explanations and we hope pedagogical derivations of the published results.* We note that some of our derivations are original in the sense that they are unpublished. Such is the case for Sec. 2.2 devoted to fluorescence and in Sec. 2.4 where the Fokker-Planck equation describing an ideally homogeneous RET process is derived with some care from the chemical master equation. We did our best to clarify the delicate points and physical approximations usually made in such studies: the difficulty in developing and using the corresponding theoretical tools is a consequence of the multi-disciplinary nature of RET which is at the carrefour between physics and chemistry. We hope to convince the reader of the interest of such studies and to promote a further development of methods inherited from statistical physics to a broader class of physico-chemical processes. This work results from a collaboration with Gediminas Jonusauskas (LOMA) who asked us questions about his experimental studies of RET and with Alice Marché who initiated this project during her master M1 internship in LOMA.

2.2 Stochastic description of fluorescence in molecular aggregates

In this section, we unveil the main properties and treat in some details *the stochastic dynamics of fluorescence in a molecular aggregate.* This problem is well known and sufficiently simple to exhibit an analytical solution. The former enables to i) calibrate the involved numerical schemes that become necessary to describe more complex physico-chemical processes developing in molecular ensembles and ii) introduce the physical concepts and hypothesis that are necessary to understand and think the underlying *chemical complexity.* In Sec. 2.2.1, we provide the general problematic underlying the description of fluorescence in molecular ensembles. A statistical description of fluorescence is developed in Sec. 2.2.2 with the derivation of the chemical master equation. The former is solved both analytically in term of a stochastic process on a graph of configurations and numerically with Monte Carlo simulations in Sec. 2.2.3. The connection between microscopic and macroscopic evolution

is made in Sec. 2.2.4 where we derive the kinetic equations for the fluorescence process from the chemical master equation. Finally we include in Sec. 2.2.5 the presence of Gaussian laser pulse exciting the molecular aggregate at times shorter than the fluorescence timescale. This is a necessary ingredient to add in order to compare to actual transient fluorescence experiments.

2.2.1 Position of the problem

Macroscopic evolution. One way through which molecules put into their electronic excited state can dissipate energy is through fluorescence. In such an elementary process, any excited molecule M_i^* can emit a spontaneous photon and come back to its ground state M_i

$$M_i^* \rightarrow M_i + h\nu \,. \tag{2.2}$$

This process is stochastic, namely the time at which the photon is emitted by the molecule M_i^* is intrinsically random. This reflects the well known fact that spontaneous emission is due to coupling of the molecular transition dipoles to vacuum quantum fluctuations of the electromagnetic reservoir [27]. We introduce Γ the rate or probability per unit time at which a spontaneous photon is emitted by any excited molecule of the ensemble. This rate is computed quantum mechanically [27]. Under the assumptions that i) *each molecule has the same rate Γ of fluorescence* and that ii) *there is no coherent effect in the underlying spontaneous emission process* [36], one expects that the average kinetics of fluorescence at the macroscopic scale is ruled by the equation

$$\frac{d}{dt}\left\langle N_{M^*}(t)\right\rangle \;=\; -\Gamma\left\langle N_{M^*}(t)\right\rangle \,, \tag{2.3}$$

with $\langle N_{M^*}(t)\rangle$ the average number of molecules in the excited state at time t and $\langle N_{M^*}(0)\rangle$ the initial condition. The solution of Eq.2.3 is a simple exponential relaxation

$$\left\langle N_{M^*}(t)\right\rangle \;=\; \left\langle N_{M^*}(0)\right\rangle e^{-\Gamma t} \,. \tag{2.4}$$

Problematic. We formulate the following problem: *how is it possible to recover Eq. 2.4 describing the macroscopic time evolution of the number of excited molecules, knowing the microscopic stochastic evolution of each molecule inside the aggregate ?*

2.2.2 Statistical description of fluorescence in molecular ensembles

Microstates and macrostates. We introduce the notion of *microstate of the molecular aggregate* as the list of excitation-states for each molecule in the ensemble $a \equiv \left\{\sigma_i^{(a)}\right\}_{i\in[|1,N|]}$, in which N is the total number of molecules and the variable $\sigma_i^{(a)} = 1(0)$ if the molecule i is in excited (ground) state $M_i^*(M_i)$. We also introduce the *macrostate of the molecular aggregate* corresponding to the microstate a as the total number of excited molecules

$N_{M^*}^{(a)} \equiv \sum_{i=1}^{N} \sigma_i^{(a)}$ in this microstate. We note that the total number of microstates is huge and equal to 2^N. For a give macrostate $N_{M^*}^{(a)}$, there are many possible microstates a given by the combinatorics factor $C_N^{N_{M^*}^{(a)}} = \frac{N!}{N_{M^*}^{(a)}!\left(N-N_{M^*}^{(a)}\right)!}$.

Chemical master equation. Under the influence of random elementary spontaneous emission processes described by Eq. 2.2, starting from a given initial condition, the system jumps randomly from one microstate to another, finally reaching a stationary state at times much larger than the fluorescence lifetime $1/\Gamma$. The time evolution of the system thus follows a stochastic Markov process that is described by the following microscopic *chemical master equation* (ME) [117]

$$\dot{P}_a(t) \quad = \quad \sum_b \left\{\Gamma_{ab} P_b(t) - \Gamma_{ba} P_a(t)\right\} \tag{2.5}$$

with $P_a(t)$ the probability of occupying the microstate a at time t and Γ_{ba} the incoherent rate or probability per unit time for the system to jump from a to b microstates. In the simple case of fluorescence, $\Gamma_{ba} = \Gamma$ for an allowed transition involving a spontaneous photon emission event as described by Eq. 2.2, and zero otherwise. We also chose to fix the initial condition at time $t = 0$ to be the microstate $a_{\rm in} \equiv \left\{\sigma_i^{(a_{\rm in})} = 1\right\}_{i\in[|1,N|]}\}$ in which all molecules are excited in the aggregate, so that

$$P_a(0) \quad = \quad \delta_{a,a_{\rm in}} \,. \tag{2.6}$$

The conjunction of Eq.2.5 and Eq.2.6 provides a complete description of the stochastic fluorescence dynamics from the initial (fully excited) microstate $a_{\rm in}$ to the final (fully relaxed) microstate $a_{\rm f} \equiv \left\{\sigma_i^{(a_{\rm f})} = 0\right\}_{i\in[|1,N|]}$ for which all molecules are back to their ground-state. In principle, the solution of the ME Eq. 2.5 provides the way to compute the average number of excited molecules we looking for

$$\langle N_{M^*}(t)\rangle \quad = \quad \sum_a N_{M^*}^{(a)} P_a(t) \,. \tag{2.7}$$

Problematic. The ME Eq. 2.5 is a system of 2^N linear equations the solution of which necessitates to diagonalize a $2^N \times 2^N$ matrix of transition rates. *This cannot be done numerically easily in the general case, when the number of molecules in the aggregate is large* $N \gg 1$.

2.2.3 Solving the chemical master equation

Exact solution. In the case of fluorescence, due to *the homogeneity* of the problem (each elementary spontaneous emission process has the same transition rate), *the sparse nature* of the transition rate matrix and *independence of each fluorescence process* with respect to the chosen emitted molecule, the ME is simple enough to allow an exact solution for the

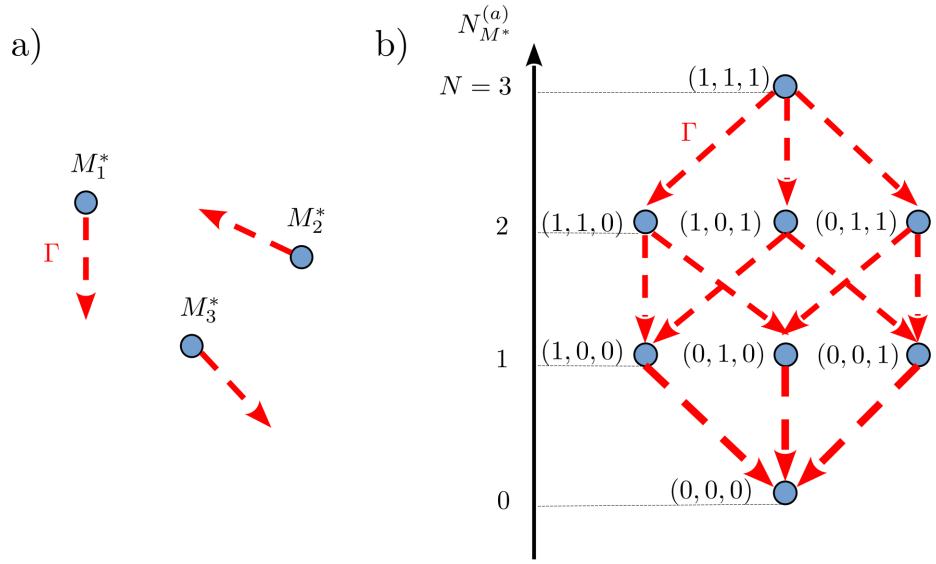

Figure 2.3: a) Scheme of a distribution of $N = 3$ molecules (blue points) labeled M_1^*,M_2^*,M_3^* that are initially excited. After some time, each molecule as a probability per unit of time Γ to emit a spontaneous photon (red dashed) arrow. b) Associated graph of possible microstates $\left(\sigma_1^{(a)}, \sigma_2^{(a)}, \sigma_3^{(a)}\right)$ (blue dots) corresponding to the macrostate $N^{(a)}_{M^*}$. The elementary transitions corresponding to a fluorescence process of rate Γ allowed by Eq. 2.5 are pictured as red dashed arrows. Unpublished Fig.

average population of excited molecules. To illustrate this, we picture in Fig. 2.3 the graph corresponding to the allowed transitions described by Eq. 2.5 in the case of $N = 3$ molecules in the aggregate. There are 8 possible microstates pictured as the vertex (blue dots) of the graph, while the possible elementary fluorescence process between those states are the oriented edges (dash red arrows) of the graph. Starting from the initial condition where all molecules are inially excited, the total number of excited molecules is then given by *the following combinatorial problem*

$$\langle N_{M^*}(t)\rangle \;=\; \sum_{p=0}^{N} p C_N^p P_1^p(t)\left(1-P_1(t)\right)^{N-p} = N e^{-\Gamma t}\,, \tag{2.8}$$

with $P_1(t) = e^{-\Gamma t}$ the single molecule probability of fluorescence. The summand Eq. 2.8 has a simple interpretation: it is the total number C_N^p (combinatorial factor) of excited molecules in microstates containing $p \in [|0, N|]$ excited molecules contributing to p times the probability that p excited molecules emit a spontaneous photon and $N - p$ molecules are in ground state and thus cannot emit a photon at time t in the fluorescence process. The latter probability factorizes into a product of single molecule probabilities due to the independence between the fluorescence process for each molecule. *As expected, Eq. 2.8 recovers the result of the macroscopic kinetic equation Eq. 2.7 with the initial condition* $\langle N_{M^*}(0)\rangle = N$.

Kinetic Monte Carlo numerical approach. The considerations of the previous paragraph can be interpreted another way. Starting from the initial microstate $(1, 1, 1)$ where

all molecule are excited, the systems can relax back by undergoing a succession of random jumps downward the graph of Fig. 2.3, during which a series of spontaneous photons are emitted (dashed red arrows) and the emitting molecules are relaxed back to their ground state. At time t, *a given number of photons has been emitted along a given stochastic trajectory on the graph*, and the average number of emitted fluorescence photons $\langle N_{M^*}(t)\rangle$ is obtained by *summing on all possible such trajectories*. The process stops when reaching the stationary state $(0,0,0)$ for which each molecule is back to ground state. The above considerations basically describe a kinetic Monte Carlo (MC) approach [52, 45], which is equivalent to solve numerically the ME Eq. 2.5. The main idea of it, is to discretize the time-window into small time-steps δt. At each time-step, one either updates randomly the a microstate of the system to the b one with probability $\propto \Gamma_{ba}\delta t$, or leaves the a-state unchanged. The number of excited molecules in the ground-state is then counted and stored. The final observable value $\langle N_{M^*}(t)\rangle$ is obtained after averaging on a large-enough number N_{traj} of stochastic trajectories of the system connecting the initial to the final state. The chosen value of $N_{\text{traj}} = 10^5$ is sufficient to reach a relative statistical uncertainty of $\approx 1/\sqrt{N_{\text{traj}}} \approx 0.3\%$ for the MC calculation. *We implemented numerically such kinetic Monte Carlo algorithm in Ref. [8] and used it to investigate more complex processes involving both fluorescence and RET in molecular aggregates.*

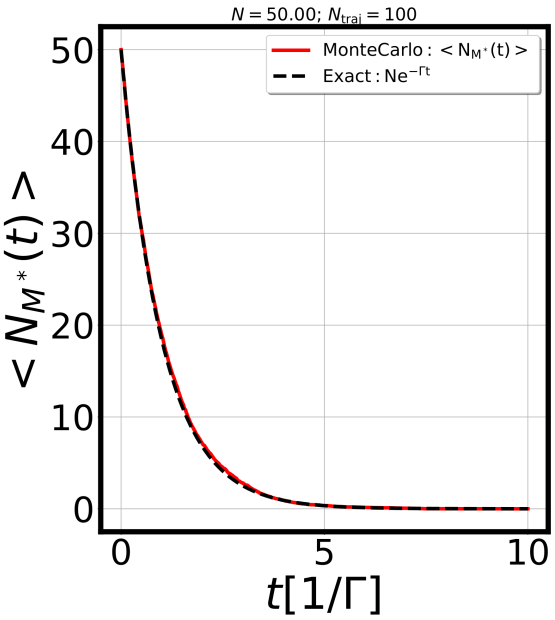

Figure 2.4: Average number of excited molecules $\langle N_{M^*}(t)\rangle$ as a function of time t in units of $1/\Gamma$, for a molecular aggregate with $N = 50$ molecules that are initially excited and further decay with a fluorescence rate Γ. Plain red curve: output of the kinetic Monte Carlo solver we implemented and used in Ref. [8] in order to solve the ME Eq. 2.5. The average is taken on $N_{\text{traj}} = 100$ stochastic trajectories. Dashed black curve : exact result given by Eq. 2.4. Unpublished Fig.

Numerical results. We show the outcome of such MC calculation in Fig. 2.4, in the case of a molecular aggregate with $N = 50$ molecules that are initially excited and further decay

with a fluorescence rate Γ. The molecules in the simulation are put on a 2D square lattice, but the computed population of excited molecules does not dependent on the spatial configuration of the molecules. Upon doing an average over $N_{\rm traj} = 100$ stochastic trajectories, we already obtained a very good agreement between the $\langle N_{M^*}(t)\rangle$ curve computed with MC (plain red curve) and the exact result given by Eq. 2.4 (dashed black curve).

2.2.4 Derivation of exact kinetic equations

Time-dependent population of excited molecules. To complete our description of fluorescence, as proposed in Sec. 2.2.1, we have now all the necessary tools to derive the macroscopic kinetic equation Eq. 2.3 from the ME Eq. 2.5. The derivation starts by taking the time derivative of $\langle N_{M^*}(t)\rangle$ at time t given by Eq. 2.7 and replacing into it the expression of $\dot{P}_a(t)$ by the right-hand-side of the ME Eq. 2.5. We obtain

$$\frac{d}{dt}\langle N_{M^*}(t)\rangle \;=\; \sum_{a,b}\Gamma_{ab}P_a(t)\left\{(N_{M^*})_b-(N_{M^*})_a\right\} = -\Gamma\sum_{(a,b)_\Gamma}P_a(t)\,, \tag{2.9}$$

with $P_a(t)$ the solution of the ME with proper initial condition and $\sum_{(a,b)_\Gamma}$ the sum constrained on all pairs of microstates (a,b) connected by a spontaneous emission rate process of rate Γ. The second equality in Eq. 2.9 is made because in the transition $a\to b$, the number of excited molecules in the microstate b after a single photon emission is lower by one unit compared to the number of excited molecules before the fluorescence event, thus leading to $(N_{M^*})_b-(N_{M^*})_a=-1$. We note that the resulting simple expression is due to the fact that $\Gamma_{ab}=\Gamma$ for all pairs of connected states, namely the homogeneity assumption of the fluorescence process.

Constraint sums. The constrained sums in Eq. 2.9 can be written more explicitly as

$$\sum_{(a,b)_\Gamma}P_a(t) \;=\; \sum_{i=1}^{N}\sum_{\{\sigma_j\}_{j\neq i}}P_{a=\left\{\sigma_i=1,\{\sigma_j\}_{j\neq i}\right\}}(t)\,, \tag{2.10}$$

where in the configuration a the site i is excited such that $\sigma_i=1$ and a single spontaneous photon emission event is possible, reaching the microstate b. The former is independent of the state of the other sites $\{\sigma_j\}_{j\neq i}$ which are thus summed independently. The output of Eq. 2.10 can be rewritten in a compact way, after *introducing $\Pi^{(1)}_{\sigma_i}(t)$, the "one-molecule" probability distribution that the molecule i is in the excitation state $\sigma_i=0,1$ at time t*

$$\Pi^{(1)}_{\sigma_i}(t) \;=\; \sum_{\{\sigma_j\}_{j\neq i}}P_{a=\left\{\sigma_i,\{\sigma_j\}_{j\neq i}\right\}}(t)\,. \tag{2.11}$$

Using the former definition in Eq. 2.10 and back into Eq. 2.9, we obtain finally the kinetic equation for the fluorescence process

$$\frac{d}{dt}\langle N_{M^*}(t)\rangle \;=\; =-\Gamma\langle N_{M^*}(t)\rangle\;, \tag{2.12}$$

with the average number of excited molecules

$$\langle N_{M^*}(t)\rangle \;=\; \sum_{i=1}^{N}\langle\sigma_i(t)\rangle \tag{2.13}$$

that are given in terms of the sum of average excitation states $\langle\sigma_i(t)\rangle$ for each molecule i

$$\langle\sigma_i(t)\rangle \equiv \sum_{\sigma_i=0,1}\sigma_i\Pi^{(1)}_{\sigma_i}(t)\,. \tag{2.14}$$

Discussion of the derivation. We note that *the obtained kinetic equation Eq. 2.12 for the fluorescence process is exact and recovers the macroscopic kinetic equation Eq. 2.3.* In the more complex cases of RET developed later this is no more so, and we will need additional assumptions to recover the macroscopic limit from the microscopic ME. Finally we note as an additional property that *the statistical averaging on microstate configurations restores the spatial homogeneity of the fluorescence process*, as is physically expected, namely that the average excitation state of molecule i

$$\langle\sigma_i(t)\rangle \;=\; \phi_{M^*}(t) = \frac{\langle N_{M^*}(t)\rangle}{N} \tag{2.15}$$

is the same for all the molecules in the aggregate. In other words, the thermodynamic limit $\lim_{N\to+\infty}\langle\sigma_i(t)\rangle$ is well defined in Eq. 2.15 and is given by the intensive quantity $\phi_{M^*}(t)$ which is the relative portion of excited molecules in the ensemble.

2.2.5 Towards a description of transient fluorescence experiments

Driving of the aggregate. To close this chapter devoted to the study of fluorescence, we introduce in the kinetic equation Eq. 2.12 an additional term standing for *the optical excitation of the molecular aggregate by a Gaussian laser pulse* (see a scheme of experiment in Fig. 2.5). In an actual transient fluorescence experiment, indeed, this pulse is necessary to excite the molecules during a timescale shorter than the typical fluorescence decay time. The fluorescence signal defined as $\mathcal{F}(t) = \langle N_{M^*}(t)\rangle / \mathrm{Max}\left(\langle \mathrm{N_{M^*}(t)}\rangle\right)$ is then collected as a function of time and is directly proportional to the number number of excited molecules in the sample. The former quantity follows the modified kinetic equation

$$\frac{d}{dt}\langle N_{M^*}(t)\rangle \;=\; -\Gamma\langle N_{M^*}(t)\rangle + W_p(t)\langle N_M(t)\rangle\;, \tag{2.16}$$

with $\langle N_M(t)\rangle = N - \langle N_{M^*}(t)\rangle$ the number of molecules in the ground state and

$$W_p(t) \;=\; W_p e^{-\frac{(t-t_0)^2}{2T_p^2}}\;, \tag{2.17}$$

the time-dependent Gaussian pulse profile. The pulse is parametrized by W_p its amplitude, t_0 its arrival time on the sample, and T_p its duration.

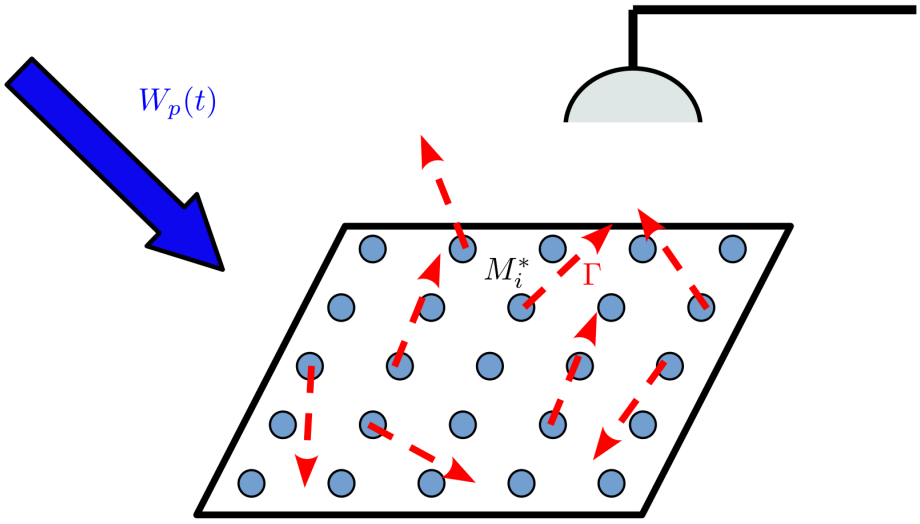

Figure 2.5: Scheme of a transient fluorescence spectroscopy experiment. A time-dependent Gaussian pulse $W_p(t)$ (thick blue arrow) is sent on a aggregate of molecules (blue dots) M_i to put them into excited state M_i^*. The excited molecules will relax to ground-state by emission a spontaneous photon (dashed red arrow) with a rate Γ. The fluorescence photons are collected by a detector (in black) and produces a time-dependent signal proportional to the number of excited molecules. Unpublished Fig.

Numerical results. We show on Fig. 2.6 the normalized transient fluorescence signal $\mathcal{F}(t)$ (plain red curve) as a function of time t in units of nanoseconds. This signal is computed by solving numerically the modified kinetic equation Eq. 2.16. We chose parameters for which $\Gamma = 0.18\ \mathrm{ns}^{-1}$, $t_0 = -0.04$ ns, $T_p = 0.14$ ns and $W_p = 0.10\ \mathrm{ns}^{-1}$. The initial condition is fixed at time $t = -0.8$ ns to the value $\mathcal{F}(t = -0.8) = 0.0$. *This choice of parameters is relevant for describing transient fluorescence experiments performed on molecular aggregates in LOMA by Gediminas Jonusauskas.* The computed fluorescence signal is simple to interpret. Initially at $t = -0.8$ ns no molecule is excited, hence no signal is collected. After some time, the Gaussian pulse arrives on the sample and a portion of the molecules are brought to their excited state thus giving rise to an increasing fluorescence signal. After at time given by the pulse duration, the sample is no more excited by the pulse and the number of excited molecule slowly decays on the fluorescence timescale given the exponential relaxation $\mathcal{F}(t) \approx e^{-\Gamma t}$ (black dashed curve). We thus recover the simple result of Fig. 2.4 in absence of drive, but with a choise of initial condition where all molecules are excited. However, to correctly reproduce the experiments, one would need to add another non-linear term in the kinetic equation standing for the presence of exciton-exciton relaxation processes [91] that are important at short times: this could be done in a straightforward manner.

Open question. During the duration of the pulse T_p, due to spatial and temporal coherence of the laser field, *we cannot exclude the formation of time-dependent manybody correlations in the molecular aggregate that are prior to the spontaneous photon emission process.*

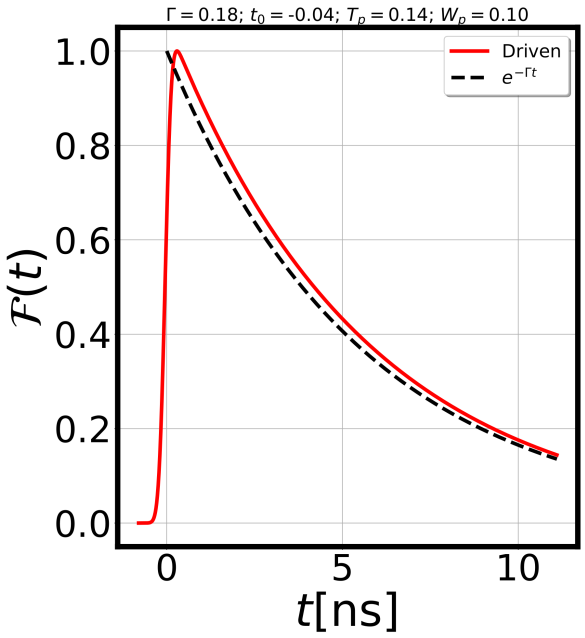

Figure 2.6: Normalized transient fluorescence signal $\mathcal{F}(t)$ (plain red curve) as a function of time t in units of nanoseconds. The aggregate is driven by the Gaussian laser pulse of Eq. 2.17 and the fluorescence signal is computed after numerical solution of the kinetic equation Eq. 2.16. For comparison, the exponential relaxation $e^{-\Gamma t}$ obtained in the absence of drive is shown as a black dashed curve. Parameters are: $\Gamma = 0.18\ \mathrm{ns}^{-1}$, $t_0 = -0.04\ \mathrm{ns}$, $T_p = 0.14\ \mathrm{ns}$, $W_p = 0.1\ \mathrm{ns}^{-1}$ and $\mathcal{F}(t = -0.8\ \mathrm{ns}) = 0.0$. Unpublished Fig.

The question of quantifying the impact of such correlations on the fluorescence process itself is beyond the scope of the theoretical treatment presented here, and is led open for future theoretical as well as experimental investigations.

2.3 Stochastic description of RET in molecular aggregates

In this section, we develop *a stochastic description of RET processes in molecular aggregates.* As far as we could investigate it, this model does not exhibit any exact solution, but enables nevertheless a thorough study of the main features underlying the RET processes. We introduce the model of RET that is relevant for describing the ultrafast relaxation of an ensemble of donor and acceptor molecules in Sec. 2.3.1. The statistical description of RET from a microscopic point of view is provided in Sec. 2.3.2 together with the analysis of a special case (with two donors and two acceptors on a regular square configuration) exhibiting an analytical solution. A hierarchy of exact kinetic equations is derived in Sec. 2.3.3 that preclude the existence of an exact solution in the general case, but provides a first hint on the collective effects involving more than two molecules in the RET process. Finally we provide in Sec. 2.3.4 some reasonable physical conditions that are sufficient to recover a mean-field description of the RET kinetics. A mapping between the microscopic rate of RET and the

macroscopic one is found and computed explicitly in the case of a disordered 2D molecular aggregate. The time-dependent populations of excited donor and acceptor molecules in the case of a regular square lattice are then computed with the Monte Carlo simulation and compared to the outcome of the mean-field approximation without any fitting parameter.

2.3.1 Position of the problem

We now consider in this section the more complex situation of a molecular aggregate made ofd N_D donor D molecules and N_A acceptor A, with a total number of molecules $N = N_A + N_D$. *After the excitation by an external laser pulse that is tuned to the donor electronic transition, all donor molecules are put into their excited state such that $N_{D^*}(0) = N_D$, but all acceptor ones remain in their ground state $N_{A^*}(0) = 0$.* Similarly to the previous Sec. 2.2, the energy deposited onto the sample can decay at a later time by fluorescence from the excited donors with a rate Γ_D. However, there is now an additional relaxation channel for energy, namely any excited donor can transfer its excitation energy to a nearby acceptor molecule. *The former process is described by a RET process that is mediated by exchange of virtual photons between the D and A molecules.* We write the whole RET process as

$$D^*_\alpha + A_j \rightarrow D_\alpha + A^*_j \,, \tag{2.18}$$

with $\alpha \in [|1, N_D|]$ labeling the donor molecule number α and $j \in [|1, N_A|]$ labeling the acceptor molecule number j. The decay rate of the rate process is given by $k_{\alpha j} \equiv k\left(r_{\alpha j} = ||\vec{r}_\alpha - \vec{r}_j)||\right)$ and depends on the relative distance $r_{\alpha j}$ between the pair of molecules (D^*_α, A_j). Standard FRET theory [46, 15] provides the expression

$$k(r_{\alpha j}) = \Gamma_D \left(\frac{R_0}{r_{\alpha j}}\right)^6 . \tag{2.19}$$

We did not take into account the more complex dependence of the rate $k(r_{\alpha j}, \theta_{\alpha j})$ with the relative orientation $\theta_{\alpha j}$ of the molecular dipoles [83], and supposed from start a sufficient orientational disorder of the molecular dipoles such that, in average, isotropy of the rates in Eq. 2.19 is restored. *In other words, we investigated the chemical complexity arising from spatial inhomogeneities of the molecular positions in the aggregate, but not from anisotropy in the distribution of the relative molecular orientations.* Finally, since the RET processes in Eq. 2.18 generates excited acceptors A^*, the former can further relax their energy by emitting a spontaneous photon with rate Γ_A. If the aggregate is macroscopically homogeneous, then we expect the following macroscopic kinetic rate equations to rule the evolution of the D adnd A molecular populations

$$\frac{d}{dt}\left\langle N_{D^*}(t)\right\rangle = -\Gamma_D \left\langle N_{D^*}(t)\right\rangle - \overline{k}\left\langle N_{D^*}(t)\right\rangle \left\langle N_A(t)\right\rangle \,, \tag{2.20}$$

$$\frac{d}{dt}\left\langle N_A(t)\right\rangle = \Gamma_A \left\langle N_{A^*}(t)\right\rangle - \overline{k}\left\langle N_{D^*}(t)\right\rangle \left\langle N_A(t)\right\rangle \,, \tag{2.21}$$

with $\overline{k}$ the mean-field rate of RET. In the case of an equimolar ensemble of donors and acceptors ($N_D = N_A = N/2$) with the same fluorescence rate ($\Gamma_D = \Gamma_A \equiv \Gamma$), the previous

macroscopic equations can be solved exactly analytically

$$\langle N_{D^*}(t)\rangle^{(\mathrm{mf})} = \frac{N}{2}\frac{\exp\left\{-\left(\Gamma+\tilde{k}\right)t+\frac{\tilde{k}}{\Gamma}\left(1-e^{-\Gamma t}\right)\right\}}{1+\tilde{k}\int_0^t d\tau\exp\left\{-\left(\Gamma+\tilde{k}\right)\tau+\frac{\tilde{k}}{\Gamma}\left(1-e^{-\Gamma\tau}\right)\right\}}\,, \tag{2.22}$$

$$\langle N_A(t)\rangle^{(\mathrm{mf})} = \frac{N}{2}\left(1-e^{-\Gamma t}\right)+\langle N_{D^*}(t)\rangle^{(\mathrm{mf})}\,, \tag{2.23}$$

with the macroscopic rate of RET $\tilde{k}$. In the thermodynamic limit where $N\to+\infty$ and $\overline{k}\to 0$, the macroscopic rate $\tilde{k}$ remains finite and

$$\tilde{k} = \lim_{N\to+\infty}\frac{N}{2}\overline{k}\,. \tag{2.24}$$

Problematic. *We ask ourselves how the macroscopic kinetic equations emerge from the microscopic stochastic RET process in the large N limit. In particular, what is the connection between the macroscopic rate of the RET $\tilde{k}$ in Eq. 2.24 and the microscopic one $k(r_{\alpha j})$ in Eq. 2.19 ? What are the eventual deviations from the mean-field kinetics described by Eqs. 2.20,2.21 that are induced by fluctuations in mesoscopic samples ?* The answers to those questions are not simple and need a more involved approach developed in the following sections.

2.3.2 Statistical description of RET in molecular ensembles

Extension of the chemical master equation. We extend the statistical description of fluorescence derived in Sec. 2.2 to the case of RET. For that purpose, one has to extend the notion of microstate to the list $a\equiv\left\{\left\{\sigma_\alpha^{(a)}\right\}_{\alpha\in[|1,N_D|]},\left\{\sigma_j^{(a)}\right\}_{j\in[|1,N_A|]}\right\}$ of states of excitation for each donor and acceptor molecule in the ensemble. The macrostate associated to the microstate a is the list of total number of excited donor and acceptor molecules $\left(N_{D^*}^{(a)}\equiv\sum_{\alpha=1}^{N_D}\sigma_\alpha^{(a)},N_{A^*}^{(a)}\equiv\sum_{j=1}^{N_A}\sigma_j^{(a)}\right)$ belonging to a. As in the case of fluorescence, in a macroscopic sample, there is a huge number of possible microstates leading to the same macrostate. *The resulting combinatorial complexity is at the origin of the chemical complexity developing in the RET process.* The description of the RET process is thus naturally done in a statistical manner and is ruled by the same chemical master equation Eq. 2.5 that we derived for fluorescence, but with the microscopic rates Γ_{ba} between the microstates a and b that are connected by the following processes:

1. $\Gamma_{ba}=\Gamma_D$ the rate for a transition involving a spontaneous photon emission event (see Eq. 2.2) from an excited donor D_α^*,

2. $\Gamma_{ba}=\Gamma_A$ the rate for a transition involving a spontaneous photon emission event (see Eq. 2.2) from an excited acceptor A_j^*,

3. $\Gamma_{ba} = k_{\alpha,j}$ the rate for a RET process (see Eq. 2.18) between an excited donor D^*_α and an acceptor A_j in its ground state.

The whole stochastic process is described by a Monte Carlo simulation that starts from the state in which all donors are excited by the laser and all acceptors are in their ground state $a_{\text{in}} \equiv \left\{ \left\{ \sigma_\alpha^{(\text{in})} = 1 \right\}_{\alpha\in[|1,N_D|]}, \left\{ \sigma_j^{(\text{in})} = 0 \right\}_{j\in[|1,N_A|]} \right\}$ and ends in the state in which all molecules have relaxed in their ground state $a_{\text{f}} \equiv \left\{ \left\{ \sigma_\alpha^{(\text{f})} = 0 \right\}_{\alpha\in[|1,N_D|]}, \left\{ \sigma_j^{(\text{f})} = 0 \right\}_{j\in[|1,N_A|]} \right\}$. *The formulation of this approach to the case of RET processes in 2D molecular aggregates of D and A molecules is derived in our Ref. [8].*

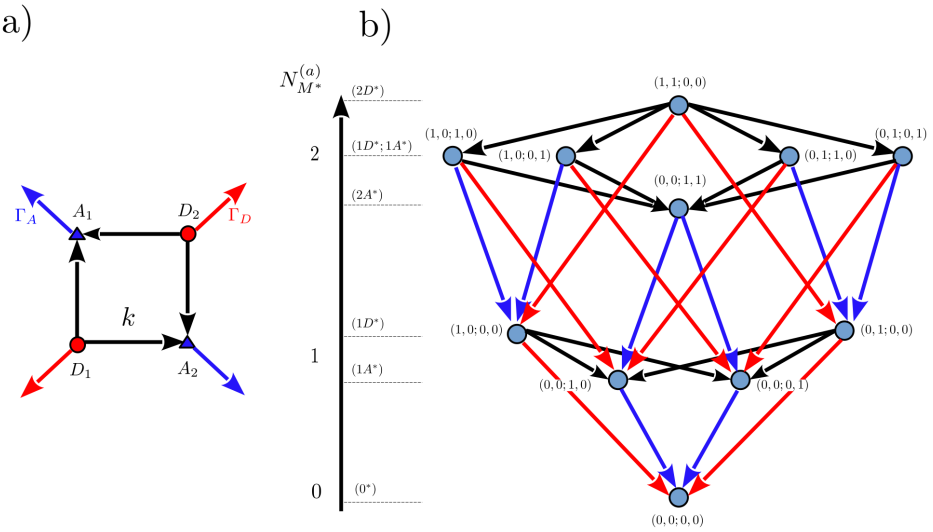

Figure 2.7: a) Scheme of a distribution of $N_D(N_A) = 2$ donor (acceptor) molecules located in a square configuration presented as red circles (blue triangles). The excited donor (acceptor) can emit a spontaneous photon shown as a red (blue) arrow. The RET process between excited donor and ground state acceptor is shown with black arrows. b) Associated graph of possible microstates $\left(\sigma_{D_1}^{(a)}, \sigma_{D_2}^{(a)}, \sigma_{A_1}^{(a)}, \sigma_{A_2}^{(a)}\right)$ (blue dots) corresponding to the macrostate $\left(N_{D^*}^{(a)}, N_{A^*}^{(a)}\right)$. The elementary transitions corresponding to fluorescence and rate processes entering in the chemical master equation Eq. 2.5 are pictured as arrows with same colors as in a). Unpublished Fig.

An exact solution in the case $N_D = N_A = 2$ molecules. In contrast to the case of fluorescence in Sec. 2.2, there is no known exact solution to the computation of the average populations $\langle N_{D^*}(t)\rangle$ and $\langle N_{A^*}(t)\rangle$. We derive in this paragraph a special case in which $N_D = N_A = 2$ and for which an exact solution can been derived. *The derivation and solution of this exact model was done for the first time by Alice Marché during her Master 1 internship in LOMA [84].* In this case, the D and A molecules are put at the vertex of a square and presented respectively as red circles and blue circles, as presented in Fig. 2.7-a).

The excited donors (acceptors) can emit a spontaneous photon presented as a red (blue) arrow. The RET process between D and A molecules are shown as black arrow. *Due to the equidistance between each pair of donor and acceptor molecules, the rate of RET are thus all the same and equal to k, thus making the RET process homogeneous.* We show in Fig. 2.7 the graph of possible microstates we consider (in total 11 microstates), that are connected by random jump events associated to either an elementary fluorescence process or by a RET process. Starting from the state $(1,1,0,0) \equiv (2D^*)$ with 2 donors and 0 acceptors excited, the system undergoes a stochastic succession of jumps to finally reach the final state $(0,0,0,0) \equiv (0^*)$ without any acceptor excited. *We note that the homogeneity of the rate process is mapped onto a general symmetry of the graph itself that reflects the permutation symmetry of the molecular ensemble with respect to the molecular indices* $1 \longleftrightarrow 2$. This leads to the following symmetry properties of the microstate populations

$$\begin{aligned} P_{(1,0,1,0)} &= P_{(1,0,0,1)} = P_{(0,1,1,0)} = P_{(0,1,0,1)} \equiv P_{(1D^*,1A^*)}\,, && (2.25)\\ P_{(1,0,0,0)} &= P_{(0,1,0,0)} \equiv P_{(1D^*)}\,, && (2.26)\\ P_{(0,0,1,0)} &= P_{(0,0,0,1)} \equiv P_{(1A^*)}\,, && (2.27) \end{aligned}$$

and the following expression of the average population of excited donors

$$\langle N_{D^*}(t)\rangle = 2P_{(2D^*)}(t) + 4P_{(1D^*1A^*)}(t) + 2P_{(1D^*)}(t)\,. \tag{2.28}$$

The chemical master equation can be simplified by the symmetry properties written above and lead to a reduced system of 3 linear equations

$$\begin{aligned} \dot{P}_{(2D^*)}(t) &= -\left(4k + 2\Gamma_D\right) P_{(2D^*)}(t)\,, && (2.29)\\ \dot{P}_{(1D^*1A^*)}(t) &= kP_{(2D^*)}(t) - \left(k + \Gamma_D + \Gamma_A\right) P_{(1D^*1A^*)}(t)\,, && (2.30)\\ \dot{P}_{(1D^*)}(t) &= 2\Gamma_A P_{(1D^*,1A^*)}(t) + \Gamma_D P_{(2D^*)}(t) - \left(2k + \Gamma_D\right) P_{(1D^*)}(t)\,. && (2.31) \end{aligned}$$

This system can be solved exactly, with the initial condition $P_{(2D^*)}(0) = 1$, $P_{(1D^*1A^*)}(0) = 0$ and $P_{(1D^*)}(0) = 0$. After substitution into Eq. 2.28, this leads to the exact solution for the population of excited donors

$$\langle N_{D^*}(t)\rangle = 2\left\{Ce^{-(2\Gamma_D+4k)t} + De^{-(\Gamma_D+\Gamma_A+k)t} + \left[1 - C - D\right]e^{-(\Gamma_D+2k)t}\right\}\,, \tag{2.32}$$

with the constant coefficients

$$\begin{aligned} C &= -\frac{2k^2}{\left(\Gamma_A - \Gamma_D - 3k\right)\left(\Gamma_D + 2k\right)}\,, && (2.33)\\ D &= -\frac{2k^2}{\left(\Gamma_A - \Gamma_D - 3k\right)\left(\Gamma_A - k\right)}\,. && (2.34) \end{aligned}$$

Analysis of the exact solution. The exact evolution of the population of excited donors encoded in Eq. 2.32 for $N_D = N_A = 2$ already contains interesting features that are relevant to understand the dynamics of larger molecular ensembles. First we see that, in contrast to the single exponential relaxation obtained for a fluorescence process (see Eq. 2.4), the time evolution of $\langle N_{D^*}(t)\rangle$ in presence of RET, is a sum of three exponential functions with three different rates. We assign those rates to three different timescales involved in the random

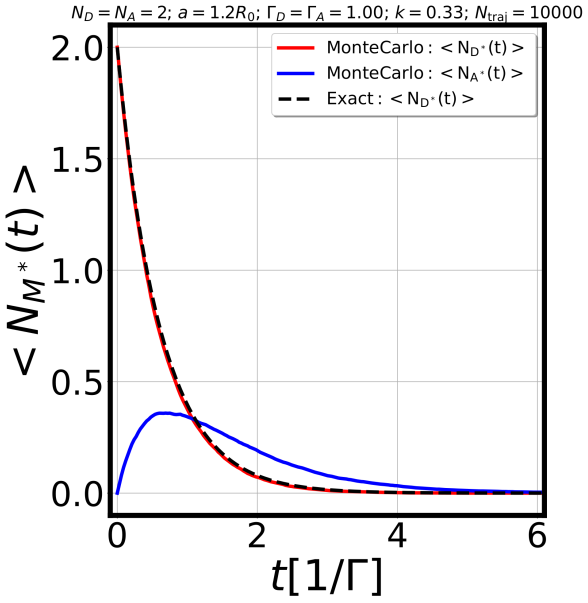

Figure 2.8: Time-dependent populations of excited donors $\langle N_{D^*}(t)\rangle$ (plain red curve) and acceptors $\langle N_{A^*}(t)\rangle$ (plain blue curve) obtained from the MC calculation, in the case of the regular square lattice made of 2 donor and 2 acceptor molecules shown in Fig. 2.7-a). Comparison is shown with the exact analytical solution of Eq. 2.32 (dashed black curve). Parameters are: $a = 1.2R_0$, $N_D = N_A = 2$, $\Gamma_D = \Gamma_A = 1.0$, $k = 0.33$, and $N_{traj} = 10^4$. Unpublished Fig.

fluorescence and RET events (when $N_D = N_A = 2$) that occurred with different probability upon varying the number of excited molecules in the aggregate. *The RET process is thus a hierarchical stochastic process in which the physics of relaxation to equilibrium depends on spatial and occupation constraints of the molecular sites at the origin of collective effects. The former are negligible at the beginning and at the end of the relaxation dynamics, but dominate in the intermediate times for which the distribution of excitations is maximally mixed in the ensemble.* Second, we show in Fig. 2.8 that the time evolution of $\langle N_{D^*}(t)\rangle$ computed with the numerical MC simulation (plain red curve) exactly matches the outcome of the analytical formula in Eq. 2.32 (dashed black curve). The evolution is monotonously decreasing to zero because, once excited, the donor molecules can only loose their energy either by fluorescence or by transferring their energy by RET. In contrast, the evolution of $\langle N_{A^*}(t)\rangle$ as computed by MC simulations (plain blue curve) is not monotonous and reaches a maximum at times $\approx 1/\Gamma$. This can be understood easily. Initially, there is no excited acceptor in the ensemble. Thus one has to wait for RET processes to occur in order that some acceptor molecules get excited and thus increase $\langle N_{A^*}(t)\rangle$. At longer times, the excited acceptor population will decay by fluorescence and relax back to zero.

Open questions. The previous example leads to the natural question of what is happening for a similar aggregate in the macroscopic limit, when both N_D and N_A are very large. It will certainly be interesting to consider and investigate the stochastic dynamics of RET in the situation of an homogeneous RET process as the non-trivial limit of a stochastic pro-

cess on a graph of increasing size: will this procedure converge to some fix point ? The emerging chemical complexity in this process will be of combinatorial nature. Such a task is largely open for future research and is at the carrefour of graph theory and statistical physics. *We suspect that the dynamics in the large N limit will be approximated by a series of exponential functions with a lot of different rates, and thus will become a multi-scale and non-linear process. This fact is of relevance for spectroscopic experiments which usually fit the time evolution of the excited molecular populations (obtained by measurement of their related fluorescence signal) with a single or few exponential, while the true evolution is certainly much richer.*

2.3.3 Hierarchy of exact kinetic equations

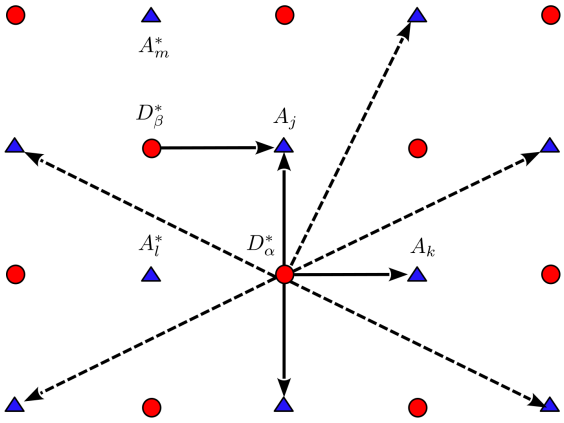

Figure 2.9: Representation of a square lattice aggegrate of D and A molecules. Some RET processes are shown emerging from the D_α^* molecule as plain black arrows when reaching a nearest neighbor A_k molecule and as dashed black arrows when reaching a next nearest neighbor one. We illustrate the competition between i) the two RET processes $D_\alpha^* + A_j \rightarrow D_\alpha + A_j^*$ and $D_\beta^* + A_j \rightarrow D_\beta + A_j^*$ and ii) the one between the two RET processes $D_\alpha^* + A_j \rightarrow D_\alpha + A_j^*$ and $D_\alpha^* + A_k \rightarrow D_\alpha + A_k^*$. The single RET process $D_\alpha^* + A_l \rightarrow D_\alpha + A_l^*$ is forbidden and thus not shown, because the acceptor molecule A_l^* is already excited. Unpublished Fig.

Derivation of an exact kinetic equation. We complement the derivation of the exact kinetic equation made for homogeneous fluorescent processes in Sec. 2.2.4 to the case where additional non homogeneous RET processes occur between D and A molecular pairs (see Eq. 2.18). *This derivation was published in our Ref. [8].* An additional term $\frac{d}{dt}\langle N_{D^*}(t)\rangle_{\rm RET}$ due to RET is thus added in Eq. 2.9

$$\frac{d}{dt}\langle N_{D^*}(t)\rangle_{\rm RET} \;=\; -\sum_{(a,b)_{\rm RET}} k_{ba} P_a(t)\,, \tag{2.35}$$

with $\sum_{(a,b)_{\rm RET}}$ the sum constrained on all pairs of microstates (a,b) connected by a spontaneous emission rate process of rate k_{ba}. The constrained sum can be expanded further

as

$$\sum_{(a,b)_{\mathrm{RET}}} P_a(t) \;=\; \sum_{\alpha=1}^{N_D}\sum_{j=1}^{N_A} k_{\alpha j} \sum_{\left\{\sigma_\beta\right\}_{\beta\neq\alpha}} \sum_{\{\sigma_l\}_{l\neq j}} P_{a=\left\{\sigma_\alpha=1,\left\{\sigma_\beta\right\}_{\beta\neq\alpha},\sigma_j=0,\{\sigma_l\}_{l\neq j}\right\}}(t)\,, \tag{2.36}$$

where the sum is taken on all initial configurations of excitation states of the molecular ensemble a for which the donor D_α is excited $\sigma_\alpha = 1$ and the acceptor A_j is in the ground state $\sigma_j = 0$. Those configurations are the only ones that can lead to a RET process $D_\alpha^* + A_j \rightarrow D_\alpha + A_j^*$ (see Fig. 2.9). The output of Eq. 2.36 can be rewritten in a compact way, after *introducing* $\Pi^{(2)}_{\sigma_\alpha\sigma_j}(t)$*, the "two-molecule" joint probability distribution that the molecule* D_α *is in the excitation state* $\sigma_\alpha = 0, 1$ *and the molecule* A_j *is in the excitation state* $\sigma_j = 0, 1$ *at time* t

$$\Pi^{(2)}_{\sigma_\alpha\sigma_j}(t) \;=\; \sum_{\left\{\sigma_\beta\right\}_{\beta\neq\alpha}} \sum_{\{\sigma_l\}_{l\neq j}} P_{a=\left\{\sigma_\alpha,\left\{\sigma_\beta\right\}_{\beta\neq\alpha},\sigma_j,\{\sigma_l\}_{l\neq j}\right\}}(t)\,. \tag{2.37}$$

Plugging the definition in Eq. 2.37 into Eq. 2.4, adding also the contribution of fluorescence process, we obtain the final kinetic equation for the RET and fluorescence process in the molecular aggregate ruling the evolution of the excited donor molecules

$$\frac{d}{dt}\left\langle N_{D^*}(t)\right\rangle \;=\; -\Gamma\left\langle N_{D^*}(t)\right\rangle - \left\langle k_{DA} N_{D^*}(t) N_A(t)\right\rangle\,, \tag{2.38}$$

with the pair correlation function of excited donors and ground state acceptors

$$\left\langle k_{DA} N_{D^*}(t) N_A(t)\right\rangle \;\equiv\; \sum_{\alpha=1}^{N_D}\sum_{j=1}^{N_A} k_{\alpha j}\left\langle \sigma_\alpha(t)\overline{\sigma}_j(t)\right\rangle\,. \tag{2.39}$$

We introduced in Eq. 2.39 *the pair correlation function of excitation states* $\langle\sigma_\alpha(t)\overline{\sigma}_j(t)\rangle$ *for each pair of molecule* D_α *and* A_j defined as

$$\left\langle \sigma_\alpha(t)\overline{\sigma}_j(t)\right\rangle \equiv \sum_{\sigma_\alpha=0,1}\sum_{\sigma_j=0,1} \sigma_\alpha\overline{\sigma}_j \Pi^{(2)}_{\sigma_\alpha\sigma_j}(t)\,, \tag{2.40}$$

with $\overline{\sigma}_j = 1 - \sigma_j$.

Comments about the kinetic equation. The kinetic equation Eq. 2.38 has a simple physical interpretation. The first term in its right-hand-side stands for the decay channel for the exited donors D_α^* by a fluorescence process of rate Γ_D. The second term on the right-hand-side, is related to RET processes with rate $k_{\alpha,j}$, that naturally correlates the excited-state of the donor D_α^* to the ground-state of the acceptor A_j. *This kinetic equation is exact. However, contrary to the macroscopic kinetic equation Eq. 2.20, it is not a closed-equation. Indeed, one has to complement Eq. 2.38 with an additional equation providing the time-evolution of the still unknown pair correlation functions* $\langle\sigma_\alpha(t)\sigma_j(t)\rangle$.

"Une mise en abîme". The process of the previous paragraph can be iterated. *It leads to a hierarchy of coupled kinetic equations, which becomes an infinite hierarchy in the large N limit.* We provide below the three first equations of this hierarchy

$$\frac{d}{dt}\langle\sigma_\alpha\rangle = -\Gamma_D\langle\sigma_\alpha\rangle - \sum_{j=1}^{N_A} k_{\alpha,j}\langle\sigma_\alpha\overline{\sigma}_j\rangle \ , \tag{2.41}$$

$$\frac{d}{dt}\langle\overline{\sigma}_j\rangle = \Gamma_A\langle\sigma_j\rangle - \sum_{\alpha=1}^{N_D} k_{\alpha,j}\langle\sigma_\alpha\overline{\sigma}_j\rangle \ , \tag{2.42}$$

$$\begin{aligned}\frac{d}{dt}\langle\sigma_\alpha\overline{\sigma}_j\rangle &= \Gamma_A\langle\sigma_\alpha\sigma_j\rangle - (\Gamma_D + k_{\alpha,j})\langle\sigma_\alpha\overline{\sigma}_j\rangle \\ &- \sum_{\beta=1,\beta\neq\alpha}^{N_D} k_{\beta,j}\langle\sigma_\alpha\sigma_\beta\overline{\sigma}_j\rangle - \sum_{k=1,k\neq j}^{N_A} k_{\alpha,k}\langle\sigma_\alpha\overline{\sigma}_k\overline{\sigma}_j\rangle \ ,\end{aligned} \tag{2.43}$$

$\cdots$ etc

The existence of a hierarchy of coupled kinetic equations makes the problem of computing exactly the average population of excited molecules as a function of time unsolvable for an arbitrary large number N of molecules. *The origin of this unsolvability has a profound physical significance: it reflects the manybody nature of the RET process that results into microscopic constraints and spatial frustrations at the origin of chemical complexity.* Already in those three first kinetic equations, we can interpret the resulting terms as follow

1. The average rate of excitation of the D_α molecule in Eq. 2.41 decreases due to *fluorescence events $D_\alpha^* \to D_\alpha + h\nu$ of rate Γ_D, which are intrinsically "one-body terms"* and thus provide a contribution proportional to $\langle\sigma_\alpha(t)\rangle$.

2. But $\langle\sigma_\alpha(t)\rangle$ can also decrease in Eq. 2.41 due to RET events $D_\alpha^* + A_j \to D_\alpha + A_j^*$ of rate $k_{\alpha j}$ transferring the excitation energy of the D_α^* molecule to all available ground state acceptor molecules A_j in the ensemble. *This is an intrinsic "two-body effect" that is possible only if the A_j site accepting the excitation are not excited, thus correlating the evolution of the population to the dynamics of the pair correlation function $\langle\sigma_\alpha(t)\overline{\sigma}_j(t)\rangle$.*

3. The pair correlation function in Eq. 2.43 correlates to single and two-body processes through fluorescence and RET events respectively. *But it also couples to three-body terms through RET events that come from a competition mechanism in the RET process between three molecules.* The former are shown in Fig. 2.9. Indeed the term $\langle\sigma_\alpha(t)\sigma_\beta(t)\overline{\sigma}_j(t)\rangle$ comes from the competition between two excited donors to transfer their exciton to the same ground state acceptor through the two RET processes $D_\alpha^* + A_j \to D_\alpha + A_j^*$ and $D_\beta^* + A_j \to D_\beta + A_j^*$. Similarly, the other term $\langle\sigma_\alpha(t)\overline{\sigma}_k(t)\overline{\sigma}_j(t)\rangle$ is associated to the competition between the following RET processes $D_\alpha^* + A_j \to D_\alpha + A_j^*$ and $D_\alpha^* + A_k \to D_\alpha + A_k^*$.

Open question. In our quest to compute the time evolution of the excited donor and acceptor molecules in the aggregate in presence of RET, *we have mapped the problem of*

solving the microscopic chemical master equation onto the problem of solving an infinite hierarchy of kinetic equations involving correlation functions of increasing order. Both problems cannot be solved exactly for arbitrary configurations and number of molecules. We thus ask ourselves in the next section how to truncate the hierarchy of kinetic equations and recover the macroscopic ones.

2.3.4 The mean-field approximation

Spatial coarse-graining. We aim at proposing a closure assumption to the kinetic equations Eqs. 2.41,2.42 which simplifies it and reproduces well the macroscopic kinetic equation Eq. 2.20 obtained in the limit of large number of molecules $N \gg 1$ in the aggregate or large sample volume Ω (given by the sample surface S in dimension two). For that purpose, we make *a first assumption* $(A1)$ *that in the large* N *limit, the spatially coarsed-grained two-molecules joint-distribution function* $\overline{\Pi}^{(2)}_{\sigma_\alpha,\sigma_j}(t)$ *defined in Eq.2.37 factorizes*, namely that

$$\overline{\Pi}^{(2)}_{\sigma_\alpha,\sigma_j}(t) \approx \overline{\Pi}^{(1)}_{\sigma_\alpha}(t)\overline{\Pi}^{(1)}_{\sigma_j}(t)\,, \tag{2.44}$$

where $\overline{A}$ means the coarsed-grained (spatially averaged) value associated to any quantity A. Using this approximation $(A1)$, we can simplify the kinetic equations Eqs. 2.41,2.42 as

$$\frac{d}{dt}\overline{\langle\sigma_\alpha\rangle} = -\Gamma_D\overline{\langle\sigma_\alpha\rangle} - \sum_{j=1}^{N_A} k_{\alpha,j}\overline{\langle\sigma_\alpha\rangle}\ \overline{\langle\overline{\sigma}_j\rangle} \tag{2.45}$$

$$\frac{d}{dt}\overline{\langle\overline{\sigma}_j\rangle} = \Gamma_A\overline{\langle\sigma_j\rangle} - \sum_{\alpha=1}^{N_D} k_{\alpha,j}\overline{\langle\sigma_\alpha\rangle}\ \overline{\langle\overline{\sigma}_j\rangle}\,. \tag{2.46}$$

Those coarse-grained kinetic equations are closed for the fields $\left\{\overline{\langle\sigma_\alpha\rangle}\right\}_\alpha$ *and* $\left\{\overline{\langle\overline{\sigma}_j\rangle}\right\}_j$*, and constitute a system of* N *non-linear mean-field equations.* Such equations can in principle be solved with proper initial conditions, although, due to the large number of unknowns and the non-linearity of the equations, this remains a heavy and difficult task.

Spatial homogeneity assumption. We now make *the last assumption* $(A2)$*, that after spatial coarse-graining performed in* $(A1)$*, the molecular system becomes spatially homogeneous in the large-N limit*, namely that translational invariance is restored at the mean-field and macroscopic level

$$\overline{\langle\sigma_\alpha(t)\rangle} \approx \phi^{(\mathrm{mf})}_{D^*}(t) = \frac{\langle N_{D^*}(t)\rangle}{N_D}\,, \tag{2.47}$$

$$\overline{\langle\overline{\sigma}_j(t)\rangle} \approx \phi^{(\mathrm{mf})}_{A}(t) = \frac{\langle N_{A}(t)\rangle}{N_A}\,. \tag{2.48}$$

Injecting back Eqs.2.47,2.48 into Eqs.2.45,2.46, we obtain the following kinetic equations

$$\frac{d}{dt}\langle N_{D^*}(t)\rangle = -\Gamma_D \langle N_{D^*}(t)\rangle - \overline{k}\,\langle N_{D^*}(t)\rangle \langle N_A(t)\rangle \;, \tag{2.49}$$

$$\frac{d}{dt}\langle N_A(t)\rangle = \Gamma_A \langle N_{A^*}(t)\rangle - \overline{k}\,\langle N_{D^*}(t)\rangle \langle N_A(t)\rangle \;, \tag{2.50}$$

which are nothing but the macroscopic kinetic equations Eqs. 2.41,2.42 but with the mean-field rate of RET

$$\overline{k} = \frac{1}{N_D N_A}\sum_{\alpha=1}^{N_D}\sum_{j=1}^{N_A} k_{\alpha j}\,. \tag{2.51}$$

Eq. 2.51 is the main result of this section and answers to one of the questions formulated in Sec. 2.3.1, namely it provides the expression of the macroscopic mean-field of RET $\overline{k}$ in terms of the microscopic rates $k_{\alpha j}$. It has a simple interpretation: the rate $\overline{k}$ is obtained as the spatial average on the whole molecular aggregate of the sum of microscopic rates connecting a D^* molecule to all other A_j molecules (see the black arrows going out from the molecule D^*_α in Fig. 2.9).

One simple example: the case of a 2D aggregate. In this paragraph, we provide an explicit expression for the macroscopic mean-field rate of RET $\tilde{k}$ evaluated in the special case of a disordered bi-dimensional aggregate of D and A molecules (see Fig. 2.10-a)). This case and the case of a perfect ordered square lattice are analyzed in depth in our Ref. [8]. *The disordered molecular ensemble is a random lattice that fulfills in the large N limit both assumptions (A1) of decoupling of the pair correlation functions and of spatial homogeneity (A2) (see Sec. 2.3.4).* Substituting the mean-field expression of Eq. 2.51 into the expression of the macroscopic rate written in Eq. 2.24, we obtain in the case $N_D = N_A = N/2$ the integral form

$$\tilde{k} = \frac{2}{N}\int d^2\vec{r}\int d^2\vec{r'}\overline{\rho_{DA}}(\vec{r},\vec{r'})k\left(||\vec{r}-\vec{r'}||\right) \tag{2.52}$$

with $k\left(||\vec{r}-\vec{r'}||\right)$ given by Eq. 2.19. The spatially averaged density of pairs of donor and acceptor molecules $\overline{\rho_{DA}}(\vec{r},\vec{r'})$ is defined as

$$\overline{\rho_{DA}}(\vec{r},\vec{r'}) = \overline{\rho_D(\vec{r})\rho_A(\vec{r'})} \tag{2.53}$$

with $\rho_D(\vec{r}) = \sum_{\alpha=1}^{N_D}\delta^2\left(\vec{r}-\vec{r}_\alpha\right)$ and $\rho_A(\vec{r'}) = \sum_{j=1}^{N_A}\delta^2\left(\vec{r'}-\vec{r}_j\right)$. *The assumption $(A2)$ of spatial homogeneity implies that the mean-field rate becomes translational invariant after spatial coarse graining or averaging on disorder configurations (which are equivalent procedures in practice due to the self-averaging property of the molecular ensemble upon increasing N)* so that $\overline{\rho_{DA}}(\vec{r},\vec{r'}) \equiv \overline{\rho_{DA}}(\vec{r}-\vec{r'})$ and

$$\tilde{k} = \frac{2S}{N}\Gamma_D R_0^6\int_{R_c}^{R} dr\int_0^{2\pi} d\theta\frac{\overline{\rho_{DA}}(r,\theta)}{r^5}\,. \tag{2.54}$$

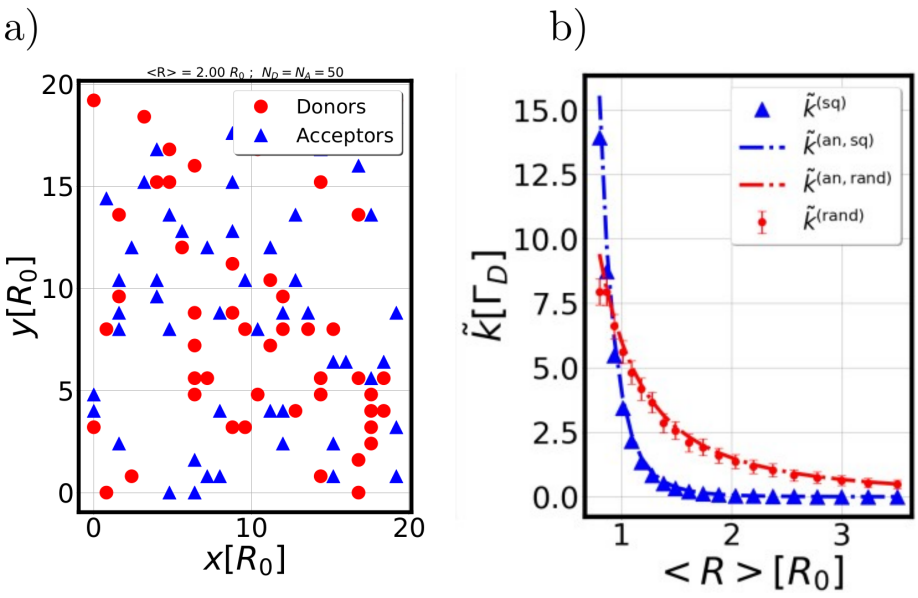

Figure 2.10: a) Representation of a disordered 2D lattice with $R_c = 0.8R_0$ the cutoff distance, and $\langle R \rangle = 2.0R_0$ the average distance between molecules. Donnor (D) and acceptor (A) molecules are shown as red dots and blue triangles respectively. The system contains $N_D = N_A = 50$ molecules of type D and A. b) Macroscopic mean-field rate of RET $\tilde{k}^{(\mathrm{rand})}$ (red points) as a function of the average distance $< R >$ between individual excited donors and their nearest-neighbor acceptor molecules. An average is performed on 1000 configurations of disorder for various random distributions of molecules on the square network in a). The error bars represent one standard deviation, illustrating the uncertainty due to fluctuations in the spatial location of molecules that varies from sample to sample. The dashed-dotted red curve is obtained from the analytical rate $\tilde{k}^{(\mathrm{an,rand})}$ in Eq. 2.56. Adapted from Ref. [8].

We introduced $S = \pi R^2$ the surface of the sample supposed to be a disk of radius R and R_c the cutoff length defined as the minimum distance between two molecules. *At this stage, this expression of $\tilde{k}$ is general and independent of the chosen bi-dimensional network of molecules. It connects the effective macroscopic rate of RET to the actual spatial distribution of molecular pairs of donors and acceptors in the macroscopic sample.* In the specific case of a random 2D lattice shown in Fig. 2.10)-a), the additional assumption $(A1)$ of factorization of the "two-molecules" correlation functions after spatial coarse graining implies that the averaged spatial density of pairs in Eq. 2.53 simplifies to

$$\overline{\rho_{DA}}(\vec{r}, \vec{r'}) \approx \overline{\rho}_D \overline{\rho}_A \,, \tag{2.55}$$

with $\overline{\rho}_D = \overline{\rho}_A \approx N/2S$ the equal concentration of donor and acceptor molecules. This provides a simpler and explicit expression for $\tilde{k}$ in Eq. 2.54 which is valid in the limit of large number of molecules $N \gg 1$ or of large sample surface $S \gg R_c^2, R_0^2$. We obtain

$$\tilde{k}^{(\mathrm{an,rand})} \approx k_0 \left(\frac{R_0}{2 \langle R \rangle} \right)^2 , \tag{2.56}$$

with $k_0 = \Gamma_D \left(R_0/R_c\right)^4$ and $\langle R \rangle = \sqrt{S/\pi N}$ the average distance between an individual excited-donor and its nearest-neighbor acceptor that is proportional to the inverse square root of the molecular concentration. *The scaling-law $\tilde{k} \propto \langle R \rangle^{-2}$ in Eq. 2.56 obtained for the macroscopic mean-field rate of RET is a surprising result.* Indeed one would have expected a scaling $\tilde{k} \propto \langle R \rangle^{-6}$ by simple inference from the microscopic rate in Eq. 2.19. This interesting effect comes from disorder in a bi-dimensional random sample, namely *the average rate of RET from a given donor D molecule results from spatial averaging of the contribution of acceptor A molecules around D that scales at the mean-field level with the molecular concentration.* We show in Fig. 2.10)-b) (red points), the dependence of $\tilde{k}^{(\mathrm{rand})}$ in units of Γ_D, as a function of $< R > /R_0$. This curve is obtained from a numerical evaluation of Eq. 2.51 for a random lattice containing $N_D = N_A = 50$ molecules after averaging on 1000 configurations of disorder. This calculation compares quantitatively very well to the predicted analytical values of $\tilde{k}^{(\mathrm{an,rand})}$ given by Eq. 2.56 (see dash-dotted red curves). The scaling law depends on the molecular network. In particular we show in Ref. [8] the expected scaling $\tilde{k} \propto \langle R \rangle^{-6}$ for the regular square network (see also Fig. 2.9 blue points).

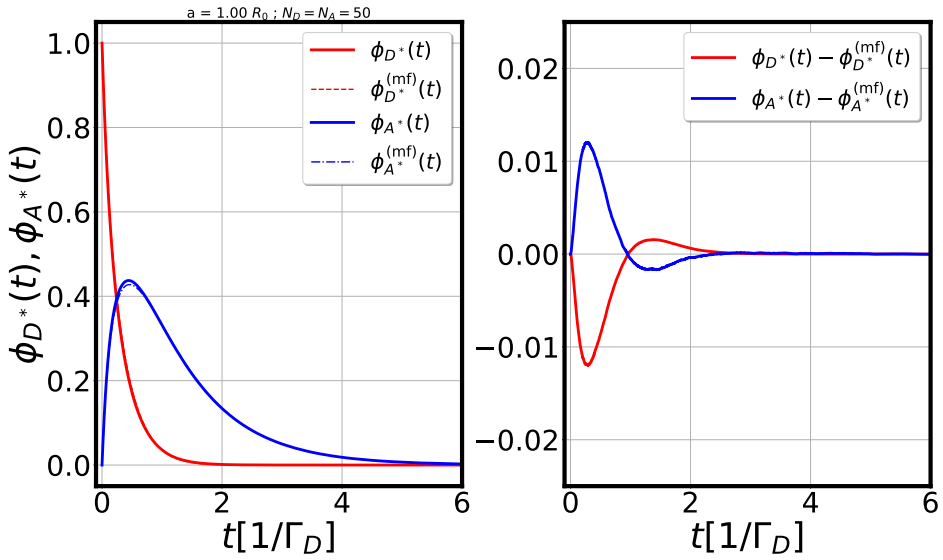

Figure 2.11: Left: Time-dependent relative populations of excited donors $\phi_{D^*}(t) = \langle N_{D^*}(t) \rangle / N_D$ (plain red curve) and acceptors $\phi_{A^*}(t) = \langle N_{A^*}(t) \rangle / N_A$ (plain blue curve) obtained from the MC calculation, in the case of the regular square lattice shown in Fig. 2.9. Comparison is shown with the macroscopic mean-field analytical results $\phi_{D^*}^{(\mathrm{mf})}(t)$ (dashed red curve) and $\phi_{A^*}^{(\mathrm{mf})}(t)$ (dash-dotted blue curve). Right : Time-dependence of the contribution due to fluctuations $\phi_{D^*}(t) - \phi_{D^*}^{(\mathrm{mf})}(t)$ (red curve) and $\phi_{A^*}(t) - \phi_{A^*}^{(\mathrm{mf})}(t)$ (blue curve). Parameters: $a = 1.0 R_0$, $\Gamma_D = \Gamma_A \equiv \Gamma$ and $N_D = N_A = 50$. The MC runs are averaged on $N_{traj} = 10^5$ stochastic trajectories. Adapted from Ref. [8].

Full time-dependence of the molecular populations. For completeness, we show in Fig. 2.11(left-panel) the outcome of the MC calculation for $\phi_{D^*}(t) \equiv \langle N_{D^*}(t) \rangle / N_D$ (plain red curve) and $\phi_{A^*}(t) \equiv \langle N_{A^*}(t) \rangle / N_A$ (plain blue curve) for the regular square lattice shown in Fig. 2.9 with $N_D = N_A = 50$ molecules. We chose the case where the distance a

between two neighbor D and A molecules equates the Förster radius R_0 such that *the rate of spontaneous emission is of the same order of magnitude as the rate of RET ($\Gamma \approx k$). There is thus a competition mechanism between both processes and a significant energy-transfer occurs towards the acceptors.* The qualitative behavior and analysis of the curves is very similar to the ones shown in Fig. 2.8, that were derived in the case $N_D = N_A = 2$, for which the analytical exact solution of Sec. 2.3.2 holds. However, the quantitative behavior is quite different. Indeed, we show in Fig. 2.11 the mean-field curves $\phi_{D^*}^{(\mathrm{mf})}(t)$ (dashed red curve obtained from Eq. 2.22) and $\phi_{A^*}^{(\mathrm{mf})}(t)$ (dash-dotted blue curve obtained from Eq. 2.22) obtained as solutions of the macroscopic rate equations with the mean-field rate in Eq. 2.51. We see that the mean-field approximation is very well approximating the exact MC calculations shown as $\phi_{D^*}(t)$ (plain red curves) and $\phi_{A^*}(t)$ (plain blue curves). *The average kinetics of the RET process in a macroscopic sample (large N limit) is thus accurately described by non-linear mean-field equations rather than by a linear relaxation process as obtained in Fig. 2.9 for a microscopic sample.* We show in the right panel of Fig. 2.11 weak deviations from the mean-field approximation that are quantitatively computed through the quantities $\phi_{D^*}(t) - \phi_{D^*}^{(\mathrm{mf})}(t)$ (red curve) and $\phi_{A^*}(t) - \phi_{A^*}^{(\mathrm{mf})}(t)$ (blue curve). *We see that the mean-field approximation is not exact and that deviations of the MC calculation occur that are due to finite-size fluctuations (here $N = 100$).*

Open question. *Our theory provides a solid approach to recover the macroscopic limit as illustrated by the computation of the coarse grained RET of rate $\overline{k}$ in Eq.2.51 or by the very good agreement between the time-dependent evolution of mean-field molecular populations and the ones computed with the MC calculation.* However deviations to the mean-field approximation are seen. It still remains to analyze the origin of those deviations and there relative amplitudes. *In particular, what are the effects of spatial inhomogeneities and dynamical constraints due to collective effects in RET on those mesoscopic fluctuations ?*

2.4 Mesoscopic fluctuations and collective aspects of RET

2.4.1 Position of the problem

In this section, we come back to the problem of quantifying the deviations from the mean-field approximation that we unveiled in the previous Sec. 2.3.4. *This is a notoriously difficult problem.* To keep some hope of progress in this task, we first simplify the model of RET that we used up to now. Our physical intuition will be guided by the exact solution we found in Sec. 2.3.2 for the model of $N_D = N_A = 2$ molecules deposited on a regular square network. Such an exact solution exists because of the homogeneity of the rates k for each microscopic RET event occurring in the sample (see Fig. 2.7-a)). This leads to the equalities in Eqs. 2.25,2.26,2.27 among various microstates that are obtained one from each other by a permutation of the index labeling the molecules. *We thus now generalize this model to an ideally homogeneous aggregate for which, whatever the pairs of molecules that undergo a RET process $D_\alpha^* + A_j \to D_\alpha + A_j^*$, the microscopic rate of RET $k_{\alpha j}$ for such an individual random*

event is the same, namely that

$$\forall\,(\alpha,j)\in[|1,N_D|]\times[|1,N_A|]\,;\;k_{\alpha j}=k\,. \tag{2.57}$$

The condition in Eq. 2.57 is a condition of all to all homogeneous coupling: it is not fulfilled in general, even in the case of the regular square lattice as soon as $N_D, N_A > 2$, because of the dependence of the RET with the intermolecular distance written in Eq. 2.19. *However, it should be a good approximation to the behavior of an aggregate after spatial coarse graining in the large N limit, for which the assumptions $(A1)$ and $(A2)$ of Sec. 2.3.4 hold and the aggregate is homogeneous in average.*

Problematic. We will rewrite the chemical master equation describing the RET process in Sec. 2.4.2 and investigate its stochastic dynamics in the case of an ideally homogeneous aggregate. *For the purpose of investigating the macroscopic limit of the molecular ensemble, we will make use of statistical physics methods that were derived and explained for the first time by van Kampen in his seminal book Ref. [117].* The final outcome will be the calculation of the Fokker-Planck equation in Sec. 2.4.3 and the calculation of corrections to the mean-field approximation in Sec. 2.4.4 that we simply wrote without justification in our Ref. [8] due to length constraints. We thought that a detailed derivation could be of interest. *This derivation is original, in the sense that, to our knowledge, such a derivation is not published nor known in the literature of RET.* Moreover, it contains interesting physical concepts and ideas that could be applied to broader classes of problems, for instance those encountered in the field of *polaritonic chemistry* (see next Chapter).

2.4.2 Chemical master equation for the homogeneous RET process

The joint probability distribution of excited D^* and A^* molecules. In this paragraph, we first consider generic macrostates (n_D, n_A) associated to all the microstates $a \in \mathcal{E}_(n_D, n_A)$ for which the total number of excited donors and acceptors is $N_{D^*}^{(a)} = n_D$ and $N_{A^*}^{(a)} = n_A$ respectively. Similarly to the simple case of Fig. 2.7, due to homogeneity of the RET events, all the microstates belonging to $\mathcal{E}_(n_D, n_A)$ have the same probability of occurrence in the microscopic chemical master equation Eq. 2.5. *It is thus natural to retain only the net contribution of all those microstates belonging to a given macrostate, thus focusing on a coarse grained description of the dynamics involving only the macrostates (n_D, n_A).* For that purpose, we introduce the corresponding joint probability distribution of having n_D excited D^* molecules and m_A excited A^* molecules $P(n_D, m_A)$ defined as

$$P(n_D,m_A,t) \;=\; \sum_{a\in\mathcal{E}_(n_D,n_A)} P_a(t)\,. \tag{2.58}$$

This distribution is the main mathematical object in terms of which the chemical master equation in Eq. 2.5 can be rewritten, in the special case of an ideally homogeneous aggregate.

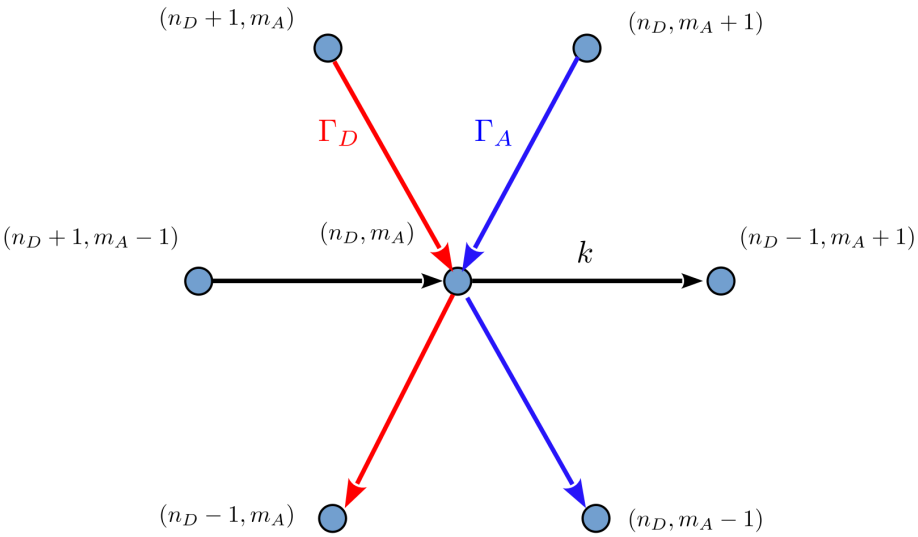

Figure 2.12: Scheme of the graph of macrostates (n_D, n_A) (blue points) corresponding to all microstates containing n_D and n_A excited donor and acceptor molecules. The elementary fluorescence events from D^* and A^* molecules are shown as red arrows and blue arrow with rates Γ_D and Γ_A respectively. The generic homogeneous RET events with rate k are shown as black arrows. Unpublished Fig.

Derivation of the homogeneous chemical master equation. We present in Fig. 2.12 the possible individual random events connecting the macrostates (n_D, n_A). We write the resulting homogeneous chemical master equation as a sum of three terms

$$\dot{P}(n_D, m_A) = \dot{P}(n_D, m_A)\Big|_{\Gamma_D} + \dot{P}(n_D, m_A)\Big|_{\Gamma_A} + \dot{P}(n_D, m_A)\Big|_{k} . \tag{2.59}$$

The first term in Eq. 2.59 stands for the contribution of fluorescence events $D^*_\alpha \to D_\alpha + h\nu$ with rate Γ_D. Such transition connects a macrostate (n_D, n_A) to another one $(n_D - 1, n_A)$ containing one less excited donor but the same number of excited acceptors (see red arrows in Fig. 2.12). We obtain

$$\dot{P}(n_D, m_A)\Big|_{\Gamma_D} = \Gamma_D \Big\{ (n_D + 1) P(n_D + 1, m_A) - n_D P(n_D, m_A) \Big\} . \tag{2.60}$$

The second term in Eq. 2.59 has a similar expression and interpretation, but in terms of fluorescence events from the excited acceptors (see blue arrows in Fig. 2.12). The last term of Eq. 2.59 encodes the contribution of all homogeneous RET processes with $D^*_\alpha + A_j \to D_\alpha + A^*_j$ with rate k. Such transition connects the macrostate (n_D, n_A) with another one $n_D - 1, m_A + 1$ containing one less D^* excitation and one more A^* excitation (see black arrows in Fig. 2.12). We obtain

$$\begin{aligned} \dot{P}(n_D, m_A)\Big|_{k} &= k \Big\{ (n_D + 1)\,(N_A - m_A + 1)\, P(n_D + 1, m_A - 1) \\ &- n_D\,(N_A - m_A)\, P(n_D, m_A) \Big\} . \end{aligned} \tag{2.61}$$

Operator form of the homogeneous chemical master equation. We can obtain an operator form for the homogeneous chemical master equation in Eq. 2.59. For that purpose, following the notation of van Kampen in Ref. [117], we introduce the $\mathbb{E}_D^{\pm 1}$ and $\mathbb{E}_A^{\pm 1}$ operators, defined by their action on any function $f(n_D, m_A)$ as

$$\mathbb{E}_D^{\pm 1} f(n_D, m_A) = f(n_D \pm 1, m_A)\,, \tag{2.62}$$
$$\mathbb{E}_A^{\pm 1} f(n_D, m_A) = f(n_D, m_A \pm 1)\,. \tag{2.63}$$

Those operators create or destroy one D^* or A^* excitation in the molecular ensemble. Using the previous definition inside Eqs. 2.60,2.61 we can give to the homogeneous chemical master equation its final operator form

$$\begin{aligned}\dot{P}(n_D, m_A) &= \Gamma_D \left(\mathbb{E}_D - 1\right) n_D P(n_D, m_A) + \Gamma_A \left(\mathbb{E}_A - 1\right) m_A P(n_D, m_A) \\ &+ k \left(\mathbb{E}_D \mathbb{E}_A^{-1} - 1\right) n_D \left(N_A - m_A\right) P(n_D, m_A)\,.\end{aligned} \tag{2.64}$$

This expression of the chemical master equation is the main result of this section. *Apart from being compact and aesthetic, Eqs. 2.64 consists now of a system of linear equations of size $(N_D+1)\times(N_A+1)$. We thus arrived to an explicit coarse grained version of the microscopic chemical master equation that scales quadratically with the system size $\propto N^2$ instead of the exponential scaling $\propto 2^N$ obtained in the microscopic chemical master equation written in Eq. 2.5.* The coarse grained evolution encoded in Eq. 2.64 is thus more suited to investigate the stochastic RET dynamics of an ideally homogeneous mesoscopic sample than the microscopic evolution of Eq. 2.5. *Unfortunately there is no known exact solution to Eq. 2.64. One thus has to resort to an approximation scheme described in the next section.*

2.4.3 Derivation of the Fokker–Planck equation for RET

The large-Ω expansion. We apply now the large-Ω expansion technique that was developed by van Kampen in Ref. [117] in order to evaluate the behavior of the average populations and their fluctuations from Eq. 2.64 in the limit of large aggregates. The parameter Ω is an extensive parameter, typically here the volume of the studied molecular system. We suppose that $N_D, N_A \gg 1$ and that the number of excited donors and acceptors in the aggregate is large $n_D, n_A \gg 1$. *Following van Kampen approach, we introduce the decomposition or change of variable of n_D, n_A into the sum of two quasi-continuous variables*

$$n_D \equiv \Omega \underline{\Phi}_D + \Omega^{\frac{1}{2}} \xi_D\,, \tag{2.65}$$
$$n_A \equiv \Omega \underline{\Phi}_A + \Omega^{\frac{1}{2}} \eta_A\,. \tag{2.66}$$

In Eqs. 2.65,2.66, *the first term is the mean-field contribution (undefined at this stage) to the excited donor population that scales linearly with the system volume $\propto \Omega$. The second term is the contribution of weak deviations or fluctuations from the mean-field term and scale with the square-root of the system size $\propto \Omega^{\frac{1}{2}}$.* In the following, we introduce $\tilde{k} \equiv k\Omega$ the macroscopic rate of RET and $\underline{\varphi}_A(t) = \underline{\Phi}_A(0) - \underline{\Phi}_A(t)$ the concentration of acceptor A molecules in the ground state, such that $\dot{\underline{\varphi}}_A(t) = -\dot{\underline{\Phi}}_A(t)$. *The idea behind the large-Ω expansion is the perform an asymptotic expansion of the homogeneous chemical master equation in the limit of large Ω.*

Continuous limit of the $\mathbb{E}_D^{\pm 1}$ and $\mathbb{E}_A^{\pm 1}$ operators. Substituting the large-Ω expansion provided by Eqs. 2.65,2.66 into the expressions of n_D and n_A, *the action of the $\mathbb{E}_D^{\pm 1}$ operators on any function $f(n_D, m_A)$ as written in Eqs. 2.62,2.63 can be approximated accurately as a series of continuous differential operators in powers of $\Omega^{-\frac{1}{2}}$*

$$\begin{aligned}\mathbb{E}_D^{\pm 1} f(n_D, m_A) &= f(n_D \pm 1, m_A) \equiv F\left(\xi_D \pm \Omega^{-\frac{1}{2}}, \eta_A\right) \\ &\approx F(\xi_D, \eta_A) \pm \Omega^{-\frac{1}{2}} \frac{\partial}{\partial \xi_D} F(\xi_D, \eta_A) + \frac{\Omega^{-1}}{2} \frac{\partial^2}{\partial \xi_D^2} F(\xi_D, \eta_A) \ . \end{aligned} \quad (2.67)$$

We thus obtain for the operators entering the homogeneous chemical master equation the following asymptotic expansions

$$\mathbb{E}_D^{\pm 1} - 1 \approx \pm \Omega^{-\frac{1}{2}} \frac{\partial}{\partial \xi_D} + \frac{\Omega^{-1}}{2} \frac{\partial^2}{\partial \xi_D^2} , \quad (2.68)$$

$$\mathbb{E}_A^{\pm 1} - 1 \approx \pm \Omega^{-\frac{1}{2}} \frac{\partial}{\partial \eta_A} + \frac{\Omega^{-1}}{2} \frac{\partial^2}{\partial \eta_A^2} , \quad (2.69)$$

$$\mathbb{E}_D \mathbb{E}_A^{-1} - 1 \approx \Omega^{-\frac{1}{2}} \left\{ \frac{\partial}{\partial \xi_D} - \frac{\partial}{\partial \eta_A} \right\} + \frac{\Omega^{-1}}{2} \left\{ \frac{\partial}{\partial \xi_D} - \frac{\partial}{\partial \eta_A} \right\}^2 . \quad (2.70)$$

Asymptotic expansion of the chemical master equation. We substitute the asymptotic expansions in Eqs. 2.68,2.69,2.70 in the chemical master equation written in operator form Eq. 2.64 for $P(n_D, m_A, t) \equiv \Pi(\xi_D, \eta_A, t)$. We get for the right hand side of the chemical master equation

$$\begin{aligned}\dot{P}(n_D, m_A)\Big|_{\text{r.h.s}} &\approx \Gamma_D \left\{ \Omega^{\frac{1}{2}} \underline{\phi}_D \frac{\partial \Pi}{\partial \xi_D} + \frac{\partial (\xi_D \Pi)}{\partial \xi_D} + \frac{\underline{\phi}_D}{2} \frac{\partial^2 \Pi}{\partial \xi_D^2} \right\} \\ &+ \Gamma_A \left\{ \Omega^{\frac{1}{2}} \underline{\phi}_A \frac{\partial \Pi}{\partial \eta_A} + \frac{\partial (\eta_A \Pi)}{\partial \eta_A} + \frac{\underline{\phi}_A}{2} \frac{\partial^2 \Pi}{\partial \eta_A^2} \right\} \\ &+ \tilde{k} \left\{ \Omega^{\frac{1}{2}} \underline{\Phi}_D \underline{\varphi}_A \left(\frac{\partial}{\partial \xi_D} - \frac{\partial}{\partial \eta_A} \right) \Pi + \left(\frac{\partial}{\partial \xi_D} - \frac{\partial}{\partial \eta_A} \right) \left[\underline{\varphi}_A \xi_D \Pi - \underline{\Phi}_D \eta_A \Pi \right] \right. \\ &+ \left. \frac{\underline{\Phi}_D \underline{\varphi}_A}{2} \left(\frac{\partial}{\partial \xi_D} - \frac{\partial}{\partial \eta_A} \right)^2 \Pi \right\} . \end{aligned} \quad (2.71)$$

We now develop the left hand side of the chemical master equation and obtain

$$\begin{aligned}\dot{P}(n_D, m_A)\Big|_{\text{l.h.s}} \equiv \frac{d\Pi}{dt} &= \frac{\partial \Pi}{\partial t} + \dot{\xi}_D(t) \frac{\partial \Pi}{\partial \xi_D} + \dot{\eta}_A(t) \frac{\partial \Pi}{\partial \xi_D} \\ &= \frac{\partial \Pi}{\partial t} - \Omega^{\frac{1}{2}} \left[\dot{\underline{\Phi}}_D(t) \frac{\partial \Pi}{\partial \xi_D} + \dot{\underline{\Phi}}_A(t) \frac{\partial \Pi}{\partial \eta_A} \right] , \end{aligned} \quad (2.72)$$

where the last line is obtained after deriving Eqs. 2.65,2.66 taking into account that in the change of variable $\dot{n}_D = \dot{m}_A = 0$ (the variables n_D, m_A do not depend explicitly on time in $P(n_D, m_A, t)$). We then equate Eq. 2.71 and Eq. 2.72 and collect all the terms of order $\Omega^{\frac{1}{2}}$ and of order Ω^0.

Recovering the mean-field equations. The terms of order $\Omega^{\frac{1}{2}}$ in the r.h.s and l.h.s of the chemical master equation should be equal for any value of the independent variables ξ_D, η_A, t. This is so if and only if

$$\dot{\underline{\Phi}}_D = -\Gamma_D \underline{\Phi}_D - \tilde{k} \underline{\Phi}_D \underline{\varphi}_A \,, \tag{2.73}$$

$$\dot{\underline{\Phi}}_A = -\Gamma_A \underline{\Phi}_A + \tilde{k} \underline{\Phi}_D \underline{\varphi}_A \,. \tag{2.74}$$

It is interesting to notice that the former equations are the same as the mean-field equations written in Eqs 2.49,2.50. *The large-Ω expansion of the joint distribution function $P(n_D, m_A, t)$ thus recovers a posteriori and in a natural way the mean-field approximation as its dominating term of order $\Omega^{\frac{1}{2}}$, thus without imposing it a priori !.*

Fokker-Planck equation for the RET process. Finally, we equate the terms of order Ω^0 in the r.h.s and l.h.s of the chemical master equation, and obtain

$$\begin{aligned} \frac{\partial \Pi}{\partial t} &= \left(\Gamma_D + \tilde{k} \underline{\varphi}_A\right) \frac{\partial \left(\xi_D \Pi\right)}{\partial \xi_D} + \left(\Gamma_A + \tilde{k} \underline{\Phi}_D\right) \frac{\partial \left(\eta_A \Pi\right)}{\partial \eta_A} + \Gamma_D \frac{\underline{\phi}_D}{2} \frac{\partial^2 \Pi}{\partial \xi_D^2} + \Gamma_A \frac{\underline{\phi}_A}{2} \frac{\partial^2 \Pi}{\partial \eta_A^2} \\ &+ \tilde{k} \Big\{ \frac{\underline{\Phi}_D \underline{\varphi}_A}{2} \left(\frac{\partial}{\partial \xi_D} - \frac{\partial}{\partial \eta_A} \right)^2 \Pi - \underline{\varphi}_A \xi_D \frac{\partial \Pi}{\partial \eta_A} - \underline{\Phi}_D \eta_A \frac{\partial \Pi}{\partial \xi_D} \Big] \,. \end{aligned} \tag{2.75}$$

The former Eq. 2.75 is the main result of this section. *It is a multivariate Fokker-Planck equation describing deviations from the mean-field approximation derived in Sec. 2.3.4. This Fokker-Planck equation answers to our problematic of investigating the role of mesoscopic fluctuations developing in the case of an ideally homogeneous and large but finite sample.*

2.4.4 Analysis of mesoscopic fluctuations in the RET process

Average deviations to the mean-field solution. We now consider $\langle F(\xi_D, \eta_A, t) \rangle = \int d\xi_D \int d\eta_A F(\xi_D, \eta_A) \Pi(\xi_D, \eta_A, t)$ the average value of any function $F(\xi_D, \eta_A)$ taken with respect to the distribution $\Pi(\xi_D, \eta_A, t)$ that is solution of the Fokker-Planck equation with proper initial conditions. We find, using Eq. 2.75, that the average deviations to the mean-field solution $\langle \xi_D(t) \rangle$ and $\langle \eta_A(t) \rangle$ are solution of the following set of linear equations

$$\frac{d}{dt} \langle \xi_D(t) \rangle = -\left(\Gamma_D + \tilde{k} \underline{\varphi}_A(t)\right) \langle \xi_D(t) \rangle + \tilde{k} \underline{\Phi}_D(t) \langle \eta_A(t) \rangle \,, \tag{2.76}$$

$$\frac{d}{dt} \langle \eta_A(t) \rangle = -\left(\Gamma_A + \tilde{k} \underline{\Phi}_D(t)\right) \langle \eta_A(t) \rangle + \tilde{k} \underline{\varphi}_A(t) \langle \xi_D(t) \rangle \,. \tag{2.77}$$

The interpretation of those equations is simple: they actually come from the study of stability of the mean-field equations Eqs. 2.73,2.74 under weak perturbations $\underline{\Phi}_D \to \underline{\Phi}_D + \delta \underline{\Phi}_D$ and $\underline{\Phi}_A \to \underline{\Phi}_A + \delta \underline{\Phi}_A$. *The resulting linear stability analysis of the variations $\delta \underline{\Phi}_D$ and $\delta \underline{\Phi}_A$ gives back the same equations as Eqs. 2.76,2.77 followed by $\langle \xi_D(t) \rangle$ and $\langle \eta_A(t) \rangle$. Thus the regression of average deviations from the mean-field solutions follows the linear variation of the mean-field equations themselves.* For instance, $\langle \xi_D(t) \rangle$ decays as a function of time due to the effective time-dependent rate $\Gamma + \tilde{k} \underline{\varphi}_A(t)$ coming from i) the fluorescence process of the excited D^* molecules and ii) from a coupling through a RET process of the $\langle \xi_D(t) \rangle$

fluctuation to the average occupation $\underline{\varphi}_A(t)$ of A molecules in their ground state. *The time dependence of this effective rate comes from the non-linearity of the mean-field kinetic equations.* The quantity $\langle \xi_D(t) \rangle$ can also increase in time due to contribution of fluctuations of the A molecular populations coupling to the average occupation of the D^* molecules $\underline{\Phi}_D(t)$, with an effective time-dependent rate $\tilde{k}\underline{\Phi}_D(t)$. A similar interpretation can be found for the evolution of $\langle \eta_A(t) \rangle$. Finally, we remark that, a consequence of the linearity of Eqs. 2.76,2.77 and of starting from an initial conditions $\langle \xi_D(0) \rangle = 0$ and $\langle \eta_A(0) \rangle = 0$, is that at all times

$$\langle \xi_D(t) \rangle = \langle \eta_A(t) \rangle = 0 \,. \tag{2.78}$$

This is the case for the dynamics we consider. *The understanding of deviations from the mean-field solution is thus encoded fully into the fluctuations of the instantaneous $\xi_D(t)$ and $\eta_A(t)$ quantities. The large-Ω expansion amounts to make a linear noise approximation where fluctuations from the average are described by a Gaussian process. However, no truncation of the chemical master equation nor any a priori ad hoc assumptions are needed to recover this behavior: it comes from the asymptotic expansion itself.*

Gaussian fluctuations around the mean-field solution. In the same way as in the previous paragraph, we derive from the Fokker-Planck equation Eq. 2.75 the time-dependent equations ruling the dynamics of the correlation functions $\langle \xi_D(t)\eta_A(t) \rangle$, $\langle \xi_D^2(t) \rangle$ and $\langle \eta_A^2(t) \rangle$. We obtain

$$\frac{d}{dt}\langle \xi_D \eta_A \rangle = -\left[\Gamma_A + \Gamma_D + \tilde{k}\left(\underline{\Phi}_D + \underline{\varphi}_A\right)\right]\langle \xi_D \eta_A \rangle + \tilde{k}\left[\underline{\varphi}_A \langle \xi_D^2 \rangle + \underline{\Phi}_D \langle \eta_A^2 \rangle - \underline{\varphi}_A \underline{\Phi}_D\right] , \tag{2.79}$$

$$\frac{d}{dt}\langle \xi_D^2 \rangle = -2\left(\Gamma_D + \tilde{k}\underline{\varphi}_A\right)\langle \xi_D^2 \rangle + 2\tilde{k}\underline{\Phi}_D \langle \xi_D \eta_A \rangle + \left(\Gamma_D + \tilde{k}\underline{\varphi}_A\right)\underline{\Phi}_D \,, \tag{2.80}$$

$$\frac{d}{dt}\langle \eta_A^2 \rangle = -2\left(\Gamma_A + \tilde{k}\underline{\Phi}_D\right)\langle \eta_A^2 \rangle + 2\tilde{k}\underline{\varphi}_A \langle \xi_D \eta_A \rangle + \Gamma_A \underline{\Phi}_A + \tilde{k}\underline{\varphi}_A \underline{\Phi}_D \,, \tag{2.81}$$

with the initial conditions $\langle \xi_D(0)\eta_A(0) \rangle = \langle \xi_D^2(0) \rangle = \langle \eta_A^2(0) \rangle = 0$. Those equations are the main results of this section. *They have a simple physical interpretation: the first term of Eq. 2.79 describes the decay in time (regression of fluctuations) of the correlation function* $\langle \xi_D(t)\eta_A(t) \rangle$ due to the decay of each $\xi_D(t)$ and $\eta_A(t)$ with the respective time-dependent rates $\Gamma_D + \tilde{k}\underline{\varphi}_A(t)$ in Eq. 2.76 and $\Gamma_A + \tilde{k}\underline{\Phi}_D(t)$ in Eq. 2.77. The second term of Eq. 2.79 corresponds to an increase of $\langle \xi_D(t)\eta_A(t) \rangle$ due to the onset of excited donor and acceptor fluctuations $\langle \xi_D^2(t) \rangle$ and $\langle \eta_A^2(t) \rangle$. Those terms could have been derived independently from Eq. 2.43, doing an a priori Gaussian ansatz closure hypothesis for the third moments $\langle \sigma_\alpha(t)\sigma_\beta(t)\overline{\sigma}_j(t) \rangle$ and $\langle \sigma_\alpha(t)\overline{\sigma}_k(t)\overline{\sigma}_j(t) \rangle$. *We note, however, that the large-Ω asymptotic expansion of van Kampen [117] is more suited to derive this result, since it recovers as a consequence of the approximation that the fluctuations are Gaussian in the macroscopic limit, without supposing it initially, nor truncating arbitrarily the chemical master equation.* Finally, the last term of Eq. 2.43 is the one that dominates at short times, since $\frac{d}{dt}\langle \xi_D(t)\eta_A(t) \rangle \approx -\tilde{k}\underline{\varphi}_A(0)\underline{\Phi}_D(0) = -\tilde{k}$ when $t \to 0^+$. *This term basically describes an anti-correlation between the populations of excited donor and acceptor molecules.* This is due to the intrinsic mechanism of RET reaction, for which each time an excited donor molecule D^* transfers its energy to an acceptor in the ground-state, the latter gets excited to A^*. *This anti-correlation is beyond the mean-field approximation which supposes statistical independence between the donor and acceptor populations.*

Analysis of the computed deviations from the mean-field solution. We close our investigation of mesoscopic fluctuations in RET by analysis the deviations from the mean-field solution computed from the Monte Carlo calculation and shown in the right panel of Fig. 2.11 as a red curve for $\phi_{D^*}(t) - \phi_{D^*}^{(\mathrm{mf})}(t)$ and a blue one for $\phi_{A^*}(t) - \phi_{A^*}^{(\mathrm{mf})}(t)$. At short times $t \ll 1/\tilde{k}$, those deviations are weakly negative, namely $\phi_{D^*}(t) - \phi_{D^*}^{(\mathrm{mf})}(t) < 0$ (red curve). Indeed the initial slope of this curve is proportional to the initial fluctuations $\frac{d}{dt}\langle \xi_D(t)\eta_A(t)\rangle \approx -\tilde{k}$, given by Eq. 2.79. *The latter exhibit a sizable anti-correlation effect due to the anti-correlated mechanism of disappearance of D^* and appearance of A^* molecules in the elementary RET process.* At later times $t > 1/\tilde{k}$, the onset of excited donor and acceptor fluctuations $\langle \xi_D^2(t)\rangle$ and $\langle \eta_A^2(t)\rangle$ in Eq. 2.79 start to couple to the curve $\phi_{D^*}(t) - \phi_{D^*}^{(\mathrm{mf})}(t)$ and leads to its increase (with even a small overshoot above zero). At long times $t \gg 1/\Gamma$, the curve $\phi_{D^*}(t) - \phi_{D^*}^{(\mathrm{mf})}(t)$ goes back to zero due to the regression of fluctuations in Eq. 2.79. *In summary, the mean-field curves $\phi_{D^*}^{(\mathrm{mf})}(t)$ and $\phi_{A^*}^{(\mathrm{mf})}(t)$ constitute very good approximations to the Monte Carlo calculation in the large-N limit, which thus validates a posteriori the use of this approximation. Deviations to it are due to mesoscopic fluctuations that incorporate information about the microscopic RET process and related "three-body" competition mechanism between donor and acceptor molecules.*

2.5 Conclusion and future research perspectives.

Conclusion. In this chapter, we have investigated in depth the stochastic dynamics developing in two-dimensional aggregates containing donor and acceptor molecules in presence of both fluorescence and resonance energy transfer. We provided reasonable physical assumptions under which a mean-field approximation for describing the RET process holds. *We could provide an explicit expression in terms of the molecular aggregate configuration of an effective mean-field rate of RET $\tilde{k}$ in the macroscopic limit.* The former expression depends in a non-trivial way of the spatial distribution of pairs of molecules inside the sample. *We showed that the rate of RET scales as $\tilde{k} \propto \langle R\rangle^{-2}$ in the case of a disordered sample of D and A molecules, expressing the fact that one random D^* molecule in the sample sees an average mean-field contribution of all available A molecules randomly located around it.* This is in contrast to the scaling $\tilde{k} \propto \langle R\rangle^{-6}$ obtained in the case where the molecules are put on the apex of an ordered square lattice (see Ref. [8] for that case). We have then computed the time-dependent populations of excited donor and acceptor molecules using a numerically exact kinetic Monte-Carlo approach and compared it to the non-linear dynamics provided by the mean-field approximation. The former shows a good agreement with the latter. *Deviations of the exact Monte Carlo calculation compared to the mean-field result were shown to be due to fluctuations and spatial correlations developing at the microscopic level and involving at least three molecules in the elementary RET process.* Those deviations should be important in finite-size clusters or mesoscopic samples of molecules, as currently seen in biology. *Finally, we provided a full derivation of the Fokker-Planck equation from the chemical master equation describing the coarsed-grained relaxation dynamics of an ideally homogeneous RET process.* From it we were able to quantify precisely the kinetics of regression of those mesoscopic fluctuations.

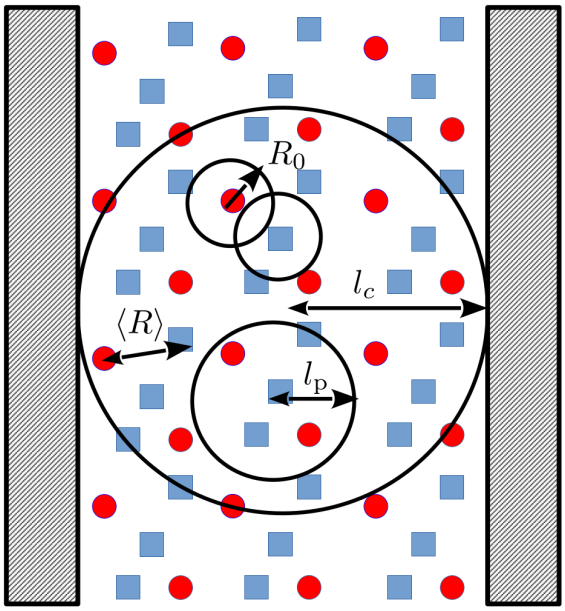

Figure 2.13: Scheme of a distribution of donor (red circles) and acceptor (blue squares) molecules embedded inside an optical Fabry-Pérot cavity. The cavity mode might be resonantly coupled with an electronic transition of either the D or A-type of molecules. The arrows correspond to l_c the cavity coherence length, l_P the spatial correlation length of molecular pairs, R_0 the Förster radius and $\langle R \rangle$ the average distance between molecular pairs involved in the RET processes. Unpublished Fig.

Future research perspectives. Our predictions for the RET dynamics should be observable in state of the art transient-fluorescence or pump-probe experiments. In the former case, additional effects at ultra-short times (shorter that the exciton-exciton annihilation time) should be observable that result from the interplay between the time-dependent drive by the pump followed by the slower relaxation dynamics due to fluorescence, exciton-exciton relaxation, and RET. *The theoretical description of such effects in spatially inhomogeneous and anisotropic samples (position and orientational disorder of the molecular dipoles) is still an open issue, that would necessitate a generalization of our approach towards the use of a generalized master equation [75].* Such generalization would be of interest to investigate another class of problems for which the D and A molecules are embedded inside an optical cavity, and compute the modification of the rate of RET inside the cavity (see experiments performed in Ref. [123]). *Such approach would mix the intrinsic chemical complexity of the RET process to the complexity induced by collective coupling of the molecular ensemble to the cavity optical modes at the origin of polariton formation.* This problem is multiscale in nature (see Fig. 2.13). We anticipate the interplay between the following length scales: l_c the cavity coherence length defining the mode volume in which coherent coupling between molecules has to be taken into account, l_P the spatial correlation length for the distribution of molecular pairs, R_0 the Förster radius and $\langle R \rangle$ the average distance between molecular pairs involved in the local RET processes. We formulate the following questions which at the present day, to our knowledge, are still unsolved.

1. *How to reconcile the collective and delocalized nature of polariton excitations in an optical cavity with the local nature of RET processes at the microscopic molecular level ?*

2. How to model and compute the modification of the RET dynamics inside cavity ?

We believe that part of the answer is encoded into the interplay between the coherent (delocalized) light-matter coupling mechanism and the stochastic dynamics (localized) of RET as described by a general chemical master equation including both the molecular aggregate and the mode dynamics. Such equation has still to be derived and solved ! We hope that the theoretical approach and results we derived in this chapter will be of interest to drive future theoretical and experimental investigations along that way. *We anticipate a modeling of the complexity of this problem in terms of a random diffusion of the system configuration onto the graph of manybody states describing its correlated light-matter excitations: this is very similar to the graph theoretical approach of RET we have shown in the simple example of Fig. 2.7.* This will be a hierarchical problem: at ultrafast femtosecond time scales, the molecules collectively synchronize to the dynamics of the cavity mode leading to the formation of a polariton. At larger times (picoseconds to nanoseconds), RET process that are local in space will occur, thus inducing a perturbation of the molecular ensemble composition and a reorganization of the polaritonic electromagnetic environment. *A mean-field description of the structured (spatially and temporally) hybrid light-matter polaritonic environment made of the coupled cavity modes and the molecular ensemble is thus clearly needed and probably is a crucial ingredient to include into the description of RET in polaritonic chemistry.* The theory in this direction is still in its infancy and I see it as a motivating path and a challenge for my future research to look for such surprising and rich effects, when chemistry meets physics inside optical Fabry-Pérot cavities. Whether this approach is successful or not for this goal is still not known and of no true importance: what matters is "the beauty and the knowledge acquired when walking along that path"...

Chapter 3

Chirality and dimensionality in the ultrastrong light-matter coupling regime

3.1 Introduction

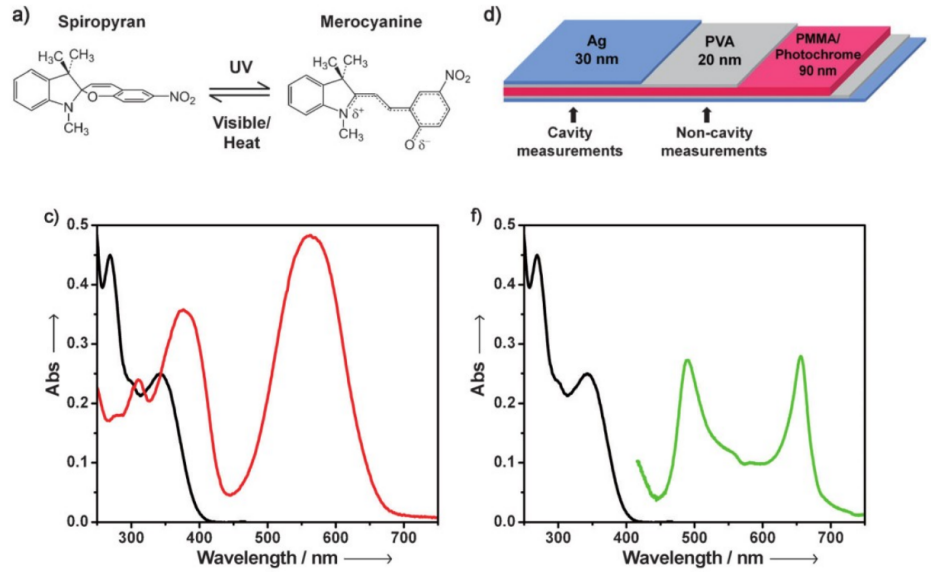

Figure 3.1: d) Scheme of an optical Fabry-Pérot cavity made of a layer of Spiropyran molecules (SPI) sandwiched between two layers of silver mirrors. a) The SPI molecules can undergo a photochemical reaction giving Merocyanine (MC) molecules. c) Absorption spectrum of the MC form in red for molecules out of cavity. f) Same absorption spectrum in green but for the MC embedded inside cavity which is resonant with the $\mathrm{MC} - \mathrm{MC}^*$ transition. Rabi split peaks appear due to the formation of polaritons. Adapted from Ref. [64].

An ultra brief introduction to polaritonic chemistry. *Polaritonic chemistry* [42, 47] is an emerging and dynamic field of research which aims at *modulating physical properties [123, 90] and chemical reactivity [64] of molecular ensembles or materials embedded inside an electromagnetic cavity.* This modulation occurs in the so-called *light-matter strong-coupling regime* when a collective interaction mechanism between electronic or vibrational molecular transitions and the quantum vacuum fluctuations of some resonant cavity mode takes place and gets faster than the total dissipation rate of the cavity. This strong coupling regime is characterized by *the formation of hybrid light-matter states called polaritons* [64, 35] which can be observed by measuring the collective vacuum Rabi splitting of the cavity absorption signal (see Fig. 3.1 for a measurement performed in the electronic strong coupling regime). However many points remain badly or only partially understood to explain the observed experiments which are related to the necessity of including into the theoretical modeling of optical cavities "a certain degree of complexity" either related to the *chemical complexity* of the molecular material or to the *optical complexity* in describing the spatial structure of the cavity electromagnetic field. *Both points are particularly salient when dealing with chiroptical effects related to the intrinsic chirality of molecules embedded inside cavity and its interplay with the spatial structure and polarization state of the cavity modes.*

The issue of chirality in the light-matter interactions mechanism. Developing a better understanding of chiral light-matter interactions appears to be an important issue in order to design more precise spectroscopic tools for molecular [121], chemical [38, 54] and biological [97, 88] sciences. This quest is however made difficult due to *the intrinsically weak intensity of chiroptical signals [28] and to the complexity and multi-scale nature [32, 113] of the related light-matter interaction process.* Indeed, at the microscopic level, a description of optical activity (OA) or circular dichroism (CD) in three dimensions involves a delicate interference process between intrinsic molecular electronic or vibrational properties and the spatial inhomogeneity of the local electromagnetic (EM) field [28, 80, 82, 116]. It is by consequence crucial to describe the system *"chiral material plus electromagnetic field"* as a whole [44, 4].

Chiral polaritonics. This problematic is at the heart of an emerging field of research known as *chiral polaritonics* [11, 86] which aims at boosting chiroptical signals through the onset of collective interaction mechanisms [42, 47] taking place in an engineered electromagnetic environment. A central question in this field is to investigate whether strong coupling between light and matter could open new paths towards *modification of the stereoselectivity of chemical reactions inside cavity*, thus leading to an *asymmetric polaritonic chemistry.* Unfortunately, one is confronted to the problem that inside a standard optical Fabry-Pérot (FP) cavity, polarization reversal of the EM waves occurs at the interfaces with the metallic mirrors [67]. This leads to no cavity-induced amplification of OA or CD signals [94, 119, 112] despite a very large collective coupling strength [87]. The idea was thus proposed to recycle the EM field helicity in so-called chiral FP cavities [122, 43, 119, 11, 86, 87, 12, 48, 21, 106] (see Fig. 3.2), thus leading to an imbalance of polarization content of the EM field stored inside cavity and possibly enhanced chiroptical properties of the cavity [86, 87]. In parallel, the theoretical description of the above mentioned interplay between collective light-matter strong coupling and chirality in such cavities is still in its infancy. There are

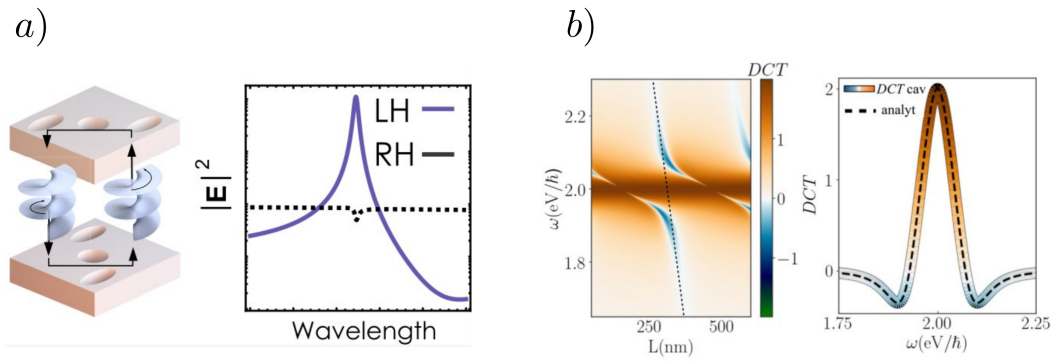

Figure 3.2: a) Scheme of single-handedness optical Fabry-Pérot cavity for which spin-preserving mirrors enable to recycle the helicity of the electromagnetic waves inside the cavity. The left handed or right handed circular polarization content of the electromagnetic energy stored inside cavity is thus imbalanced close to some spin-preserving frequency. Adapted from Ref. [119]. b) Differential circular dichroism (DCT) signal for such a cavity computed as a function of cavity length and frequency. Close to the spin-preserving frequency of the mirrors, the DCT chiroptical signal is enhanced significantly, thus realizing a chiral Fabry-Pérot cavity. Adapted from our recent Ref. [86].

many recent efforts enabling to describe accurately either the EM field structure in the cavity [119, 86, 87], or the molecular electronic and vibrational structure using *mixed quantum electrodynamics approaches* [116, 95] with *ab initio quantum chemical methods* [101, 109, 100]. Those works consider either three dimensional chiral cavities filled homogeneously with an optically active material, or single to few molecules coupled to a spatially homogeneous and single quantum EM mode of the cavity. However, by their very approaches, *these works do not perceive one crucial aspect that is fundamental to the phenomenon of chirality, namely the role played by dimensionality when looking at a chiral molecular system embedded inside a given electromagnetic environment.*

Problematic of the present chapter. We address in the present chapter the following questions related to chiral light matter interactions but in a standard FP cavity with normal metallic mirrors

1. What is the role of *reducing dimensionality from dimension three (3D) to dimension two (2D)* of the coupled molecular system embedded inside cavity ?

2. How to deal with *the spatial dispersion along the optical axis of the EM field structure inside cavity*, that is necessary to describe chiral signatures on optical properties of the cavity ?

3. Is there some *enantio-dependent shift of the cavity polaritonic spectra* and how do they depend on experimentally relevant parameters like the concentration of the chiral molecules, the position of the 2D layer along the mode spatial profile or the intrinsic molecular chirality ?

We formulate a partial answer to those problems in three steps. We provide first *a general introduction to the physics of polaritons in optical cavities* in Sec. 3.2: this shows how to compute the polaritonic spectra and what is the effect of *the unavoidable presence of inhomogeneous disorder* in the material inside cavity. We then study in more detail the polaritonic spectra including *the peculiarities induced upon entering the ultrastrong coupling regime* in Sec. 3.3: an in-depth analysis is given of the polaritonic dispersion curves and *an analogy is developed between the underlying physical mechanism with an equivalent problem of classical Newtonian mechanics.* We then investigate in Sec. 3.4 *the chiral light matter interaction mechanism emerging between a 2D layer of chiral molecules an the states of polarization of an optical FP cavity.* We provide an analytical scaling law of chiroptical polaritonic dispersions that can be tested experimentally. On top of that, *intertwining chirality with dimensionality points towards a fundamental role played by topology.* To unveil the underlying topological structure of our quantum theory, we analyzed the analogous classical dynamics of the interacting chiral light-matter system in its phase space. *We show a one to one correspondence between the enantio-dependent shifts of the predicted polaritonic spectra and the dynamics of the equivalent classical trajectories exhibiting a modified anholonomy angle due to the onset of gyrotropic coupling.* Finally, a conclusion and some perspectives and open questions for future research are given in the conclusion in Sec. 3.5. This work on chirality is mainly the output of a collaboration with Cyriaque Genet (ISIS) that is part of the scientific work I made during my one year visit in his laboratory. It is reported in our recent Ref. [6]. This opens many doors to question our understanding of chiral light-matter interactions both theoretically and experimentally.

3.2 Canonical model of polariton formation

In this section, we provide an introduction to the mechanism of polariton formation in standard Fabry-Pérot cavities. This introduction is inspired by the pioneer work of Houdré [63] whose beautiful paper introduced the general concepts that are necessary to grasp and understand the effect of inhomogeneous broadening due to molecular disorder in polariton physics. *We provide here a personal derivation of those main physical concepts and formulate them in such a way to be readily generalizable to a broader class of problems, for instance for problems involving the coupling between a molecular ensemble and more than one electromagnetic cavity mode.* For that purpose, we first introduce the general description of the coupling between a distribution of molecules and a single optical cavity mode in Sec. 3.2.1 and then provide the corresponding microscopic Hamiltonian in Sec. 3.2.2. In order to simplify this problem and make it tractable analytically, the rotating-wave approximation is introduced and justified in Sec. 3.2.3. *The eigenspectrum of such Hamiltonian in the strong coupling regime provides the desired polaritonic spectra*: the former are obtained as the multiple solutions of a non-linear secular equation written and solved in Sec. 3.2.4. While an exact analytical solution is available for the case of an homogeneous coupling of the molecules to the cavity mode as written in Subsec. 3.2.4, the case of inhomogeneous coupling is more complex to treat. For that purpose, we introduce with some care a way to define and treat the unavoidable energetic and orientational disorder of the molecular ensemble. From those considerations, the crucial issue of the thermodynamic limit is tenta-

tively discussed. *This discussion about the thermodynamic limit is, we think, original to this manuscript and remains on many aspects an open and lively problem in the field of molecular polaritonics.* Finally, the complete analysis of the polaritonic spectra in presence of such inhomogeneous coupling of molecules to the cavity is provided.

3.2.1 Position of the problem

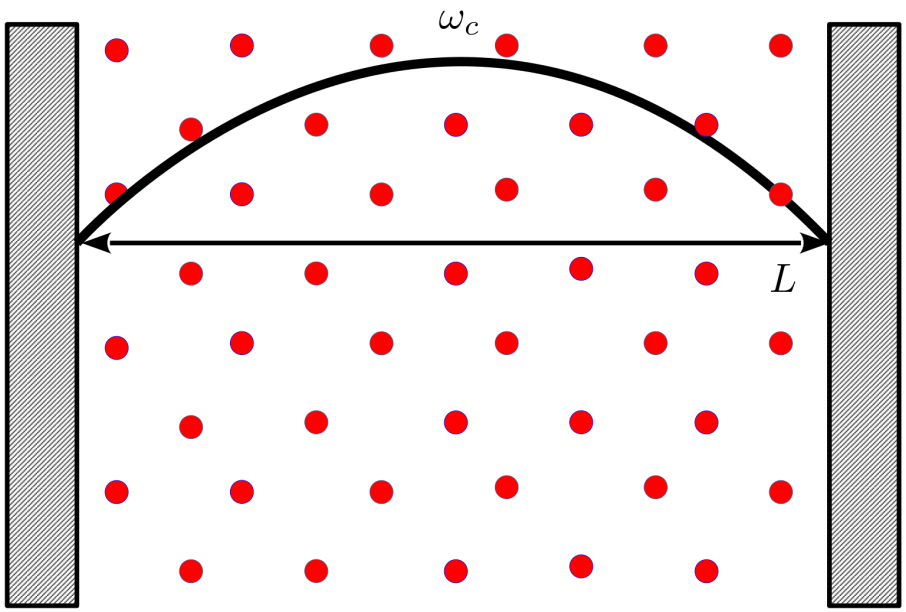

Figure 3.3: Sketch of a canonical Fabry-Pérot cavity of length L and with a cavity mode ω_c that is resonant or close to be resonant with the electronic transition Δ of cavity-embedded molecules (red points).

We consider the paradigmatic model of Fabry-Pérot cavity shown schematically in Fig. 3.3. This cavity is made of perfect metallic mirrors of length L and is filled with molecules (red points) having an electronic transition frequency Δ between their ground and excited state. The cavity is such that there is one cavity electromagnetic (EM) mode of frequency ω_c (the fundamental mode is shown as an example in Fig. 3.3) that is resonant or close to be resonant with the electronic transition $\omega_c \approx \Delta$. *We consider the typical experimental situation in which the optical response of the cavity is probed by excitation of a weak incoming laser signal at normal incidence.* The resulting optical absorption spectrum is then measured and reveals the energetics of the cavity optical excitations arising from the interaction between the cavity EM field and the embedded molecules. We ask ourselves how to compute those optical spectra. This is a complex problem that can be formulated in several ways. One way is to model the cavity as a layered dielectric material with metallic mirrors of finite length and a dielectric material standing for the continuous medium made by the molecules inside cavity. One then solves the classical Maxwell equations for the EM field and computes the transmission, reflection and absorption signals of the cavity using transfer matrix approaches. We developed and used that fully classical approach in our recent Refs. [86, 87]. Another approach inspired from cavity quantum electrodynamics [58] is to build a full

quantum mechanical microscopic description of the resonant cavity modes coupled to the molecules inside cavity, the mirrors being incorporated as hard boundary conditions for the EM field. One then obtains the desired optical spectrum as the eigenspectrum of the Hamiltonian describing the cavity. The first approach provides a complete description of the classical EM field structure inside and outside cavity but poorly describes the material response inside. The second approach instead describes accurately the quantum mechanical properties of the molecules coupled to a single quantum cavity mode, but neglects the spatial structure as well as the dispersive and multimode nature of the EM field inside cavity. *It would be very interesting to mix both approaches in order to retain the desirable level of "optical complexity" in the description of both the EM field and material inside cavity but this problem would in general result in non-tractable or very hard problems to solve.* We thus chose in this section to follow the Hamiltonian formulation of light-matter interactions inside cavity within the simplest possible model, adding *optical complexity* to the theoretical modeling when this will be necessary to describe a given physical question.

Open question. *Given the paradigmatic and simplest theoretical model sketched in Fig. 3.3, we ask ourselves how to compute the eigenspectrum of the microscopic Hamiltonian describing the problem of molecules coupled quantum mechanically to the cavity EM field.*

3.2.2 Microscopic Hamiltonian of the Fabry-Pérot cavity

Homogeneous Hamiltonian. We write the homogeneous Hamiltonian $\hat{H}^{(\mathrm{hom})}$ describing light-matter interactions at the quantum level between a single EM cavity-mode and a distribution of N identical molecules as

$$\begin{aligned}\hat{H}^{(\mathrm{hom})} &= \hbar\omega_c\left(a^\dagger a+\frac{1}{2}\right)+\hbar\frac{\Delta}{2}\sum_{i=1}^{N}\left(c_{ei}^\dagger c_{ei}-c_{gi}^\dagger c_{gi}\right)\\ &- i\hbar g\left(a-a^\dagger\right)\sum_{i=1}^{N}\left(c_{ei}^\dagger c_{gi}+c_{gi}^\dagger c_{ei}\right)+\hbar\frac{g^2}{\omega_c}\left|\sum_{i=1}^{N}\left(c_{ei}^\dagger c_{gi}+c_{gi}^\dagger c_{ei}\right)\right|^2, \quad (3.1)\end{aligned}$$

with $c_{ei}^\dagger$ ($c_{gi}^\dagger$) a fermionic creation operator putting the molecule number i into its electronic excited (ground) state and g the homogeneous electric-dipole coupling constant between molecule i and the cavity-mode. The first term stands for the Hamiltonian describing the single cavity mode of frequency ω_c. The second one describes the population of molecules inside cavity that we consider to be approximated by N identical two-level systems of frequency Δ. The third term is *the standard light-matter electric dipole interaction term* with g the homogeneous electric-dipole coupling constant between molecule i and the cavity-mode. The last term is the self-dipole interaction term that was shown to be necessary to *ensure gauge invariance and the existence of a finite ground-state energy for the coupled system in the ultrastrong light-matter coupling regime* [101, 109]. We note that this homogeneous Hamiltonian holds under the following assumptions

1. We suppose that there is only one cavity mode of frequency ω_c that couples to identical molecules and we suppose the EM field is spatially homogeneous.

2. Each molecule is embedded inside a mode volume in which it couples in the same way to the cavity-mode with coupling strength g.

3. *The electric dipole approximation is made for which the spatial variation of the electric field is neglected on the size of the molecular orbitals*, leading to an homogeneous and coherent light-matter coupling.

4. *We neglect losses* due to finite reflectivity of the cavity mirrors or direct spontaneous emission of the molecules to the cavity structured electromagnetic bath.

5. We do not describe accurately the multilevel electronic structure of the molecule nor effects related to its vibrational structure or to electron-electron Coulomb interactions between the molecules.

Inhomogeneous Hamiltonian. All those assumptions at the origin the homogeneous Hamiltonian model in Eq. 3.1 can be questionable to describe the physical problem of Fig. 3.3. The simplest hypothesis to relax is the homogeneity assumption, namely to consider that each molecule i may be embedded inside a slightly different *fluctuating local electrostatic environment* at the origin of a shifted electronic transition frequency $\Delta_i = \Delta + \varepsilon_i$. A different coupling strength g_i between this molecule and the cavity mode also arises due to *either the spatial dependence of the cavity mode electromagnetic field or to molecular orientations fluctuating from place to place in the cavity.* This leads to the inhomogeneous Hamiltonian $\hat{H}^{(\mathrm{inhom})}$ taking into account both *local energetic disorder and off-diagonal orientational disorder* for the light-matter interaction problem

$$\begin{aligned}\hat{H}^{(\mathrm{inhom})} &= \hbar\omega_c\left(a^\dagger a+\frac{1}{2}\right)+\hbar\sum_{i=1}^{N}\frac{\Delta+\varepsilon_i}{2}\left(c_{ei}^\dagger c_{ei}-c_{gi}^\dagger c_{gi}\right)\\ &- i\hbar\left(a-a^\dagger\right)\sum_{i=1}^{N}g_i\left(c_{ei}^\dagger c_{gi}+c_{gi}^\dagger c_{ei}\right)+\hbar\frac{1}{\omega_c}\left|\sum_{i=1}^{N}g_i\left(c_{ei}^\dagger c_{gi}+c_{gi}^\dagger c_{ei}\right)\right|^2 \end{aligned} \quad (3.2)$$

Open problem. *In general the exact eigenspectrum of $\hat{H}^{(\mathrm{inhom})}$ is not known, either due the energetic and orientational disorder or to the anharmonic nature of the light-matter interaction.* We thus need approximate methods to derive the spectrum of light-matter excitations.

3.2.3 Projected Hamiltonian in the single-photon excitation sector

Rotating-wave approximation. We simplify the inhomogeneous Hamiltonian in Eq. 3.2 by doing the rotating-wave approximation (RWA) obtaining

$$\begin{aligned}\hat{H}^{(\mathrm{RWA})} &= \hbar\omega_c\left(a^\dagger a+\frac{1}{2}\right)+\hbar\sum_{i=1}^{N}\frac{\Delta+\varepsilon_i}{2}\left(c_{ei}^\dagger c_{ei}-c_{gi}^\dagger c_{gi}\right)\\ &- i\hbar\sum_{i=1}^{N}g_i\left(ac_{ei}^\dagger c_{gi}-c_{gi}^\dagger c_{ei}a^\dagger\right)\,. \end{aligned} \quad (3.3)$$

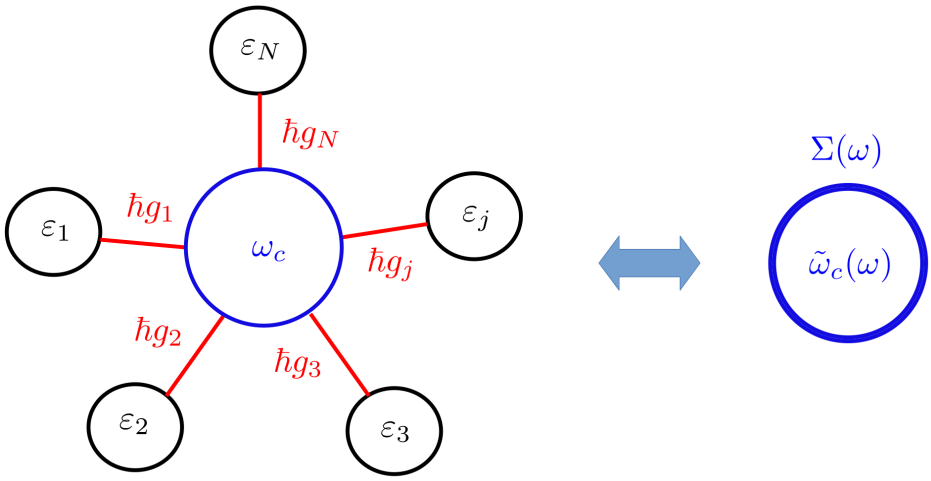

Figure 3.4: Left: Connectivity graph of the Hamiltonian written in Eq. 3.10. The cavity mode of frequency ω_c is shown as a blue circle while the N molecules of transition frequencies $\Delta + \varepsilon_i$ are shown as black circles. The light-matter couplings g_i are pictured as red links. Right: Graph of the renormalized optical mode frequency $\tilde{\omega}_c(\omega) = \omega_c + \Sigma_N(\omega)$ after tracing out the excitonic bath degrees of freedom (thick blue circle). Unpublished Fig.

This approximation is valid within the following assumptions

1. The cavity frequency ω_c is close to resonance with the molecular transition Δ so that in the rotated frame (rotating at angular frequency ω_c) one neglects fast oscillating terms at frequency ω_c compared to static or quasi-static ones: this amounts to keep in the dipole interaction Hamiltonian only terms that conserve the total energy of the system. *The former terms are those in which a cavity photon is destroyed and absorbed by one molecule, or a cavity photon is created and emitted from one of the excited molecule.*

2. One neglects the self-dipole interaction terms which are of typical relative lower order $\max(\mathrm{g_i})/\omega_\mathrm{c} \ll 1$ compared to the rotating terms in the dipole interaction term.

Both conditions of throwing out the counter-rotating terms in the dipole interaction term and of neglecting the self-dipole interaction term are consistent and well justified for coupling strengths $\max(\mathrm{g_i}) \ll \omega_\mathrm{c}$. *Hence the Hamiltonian in Eq. 3.3 describes well the excitation spectrum for light-matter coupling strengths that are smaller than the cavity frequency thus out of the so-called ultrastrong coupling regime, but which can still be much larger than the total dissipation rate due to the cavity and material losses thus in the strong (but not ultrastrong!) coupling regime.*

Projection onto the single-photon excitation sector. In this paragraph, we derive an algebraic approach to compute the polaritonic excitation spectrum from the $\hat{H}^{(\mathrm{RWA})}$ Hamiltonian projected onto the low-energy single-photon and single molecular-exciton sector. This additional approximation is valid for weak average number of photons populating the

cavity mode $\langle a^\dagger a \rangle \ll 1$ and a low density of electronic excitations $\sum_{i=1}^N \left\langle c_{ei}^\dagger c_{ei} \right\rangle \ll N$. This the case if the cavity is not driven or the damping the cavity is sufficiently large to bring back the cavity close to its vacuum ground state. When this condition is fulfilled, we look for eigenvectors $|\lambda\rangle$ of $\hat{H}^{(\mathrm{RWA})}$ in the form

$$|\lambda\rangle = a_c |G;1_c\rangle + \sum_{j=1}^N b_j |(e_j);0_c\rangle , \tag{3.4}$$

with the basis of manybody light-matter states written

$$|G;0_c\rangle = |g_1 \cdots g_N\rangle \otimes |0_c\rangle , \tag{3.5}$$
$$|G;1_c\rangle = a^\dagger |G;0_c\rangle = |g_1 \cdots g_N\rangle \otimes |1_c\rangle \tag{3.6}$$
$$|(e_i);0_c\rangle = b_i^\dagger |G;0_c\rangle = |g_1 \cdots g_{i-1}(e_i)g_{i+1} \cdots g_N\rangle \otimes |0_c\rangle . \tag{3.7}$$

The excitation spectrum in the single-photon sector of the truncated Hamiltonian $\hat{H}^{(\mathrm{RWA})}$ is then solution of the following linear system of equations

$$\lambda a_c = \omega_c a_c + \sum_{j=1}^N g_j^* b_j , \tag{3.8}$$
$$\lambda b_j = (\Delta + \varepsilon_j) b_j + g_j a_c . \tag{3.9}$$

which can be written as an eigenvalue problem for the effective matrix $H^{(1)}$ written in this basis

$$H^{(1)} = \hbar \begin{bmatrix} \omega_c & ig_1 & ig_2 & ig_3 & \cdots & ig_N \\ -ig_1 & \Delta+\varepsilon_1 & 0 & 0 & \cdots & 0 \\ -ig_2 & 0 & \Delta+\varepsilon_2 & 0 & \cdots & 0 \\ -ig_3 & 0 & 0 & \Delta+\varepsilon_3 & \cdots & 0 \\ \cdots & \cdots & \cdots & \cdots & \cdots & \cdots \\ -ig_N & 0 & 0 & 0 & \cdots & \Delta+\varepsilon_N \end{bmatrix} . \tag{3.10}$$

This effective Hamiltonian can be represented by a graph of interactions shown in Fig. 3.4-left) with a star connectivity, the cavity mode being coupled to all molecules in the ensemble.

Tracing out the excitonic bath. The linear equation Eq. 3.9 enables to eliminate explicitly the b_j excitonic degree of freedom, expressed as

$$b_j = \frac{g_j}{\lambda - (\Delta + \varepsilon_j)} a_c , \tag{3.11}$$

thus leading to the following secular equation for the unknown eigenvalue $\lambda \equiv \mu + \Delta$ given by

$$\mu - \delta_c = \Sigma_N(\mu) , \tag{3.12}$$
$$\Sigma_N(\mu) = \sum_{j=1}^N \frac{|g_j|^2}{\mu - \varepsilon_j} , \tag{3.13}$$

where we introduced $\delta_c = \omega_c - \Delta$ the cavity mode detuning frequency and $\Sigma_N(\mu)$ the self-energy depending on the unknown eigenvalue μ that renormalizes the bare cavity frequency ω_c. *This tracing out of the exciton bath degree of freedom that results in a renormalization of ω_c is shown in Fig. 3.4-right).* Formally, the solution of the secular equation Eq. 3.12 provides the expected polariton spectrum of the cavity.

3.2.4 Effect of disorder on the polariton spectra

Polaritons in the homogeneous case

We consider the homogeneous case for which $g_j = g$ and $\varepsilon_j = 0$ for all molecule j. *This corresponds to identical molecules without energetic and orientational disorder that are coupled to the same cavity mode.* The secular equations Eqs. 3.12,3.13 can be solved exactly, providing the excitation spectra as

$$\lambda_{\eta=\pm}(\delta_c) = \Delta + \frac{\delta_c}{2} + \eta\frac{\Omega_R(\delta_c)}{2}\,, \tag{3.14}$$

$$\Omega_R(\delta_c) = 2\sqrt{Ng^2 + \left(\frac{\delta_c}{2}\right)^2}\,. \tag{3.15}$$

There are thus two branches of solutions: a lower polariton (LP) branch λ_- and a upper polariton (UP) branch λ_+ that are splitted by the collective vacuum Rabi splitting $\Omega_R(\delta_c)$. At resonance $\delta_c = 0$ we obtain for the excitation spectra and corresponding eigenstates

$$\lambda^{\rm res}_{\eta=\pm} = \Delta + \eta\frac{\Omega^{\rm res}_R}{2}\,, \tag{3.16}$$

$$\Omega^{\rm res}_R = 2g\sqrt{N}\,, \tag{3.17}$$

$$|\lambda\rangle^{\rm res}_\eta = \frac{1}{\sqrt{2}}\left\{|G,1_c\rangle + \frac{\eta}{\sqrt{N}}\sum_{j=1}^{N}|(e_j),0_c\rangle\right\}\,. \tag{3.18}$$

Hence the eigenstates written in Eq. 3.18 are collective and hybrid light-matter excitations called polaritons that have a component that is delocalized on the molecular ensemble. The collective Rabi splitting is scaling with the square root of molecular concentration in the ensemble [58]. We show in Fig. 3.6 those polaritonic branches at resonance as dashed red (blue) lines corresponding to the UP (LP) branches. It is interesting to notice that the LP and UP branches written in Eq. 3.16 can be obtain as the solution of an analogous problem of two coupled oscillators: one which is the cavity oscillator of frequency ω_c and the other the collective exciton oscillator of frequency Δ, the coupling between them being the collective coupling $g\sqrt{N}$. In other words the LP and UP polaritons in rotating wave approximation could be obtained as the eigenmodes of the following effective Hamiltonian $H^{(2-\text{modes})}$ written as

$$H^{(2-\text{modes})} = \hbar\begin{bmatrix} \omega_c & ig\sqrt{N} \\ -ig\sqrt{N} & \Delta \end{bmatrix}\,. \tag{3.19}$$

It is then physically clear that the emergence of Rabi split LP and UP in in Eq. 3.18 can be interpreted as the anti-crossing between two coupled oscillators. We leave the justification

and further physical interpretation of those spectra for the next section Sec. 3.3.3. We note that there is no threshold for the appearance of the splitting: this is an artifact of our model which neglects dissipation in the cavity. Dissipation can be included in a phenomenological way by adding a non-hermitian contribution to $H^{(2-\text{modes})}$ in Eq. 3.19. We also remark that we recover the standard single-photon excitation spectra of the paradigmatic Tavis-Cummings model in quantum optics [115].

Disorder and orientational averaging in the inhomogeneous case

We now consider the general case where onsite energetic disorder and orientational disorder are both present. *In this paragraph, we define a precise way to perform ensemble averages on the configurations of molecular energetic disorder and orientational disorders.* For that purpose, we consider a general function $f\left(\{\varepsilon_j, \Omega_j\}_{j\in[|1,N|]}\right)$ of the distribution of molecular exciton energies ε_j and orientation angles $\Omega_j \equiv \{\theta_j, \psi_j, \phi_j\}$ with the Euler angles $(\theta_j, \psi_j, \phi_j) \in [0,\pi] \times [0, 2\pi[\times[0, 2\pi[$ giving the direction of the electric transition dipole of molecule j. We define the disorder and orientational average $\left\langle f\left(\{\varepsilon_j, \Omega_j\}_j\right)\right\rangle_{\Omega,W}$ of the f-function as

$$\left\langle f\left(\{\varepsilon_j, \Omega_j\}_j\right)\right\rangle_{\Omega,W} = \prod_{j=1}^{N}\int_{-W}^{W}\frac{d\varepsilon_j}{2W}\int_0^{\pi}\frac{d\theta_j}{8\pi^2}\sin(\theta_j)\int_0^{2\pi}d\psi_j\int_0^{2\pi}d\phi_j f\left(\{\varepsilon_j, \Omega_j\}_j\right). \tag{3.20}$$

In Eq. 3.20, we made the following assumptions that

1. *The distribution of onsite energetic disorder and molecular orientation disorder are independent.*
2. *The distribution of both molecular disorder and orientations are spatially uncorrelated and independent from molecule to molecule.*
3. *The random onsite energy ε_j varying from molecule to molecule is equally distributed in the range $[-W, W]$* with W the disorder strength, thus realizing an Anderson-type of disorder.
4. *The system is supposed to be isotropic*, namely each choice of random solid angle is equiprobable.

This choice of averaging enables to simplify the calculation of disorder and orientational averages. In particular the average in the case where $f\left(\{\varepsilon_j, \Omega_j\}_j\right) = f_1\left(\{\varepsilon_j\}_j\right) f_2\left(\{\Omega_j\}_j\right)$ can be obtained as a factorized expression

$$\left\langle f\left(\{\varepsilon_j, \Omega_j\}_j\right)\right\rangle_{\Omega,W} = \left\langle f_1\left(\{\varepsilon_j\}_j\right)\right\rangle_W \left\langle f_2\left(\{\Omega_j\}_j\right)\right\rangle_\Omega, \tag{3.21}$$

with $\left\langle f_1\left(\{\varepsilon_j\}_j\right)\right\rangle_W$ the average performed on onsite disorder for the f_1-function and $\left\langle f_2\left(\{\Omega_j\}_j\right)\right\rangle_\Omega$ the average performed on molecular orientations for the f_2-function. *The*

latter assumptions on disorder can be generalized to any kind of spatially correlated disorder at the prize of an harder or even impossible analytical calculation of the averaged f-function !

Issue of the thermodynamic limit

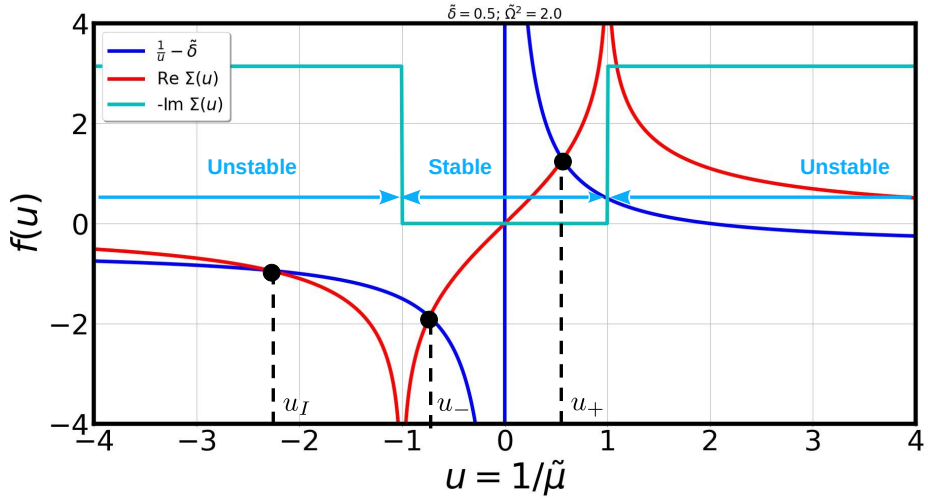

Figure 3.5: Graphical solutions (black dots) of the secular Eqs 3.34,3.35. We find here two stable solutions $u_\pm$ and one unstable solution u_I. Unpublished Fig.

Problematic of the thermodynamic limit. In this section, we want to investigate the behavior of the polaritonic spectra for the inhomogeneous molecular systems in the thermodynamic limit $N \to +\infty$, $V \to +\infty$ but N/V finite. *This is a subtle question which up to the present day, did not received a completely satisfactory answer in the field of polaritonic chemistry.* To make some progress towards this goal, we propose to investigate the behavior of the solution of the secular equations Eqs. 3.12,3.13 derived in the previous Sec. 3.2.3 after performing disorder and orientational average on the self-energy $\langle \Sigma_N(\mu) \rangle_{\Omega,W}$ in the limit $N \to \infty$. *This procedure is ambiguous because there are at least two ways of defining this limit* depending on the order that is chosen to perform the disorder and orientational averaging or the limit $N \to \infty$. We introduce consistently two quantities

$$\langle \Sigma(\mu) \rangle_1 = \lim_{N \to +\infty} \left\langle \sum_{j=1}^{N} \frac{|g_j|^2}{\mu - \varepsilon_j} \right\rangle_{\Omega,W} , \tag{3.22}$$

$$\langle \Sigma(\mu) \rangle_2 = \left\langle \lim_{N \to +\infty} \sum_{j=1}^{N} \frac{|g_j|^2}{\mu - \varepsilon_j} \right\rangle_{\Omega,W} . \tag{3.23}$$

The study of the thermodynamic limit thus amounts to analyze mathematically the convergence properties with respect to N of both series in Eq. 3.22,3.23 and if the $N \to \infty$ limit and the $\langle \cdots \rangle_{\Omega,W}$ average can be permuted or not. We anticipate the following possible situation for which

$$\langle \Sigma(\mu) \rangle_1 \neq \langle \Sigma(\mu) \rangle_2 , \tag{3.24}$$

namely *the large N-limit does not commute with the spatial averaging resulting in a difference between both approaches to the thermodynamic limit. Similar analysis of a phase-transition when approaching the macroscopic limit were investigated in mesoscopic physics by Pastawski [92].* A sufficient condition for having equality between both averages happens when both series in Eq. 3.22,3.23 converge absolutely (uniform convergence) so that one can permute the large N-limit with the spatial averages. We show in the next paragraph when this is the case.

Convergence of the self-energy series. Using the assumptions of Sec. 3.2.4 for the spatially uncorrelated energetic and orientational disorders, we can write the following explicit expressions for the average self-energies

$$\langle \Sigma(\mu) \rangle_1 = \lim_{N \to +\infty} N \langle g^2 \rangle_\Omega \sum_{p=0}^{N} \frac{\langle \varepsilon^{2p} \rangle_W}{\mu^{2p+1}} , \tag{3.25}$$

$$\langle \Sigma(\mu) \rangle_2 = N \langle g^2 \rangle_\Omega \left\langle \frac{1}{\mu - \varepsilon} \right\rangle_W , \tag{3.26}$$

with $2\sqrt{N \langle g^2 \rangle_\Omega}$ *the "macroscopic" or spatially coarsed grained collective Vacuum Rabi Splitting* that recovers the expression given by Eq. 3.17 in the homogeneous case. The moments of the Anderson probability distribution in Eq. 3.25 are readily obtained as

$$\left\langle \varepsilon^{2p+1} \right\rangle_W = 0 , \tag{3.27}$$

$$\left\langle \varepsilon^{2p} \right\rangle_W = \frac{W^{2p}}{2p+1} , \tag{3.28}$$

which after a direct calculation provide the final expressions of the average self-energies

$$\langle \Sigma(\mu) \rangle_1 = \frac{N \langle g^2 \rangle_\Omega}{W} \operatorname{arctanh}\left(\frac{W}{\mu}\right) ; \ \forall W < |\mu| , \tag{3.29}$$

$$\langle \Sigma(\mu) \rangle_2 = \frac{N \langle g^2 \rangle_\Omega}{2W} \left\{ \ln \left| \frac{\mu + W}{\mu - W} \right| - i\pi \mathrm{Rect}_\mu [-W, W] \right\} ; \ \forall \mu \in \mathbb{R} \backslash \{-W, W\} . \tag{3.30}$$

Those analytical expressions are remarkable since they enable a complete analysis of the series convergence. We find that the positive series $\langle \Sigma(\mu) \rangle_1$ in Eq. 3.25 is convergent and thus absolutely convergent for $W/|\mu| < 1$ and divergent for $W/|\mu| > 1$. *Its radius of convergence is thus* $|\mu| = W$. The series $\langle \Sigma(\mu) \rangle_2$ in Eq. 3.30 is also well defined for $W/|\mu| < 1$: *as expected, inside the radius of convergency both self-energies do coincide* $\langle \Sigma(\mu) \rangle_1 = \langle \Sigma(\mu) \rangle_2$. However, in contrast to $\langle \Sigma(\mu) \rangle_1$ which diverges out of its radius of convergency, we find that the self-energy $\langle \Sigma(\mu) \rangle_2$ stays well defined and acquires a finite imaginary part. *The latter phenomenon is assigned to an emergent and finite lifetime* $\tau_d(\lambda)$ *acquired by polaritonic excitations in the thermodynamic limit, due to the coupling to the disordered molecular excitonic bath*

$$\frac{1}{\tau_d(\mu)} \equiv -\mathrm{Im} \left(\langle \Sigma(\mu) \rangle_2 \right) = \pi \frac{N \langle g^2 \rangle_\Omega}{2W} \mathrm{Rect}_\mu [-W, W] . \tag{3.31}$$

The interpretation of the finite lifetime is the following. The Hamiltonian matrix in Eq. 3.10 is characterized by $N+1$ eigenvalues. In absence of disorder, two of those eigenvalues are the LP and UP polariton excitations located at energies given by Eq. 3.14. But there remains $N-1$ dark states that are orthogonal to the LP and UP that are located at energy Δ. Due to disorder, those dark states get split into a distribution of $N-1$ states of width W around the average exciton energy Δ. In the thermodynamic limit $N \to +\infty$, this band becomes a continuum of states forming an excitonic bath. *The polaritons falling inside this band acquire a finite lifetime due to inhomogeneous broadening by disorder which is given by Fermi Golden Rule* (in units $\hbar = 1$)

$$\frac{1}{\tau_d(\mu)} = 2\pi \left\langle g^2 \right\rangle_\Omega \left\langle \rho(\mu) \right\rangle_W , \tag{3.32}$$

$$\left\langle \rho(\mu) \right\rangle_W = \frac{N}{2W} \mathrm{Rect}_\mu \left[-W, W\right] , \tag{3.33}$$

with $\left\langle \rho(\lambda) \right\rangle_W$ the averaged density of states of the dark-states excitonic bath. *Outside the miniband of dark states, there is no density of states so that the broadening of states vanishes: this explains the existence of a threshold behavior as resulting from both the thermodynamic limit (necessary to induce a continuum of states at the origin of irreversibility) and the specific nature of disorder (the fact that there is an energy cutoff W in the disorder strength and thus in the density of states).* We note that the finite lifetime cannot be obtained by truncating the series $\left\langle \Sigma(\lambda) \right\rangle_1$ at any fixed order N (even very large!). *It is found as the analytical continuation of the series out of its radius of convergency with a sign of its imaginary part associated to the retarded response of the medium.*

Polaritons in the inhomogeneous case

In this paragraph, we look for the solution of the secular Eq. 3.12 with the expression of the averaged self-energy in the thermodynamic limit given by Eq. 3.30. In general, complex solutions are to be searched in the form $\mu = \mu' + i\mu''$ thus giving two real equations

$$\frac{1}{u} - \tilde{\delta}_c = \frac{\tilde{\Omega}^2}{2} \ln \left| \frac{1+u}{1-u} \right| , \tag{3.34}$$

$$-\mu'' = \frac{1}{\tau_d(\mu')} , \tag{3.35}$$

with

$$u = \frac{W}{\mu'};\ \tilde{\delta}_c = \frac{\delta_c}{W};\ \tilde{\Omega}^2 = \frac{N \left\langle g^2 \right\rangle_\Omega}{W^2} . \tag{3.36}$$

We note that Eq. 3.34 is a non-linear and transcendental equation: it thus cannot be solved explicitly analytically. We thus resort to a graphical solution shown in Fig.3.5 for a normalized detuning $\tilde{\delta}_c = 0.5$ and coupling strength $\tilde{\Omega}^2 = 2.0$. In this range of parameters, we find two stable solutions $u_\pm$ with infinite lifetime $\lambda''_\pm = 0$ corresponding to the UP u_+ and LP u_- branches. *In this case there is no disorder-induced inhomogeneous broadening of the polaritons, even if the disorder-strength is quite large*: this is consistent with the pioneer work

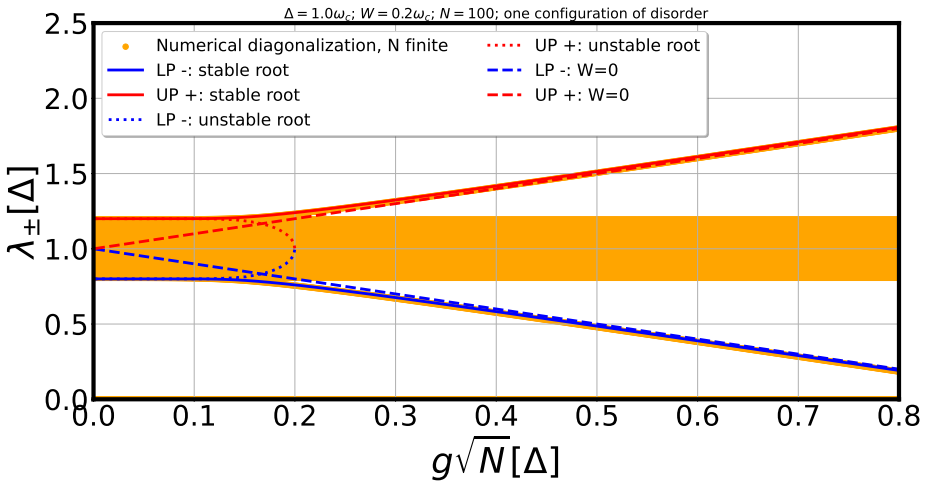

Figure 3.6: Polaritonic excitations computed from numerical solution of the transcendental Eq. 3.34, as a functions of the light-matter coupling strength $g\sqrt{N}$. At resonance $\delta_c = 0$, we find two stable solutions corresponding to the LP (plain blue) and UP (plain red) excitations. Two unstable solutions are also found and shown as dotted curves. The yellow points are the result of numerical diagonalization of the Hamiltonian written in Eq. 3.10 for fixed a number $N = 100$ molecules and one configuration of energetic Anderson disorder. Parameters are: $\Delta = \omega_c = 1.0$, $W = 0.2$, $N = 100$. Unpublished Fig.

of Houdré et al. [63] that reports an homogeneous linewidth for the LP and UP at finite N values despite the presence of disorder. Those solutions of the secular equation in the range of parameters for which $\left|\mu'_{\pm}\right| > W$, correspond to polaritons located out of the miniband of dark-states. We also find one additional unstable solution u_I with finite lifetime $\mu''_I \neq 0$ for which $|\mu'_I| < W$, namely when the collective excitation falls inside the dark-state miniband. *The former solution acquires a large inhomogenous broadening and the UP and LP get "diluted" in the disordered dark-state manifold. There is thus a threshold behavior characterizing the thermodynamic limit that is similar to a phase transition.* This threshold behavior could not be obtained in Ref.[63] because of the performed truncation at finite number N of molecules. Finally, we show in Fig.3.6, the polaritonic excitation spectrum computed from numerical solution of the transcendental Eq. 3.34 as a function of light-matter coupling strength $g\sqrt{N}$. At resonance $\delta_c = 0$, we find two stable solutions corresponding to the LP (plain blue) and UP (plain red) excitations. Two unstable solutions are also found and shown as dotted curves. The stable solutions of the secular equation Eq. 3.34 do match very well with the results of the full numerical diagonalization of the Hamiltonian with a finite number $N = 100$ of molecules (yellow points). *Inside the band we see that the polariton branches are not stable and are expelled out of it, namely they are pushed at the frontier of the radius of convergency of the self-energy series in Eq. 3.29.* We note that recent theoretical papers appeared that discuss the spectral properties of such inhomogeneous models [85], which, to our point of view, are still not completely understood.

Open questions. The reasoning we made about the thermodynamic limit and the vanishing of the inhomogeneous broadening of polaritons due to disorder in Eq. 3.31 has some

limitations. In particular, *the fact that the polariton excitation out of the mini-band of dark states does not have any additional inhomogeneous linewidth is due to our particular model of disorder that is finite range in energy.* A Gaussian disorder or any kind of model of disorder without finite support would lead to a finite (even very weak) additional broadening of the polaritons. Finally, we remark that *in taking the thermodynamic limit, one has to take into account the finite coherent length of the molecular aggregate that is coupled to the cavity mode.* It is still an open but crucial question in the field of polaritonic chemistry to define a precise and quantitative way to perform this limit.

3.3 A jump into the ultrastrong coupling regime

In this section we investigate the physics of polariton formation in the electronic ultrastrong coupling regime, namely when the light-matter coupling strength gets of the same order as the cavity mode frequency. For that purpose, we develop in Sec. 3.3.1 a variational approach to compute the polariton spectra that includes multi-photon effects. The former approach is compared to a bosonization method to get the polaritonic spectra as presented in Sec. 3.3.2. This amounts to solve non-perturbatively an equivalent problem of coupled quantum mechanical oscillators, as was first proposed by Hopfield in his pioneer work describing excitons in solids Ref. [62]. An exact analytical solution to this problem is derived in Sec. 3.3.3 after proposing *a mapping of the Hopfield polariton problem to an equivalent model of classical mechanics in which a mass-weighted fictitious particle is coupled to an external effective magnetic field in a two dimensional harmonic trap.* This mapping is original to this work and, to our knowledge, was not completely noticed in the field of molecular polaritonics. We finally analyze in Sec. 3.3.4 the peculiarities of the polaritonic spectra developing in the ultrastrong coupling regime, recovering early theoretical results of Ciuti et al. in Ref. [25] and experimental ones by George et al. in Ref. [50].

3.3.1 A variational approach to the polariton problem

Problematic. We come back to the polaritonic problem described by the homogeneous Hamiltonian written in Sec. 3.2.2 in Eq. 3.1. *We aim at improving the rotating-wave approximation made in Sec. 3.2.3 in order to explore the electronic ultrastrong coupling regime, first in the case where no molecular disorder nor spatial inhomogeneities of the field are involved.* Indeed, upon increasing the coupling strength g towards values close to the cavity mode frequency ω_c, one cannot anymore neglect the counter-rotating and the self-dipole interaction terms to the light-matter interaction mechanism which are both of the same non-negligible order g^2/ω_c: one thus need to include all the terms in the Hamiltonian written in Eq. 3.1. *The brute force calculation of the eigenspectrum for the Hamiltonian $\hat{H}^{(\mathrm{hom})}$ is not possible for any value of N, since the size of the Hilbert space describing the states of the system increases exponentially with the number N of molecules.* We thus are doomed to propose reasonable and hopefully not uncontrolled approximations to compute the polaritonic excitation spectrum.

Including the multiple-photon excitations. In this section, we propose a variational approach to solve for the polaritonic spectra. Compared to Sec. 3.2.3, we keep the condition of low density of electronic excitations $\sum_{i=1}^{N} \left\langle c_{ei}^{\dagger} c_{ei} \right\rangle \ll N$, but relax the condition of having a low number of photons populating the cavity mode, namely *in the ultrastrong coupling regime, we allow the molecular system to couple to virtual transitions with an arbitrary number of photons populating the cavity mode.* We thus propose the following trial manybody wavefunction improving the previous expansion of Eq. 3.4

$$|\lambda\rangle = \sum_{n_c=0}^{N_{\rm ph}} \left\{ a_{n_c} |G; n_c\rangle + \sum_{j=1}^{N} b_{j;n_c} |(e_j); n_c\rangle \right\}, \tag{3.37}$$

with $|n_c\rangle \equiv \frac{a^{\dagger n}}{\sqrt{n!}} |0_c\rangle$ the number state containing n_c photons in the cavity mode and $N_{\rm ph}$ the maximum number of photon occupation that will be varied up to convergence of the computed spectra. *We note that this approach is the starting point of a more systematic variational approach that would include higher-order molecular excited states into its description: clearly here, since we only kept single molecular excitons in the wave-function while any multiple photon excitation is included, this approach is not fully consistent in the way it treats light and matter in the interaction mechanism.* It has however the good property of being quite straightforward to solve numerically. We thus proceed by projecting and truncating the Hamiltonian $\hat{H}^{(\rm hom)}$ written in Eq. 3.1 on the basis of manybody states $\{|G; n_c\rangle, |(e_i); n_c\rangle\}_{n_c \in [|0, N_{\rm ph}|]}$. We obtain the following tri-diagonal-per-bloc matrix $H^{(\rm N_{ph})}$ of size $[(N+1)(N_{\rm ph}+1)] \times [(N+1)(N_{\rm ph}+1)]$ which improves on the Hamiltonian matrix $H^{(1)}$ truncated in the single-photon sector in Eq. 3.10

$$H^{(\rm N_{ph})} = \begin{bmatrix} H_0 & V & 0 & 0 & \cdots & 0 \\ V^{\dagger} & H_0 + \hbar\omega_c \mathrm{Id} & V\sqrt{2} & 0 & \cdots & 0 \\ 0 & V^{\dagger}\sqrt{2} & H_0 + 2\hbar\omega_c \mathrm{Id} & V\sqrt{3} & 0 & \cdots \\ 0 & 0 & V^{\dagger}\sqrt{3} & H_0 + 3\hbar\omega_c \mathrm{Id} & \cdots & 0 \\ \cdots & \cdots & 0 & \cdots & \cdots & V\sqrt{N_{\rm ph}} \\ 0 & 0 & \cdots & 0 & V\sqrt{N_{\rm ph}} & H_0 + N_{\rm ph}\hbar\omega_c \mathrm{Id} \end{bmatrix}. \tag{3.38}$$

We introduced H_0 the molecular matrix of size $(N+1) \times (N+1)$

$$H_0 = \hbar \begin{bmatrix} \omega_{gs} & 0 & 0 & 0 & \cdots & 0 \\ 0 & \omega_{gs} + \Delta & 2\frac{g^2}{\omega_c} & 2\frac{g^2}{\omega_c} & \cdots & 2\frac{g^2}{\omega_c} \\ 0 & 2\frac{g^2}{\omega_c} & \omega_{gs} + \Delta & 2\frac{g^2}{\omega_c} & \cdots & 2\frac{g^2}{\omega_c} \\ 0 & 2\frac{g^2}{\omega_c} & 2\frac{g^2}{\omega_c} & \omega_{gs} + \Delta & \cdots & 2\frac{g^2}{\omega_c} \\ \cdots & \cdots & \cdots & \cdots & \cdots & \cdots \\ 0 & 2\frac{g^2}{\omega_c} & 2\frac{g^2}{\omega_c} & 2\frac{g^2}{\omega_c} & \cdots & \omega_{gs} + \Delta \end{bmatrix}, \tag{3.39}$$

(3.40)

with the energy ω_{gs} defined as

$$\hbar\omega_{gs} = \hbar\frac{\omega_c - N\Delta}{2} + N\hbar\frac{g^2}{\omega_c}. \tag{3.41}$$

The light-matter coupling matrix V of size $(N+1)\times(N+1)$ is written

$$V = -i\hbar g \begin{bmatrix} 0 & 1 & 1 & 1 & \cdots & 1 \\ 1 & 0 & 0 & 0 & \cdots & 0 \\ 1 & 0 & 0 & 0 & \cdots & 0 \\ 1 & 0 & 0 & 0 & \cdots & 0 \\ \cdots & \cdots & \cdots & \cdots & \cdots & \cdots \\ 1 & 0 & 0 & 0 & \cdots & 0 \end{bmatrix}. \tag{3.42}$$

(3.43)

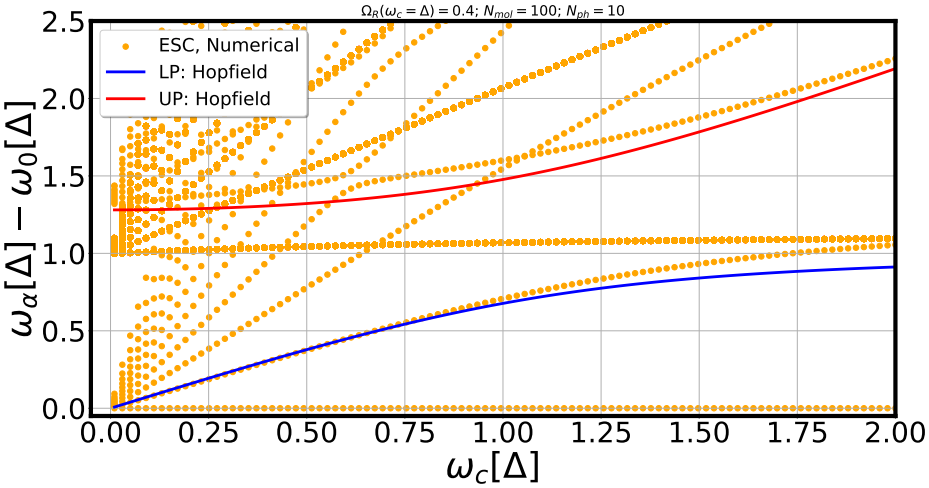

Figure 3.7: Spectrum of eigenstates (relative the ground-state) of the $H^{(\mathrm{N_{ph}})}$ Hamiltonian matrix containing multi-photon processes(see Eq. 3.38) as a function of cavity frequency ω_c. Numerical eigenvalues are presented as yellow points, while the plain curves are those given by analytic formula in Eq. for the polaritons computed in the harmonic approximation of Sec.. Parameters are $\Delta = 1.0$, $\Omega_R(\omega_c = \Delta) = 0.4$, $N = 100$ molecules, and $N_{ph} = 10$. Unpublished Fig.

Polaritons with multi-photon excitations. We compute numerically the eigenspectrum of the $H^{(\mathrm{N_{ph}})}$ Hamiltonian matrix containing multi-photon processes written in Eq. 3.38. We show the excitation spectra (relative to the ground state) as yellow points in Fig. 3.7 for the case $N = 100$ and $N_{\mathrm{ph}} = 10$ for which the eigenvalues in the low-energy sector have converged in the chosen range of parameters. This spectrum is quite complicated to analyze. *It includes both collective polariton and dark state polariton excitations, as well as higher energy multi-photon polariton excitations that are an hallmark of the strong coupling regime: they introduce essential anharmonic features in the polariton problem.* We let the analysis and interpretation of such spectra to the next section.

3.3.2 A bosonization of the polariton problem

Problematic. In this section, we come back to the original eigenvalue problem associated to the homogeneous Hamiltonian in Eq. 3.1. Compared to the previous Sec. 3.3.1, *instead of*

postulating an approximate variational solution to this problem, we hereby propose an analogous but simpler approximate Hamiltonian problem that we are able to solve exactly.

Bosonization of the homogeneous Hamiltonian. For that purpose, we start by rewriting the $\hat{H}^{(\mathrm{hom})}$ Hamiltonian in the equivalent form

$$\begin{aligned}\hat{H}^{(\mathrm{hom})} &= \hbar\omega_c\left(a^\dagger a+\frac{1}{2}\right)+\hbar\Delta\sum_{i=1}^{N}\left(c_{ei}^\dagger c_{ei}-c_{gi}^\dagger c_{gi}\right)\\ &- i\hbar\Omega_R\left(a-a^\dagger\right)\left(B+B^\dagger\right)+\hbar D\left(B+B^\dagger\right)^2\,, \end{aligned} \tag{3.44}$$

where we introduced *the fully symmetric collective molecular exciton destruction operator*

$$B = \frac{1}{\sqrt{N}}\sum_{i=1}^{N} b_i\,, \tag{3.45}$$

with $b_i \equiv c_{ei}^\dagger c_{gi}$ the destruction operator of a single molecular exciton on molecule i. We also introduced in Eq. 3.44 the collective Rabi frequency Ω_R due to electric-dipole interactions and the self-dipole interaction term D expressed respectively as

$$\Omega_R = g\sqrt{N}\equiv\frac{\omega_P}{2}\sqrt{\frac{\omega_c}{\Delta}}\,, \tag{3.46}$$

$$D = \frac{\omega_P^2}{4\Delta}\,, \tag{3.47}$$

with ω_P the typical plasma frequency of the intracavity medium. We note that the b_i operator shares some analogy with a bosonic operator, but is not strictly speaking a boson, since it does not fulfill the proper bosonic commutation relations

$$\left[b_i,b_j^\dagger\right] = \delta_{ij}\left(\hat{\mathrm{Id}}_i-2c_{ei}^\dagger c_{ei}\right)\,. \tag{3.48}$$

Upon exchange of two excitons, there is an additional exchange-interaction to pay that is proportional to the number of excitations on molecule i. *We thus prefer to talk about composite boson excitations instead of bosonic excitations for describing that exciton.* The commutation relations of the collective B operator in Eq. 3.45 follows directly

$$\left[B,B^\dagger\right] = \delta_{ij}\left(\hat{\mathrm{Id}}-\frac{2}{N}\sum_{i=1}^{N}c_{ei}^\dagger c_{ei}\right)\,. \tag{3.49}$$

The quasi-bosonic nature of the B-operator appears in the regime of low density of electronic excitations $\sum_{i=1}^{N}\left\langle c_{ei}^\dagger c_{ei}\right\rangle \ll N$ for which the second part of Eq. 3.49 can be neglected. *We thus make the following harmonic approximation, for which we write an analogous Hamiltonian $\hat{H}_{\mathrm{bos}}^{(\mathrm{hom})}$ made of an ensemble of N coupled harmonic oscillators describing approximately the physics of the electronic strong coupling problem in the limit of low density electronic excitons in the ensemble*

$$\begin{aligned}\hat{H}_{\mathrm{bos}}^{(\mathrm{hom})} &= \hbar\omega_c\left(a^\dagger a+\frac{1}{2}\right)+\hbar\Delta\sum_{i=1}^{N}\left(b_i^\dagger b_i+\frac{1}{2}\right)\\ &- i\hbar\Omega_R\left(a-a^\dagger\right)\left(B+B^\dagger\right)+\hbar D\left(B+B^\dagger\right)^2\,. \end{aligned} \tag{3.50}$$

The spectrum of this Hamiltonian can be found exactly. *However we note that the original Hamiltonian $\hat{H}^{(\mathrm{hom})}$ in Eq. 3.44 is not harmonic due to the presence of the two level systems. The presence of anharmonicities in the light-matter interaction problem makes the former harder to solve.*

Bogoliubov transformation. The Hamiltonian $\hat{H}^{(\mathrm{hom})}_{\mathrm{bos}}$ in Eq. 3.50 being quadratic in the bosonic operators a and b_i, it can be diagonalized exactly. This amounts to find the new eigenmodes of the coupled harmonic oscillator problem by doing a Bogoliubov transformation, as was done for similar problems in Refs. [62, 50, 25]). We thus look for eigenmode bosonic operators of the form

$$\chi_s = \alpha a + \beta B + \gamma a^\dagger + \delta B^\dagger \,, \tag{3.51}$$

that are linear combination of the initial creation and destruction operators. By construction, those operators should fulfill the following conditions

$$\left[\chi_s, \chi_s^\dagger\right] = 1 \,, \tag{3.52}$$

$$\omega \chi_s = \frac{1}{\hbar}\left[\chi_s, \hat{H}^{(\mathrm{hom})}_{\mathrm{bos}}\right] . \tag{3.53}$$

The equation Eq. 3.52 is a commutation rule expressing the fact that the $\chi_s^\dagger$ operator is an operator that creates a bosonic collective excitation (polariton), and the equation Eq. 3.53 is the condition that this χ_s excitation is an eigenmode in Heisenberg representation for the Hamiltonian $\hat{H}^{(\mathrm{hom})}_{\mathrm{bos}}$. We now introduce the vector of operators $\underline{\hat{A}} = \left[a, B, a^\dagger, B^\dagger\right]$ and the unknown vector of Hopfield coefficients $\underline{C} = [\alpha, \beta, \gamma, \delta]$ from which, Eq. 3.51 can be written $\chi_s = \underline{\hat{A}}^t \cdot \underline{C}$. Using this notation, the spectrum of polariton collective excitations can be found from Eqs. 3.52,3.53 as the solution of the following linear eigenvalue problem

$$\underline{C}^\dagger \cdot \underline{\underline{g}} \cdot \underline{C} = 1 \,, \tag{3.54}$$

$$\omega \underline{\hat{A}}^t \cdot \underline{C} = \underline{\hat{A}}^t \cdot \underline{\underline{\mathcal{H}}} \cdot \underline{C} \,, \tag{3.55}$$

with the $\underline{\underline{g}}$ metric and $\underline{\underline{\mathcal{H}}}$ Hopfield-matrix respectively given by

$$\underline{\underline{g}} = \mathrm{diag}\,(1, 1, -1, -1) \,, \tag{3.56}$$

$$\underline{\underline{\mathcal{H}}} = \begin{bmatrix} \omega_c & -i\Omega_R & 0 & i\Omega_R \\ i\Omega_R & \Delta + 2D & i\Omega_R & -2D \\ 0 & i\Omega_R & -\omega_c & -i\Omega_R \\ i\Omega_R & 2D & i\Omega_R & -\Delta - 2D \end{bmatrix} . \tag{3.57}$$

The Hopfield-matrix $\underline{\underline{\mathcal{H}}}$ in Eq. 3.57 can be diagonalized numerically exactly with the constraint of normalization given by Eq. 3.56, providing the desired polariton spectrum.

Comparison with the variational approach. We plot in Fig 3.7 the spectrum of the LP (in blue) and UP (in red) polaritons obtained as numerical solution of the above Hopfield-matrix problem. This spectrum is superimposed and compared to the numerical solution

of the variational approach described in Sec. 3.3.1 (yellow points). We note that those low-energy polaritons are qualitatively the same with both methods. *However, there are some quantitative differences, that we assign to the intrinsic anharmonicities of the variational approach while the Hopfield-matrix problem is a strictly harmonic one.* This enlightens the difficulty and sensibility of the chosen approximation methods to derive the polariton spectra in the ultrastrong coupling regime. *We thus adopt the following pragmatic approach of choosing the Hopfield-matrix approach for exploring ultrastrong light-matter interaction problems due to its simplicity and capacity to both exhibit analytical results and transparent physical interpretation of the computed analytical spectra.* This choice is not unique: it is still an open and relevant problem of manybody physics to investigate the ultrastrong light-matter coupling regime with non-pertubative methods that are both gauge invariant and well controlled.

3.3.3 Classical analog and exact solution to the Hopfield problem

Classical limit of the Hopfield problem. *In this section, we provide a mapping of the previous quantum mechanical problem described by the $\hat{H}_{\rm bos}^{\rm (hom)}$ in Eq. 3.50 to an equivalent classical Hamiltonian $H^{\rm (cl)}$ obtained as the classical limit of the previous one.* This enables to propose a fruitful analogy between the polariton physics and an equivalent problem of classical mechanics. The classical limit is achieved using the natural mass-weighted coordinates (q_c, Q) and momenta (p_c, P) of the harmonic oscillators associated respectively to the optical cavity mode operator a and the collective molecular excitation operator B relative to the dielectric polarization of the molecular ensemble. We have

$$q_c = \sqrt{\frac{\hbar}{2\omega_c}}\left(a + a^\dagger\right) , \tag{3.58}$$

$$p_c = \sqrt{\frac{\hbar\omega_c}{2}}\frac{a - a^\dagger}{i} , \tag{3.59}$$

$$Q = \sqrt{\frac{\hbar}{2\Delta}}\left(B + B^\dagger\right) , \tag{3.60}$$

$$P = \sqrt{\frac{\hbar\Delta}{2}}\frac{B - B^\dagger}{i} . \tag{3.61}$$

In the classical limit, those operators are taken to be classical and thus commuting variables. This leads to the following form of classical Hamiltonian $H^{\rm (cl)}$ equivalent to $\hat{H}_{\rm bos}^{\rm (hom)}$ in the classical limit

$$H^{\rm (cl)} = \left[\frac{p_c^2}{2} + \frac{\omega_c^2}{2}q_c^2\right] + \left[\frac{P^2}{2} + \frac{\Delta^2}{2}Q^2\right] + \left[\omega_P p_c Q + \frac{\omega_P^2}{2}Q^2\right] . \tag{3.62}$$

As expected, the eigenmodes of the classical Hamiltonian $H^{\rm (cl)}$ in Eq. 3.62 are the same as the eigenvalues of the Hopfield matrix $\underline{\underline{\mathcal{H}}}$ in Eq. 3.57. *This is so because the problem of Hopfield polaritons is an harmonic one in which the underlying physical problem is equivalent to find the eigenmodes of a collection of interacting harmonic oscillators.*

Classical equations of motion. We now study in more details the problem of classical mechanics associated to $H^{\rm (cl)}$ in Eq. 3.62. For that purpose, *we first derive the classical*

Hamilton equations associated to the variables (q_c, Q, p_c, P)

$$\dot{q}_c = p_c + \omega_P Q \,, \tag{3.63}$$
$$\dot{Q} = P \,, \tag{3.64}$$
$$\dot{p}_c = -\omega_c^2 q_c \,, \tag{3.65}$$
$$\dot{P} = -\tilde{\Delta}^2 Q - \omega_P p_c \,, \tag{3.66}$$

where we introduced the renormalized molecular exciton frequency $\tilde{\Delta}$ as

$$\tilde{\Delta} = \sqrt{\Delta^2 + \omega_P^2} \,. \tag{3.67}$$

From those Hamilton equations, we can obtain *the Newton equations of motion associated to the classical variables* (q_c, Q) *of the interacting oscillator coordinates*

$$\ddot{q}_c = -\omega_c^2 q_c + \omega_P \dot{Q} \,, \tag{3.68}$$
$$\ddot{Q} = -\Delta^2 Q - \omega_P \dot{q}_c \,. \tag{3.69}$$

We note that contrary to Hamilton equations Eqs. 3.63,3.64,3.65,3.66 which involve the renormalized molecular exciton frequency $\tilde{\Delta}$, the Newton equations Eqs. 3.68,3.69 involve the bare exciton frequency Δ. The former equations can be rewritten in a more transparent vectorial form, introducing a fictitious mobile of unit mass located at position $\vec{x}(t) \equiv q_c(t)\vec{e}_x + Q(t)\vec{e}_y$ such that

$$\ddot{\vec{x}}(t) = -\underline{\underline{k}}\vec{x}(t) + \dot{\vec{x}}(t) \times \vec{\Omega} \,, \tag{3.70}$$

with the dyadic spring-tensor $\underline{\underline{k}} \equiv \omega_c^2 \vec{e}_x \otimes \vec{e}_x + \Delta^2 \vec{e}_y \otimes \vec{e}_y$ standing for an anisotropic harmonic restoring force applied to the mobile a fictitious effective magnetic field or Larmor vector $\vec{\Omega} \equiv \omega_P \vec{e}_z$. *We thus obtained that solving for the polariton spectrum of the Hopfield matrix described by Eq. 3.57 is equivalent to solving for the equation of motion of a classical mass-weighted mobile in an anisotropic two-dimensional harmonic trap in presence of a static transverse B-field (see Fig. 3.8-b)), as described by Eq. 3.70.* This is the main result of this section.

Exact solution to the Hopfield polariton problem. The classical model developed above provides an elegant way to find an exact solution to the initial Hopfield problem derived in Sec. 3.3.2. For doing so, we look for solutions of the Newton equations of motion Eqs. 3.68,3.69 in the form of a Fourier eigenmode

$$q_c(t) = q_c(\omega) e^{i\omega t} \,, \tag{3.71}$$
$$Q(t) = Q(\omega) e^{i\omega t} \,, \tag{3.72}$$

thus leading to the system of coupled linear equations

$$\left(\omega^2 - \omega_c^2\right) q_c(\omega) + i\omega\omega_P Q(\omega) = 0 \,, \tag{3.73}$$
$$-i\omega\omega_P q_c(\omega) + \left(\omega^2 - \Delta^2\right) Q(\omega) = 0 \,. \tag{3.74}$$

A non-trivial solution is obtained if the following secular determinant equation is fulfilled

$$\left(\omega^2 - \omega_c^2\right)\left(\omega^2 - \Delta^2\right) = \omega^2 \omega_P^2 \,. \tag{3.75}$$

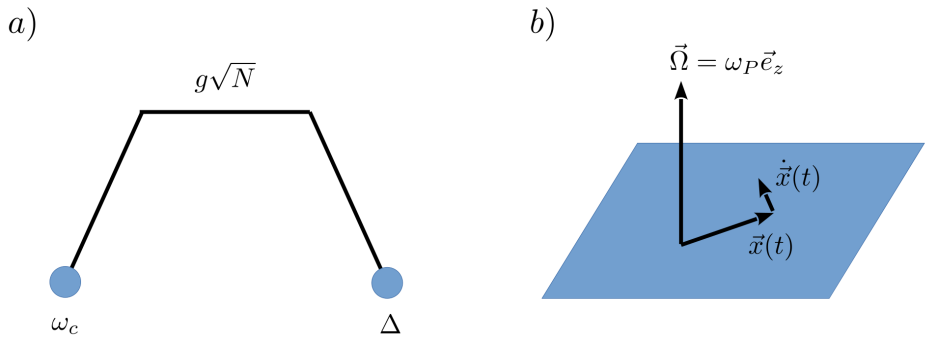

Figure 3.8: a) Scheme of equivalent model of coupled classical mechanical oscillators equivalent to the polariton problem within rotating wave approximation. b) Equivalent model of polaritons in the ultrastrong coupling regime for which a mass-weighted fictitious classical particle is coupled to an effective magnetic field in a two dimensional harmonic trap.

The solutions of Eq.3.75 provide the polariton spectra we are looking for. We obtain 4 eigenmodes $(\omega_+, \omega_-, -\omega_-, -\omega_+)$, with

$$\omega_\pm = \sqrt{\frac{\omega_c^2 + \tilde{\Delta}^2}{2} \pm \sqrt{\left(\frac{\omega_c^2 - \tilde{\Delta}^2}{2}\right)^2 + \omega_c^2 \omega_P^2}}\,, \tag{3.76}$$

$$\tilde{\Delta} = \sqrt{\Delta^2 + \omega_P^2}\,. \tag{3.77}$$

The frequency ω_+ corresponds to the frequency of the upper polariton (UP) excitation , while ω_- corresponds to the frequency of the lower polariton (LP) excitation. The eigenmode solutions of negative energy are not relevant in this context, since we are looking for excitation energies (with respect to the ground-state energy) thus being of positive energies.

3.3.4 Polariton spectra in the electronic ultrastrong coupling regime

Polariton dispersion

We show in Fig. 3.9 the polariton dispersion $\omega_\pm$ as a function of cavity frequency ω_c for a given value of $\Omega_R(\omega_c = \omega_v) = \frac{\omega_P}{2} = 0.4\Delta$. The upper (lower) polariton are obtained from numerical diagonalization of the Hopfield matrix written in Eq. 3.57 and shown as a red (cyan) plain curve. The dashed black lines are the outcome of the exact analytical formula obtained by solving the problem of classical coupled harmonic oscillators as written in Eq. 3.76, while the dashed cyan and red lines are the LP and UP outcome of performing the rotating wave approximation as written in Eq. 3.15. *We note first that, as expected, the curves corresponding to the exact analytical formula (dashed black lines) match perfectly the outcome of the numerical diagonalization of the Hopfield matrix (plain lines), showing the equivalence between a problem of classically coupled oscillators and the calculation of polaritonic spectra in the electronic ultrastrong coupling regime.* However, in this regime, the RWA (dashed colored lines) has some discrepancies compared to the exact result. While the RWA reproduces

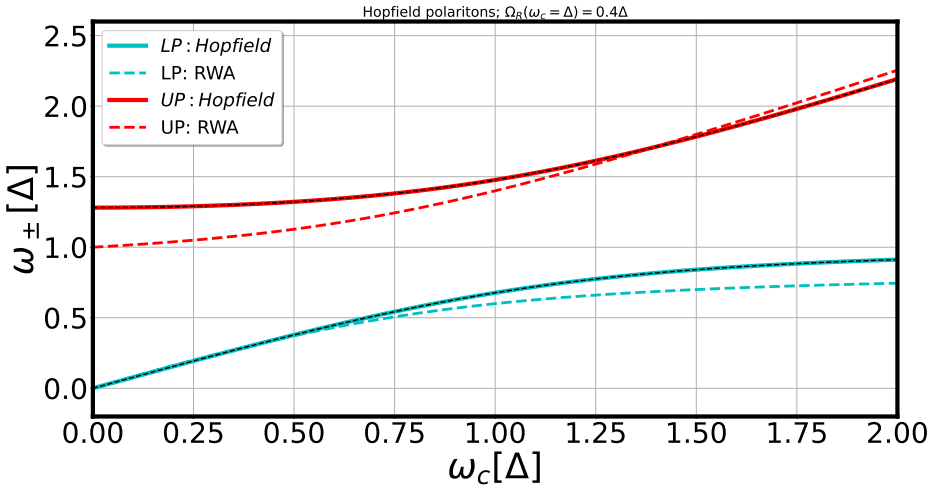

Figure 3.9: Polariton dispersion $\omega_\pm$ as a function of cavity frequency ω_c. The upper (lower) polariton are shown as red (cyan) lines. Plain lines are obtained by diagonalizing numerically the Hopfield matrix (Eq. 3.57), while dashed black lines are the outcome of the analytical exact formula (Eq. 3.76). Dashed lines are the outcome of performing the rotating wave approximation as written in Eq. 3.14. Parameters are: $\Delta = 1.0$, $\Omega_R(\omega_c = \Delta) = \frac{\omega_P}{2} = 0.4$. Unpublished Fig.

qualitatively the physics of avoided crossing between the cavity EM oscillator of frequency ω_c and the collective molecular exciton of frequency Δ ((see Fig. 3.8-a)) as anticipated in Sec. 3.2.4, it fails to match quantitatively with the exact results both in and out of resonance. We illustrate this phenomenon by considering the asymptotic behaviors at low frequencies ($\omega_c \ll \Delta$) obtained from the exact Eq. 3.76

$$\omega_+(\omega_c \to 0^+) \approx \tilde{\Delta}\,, \tag{3.78}$$
$$\omega_-(\omega_c \to 0^+) \approx 0^+\,, \tag{3.79}$$

and at large frequencies ($\omega_c \gg \Delta$)

$$\omega_+(\omega_c \to +\infty) \approx \omega_c\,, \tag{3.80}$$
$$\omega_-(\omega_c \to +\infty) \approx \Delta\,. \tag{3.81}$$

The former recovers, as expected, the eigenmodes of the uncoupled cavity and bare molecular exciton. We further define the *polaritonic gap* $\omega_{P;g}$ as

$$\begin{aligned}\omega_{P;g} &\equiv \omega_+(\omega_c \to 0^+) - \omega_-(\omega_c \to +\infty) \\ &= \tilde{\Delta} - \Delta\,.\end{aligned} \tag{3.82}$$

We note that this polaritonic gap is a fingerprint of the electronic ultrastrong coupling regime: it corresponds to a spectral region of frequencies in the range $\omega \in [0, \omega_{P;g}]$ *for which no polariton excitation exists. The existence of the polaritonic gap is not reproduced by the RWA.* Finally, the ultrastrong coupling regime implies that the condition of resonance is now shifted from $\omega_c = \Delta$ to $\omega_c = \tilde{\Delta}$ due to the renormalized collective molecular exciton frequency $\tilde{\Delta}$ written in Eq. 3.77. We also show in Fig. 3.9 that at frequency $\omega_c = \Delta$ (thus out of the true

resonance condition), the polariton lines are blue-shifted with respect to the RWA. *This blue shift is a Lamb-shift effect induced by coupling quantum vacuum fluctuations of the cavity mode to the collective molecular exciton through both counter-rotating terms and self-dipole interaction terms of* $\hat{H}_{\rm bos}^{(\rm hom)}$ *in Eq. 3.50.*

Study at resonance ($\omega_c = \tilde{\Delta}$)

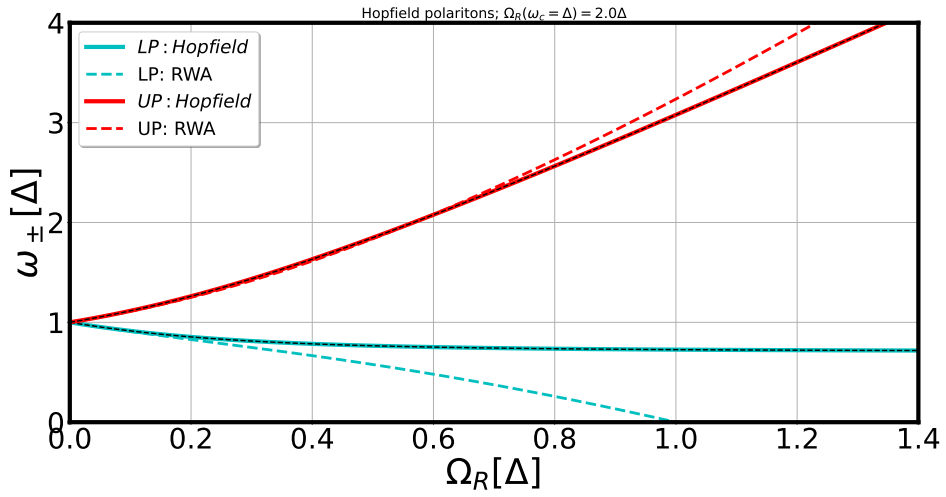

Figure 3.10: Polariton dispersion $\omega_\pm$ as a function of the Rabi frequency $\Omega_R(\omega_c = \Delta) = \frac{\omega_P}{2}$ for a cavity at resonance ($\omega_c = \tilde{\Delta}$). The legend is similar to the previous Fig. 3.9. Unpublished Fig.

We show in Fig. 3.10 the polariton dispersion $\omega_\pm$ as a function of the Rabi frequency $\Omega_R(\omega_c = \Delta) = \frac{\omega_P}{2}$ for a cavity at true resonance with the molecular material $\omega_c = \tilde{\Delta}$. At low coupling regime ($\omega_P \ll \Delta$), we obtain the asymptotic behavior for the polaritons

$$\omega_\pm(\omega_P \to 0^+) \approx \Delta \pm \frac{\omega_P}{2} + \frac{3\omega_P^2}{8\Delta}\,. \tag{3.83}$$

In this weak-coupling regime, the agreement between the exact result (plain curves) and the rotating wave approximation is very good and the vacuum Rabi splitting is well approximated by the RWA result $\omega_+ - \omega_- \approx \omega_P = 2\Omega_R(\omega_c = \Delta)$. In the opposite regime of ultrastrong coupling ($\omega_P \gg \Delta$), we obtain the following asymptotic behaviors

$$\omega_+(\omega_P \to +\infty) \approx \omega_P\sqrt{2}\,, \tag{3.84}$$

$$\omega_-(\omega_P \to +\infty) \approx \frac{\Delta}{\sqrt{2}}\,. \tag{3.85}$$

In this ultrastrong coupling regime, there is no more agreement between the exact result (plain curves) and the outcome of the RWA (dashed curves). While the exact UP frequency is lower than the one computed with RWA, the discrepancy in the case of the LP is much worse. *Indeed, the RWA predicts an unphysical absence of lower-bound for the energy of the LP. Including both counter-rotating and self-dipole interaction terms is thus essential for the true LP to achieve a finite (and positive) energy at large-couplings* $\omega_P \gg \Delta$. The results shown in Figs. 3.9,3.10 are consistent with an earlier work by Ciuti et al. in Ref. [25].

3.4 Chiral light-matter interactions in optical cavities

In this section, we investigate the issue of computing and analyzing the polaritonic spectra for a 2D-layer of chiral molecules embedded inside an optical Fabry-Pérot cavity. In Sec. 3.4.1, we give a sketch of the main issues underlying this problem. We provide in Sec. 3.4.2 a microscopic model describing chiral light-matter interactions in an optical cavity beyond the strict dipole approximation. We bosonize this problem in Sec. 3.4.3 and derive an analytical expression for the resulting polaritonic spectra: *we unveil a new gyrotropic coupling mechanism between a 2D-layer aggregate of chiral molecules and the cavity modes at the origin of enantioselective signatures on the polaritonic spectra.* We show in Sec. 3.4.4 that *solving the former quantum mechanical problem of polaritons in dimension 2 is equivalent to solve an analogous problem of classical mechanics involving the dynamics of a fictitious mobile in dimension 2+1 in presence of a weakly anistotropic harmonic trap and effective magnetic field.* In Sec. 3.4.5 we analyze the nature of the mobile trajectories in the analogous classical problem. An analogy with the motion of a Foucault pendulum is proposed in the weak coupling regime, while in the ultrastrong coupling regime, the proper analogy is with a cyclotron gyration problem. *The differential shift in the polaritonic spectra is shown to be directly proportional to the anholonomy angle of the computed classical trajectories.* This work was developed in collaboration with Cyriaque Genet (ISIS) during my one year visit in his team and reported in our recent Ref. [6].

3.4.1 Position of the problem

In this section, we come to the general problem of describing light-matter interactions inside an optical cavity. Compared to the previous section Sec. 3.2, we add some *optical complexity* in the modeling of both the molecular aggregate and cavity mode microscopic description, by considering the following additional features (shown in Fig. 3.11)

1. The molecules are embedded in *a two dimensional layer configuration* that is located at distance $z = z_L$ along the cavity optical axis.

2. The molecules have *both electric and magnetic transition dipole features at the origin of intrinsic molecular chirality.* Each molecules are however the same with no energetic nor orientational disorder.

3. The cavity mode that is resonantly coupled to the molecular aggregate has two components corresponding to *the two states of polarization of the optical mode and a spatial dispersion along the optical z-axis.*

Those additional features enable to describe *the interplay between intrinsic molecular chirality and spatial dispersion and polarization of the cavity in the light-matter interaction mechanism*, thus probing the onset of cavity-induced chiral polariton formation beyond the strict dipole approximation. This problem depends crucially on the dimensionality of the molecular aggregate as we will show in the following.

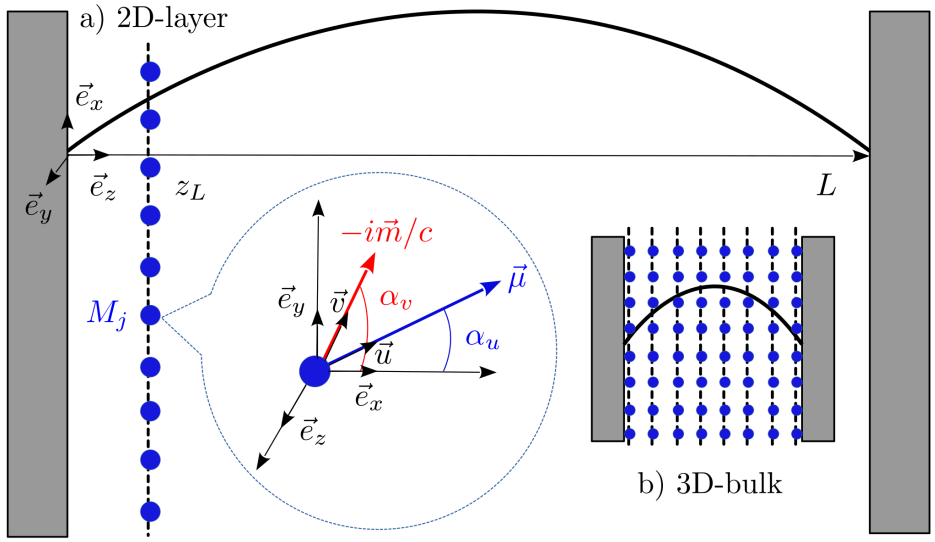

Figure 3.11: a) Main panel. Scheme of optical Fabry-Pérot cavity of length L. A 2D layer of molecules is located at position $z = z_L$ on the optical axis and couples to the two degenerate cavity modes with polarization $\alpha = x, y$ corresponding to the same mode index m and zero transverse wave vector $\vec{k}_\perp = \vec{0}$. Inset: Zoom of the molecule $M_j(x_j, y_j, z_L)$ (blue dot) seen from above the $\vec{e}_z$ direction with electric (blue) and magnetic (red) transition dipoles $\vec{\mu}$ and $\vec{m}$ respectively. We considered here the case where $u_z = v_z = 0$ so that $\vec{u} = \vec{u}_\perp$ and $\vec{v} = \vec{v}_\perp$. b) Lower panel. Same scheme but for a 3D bulk configuration of molecules filling homogeneously the cavity. Adapted from our Ref. [6].

3.4.2 Microscopic model of a 2D-layer inside an optical cavity

Description of the cavity modes. In order to describe chiral light-matter interactions developing between the 2D-layer of molecules shown in Fig. 3.11 and the optical cavity modes, *we need to take into account the vectorial structure of the quantized electromagnetic (EM) field inside cavity.* In Coulomb gauge, the EM field can be expanded can be expanded in terms of transverse optical cavity modes

$$\hat{\vec{A}}(\vec{r}) = \sum_\alpha \sqrt{\frac{\hbar}{2\varepsilon_0\omega_\alpha}} \left\{ a_\alpha \vec{\mathcal{L}}_\alpha(\vec{r}) + a_\alpha^\dagger \vec{\mathcal{L}}_\alpha^*(\vec{r}) \right\}, \tag{3.86}$$

$$\hat{\vec{E}}(\vec{r}) = i\sum_\alpha \sqrt{\frac{\hbar\omega_\alpha}{2\varepsilon_0}} \left\{ a_\alpha \vec{\mathcal{L}}_\alpha(\vec{r}) - a_\alpha^\dagger \vec{\mathcal{L}}_\alpha^*(\vec{r}) \right\}, \tag{3.87}$$

$$\hat{\vec{B}}(\vec{r}) = \sum_\alpha \sqrt{\frac{\hbar}{2\varepsilon_0\omega_\alpha}} \left\{ a_\alpha \vec{\nabla} \times \vec{\mathcal{L}}_\alpha(\vec{r}) + a_\alpha^\dagger \vec{\nabla} \times \vec{\mathcal{L}}_\alpha^*(\vec{r}) \right\}, \tag{3.88}$$

$$\tag{3.89}$$

with $\hat{\vec{A}}(\vec{r})$ the vector-potential operator, $\hat{\vec{E}}(\vec{r})$ the electric field operator and $\hat{\vec{B}}(\vec{r})$ the magnetic field operator. We introduced $a_\alpha^\dagger$ (a_α) the operator creating (destroying) a photon in the cavity mode α corresponding to a spatially dependent cavity mode lineshape $\vec{\mathcal{L}}_\alpha(\vec{r})$. We wrote $\hbar$ the reduced Planck constant, ε_0 the vacuum permittivity, c the speed of light,

L the cavity length along the optical axis and V the cavity mode volume. *The minimal theoretical model describing gyrotropic coupling necessitates at least coupling of the molecules to two cavity modes.* We consider such two modes with degenerate frequency $\omega_c = m\pi c/L$, a normal k-vector $\vec{k}_\perp = \vec{0}$, an integer mode index m and two possible linear polarization $\vec{\varepsilon}_\alpha$ along the directions $\alpha = x, y$ orthogonal to the optical axis. *This mode structure enables to compute the polaritonic spectra of an optical cavity probed at normal incidence.* The polaritonic spectra result from the hybridization of the embedded molecules electronic structure with the EM field described by the z-dependent cavity mode lineshape

$$\vec{\mathcal{L}}_{\alpha=x,y}(z) \;=\; \sqrt{\frac{2}{V}} \sin\left(m\frac{\pi}{L}z\right) \vec{\varepsilon}_\alpha \,. \tag{3.90}$$

Description of the molecular aggregate. As in Sec. 3.2.2, the molecules in the 2D-layer are described as a collection of N two-level systems with an optical transition at frequency Δ. However, *the molecules have now both an electric-transition dipole operator $\hat{\vec{\mu}}_j$ and a magnetic transition dipole operator $\hat{\vec{m}}_j$* expressed as

$$\hat{\vec{\mu}}_j \;=\; \sum_{j=1}^{N} \vec{\mu}_j \left\{ c_{ej}^\dagger c_{gj} + c_{gj}^\dagger c_{ej} \right\} \,, \tag{3.91}$$

$$\hat{\vec{m}}_j \;=\; \sum_{j=1}^{N} \left\{ \vec{m}_j c_{ej}^\dagger c_{gj} - \vec{m}_j^* c_{gj}^\dagger c_{ej} \right\} \,, \tag{3.92}$$

with $\vec{\mu}_j$ the real electric transition dipole and $\vec{m}_j$ the pure imaginary magnetic transition dipole of the molecule j. *The interference between the electric and magnetic molecular polarizations is at the origin of intrinsic chirality of the molecular aggregate.* If those molecules were randomly dispersed in a 3D-bulk homogeneous and isotropic medium and were to interact with an incoming light of left (L) or right (R) circularly polarization, the intrinsic chirality of such molecules would give rise to a differential rate of optical absorption $\Delta\Gamma = \Gamma_L - \Gamma_R$ (after averaging on the molecular orientation) derived in the book of Craig et al. Ref. [116]

$$\Delta\Gamma \;=\; \frac{8\pi N}{3\hbar c} \frac{n\hbar c k}{2\varepsilon_0 V} \rho \,\mathrm{Im}\, \left(\vec{\mu}\cdot\vec{m}^*\right) \,, \tag{3.93}$$

with n the medium index of refraction, k the norm of the $\vec{k}$-vector and ρ the optical density of states in free EM vacuum. The corresponding rate Γ of absorption for achiral molecules is

$$\Gamma \;=\; \frac{2\pi N}{3\hbar} \frac{n\hbar c k}{2\varepsilon_0 V} \rho \left\|\vec{\mu}\right\|^2 \,. \tag{3.94}$$

This suggest to introduce as a natural measure of the intrinsic molecular chirality the relative ratio $\Delta\Gamma/\Gamma$ that quantifies circular dichroism of the molecular medium.

$$\frac{\Delta\Gamma}{\Gamma} \;=\; 4\frac{\mathrm{Im}\, \left(\vec{\mu}\cdot\vec{m}^*\right)}{\left\|\vec{\mu}\right\|^2 c} \equiv -4\mathcal{R}\vec{u}\cdot\vec{v}\,, \tag{3.95}$$

where we labeled the directions of both $\vec{\mu}$ and $\vec{m}$ transition dipoles by the unit vectors $\vec{u}$ and $\vec{v}$. We also introduced the dimensionless quantity $\mathcal{R}$ given by

$$\mathcal{R} \;=\; \frac{\|\vec{m}\|}{\|\vec{\mu}\|\, c}\,. \tag{3.96}$$

The intrinsic molecular chirality (here with respect to circular dichroism) is thus quantified by the natural pseudo-scalar parameter $\mathcal{C}$ defined as

$$\mathcal{C} \;=\; \mathcal{R}\vec{u}\cdot\vec{v}\,. \tag{3.97}$$

Upon embedding those molecules in the 2D-layer inside cavity, their intrinsic molecular chirality are changed in this model by changing the sign of the pseudo-vector $\mathcal{R}\vec{v}$, thus changing the sign of $\mathcal{C}$. Typical orders of magnitude of $\mathcal{R} \approx 10^{-4} - 10^{-3}$ are given in Ref. [116].

Microscopic Chiral Hamiltonian. In order to describe the regime of ultrastrong light-matter coupling, we include in the microscopic light-matter interaction Hamiltonian both counter-rotating and self-dipole interaction terms [25]. *We propose the following generalization of the Hamiltonian $H^{(2\mathrm{D})}$ written in Eq. 3.2 describing chiral light-matter interactions of the 2D molecular aggregate inside cavity*

$$H^{(2\mathrm{D})} \;=\; H_c + H_e + H_D + H_M + H_{SD}\,, \tag{3.98}$$

with H_c the Hamiltonian of the free cavity-mode with both states of polarization $\alpha = x, y$

$$H_c \;=\; \hbar\omega_c \left\{a_x^\dagger a_x + a_y^\dagger a_y + 1\right\}\,, \tag{3.99}$$

with a_α ($a_\alpha^\dagger$), the bosonic operator that destroys (creates) an excitation in the mode α. The Hamiltonian of the free molecules is still written

$$H_e \;=\; \hbar\frac{\Delta}{2}\sum_{j=1}^{N}\left\{c_{e_j}^\dagger c_{e_j} - c_{g_j}^\dagger c_{g_j}\right\}\,, \tag{3.100}$$

The molecules interact with the cavity-modes through the electric-dipole interaction Hamiltonian H_D and magnetic-dipole interaction Hamiltonian H_M

$$\begin{aligned} H_D \;&=\; -\sum_{j=1}^{N}\hat{\vec{\mu}}_j\cdot\hat{\vec{E}}(\vec{r}_j) \\ &\equiv\; -i\hbar\sum_{j=1}^{N}\left(b_j + b_j^\dagger\right)\left\{g_{jx}\left(a_x - a_x^\dagger\right) + g_{jy}\left(a_y - a_y^\dagger\right)\right\}\,, \end{aligned} \tag{3.101}$$

$$\begin{aligned} H_M \;&=\; -\sum_{j=1}^{N}\hat{\vec{m}}_j\cdot\hat{\vec{B}}(\vec{r}_j) \\ &\equiv\; -i\hbar\sum_{j=1}^{N}\left(b_j - b_j^\dagger\right)\left\{\nu_{jx}\left(a_y + a_y^\dagger\right) - \nu_{jy}\left(a_x + a_x^\dagger\right)\right\}\,, \end{aligned} \tag{3.102}$$

where we introduced $b_j^\dagger = c_{e_j}^\dagger c_{g_j}$ the operator that creates an electronic excitation on molecule number j and

$$\hbar\vec{g}_j \equiv \sqrt{\frac{\hbar\omega_c}{\varepsilon_0 V}}\,\vec{\mu}_j \sin\left(\theta_{z_j}\right) \in \mathbb{R}^3\,, \tag{3.103}$$

$$\hbar\vec{\nu}_j \equiv -i\frac{1}{c}\sqrt{\frac{\hbar\omega_c}{\varepsilon_0 V}}\,\vec{m}_j \cos\left(\theta_{z_j}\right) \in \mathbb{R}^3\,. \tag{3.104}$$

respectively *the electric-dipole and magnetic-dipole coupling vectors* with the z-dependent angle $\theta_{z_j} = m\frac{\pi}{L}z_j$ obtained after writing the $\vec{E}$ and $\vec{B}$ electric and magnetic field vectors deriving from the cavity mode lineshape written in Eq. 3.90. Finally, the self-dipole interactions term H_{SD} that is necessary to deal with the ultrastrong coupling regime is written

$$H_{SD} = \frac{\hbar}{\omega_c}\sum_{\alpha=x,y}\left|\sum_{j=1}^{N} g_{j,\alpha}\left(b_j + b_j^\dagger\right)\right|^2\,. \tag{3.105}$$

Open issues. The Hamiltonian $H^{(2\mathrm{D})}$ written in Eq. 3.98 contains terms beyond the strict dipole approximation, which is not without implying any issue. We indeed note the following limitations of our model

1. *The multipolar expansion of the interaction Hamiltonian $H^{(2\mathrm{D})}$ contains also electric quadrupolar terms that are of the same order of magnitude as the magnetic dipolar one [95].* We did not take them into account in the present study, but they could be in principle added to incorporate the description of a broader class class of chiral molecules.

2. *This multipolar expansion contains additional diamagnetic self-dipole terms that explicitly break translational invariance of the interaction Hamiltonian but are smaller than the electric self-dipole terms H_{SD} [95]* due to the smallness of the chiroptical constant $\mathcal{R}$: we consistently neglected those terms in the writing of $H^{(2\mathrm{D})}$.

3. *We neglected entirely the effect of purely electrostatic longitudinal interactions between molecules within the cavity mode volume.* In principle the former are described in Coulomb gauge by adding the continuum part of the electromagnetic spectrum leading to electrostatic interactions mediated via exchange of virtual photons [3] inside the cavity.

How to consistently introduce those points in a more complex but still tractable theoretical model of chiral light-matter interactions inside cavity still constitutes an open problem in molecular polaritonics. We chose to incorporate step by step the inherent *optical complexity* of this problem and focused on what we think are the first dominant corrections to the dipole approximation associated to spatial inhomogeneities of the EM cavity field that contain most of the qualitative features of the polaritonic spectra.

3.4.3 Hopfield polaritonic spectra in the 2D-layer configuration

Homogeneous molecular aggregate

We now make the additional homogeneity assumption that *all the molecules in the chiral 2D-layer are supposed to all have the same orientation and magnitude of their electric and magnetic transition dipoles* thus realizing an homogeneous but anisotropic aggregate in which each molecule of the ensemble couples in the same way to the EM cavity modes. We thus write for each molecule M_j the electric and magnetic transition dipole vectors

$$\vec{\mu} \equiv \mu\vec{u}\sin\left(\theta_{z_L}\right) , \tag{3.106}$$

$$\vec{m}/c \equiv i\mathcal{R}\mu\vec{v}\cos\left(\theta_{z_L}\right) . \tag{3.107}$$

shown in Fig. 3.11 as red and blue arrows respectively. Those vectors point in a direction given by the unit vectors $\vec{u} = u_z\vec{e}_z + \vec{u}_\perp$ and $\vec{v} = v_z\vec{e}_z + \vec{v}_\perp$ which have in general a non zero z-component on the optical axis. In the following, we write $\vec{u}_\perp$ the component of any vector $\vec{u}$ that is orthogonal to the optical z-axis. We consider in Fig. 3.11 and in the rest of this work the situation for which the proposed gyrotropic coupling mechanism is maximum. This happens when $u_z = v_z = 0$ and thus $\vec{u} = \cos\left(\alpha_u\right)\vec{e}_x + \sin\left(\alpha_u\right)\vec{e}_y$ and $\vec{v} = \cos\left(\alpha_v\right)\vec{e}_x + \sin\left(\alpha_v\right)\vec{e}_y$ with $\alpha_v = \alpha_u + \alpha$. *However our theoretical approach and analytical formulas are still valid in the case where the transition dipoles do not necessarily lie in the transverse plane.* In the following paragraphs, we found convenient for analytical calculations to use the simpler notation for the homogeneous coupling vectors in Eq. 3.103,3.104

$$\vec{g}_j \equiv \vec{g} , \tag{3.108}$$

$$\vec{\nu}_j \equiv \vec{\nu} , \tag{3.109}$$

with the convention that the results for the homogeneous 2D-layer written Eqs. 3.106,3.107 can be obtained from Eqs. 3.108,3.109 by multiplying all the expressions involving $\vec{g}$ and $\vec{\nu}$ by $\sin\left(\theta_{z_L}\right)$ and $\cos\left(\theta_{z_L}\right)$ respectively.

Bosonization of the interaction Hamiltonian and Bogoliubov transformation

Using the same bosonization method as the one described previously in Sec. 3.3.2, *we write the effective quadratic Hamiltonian equivalent to the $H^{(2D)}$ microscopic Hamiltonian of Eq. 3.98 but in the case of harmonic approximation and homogeneous coupling* (see also Eqs. 3.106,3.107) as

$$\begin{aligned} H_{\text{bos}}^{(2D)} &= \hbar\omega_c\left\{a_x^\dagger a_x + a_y^\dagger a_y + 1\right\} + \hbar\Delta\sum_{j=1}^{N}\left\{b_j^\dagger b_j + \frac{1}{2}\right\} \\ &- i\hbar\Omega_R\left(B + B^\dagger\right)\left\{u_x\left(a_x - a_x^\dagger\right) + u_y\left(a_y - a_y^\dagger\right)\right\} \\ &- i\hbar\mathcal{R}\Omega_R\left(B - B^\dagger\right)\left\{v_x\left(a_y + a_y^\dagger\right) - v_y\left(a_x + a_x^\dagger\right)\right\} \\ &+ \hbar D\left(B + B^\dagger\right)^2 . \end{aligned} \tag{3.110}$$

In Eq. 3.110, we introduced the collective molecular polarization or collective molecular exciton operator mode

$$B = \frac{1}{\sqrt{N}} \sum_{j=1}^{N} b_j \,, \tag{3.111}$$

as well as the collective vacuum Rabi splitting and self-dipole interaction terms

$$\Omega_R = g\sqrt{N} \equiv \frac{1}{\hbar}\sqrt{\frac{\hbar\omega_c N}{\varepsilon_0 V}}\,\mu \,, \tag{3.112}$$

$$D = \frac{\Omega_R^2}{\omega_c}\left\|\vec{u}_\perp\right\|^2 . \tag{3.113}$$

As in Sec. 3.3.2, the diagonalization of $H_{\rm bos}^{(2D)}$ in Eq. 3.110 amounts to find its eigenvectors χ in the form of a linear combination of destruction and creation operators of the cavity and collective exciton modes

$$\chi = \underline{\hat{A}}^t \cdot \underline{C} \,, \tag{3.114}$$

$$\underline{\hat{A}} = \left[a_x, a_y, B, a_x^\dagger, a_y^\dagger, B^\dagger\right] , \tag{3.115}$$

$$\underline{C} = \left[\alpha_x, \alpha_y, \gamma, \beta_x, \beta_y, \delta\right] , \tag{3.116}$$

with $\underline{C}$ a vector of unknown coefficients. The χ-operators follow a linear eigenvalue problem

$$\omega \underline{\hat{A}}^t \cdot \underline{C} = \underline{\hat{A}}^t \cdot \underline{\underline{\mathcal{H}}} \cdot \underline{C} \,, \tag{3.117}$$

$$\underline{C}^\dagger \cdot \underline{\underline{g}} \cdot \underline{C} = 1 \,, \tag{3.118}$$

with $\underline{\underline{g}}$ the underlying metric

$$\underline{\underline{g}} = \text{diag}\left(1,1,1,-1,-1,-1\right) , \tag{3.119}$$

and $\underline{\underline{\mathcal{H}}}$ the Hopfield-matrix of dimension 6×6

$$\underline{\underline{\mathcal{H}}} = \begin{bmatrix} \omega_c & 0 & -i\Omega_R w_{xy}^+ & 0 & 0 & i\Omega_R w_{xy}^- \\ 0 & \omega_c & -i\Omega_R w_{yx}^- & 0 & 0 & i\Omega_R w_{yx}^+ \\ i\Omega_R w_{xy}^+ & i\Omega_R w_{yx}^- & \Delta + 2D & i\Omega_R w_{xy}^- & i\Omega_R w_{yx}^+ & -2D \\ 0 & 0 & i\Omega_R w_{xy}^- & -\omega_c & 0 & -i\Omega_R w_{xy}^+ \\ 0 & 0 & i\Omega_R w_{yx}^+ & 0 & -\omega_c & -i\Omega_R w_{yx}^- \\ i\Omega_R w_{xy}^- & i\Omega_R w_{yx}^+ & 2D & i\Omega_R w_{xy}^+ & i\Omega_R w_{yx}^- & -(\Delta + 2D) \end{bmatrix} . \tag{3.120}$$

were we introduced the components $w_{jk}^\pm \equiv u_j \pm \mathcal{R} v_k$. The polariton spectrum of $\underline{\underline{\mathcal{H}}}$ is found by numerical diagonalization. *We find* 3 *positive eigenvalues of the* $\underline{\underline{\mathcal{H}}}$*-matrix: one lower polariton* ω_-^{2D}*, one upper polariton* ω_+^{2D}*, and one middle polariton* ω_0^{2D}*.*

Exact solution to the Hopfield polariton spectra

We remark that the characteristic polynomial $P(\lambda) = \det\left(\lambda\underline{\underline{\mathrm{Id}}} - \underline{\underline{\mathcal{H}}}\right)$ of the Hopfield-matrix (see Eq. 3.120) can be obtained analytically as

$$\begin{aligned} P(\lambda) &= \left(\lambda^2 - \omega_c^2\right)^2 \left(\lambda^2 - \Delta^2\right) - 16\mathcal{R}^2\lambda^2\Omega_R^4 \left(\vec{u}_\perp \cdot \vec{v}_\perp\right)^2 \\ &- 4\frac{\Omega_R^2}{\omega_c}\left(\lambda^2 - \omega_c^2\right)\left\{\Delta \left\|\vec{u}_\perp\right\|^2 \lambda^2 + 2\mathcal{R}\lambda^2\omega_c\vec{e}_z \cdot \left(\vec{u}_\perp \times \vec{v}_\perp\right) + \mathcal{R}^2\Delta\omega_c^2 \left\|\vec{v}_\perp\right\|^2\right\} . \end{aligned} \tag{3.121}$$

In the physically relevant limit $\mathcal{R} \ll 1$, the roots of this characteristic polynomial can be found analytically, leading to an explicit expression of the differential shift $\delta_\eta^{2\mathrm{D}}$ in the polariton frequencies. Reintroducing the z-dependence of coefficients of $P(\lambda)$ with the cavity mode lineshape, we obtain the following expression

$$\delta_\eta^{2\mathrm{D}} = \omega_{\eta;\mathcal{R}} - \omega_{\eta;\mathcal{R}=0} \approx \eta\chi(z_L)\left(\frac{\Omega_R}{\tilde{\Omega}}\right)^2 \omega_{\eta;0} , \tag{3.122}$$

$$\chi(z_L) = \mathcal{R}\left[\vec{e}_z \cdot \left(\vec{u} \times \vec{v}\right)\right] \sin\left(2\theta_{z_L}\right) , \tag{3.123}$$

with $\eta = +(-)$ labeling for the upper (lower) polariton branch and $\chi(z_L)$ *the gyrotropic coupling induced by the cross-coupling between electric and magnetic transition dipoles* $\vec{\mu}$ *and* $\vec{m}$ *and the cavity mode spatial lineshape.* We also introduced in Eq. 3.122 the renormalized collective Rabi frequency $\tilde{\Omega}$ and collective molecular exciton frequency $\tilde{\Delta}$ written as

$$\tilde{\Omega}^2 = \sqrt{\left(\frac{\omega_c^2 - \tilde{\Delta}^2}{2}\right)^2 + 4\Delta\omega_c\Omega_R^2 \left\|\vec{u}_\perp\right\|^2 \sin^2\left(\theta_{z_L}\right)} , \tag{3.124}$$

$$\tilde{\Delta} = \sqrt{\Delta^2 + 4\frac{\Delta}{\omega_c}\Omega_R^2 \left\|\vec{u}_\perp\right\|^2 \sin^2\left(\theta_{z_L}\right)} , \tag{3.125}$$

and the polariton frequency in the case when $\mathcal{R} = 0$ recovering Eq. 3.76 in Sec. 3.3.4

$$\omega_{\eta;0} = \sqrt{\frac{\omega_c^2 + \tilde{\Delta}^2}{2} + \eta\tilde{\Omega}^2} . \tag{3.126}$$

Both Eqs. 3.122,3.123 are the main results of this section. Those expressions were derived first in our recent Ref.[6]. They provide an explicit analytical formula for the cavity-induced modification of polaritonic spectra in the case of a 2D-layer of chiral molecules embedded inside cavity. *We note that this expression involves the gyrotropic coupling* $\chi(z_L)$ *in Eq. 3.123 which is a fundamental dimensionless quantity with true scalar behavior with respect to both rotations and planar reflections. The gyrotropic coupling results from the hybridization between the chiral molecules and the cavity modes:* it is the product of one term proportional to $\mathcal{R}$ times the projection of $\vec{u} \times \vec{v}$ on the z-direction characterizing the molecular orientation and enantiomeric class, by a second term $\sin\left(2\theta_{z_L}\right)$ associated to the spatial z-dependence of the cavity mode lineshape along the optical axis. *The* $\chi(z_L)$ *parameter depends crucially on the interplay between the dimensionality of the molecular ensemble and the spatial distribution of the cavity modes profile.* It can change sign either by changing the molecular orientation, the intrinsic molecular chirality parameter $\mathcal{C}$ in Eq. 3.97, or by changing the 2D-layer position z_L with respect to a spatial plane of symmetry of the cavity mode profile.

Analysis of the Hopfield polaritonic spectra

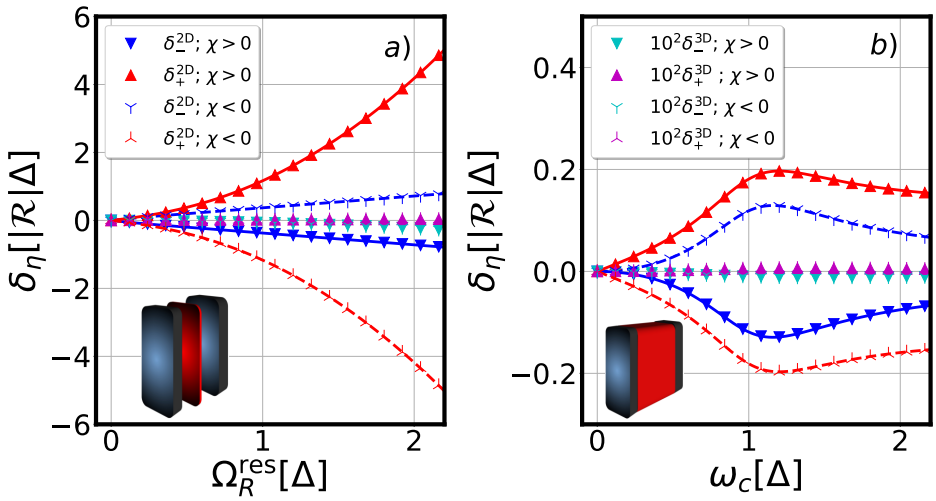

Figure 3.12: a) Plots of the relative shift in the polaritonic frequency $\delta_\eta = \omega_{\eta;\mathcal{R}} - \omega_{\eta;\mathcal{R}=0}$ (in units of $|\mathcal{R}|\,\Delta$) computed at resonance ($\omega_c = \tilde{\Delta}$) as a function of the collective vacuum Rabi splitting $\Omega_R^{\rm res}$. The upper (lower) triangles and crosses are the spectra of the upper (lower) polariton $\eta = 1(-1)$ computed after numerical diagonalization of the Hopfield matrix. Triangles (crosses) are obtained for molecules with relative angle $\alpha = \frac{\pi}{4}\left(\frac{5\pi}{4}\right)$ between their transition dipoles, intrinsic chirality $\mathcal{C} = \pm\frac{\mathcal{R}}{\sqrt{2}}$ and gyrotropic coupling equal to $\chi(z_L) = \mathcal{C}$ with the chosen parameters. Plain and dashed lines are analytical results of Eq. 3.122 for the 2D layer case (see the scheme in lower inset). The corresponding shifts in the 3D bulk case are shown after multiplication by a factor 10^2. b) Same quantities plotted as a function of cavity frequency ω_c at fixed $\Omega_R^{\rm res} = 0.3$. Lower inset is a scheme of the 3D bulk case. Parameters common to both panels: $\Delta = 1.0$, $m = 1$, $z_L = \frac{L}{4}$, $u_z = v_z = 0$, $\alpha_u = \frac{\pi}{3}$, and $\mathcal{R} = 10^{-3}$. The legends are common to both panels. Adapted from our Ref. [6]

2D-layer case. We show in Fig. 3.12-a), the $\delta_\eta^{\rm 2D}$-signals computed after exact numerical diagonalization of the Hopfield matrix (see Eq. 3.120) describing the 2D-layer of chiral molecules coupled to the cavity modes, as a function of the collective vacuum Rabi splitting $\Omega_R^{\rm res} = \Omega_R$. Same quantities are shown in Fig. 3.12-b), but as a function of cavity frequency ω_c. A very good agreement is obtained between the analytical result of Eq. 3.122 shown as plain and dashed curves and the exact numerical solution shown as triangles and crosses. We find that the upper polariton $\delta_+^{\rm 2D}$-signal is positive for $\chi(z_L) > 0$ (upper red triangles) and negative for $\chi(z_L) < 0$ (upper red crosses). The reversed signs are obtained for the lower polariton $\delta_-^{\rm 2D}$-signals (see blue curves). Consistently with Eqs. 3.123,3.122, *the computed signals exhibit on the full range of parameters the remarkable antisymmetry property*

$$\delta_\eta^{\rm 2D}\left(-\chi(z_L)\right) \;=\; -\delta_\eta^{\rm 2D}\left(\chi(z_L)\right)\,, \tag{3.127}$$

upon sign reversal of $\chi(z_L)$ obtained by changing the sign of the intrinsic molecular chirality $\mathcal{C}$ in Fig. 3.12. *The enantiodependent relation in Eq. 3.127 is the main signature of the*

reduced 2D dimensionality of the cavity configuration on the considered chiroptical observables. We note that for low values of the collective Rabi coupling $\Omega_R \ll \omega_c$, Eq. 3.122 predicts that

$$\delta_\eta^{\mathrm{2D}} \approx \frac{\chi(z_L)}{2}\left(\eta\frac{\Omega_R}{\|\vec{u}_\perp\|}+\frac{\Omega_R^2}{\Delta}\right). \tag{3.128}$$

The latter signal is thus approximately linear with Ω_R, consistently with the collective nature of the polaritons which leads to $\delta_-^{\mathrm{2D}}(\chi(z_L)) \approx -\delta_+^{\mathrm{2D}}(\chi(z_L))$. For typical values of the cVRS $\Omega_R \approx 1$ eV$/\hbar$ reported in the electronic strong coupling regime [64, 74, 35], we obtain in Fig. 3.12 values of $\left|\delta_+^{\mathrm{2D}}\right| \approx 0.38\mathcal{R}\Delta \approx 7.6\times10^{-5}-7.6\times10^{-4}$ eV$/\hbar$ at resonance $\omega_c = \tilde{\Delta} \approx 2eV/\hbar$ and for $\mathcal{R} \approx 10^{-4}-10^{-3}$. However, departures do occur for larger Ω_R (first quadratically) that are more pronounced for the upper than for the lower polariton. In the developed ultrastrong coupling regime, no such antisymmetry relation exists between the δ_+^{2D} and δ_-^{2D}-signals which in general are not opposite $\delta_-^{\mathrm{2D}}(\chi(z_L)) \neq -\delta_+^{\mathrm{2D}}(\chi(z_L))$. We assign the latter inequality to the contribution of both counter-rotating and self-dipole interaction terms [101, 109] in the microscopic Hamiltonian which similarly to the case of polaritonic gaps [25, 50] provide here *asymmetric or differential polaritonic band gaps fingerprints upon entering the ultrastrong coupling regime.* As shown in Fig. 3.12-b), the $\delta_\eta^{\mathrm{2D}}$-signals acquire *a non-monotonic behavior upon sweeping ω_c reaching thereby a maximum of $\left|\delta_\eta^{\mathrm{2D}}\right|$ close to resonance ($\omega_c \approx \Delta$).*

3D-layer case. For completeness, we consider in Figs. 3.12-a), and b), *the case of a 3D bulk configuration (shown as inset in Fig. 3.12-b)) where all chiral molecules are dispersed in the whole cavity mode volume.* The computed $\delta_\eta^{\mathrm{3D}}$-signals are shown multiplied by 10^2 (magenta and cyan triangles and crosses) as a function of both $\Omega_R^{\mathrm{res}} = \Omega_R/\sqrt{2}$ and ω_c. In contrast to the 2D case , the $\delta_\eta^{\mathrm{3D}}$-signals are much weaker and do not change sign upon sign reversal of $\chi(z_L)$. This is due to the fact that $\delta_\eta^{\mathrm{3D}}$ is obtained by integration of opposite terms $\delta_\eta^{\mathrm{2D}}(z_L)$ and $\delta_\eta^{\mathrm{2D}}(L-z_L) = -\delta_\eta^{\mathrm{2D}}(z_L)$ with respect to the plane of symmetry $z_L = L/2$ of the chosen (here $m=1$) cavity mode. This argument can be generalized for any mode $m>1$. As we have shown in our recent Ref. [6], in contrast to Eq. 3.127, *this leads finally to a cancellation of all odd contributions in $\mathcal{R}$ in the expression of $\delta_\eta^{\mathrm{3D}} \propto \mathcal{R}^2$ and to the symmetry relation*

$$\delta_\eta^{\mathrm{3D}}(\chi(z_L)) = \delta_\eta^{\mathrm{3D}}(-\chi(z_L)), \tag{3.129}$$

and thus to no discrimination of the LP and UP upon switching molecular chirality. We note that this behavior is consistent with our previous Refs. [86, 87] where we have shown in the framework of classical Maxwell equations the absence of cavity-amplified chiroptical signals emerging at normal incidence of a 3D bulk cavity made of normal metallic mirrors. *The emerging antisymmetry properties encoded in Eq. 3.127 of the computed differential δ_η-signals upon reducing dimensionality of the cavity-embedded molecular ensemble from 3D to 2D is one of the main results of the present investigations, and was reported for the first time in our recent Ref. [6].*

3.4.4 Analogous classical model in dimension 2+1

Derivation of the classical equations of motion.

In this section, we analyze the classical limit for the previous model of 2D-layer aggregate embedded inside a Fabry-Pérot cavity derived in Sec. 3.4.2. Similarly to the approach developed in the previous Sec. 3.3.3, we introduce the conjugated position and momentum variables defined as

$$q_{x(y)} = \sqrt{\frac{\hbar}{2\omega_c}}\left(a_{x(y)} + a^\dagger_{x(y)}\right), \tag{3.130}$$

$$p_{x(y)} = \sqrt{\frac{\hbar\omega_c}{2}}\frac{a_{x(y)} - a^\dagger_{x(y)}}{i}, \tag{3.131}$$

$$Q = \sqrt{\frac{\hbar}{2\Delta}}\left(B + B^\dagger\right), \tag{3.132}$$

$$P = \sqrt{\frac{\hbar\Delta}{2}}\frac{B - B^\dagger}{i}, \tag{3.133}$$

and associated to the two polarization states $q_{\alpha=x,y}$ of the cavity mode and to the collective excitonic polarization Q of the molecular ensemble. In the classical limit, we can map the $H^{(\mathrm{2D})}_{\mathrm{bos}}$ Hamiltonian written in Eq. 3.110 into the following classical Hamiltonian, considering that all conjugated variables $(q_x, q_y, Q, p_x, p_y, P)$ are commuting variables

$$\begin{aligned} H^{(\mathrm{cl})}_{\mathrm{2D}} &= \left[\frac{\|\vec{p}_\perp\|^2}{2} + \frac{\omega_c^2}{2}\|\vec{q}_\perp\|^2\right] + \left[\frac{P^2}{2} + \frac{\Delta^2}{2}Q^2\right] \\ &+ \left[\omega_P\vec{u}_\perp\cdot\vec{p}_\perp Q + \left(\vec{\Omega}_g\times\vec{v}_\perp\right)\cdot\vec{q}_\perp P\right] + \frac{\omega_P^2}{2}\|\vec{u}_\perp\|^2 Q^2, \end{aligned} \tag{3.134}$$

with the quantities defined by

$$\omega_P = 2\sqrt{\frac{N\Delta}{\omega_c}}g, \tag{3.135}$$

$$\vec{\Omega}_g = \Omega_g\vec{e}_z = \mathcal{R}\frac{\omega_c}{\Delta}\omega_P\vec{e}_z. \tag{3.136}$$

The classical Hamilton equations of motion resulting from Eq. 3.134 are readily obtained as

$$\dot{\vec{q}}_\perp = \vec{p}_\perp + \omega_P Q\vec{u}_\perp, \tag{3.137}$$

$$\dot{Q} = P + \left(\vec{\Omega}_g\times\vec{v}_\perp\right)\cdot\vec{q}_\perp, \tag{3.138}$$

$$\dot{\vec{p}}_\perp = -\omega_c^2\vec{q}_\perp - \left(\vec{\Omega}_g\times\vec{v}_\perp\right)P, \tag{3.139}$$

$$\dot{P} = -\Delta^2 Q - \omega_P\vec{u}_\perp\cdot\vec{p}_\perp - \omega_P^2\|\vec{u}_\perp\|^2 Q. \tag{3.140}$$

From the former equations, *one can derive classical Newton equation of motions for the* $(\vec{q}_\perp, Q)$ *coordinates alone* and obtain the following system of coupled linear equations

$$\ddot{Q} = -\Delta^2 Q - \left(\omega_P\vec{u}_\perp - \vec{\Omega}_g\times\vec{v}_\perp\right)\cdot\dot{\vec{q}}_\perp, \tag{3.141}$$

$$\ddot{\vec{q}}_\perp = -\omega_c^2\vec{q}_\perp + \left(\vec{\Omega}_g\times\vec{v}_\perp\right)\left[\left(\vec{\Omega}_g\times\vec{v}_\perp\right)\cdot\vec{q}_\perp\right] + \left(\omega_P\vec{u}_\perp - \vec{\Omega}_g\times\vec{v}_\perp\right)\dot{Q}. \tag{3.142}$$

Eigenmodes of the Newton equations.

We look for Fourier eigenmodes

$$\vec{q}_\perp(t) = \vec{q}_\perp(\omega)e^{-i\omega t}\,, \tag{3.143}$$
$$Q(t) = Q(\omega)e^{-i\omega t}\,, \tag{3.144}$$

of the Newton equations Eqs. 3.141,3.142, thus leading to a system of three coupled linear equations for the Fourier amplitudes

$$\left(\omega^2-\Delta^2\right)Q(\omega)+i\omega\left(\omega_P\vec{u}_\perp-\vec{\Omega}_g\times\vec{v}_\perp\right)\cdot\vec{q}_\perp(\omega)=0\,, \tag{3.145}$$
$$\left(\omega^2-\omega_c^2\right)\vec{q}_\perp(\omega)+\left(\vec{\Omega}_g\times\vec{v}_\perp\right)\left[\left(\vec{\Omega}_g\times\vec{v}_\perp\right)\cdot\vec{q}_\perp(\omega)\right]-i\omega\left(\omega_P\vec{u}_\perp-\vec{\Omega}_g\times\vec{v}_\perp\right)Q(\omega)=0 \tag{3.146}$$

.

Non-trivial solutions for $(\vec{q}_\perp(\omega),Q(\omega))$ are found as zeros of the secular determinant $\Delta_{\rm 2D}^{\rm (cl)}(\omega)$

$$\begin{aligned}\Delta_{\rm 2D}^{\rm (cl)}(\omega) &= \left(\omega^2-\omega_c^2\right)^2\left(\omega^2-\Delta^2\right)-\mathcal{R}^2\omega^2\omega_c^2\frac{\omega_P^4}{\Delta^2}\left(\vec{u}_\perp\cdot\vec{v}_\perp\right)^2\\ &- \frac{\omega_P^2}{\Delta}\left(\omega^2-\omega_c^2\right)\left\{\Delta\left\|\vec{u}_\perp\right\|^2\omega^2+2\mathcal{R}\omega^2\omega_c\vec{e}_z\cdot\left(\vec{u}_\perp\times\vec{v}_\perp\right)+\mathcal{R}^2\Delta\omega_c^2\left\|\vec{v}_\perp\right\|^2\right\}\,.\end{aligned} \tag{3.147}$$

Considering that $\omega_P^2=4\Delta\Omega_R^2/\omega_c$, it is simple to show that the secular determinant $\Delta_{\rm 2D}^{\rm (cl)}(\omega)$ in Eq. 3.147 is the same as the characteristic polynomial $P(\omega)$ of the Hopfield-matrix written in Eq. 3.121. *Thus both problems have the same eigensolutions and describe the same collective polariton spectra given by the analytical formula Eq. 3.122 derived in Sec. 3.4.3.* As in the previous Sec. 3.3.3, we find again the remarkable fact that the solution of the harmonic quantum Hamiltonian problem provides the same polaritonic spectra as the solution of the classical coupled-mode problem derived in this section. This is again a consequence of the harmonic approximation made in the $H_{\rm bos}^{\rm (2D)}$ Hamiltonian in Eq. 3.110 that is quadratic in the matter and cavity mode fields.

Interpretation of the classical Newtonian dynamics.

We provide in this paragraph a physical interpretation of the Newton Eqs. 3.141,3.142 describing the dynamics of the polarization states of the cavity-mode $(q_x(t),q_y(t))$ coupled to the collective excitonic state of polarization $Q(t)$. For that purpose, we introduce the vector

$$\vec{x}(t) = q_x(t)\vec{e}_x+q_y(t)\vec{e}_y+Q(t)\vec{e}_z\,, \tag{3.148}$$

associated to *the motion of a fictitious classical mobile of unit mass and unit charge. This mobile is subject to effective forces and its dynamics is solution of the following Newton equation* that is equivalent to Eqs. 3.141,3.142) but written in vectorial form and restoring the z-dependence of the involved physical quantities due to the cavity mode lineshape

$$\ddot{\vec{x}}(t) = -\underline{\underline{k}}_{\mathcal{R}}\vec{x}(t)+\dot{\vec{x}}(t)\times\vec{B}_{\mathcal{R}}\,. \tag{3.149}$$

with $\underline{\underline{k}}_{\mathcal{R}} = \text{diag}\left(\omega_c^2, \omega_c^2, \Delta^2\right) + \delta\underline{\underline{k}}_{\mathcal{R}}$ *a spring tensor corresponding to an anisotropic elastic restoring force* where

$$\delta\underline{\underline{k}}_{\mathcal{R}} = 4\frac{\omega_c}{\Delta}\mathcal{R}^2\Omega_R^2\cos^2\left(\theta_{z_L}\right)\begin{bmatrix} -v_y^2 & v_x v_y & 0 \\ v_x v_y & -v_x^2 & 0 \\ 0 & 0 & 0 \end{bmatrix}. \tag{3.150}$$

The particle is also subject to a Lorentz force with the effective magnetic field

$$\vec{B}_{\mathcal{R}} = -2\sqrt{\frac{\Delta}{\omega_c}}\vec{e}_z \times \vec{\Omega}_{\text{P},\mathcal{R}} \tag{3.151}$$

$$\vec{\Omega}_{\text{P},\mathcal{R}} = \Omega_R\left\{\sin\left(\theta_{z_L}\right)\vec{u}_\perp - \mathcal{R}\frac{\omega_c}{\Delta}\cos\left(\theta_{z_L}\right)\vec{e}_z \times \vec{v}_\perp\right\}, \tag{3.152}$$

with $\vec{\Omega}_{\text{P},\mathcal{R}}$ the precession vector. In absence of gyrotopic coupling ($\mathcal{R} = 0$) the spring tensor $\underline{\underline{k}}_0$ is diagonal and encodes free oscillations of the $q_{\alpha=x,y}(t)$ and $Q(t)$ modes at respective frequencies ω_c and Δ. The $\vec{B}_0$ field $\propto \Omega_R\vec{e}_z \times \vec{u}_\perp$ stands for *a Larmor-like precession due to the molecules-cavity electric dipole interactions that dominate upon entering the standard ultrastrong coupling regime*, as already obtained in Sec. 3.3.3. At finite values of $\mathcal{R}$, *magnetic dipole interactions induce a correction to the $\vec{B}_{\mathcal{R}}$-field $\propto \mathcal{R}\Omega_R\vec{v}_\perp$ at the origin of gyrotropic coupling.* The $\delta\underline{\underline{k}}_{\mathcal{R}}$-tensor is of lower order $\propto \mathcal{R}^2$ and encodes for a negligible renormalization of ω_c and elastic coupling between the cavity modes.

A preliminary conclusion. *The previous analogy between the problem of computing the polaritonic spectra for a 2D-layer of chiral molecules embedded inside an optical cavity and the problem of the dynamics of a classical mobile in dimension 2+1, is the main result of this section.* It is extremely simple and elegant. In particular, the emergence of an effective Lorentz-force in Eq. 3.151 is a peculiarity of dimension 3, which arises because we considered here i) only two cavity modes coupling at normal incidence to the molecular ensemble, and ii) a 2D-layer configuration of coupled molecules inside cavity. The 2D-layer configuration is a simple case where the effective Lorentz-force has some effect on the topology in the classical trajectories describing the dynamics of the polaritons. The case of 3D-bulk configuration is more complicated and was studied in detailed in our Ref. [6]. The Newton Eqs. 3.149 are integrable. *Their solution is a linear combination of three eigenmodes of frequencies coinciding with the Hopfield polaritonic spectra in Eq. 3.122 thus confirming the essential classical nature of the polaritons* [124, 62]. We also note that Eq. 3.149 shows similarities (although being not the same) with the dynamics of an harmonically trapped and rotating Bose gaz [103].

3.4.5 Analysis of the analogous classical trajectories

Analytical solution for the trajectories

We rewrite the Newton Eqs. 3.141,3.142 with a simpler notation $x(t) = q_x(t)$, $y(t) = q_y(t)$ and $z(t) = Q(t)$. In the limit $\mathcal{R} \ll 1$, they can be simplified to obtain the following system

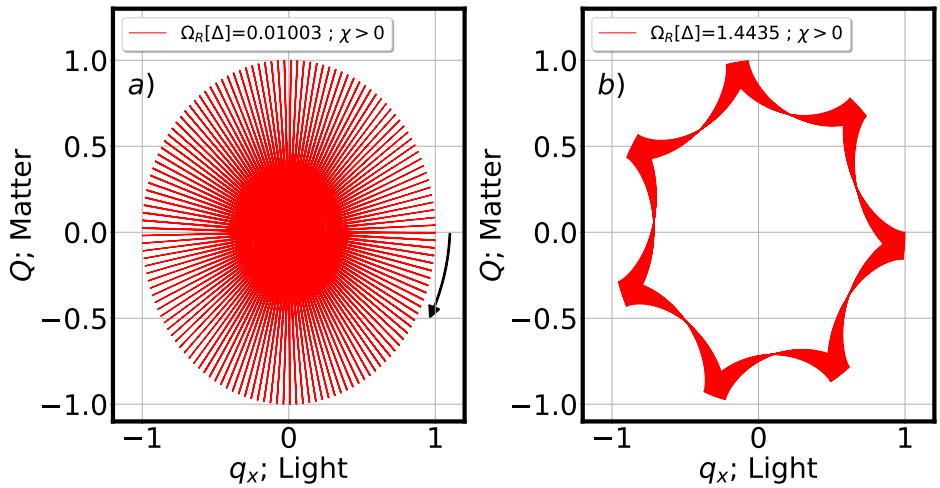

Figure 3.13: a) Plot of the classical trajectory $(q_x(t), q_y(t), Q(t))$ in the plane (q_x, Q), that is solution of Newton Eq. 3.149 during the time interval $t \in [0, 1280/\Delta]$. The collective vacuum Rabi splitting is $\Omega_R \approx 0.01$ and the gyrotropic coupling $\chi(z_L) = \frac{\mathcal{R}}{\sqrt{2}}$. b) Same plot but with $\Omega_R \approx 1.44$ and during time $t \in [0, 700/\Delta]$. Parameters are: $\Delta = 1.0$, $\omega_c = 1.0$, $m = 1$, $u_z = v_z = 0$, $\alpha_u = 0.0$, $\alpha = \frac{\pi}{4}$, $\mathcal{R} = 10^{-3}$, $z_L = \frac{L}{4}$, $q_x(0) = 1.0$, $q_y(0) = Q(0) = 0.0$, and $\dot{q}_x(0) = \dot{q}_y(0) = \dot{Q}(0) = 0.0$. Adapted from our Ref. [6].

of linear equations describing the motion of the fictive particle

$$\ddot{x}(t) \approx -\omega_c^2 x(t) + \Omega \cos(\beta)\, \dot{z}(t)\,, \tag{3.153}$$
$$\ddot{y}(t) \approx -\omega_c^2 y(t) + \Omega \sin(\beta)\, \dot{z}(t)\,, \tag{3.154}$$
$$\ddot{z}(t) \approx -\Delta^2 z(t) - \Omega \{\cos(\beta)\, \dot{x}(t) + \sin(\beta)\, \dot{y}(t)\}\,, \tag{3.155}$$

where we introduced the vector

$$\vec{\Omega} \equiv \Omega \{\cos(\beta)\, \vec{e}_x + \sin(\beta)\, \vec{e}_y\} = \omega_P \vec{u}_\perp - \vec{\Omega}_g \times \vec{v}_\perp\,, \tag{3.156}$$

as *a sum of one contribution due the electric transition-dipole and one due to the magnetic transition-dipole.* After doing a rotation of angle β in the plane (x, y), the linear system of Eqs. 3.153,3.154,3.155 can be simplified in the rotated frame (X, Y, z)

$$\ddot{X}(t) = -\omega_c^2 X(t) + \Omega \dot{z}(t)\,, \tag{3.157}$$
$$\ddot{z}(t) = -\Delta^2 z(t) - \Omega \dot{X}(t)\,, \tag{3.158}$$
$$\ddot{Y}(t) = -\omega_c^2 Y(t)\,. \tag{3.159}$$

We see that the $Y(t)$-mode in Eq. 3.159 decouples from the other $(X(t), z(t))$-modes. The $Y(t)$-mode is thus a free running sinusoidal oscillation at frequency ω_c. In the following, we will focus on the case $\omega_c = \Delta$ for which the classical trajectories are simpler to analyze. We introduce the complex variable $\xi(t) = X(t) + iz(t)$, which after using Eqs. 3.157,3.158, follows the simple differential equation

$$\ddot{\xi}(t) = -i\Omega \dot{\xi}(t) - \omega_c^2 \xi(t)\,. \tag{3.160}$$

This equation can be solved exactly as

$$\xi(t) \;=\; e^{-i\frac{\Omega}{2}t}\left\{\xi(0)\left[\cos\left(\tilde{\omega}_c t\right)+i\frac{\Omega}{2\tilde{\omega}_c}\sin\left(\tilde{\omega}_c t\right)\right]+\frac{\dot{\xi}(0)}{\tilde{\omega}_c}\sin\left(\tilde{\omega}_c t\right)\right\}. \tag{3.161}$$

with the renormalized cavity frequency $\tilde{\omega}_c$, provided by

$$\tilde{\omega}_c \;=\; \sqrt{\omega_c^2+\left(\frac{\Omega}{2}\right)^2}. \tag{3.162}$$

In the following, we use the initial conditions $x(0)=1$, $y(0)=z(0)=0$, $\dot{x}(0)=\dot{y}(0)=\dot{z}(0)$ and a direction of the electric transition dipole along the x-axis $\vec{u}=\vec{e}_x$ for which the rotation angle vanishes $\beta\approx 0$ in the limit $\mathcal{R}\ll 1$. For arbitrary initial conditions, the obtained classical trajectories can be quite complex: *they are indeed quasiperiodic and bounded (for nonvanishing restoring force) but not closed [5], unless some specific commensurate values of the eigenmode frequencies are chosen.* From the solved time dependence of $\xi(t)$ in Eq. 3.161, we can find exact expressions for the rotated-variables $(X(t),z(t))$ and obtain from it *an exact analytical solution for the trajectory* $(x(t),y(t),z(t))$ *of the fictive mobile in the non-rotated frame* as

$$x(t) \;=\; \cos\left(\frac{\Omega t}{2}\right)\cos\left(\tilde{\omega}_c t\right)+\frac{\Omega}{2\tilde{\omega}_c}\sin\left(\frac{\Omega t}{2}\right)\sin\left(\tilde{\omega}_c t\right), \tag{3.163}$$

$$y(t) \;=\; 0\,, \tag{3.164}$$

$$z(t) \;=\; -\sin\left(\frac{\Omega t}{2}\right)\cos\left(\tilde{\omega}_c t\right)+\frac{\Omega}{2\tilde{\omega}_c}\cos\left(\frac{\Omega t}{2}\right)\sin\left(\tilde{\omega}_c t\right). \tag{3.165}$$

Analogy with the Foucault pendulum ($\Omega\ll\omega_c$)

Precession of the effective Foucault pendulum. We then consider the regime of weak light-matter interactions for which $\Omega\ll\omega_c$ in which case $\tilde{\omega}_c\approx\omega_c$ in Eq. 3.162. Neglecting the terms of order Ω/ω_c in Eqs. 3.163,3.165, the latter equations can by simplified to

$$x(t) \;\approx\; \cos\left(\omega_c t\right)\cos\left(\frac{\Omega t}{2}\right), \tag{3.166}$$

$$y(t) \;=\; 0.0\,, \tag{3.167}$$

$$z(t) \;\approx\; -\cos\left(\omega_c t\right)\sin\left(\frac{\Omega t}{2}\right). \tag{3.168}$$

Those equations describe beating oscillations in the (x,z)-plane at a fast frequency $\approx\omega_c$, together with a slow precession frequency $\Omega_{\rm P}\equiv\Omega/2=\left\|\vec{\Omega}_{\rm P,\mathcal{R}}\right\|$ given by the norm of the precession vector $\vec{\Omega}_{\rm P,\mathcal{R}}$ already introduced after Eq. 3.152

$$\Omega_{\rm P} \;=\; \frac{\omega_P}{2}\left\|\vec{u}_\perp\right\|\left\{1+\mathcal{R}\frac{\vec{e}_z\cdot\left(\vec{u}\times\vec{v}\right)}{\left\|\vec{u}_\perp\right\|^2}\right\}. \tag{3.169}$$

In this regime, both the equations of motion, and the obtained trajectories thus get equivalent to the ones describing the motion of a Foucault pendulum located at the North pole: in this analogy, the oscillation frequency of the pendulum is played by the cavity-frequency ω_c, while its precession frequency due to the earth rotation becomes $\Omega_{\rm P}$ in the effective model.

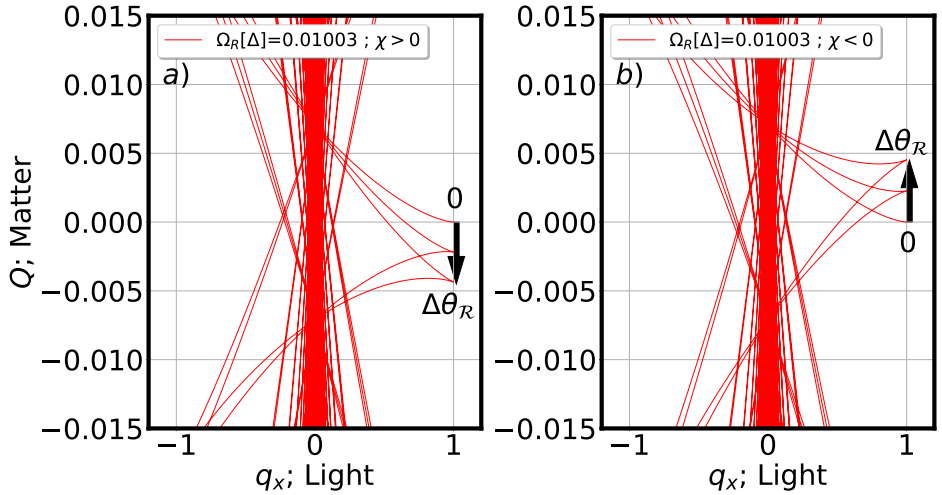

Figure 3.14: Same plots as in Fig. 3.13-a). a) Case with $\alpha = \frac{\pi}{4}$ and $\chi(z_L) = \frac{\mathcal{R}}{\sqrt{2}} > 0$. The black arrow shows the anholonomy angle $\Delta\theta_{\mathcal{R}} \approx \Delta\Delta\theta_{\mathcal{R}} > 0$ given by Eq. 3.170 for this range of parameters. b) Case with $\alpha = \frac{5\pi}{4}$ and opposite $\chi(z_L) = -\frac{\mathcal{R}}{\sqrt{2}} < 0$. The angle $\Delta\theta_{\mathcal{R}} < 0$ reverses sign. All the other parameters are those of Fig. 3.13-a). Adapted from our Ref. [6].

Anholonomy of the classical trajectories. We show in Fig. 3.13-a) the obtained trajectory corresponding to Eqs. 3.166,3.167,3.168 for a gyrotropic coupling $\chi_(z_L) > 0$. As expected by the above analysis, the effective pendulum trajectory lies in the (x, y) and rotates clockwise (black arrow) from the initial point $\vec{x}(0) = (1, 0, 0)$ with a slow precession frequency give by $\Omega_{\rm P}$ in Eq. 3.169. *Waiting for times larger than the precession time ($t \gg 2\pi/\Omega_{\rm P}$), the trajectory of the classical mobile becomes dense in the plane (q_x, Q) due to its already noticed quasiperiodic nature.* In order to unveil the role of gyrotropic coupling on the previous trajectories, we show in Fig. 3.14 a zoom of Fig. 3.13-a) close to the region $Q = 0$. The initial point $\vec{x}(0)$ is labeled 0 and the black arrow visualizes the change in angle $\Delta\theta_{\mathcal{R}}$ of the inertial plane of oscillations after one full precession of the fictitious Foucault pendulum. *The latter Hannay's angle [57] is a signature of anholonomy of the pendulum trajectory, namely of its property to not come back to its initial condition after one complete precession.* This anholonomy of classical trajectories has some deep topological meaning [17, 18, 2, 34]. *We define the relative change in Hannay's angle $\Delta\Delta\theta_{\mathcal{R}} = \Delta\theta_{\mathcal{R}} - \Delta\theta_0$ as a quantitative measure of the gyrotropic coupling contribution to $\Delta\theta_{\mathcal{R}}$ that follows from a bit faster (slower) precession frequency due to positive (negative) $\chi(z_L)$.* We choose parameters such that $|\Delta\theta_0| \ll |\Delta\Delta\theta_{\mathcal{R}}|$ and visualize directly the quantity $\Delta\Delta\theta_{\mathcal{R}} \approx \Delta\theta_{\mathcal{R}}$ for which the following analytical expression is derived from Eq. 3.169. Restoring the z-dependence of the physical quantities induced by the cavity mode lineshape, we obtain

$$\Delta\Delta\theta_{\mathcal{R}} \;=\; 2\pi\mathcal{R}\,\mathrm{cotan}\,(\theta_{z_L})\,\frac{\vec{e}_z\cdot(\vec{u}\times\vec{v})}{\|\vec{u}_\perp\|^2}\,. \tag{3.170}$$

Using Eq. 3.123, we see that $\Delta\Delta\theta_{\mathcal{R}}$ is directly proportional to the gyrotropic coupling parameter $\chi(z_L)$, namely that

$$\Delta\Delta\theta_{\mathcal{R}} \;=\; \pi\chi(z_L)/\,\|\vec{u}_\perp\|^2\sin^2(\theta_{z_L})\,. \tag{3.171}$$

This relation is a major result first derived in our Ref. [6]. It connects the differential shift in the polaritonic spectra induced by gyrotropic coupling to the variation of anholonomy angle of the classical trajectories in the analogous classical model. We check in Fig. 3.14-a) that $\Delta\Delta\theta_{\mathcal{R}} > 0$ when $\chi(z_L) > 0$, while in Fig. 3.14-b) $\Delta\Delta\theta_{\mathcal{R}} < 0$ reverses sign upon sign reversal of $\chi(z_L) < 0$.

Entering the ultrastrong coupling regime $(\Omega \geq \omega_c)$

Analogy to a Spirograph drawing game. We show in Fig. 3.13-b) the classical mobile trajectories for higher values of the collective vacuum Rabi coupling $\Omega_R \approx 1.4\omega_c > \omega_c$. In this regime the trajectories are dramatically modified compared to those of the weak coupling regime. Indeed, *the analogy with a Foucault pendulum breaks down and the approximate Eqs. 3.166,3.167,3.168 do not capture well the presence of cusp singular points in the trajectories* present in both Fig. 3.13-b) and Fig. 3.14. To obtain them, one needs to push the calculation in Eqs. 3.163,3.164,3.165 beyond the lowest order in $\Omega/2\omega_c$. Actually, as shown in Fig. 3.13-b), *in the ultrastrong coupling regime, the classical dynamics of the fictive particle exhibits cyclotron gyrations around the direction of the effective $\vec{B}_{\mathcal{R}}$ magnetic field written in Eq. 3.151.* We thus come back to the analysis of the exact Eqs. 3.163,3.164,3.165 describing the mobile trajectory. They can be rewritten in the following canonical form

$$x(\theta) = r\left\{(q-1)\cos(\theta) + \cos\left[(q-1)\theta\right]\right\}, \tag{3.172}$$

$$y(\theta) = 0.0, \tag{3.173}$$

$$z(\theta) = r\left\{(q-1)\sin(\theta) - \sin\left[(q-1)\theta\right]\right\}, \tag{3.174}$$

where we introduced the (θ, r, q) parameters

$$\theta = \left(\tilde{\omega}_c - \frac{\Omega}{2}\right)t, \tag{3.175}$$

$$r = \frac{1}{2}\left\{1 - \frac{\Omega}{2\tilde{\omega}_c}\right\}, \tag{3.176}$$

$$q = \frac{2}{1 - \frac{\Omega}{2\tilde{\omega}_c}}. \tag{3.177}$$

In this form, Eqs.3.172,3.174 are particularly transparent and provide an accurate description of the classical trajectories in the full range of parameters investigated in our recent Ref.[6]. They describe an hypocycloid trajectory [1] *in the (x, z)-plane*, with a radius $R = 1$ of the external fixed-circle provided by the choice of initial conditions and conservation of mechanical energy (the $\vec{B}_{\mathcal{R}}$-field does not work), and a radius $r = R/q$ of the internal moving-circle. The angle θ describes an oscillation at angular frequency $\tilde{\omega}_c - \frac{\Omega}{2}$, while the parameter $q = R/r$ is the ratio between the radius of the fixed-circle and the moving-circle. *Interestingly the trajectory of the effective classical mobile can be obtained with a Spirograph drawing game* (see Ref. [56] as an illustration). It is remarkable that the complex physics of polaritons in presence of chiral light-matter interactions could be mapped onto a simple drawing game played by children: this appeared to me as a source of wonder and joy !

[1] See for instance `https://mathcurve.com/courbes2d/hypocycloid/hypocycloid.shtml` for graphical illustrations and selected animations of hypocycloid curves, with some of their mathematical properties.

Topology and cusp singularities of the trajectory. *The hypocycloid trajectory of the fictive mobile derived above takes place inside a ring-manifold* with big-circle of radius R and low-circle of radius $R_{\min} = R - 2r$ given by

$$R_{\min} \;=\; \frac{\Omega}{2\tilde{\omega}_c}\,. \tag{3.178}$$

This dimensionless parameter contains both effects of the light-matter coupling-strength and the chiral-coupling encoded in Eq. 3.169. In the weak-coupling regime ($\Omega \ll \omega_c$), the lower-circle of the ring has a vanishing radius $R_{\min} \approx 0$ and thus converges to a single point at the center of the fixed-circle, recovering the trajectory of a precessing Foucault pendulum as shown in Fig. 3.13-a). In the deep ultrastrong coupling regime ($\Omega \gg \omega_c$ and $\tilde{\omega}_c \approx \Omega/2$), the lower-circle of the ring gets close to the fixed-circle with a radius $R_{\min} \approx 1$: the mobile thereby undergoes cyclotron gyrations around the direction of the effective $\vec{B}$-field, with a radial velocity $\approx \Omega/2$. In the ultrastrong coupling regime ($\Omega \geq \omega_c$), the trajectory takes the form of a developed hypocycloid as shown in Fig. 3.13-b). *The hole at the center of this ring manifold spanned by the trajectory at long times is thus a striking topological signature of entering the strong coupling regime for light-matter interactions.* To close this study, it is interesting to notice that the cusp singularities of the hypocycloid curves are achieved at times $t_k \geq 0$ given by the expression

$$t_k \;=\; \frac{k}{q}\frac{2\pi}{\tilde{\omega}_c - \frac{\Omega}{2}};\; k \in \mathbb{N}\,. \tag{3.179}$$

The trajectory is thus closed, namely it comes back to its initial point, if and only if q is a rational number ($q \in \mathbb{Q}$ with $q \geq 2$). The latter condition imposes the following constraint on Ω/ω_c

$$\frac{\Omega}{2\omega_c} \;=\; \frac{q-2}{2\sqrt{q-1}};\; q \in \mathbb{Q} \cap [2, +\infty[\;. \tag{3.180}$$

If q is an irrational number, the trajectories are not closed and thus fill the ring manifold in a dense-way as a result of the quasi-periodic nature of the trajectories [5].

3.5 Conclusion and future research perspectives

Conclusion. In this chapter, we have investigated several aspects of the light-matter strong-coupling regime developing inside optical Fabry-Pérot cavities. The basic concepts and theoretical tools were derived for understanding and computing the polaritonic spectra measured at normal incidence out of the cavity: *the former excitations result from the hybridization between the electronic properties of the molecular material embedded inside cavity and the cavity electromagnetic modes.* We have shown *the crucial role played by the dimensionality of the cavity-embedded molecular aggregate* when dealing with the the polaritonic spectra generated by chiral molecules. We predicted that, when the coupled molecules are arranged in a mesoscopic 2D chiral layer, *the emergence of a gyrotropic coupling between the chiral molecules and the cavity modes is at the origin of a differential shift of the polaritonic spectra that become enantiodependent.* The latter effect results from a subtle interplay

between the orientations, the enantiomeric class of the chiral molecules, and the spatial distribution of the cavity modes profile along the optical z-axis. For macroscopic 3D chiral bulk samples, such differential shift disappears. We interpreted this 2D chiral effect by developing an analogous classical Newtonian model in dimension 2+1. *We have shown that the molecular gyrotropic coupling is directly responsible for a perturbation of the anholonomy angle of the analogous classical trajectories.* The predicted differential polaritonic signals while very weak could in principle be observed with state-of-the-art optical spectroscopy [48]. We anticipate the latter signals to be robust to partial orientational disorder but to be destroyed upon full rotational averaging of the molecular orientations. *We hope that our work will stimulate new theoretical efforts to find and analyze the nature and topology of analogous classical models of chiral light-matter interactions like the present one.* Such efforts would thereby lead to revisiting our current interpretations of materials chiroptical properties in the ultrastrong coupling regime.

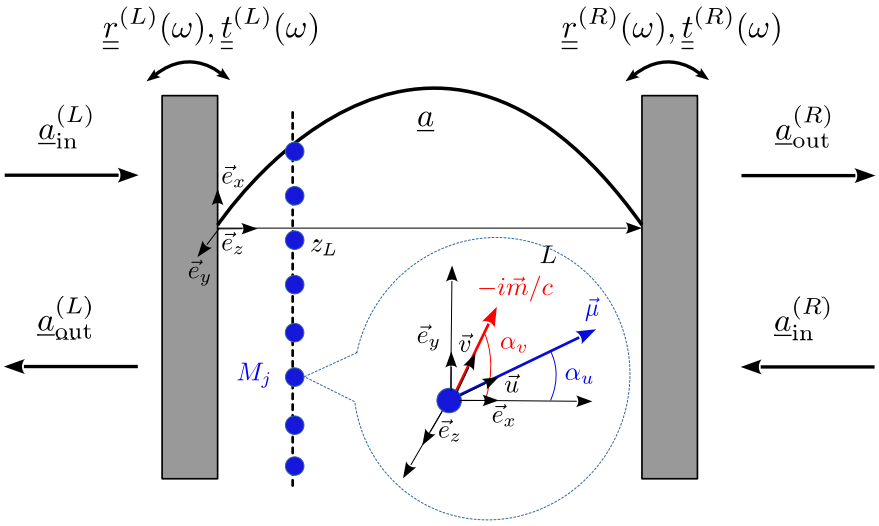

Figure 3.15: Prospective figure showing the same optical Fabry-Pérot cavity as in Fig. 3.11 in which a 2D-layer of chiral molecules interacts with one or several cavity modes. The finite reflection and transmission coefficients of the left L and right R mirrors are taken into account thanks to the polarization and frequency dependent matrices $\left\{\underline{\underline{r}}^{(\mathrm{L(R)})}(\omega), \underline{\underline{t}}^{(\mathrm{L(R)})}(\omega)\right\}$. An input optical signal $\underline{a}_{\rm in}^{(\mathrm{L(R)})}$ with given polarization content enters the cavity through the L(R) mirror and goes out as an output signal $\underline{a}_{\rm out}^{(\mathrm{L(R)})}$ after coupling to the states of polarization of the cavity mode $\underline{a}$. Unpublished Fig.

Future research perspectives. We provide here several prospective roads for future research works devoted to investigating chiral light-matter interactions developing inside optical cavities, following the lines we proposed in this chapter. The main open issues which, we think, are of great interest for the field of chiral polaritonics are the following

1. How to characterize formally in a deeper mathematical way the connection between the topology of classical trajectories and the underlying polariton formation under cavity-induced chiral light matter interactions ? *This could probably be done in general*

cases by deriving a Berry curvature associated to the electromagnetic gauge field both in the initial quantum mechanical model and in the equivalent classical model.

2. Are there some more general way of thinking about *the symmetries and conservation laws (like conservation of orbital angular momentum and spin) of the coupled entity made of interacting quantum cavity modes and collective and delocalized electronic excitons of the 2D-layer chiral material?* While many works analyze chiroptical features of materials or of the electromagnetic field itself separately, very few works have been done to clarify what happens for the case of strongly coupled polaritonic materials embedded inside optical cavities.

3. *What is the role of dissipation and fluctuations induced by finite losses of the cavity and of the material embedded inside ?* Do they have an effect on the crossover from weak to strong light-matter coupling regimes, like introducing a threshold effect or the emergence of exceptional points ?

4. *What is the connection between the computed polaritonic spectra and the chiroptical signals that are actually measured in a real experiment ?* How to compute experimentally relevant signals from the output of the existing quantum mechanical model of chiral light-matter interactions (which is intrinsically a closed system) ?

5. *Is it possible to propose chiral electromagnetic environments generated by the cavity in order to modify the chemical reactivity and enantioselectivity of chemical reactions* for materials embedded inside a Fabry-Pérot cavity in the strong coupling regime ?

Those questions are all open either from the side of theory or of experiments. Those are quite hard ones and it seems at first sight quite difficult to propose any significant progress along those directions. Regarding the points number 3,4, however, there is a way out which is illustrated in Fig. 3.15. Indeed, to connect our work to actual experiments, *one needs to "open the system" and take into account the coupling of the electromagnetic modes of the cavity to the external electromagnetic environment through the left L and right R mirror.* This can be done through the polarization and energy dependent reflection and transmission matrices characterizing those mirrors $\left\{\underline{\underline{r}}^{(\mathrm{L(R)})}(\omega), \underline{\underline{t}}^{(\mathrm{L(R)})}(\omega)\right\}$. An input optical signal $\underline{a}_{\mathrm{in}}^{(\mathrm{L(R)})}$ with given polarization content enters the cavity through the L(R) mirror and goes out as an output signal $\underline{a}_{\mathrm{out}}^{(\mathrm{L(R)})}$ after coupling to the states of polarization of the cavity modes $\underline{a}$. *One thus has to write quantum Langevin equations within an "input-output theory" and solve them to find the polarization-dependent chiroptical measurable signals in transmission or reflection out of the cavity.* Those quantum Langevin equations will include by construction dissipation and fluctuations (thermal or quantum) induced by the cavity finite quality factor. *We will pursue such a research project in collaboration with David Haggenmüller (ISIS) and Cyriaque Genet (ISIS) and a future postdoctorate researcher that will be financed by the PEPR LUMA TORNADO national project for that purpose.*

Bibliography

[1] D. Abramavicius et al. “Coherent Multidimensional Optical Spectroscopy of Excitons in Molecular Aggregates; Quasiparticle versus Supermolecule Perspectives”. In: *Chemical Reviews* 109.6 (2009), pp. 2350–2408. DOI: 10.1021/cr800268n. URL: https://doi.org/10.1021/cr800268n.

[2] Jeeva Anandan. “The geometric phase”. In: *Nature* 360.6402 (1992), pp. 307–313. DOI: https://doi.org/10.1038/360307a0.

[3] D.L. Andrews. “A unified theory of radiative and radiationless molecular energy transfer”. In: *Chemical Physics* 135.2 (1989), pp. 195–201. ISSN: 0301-0104. DOI: https://doi.org/10.1016/0301-0104(89)87019-3.

[4] David L Andrews. “Quantum formulation for nanoscale optical and material chirality: symmetry issues, space and time parity, and observables”. In: *Journal of Optics* 20.3 (2018), p. 033003. DOI: 10.1088/2040-8986/aaaa56.

[5] Vladimir Igorevich Arnol’d. *Mathematical methods of classical mechanics*. Vol. 60. Springer Science & Business Media, 2013.

[6] R Avriller and C Genet. “Chirality and dimensionality in the ultrastrong light-matter coupling regime”. In: *arXiv preprint arXiv:2408.01275* (2024). DOI: https://doi.org/10.48550/arXiv.2408.01275.

[7] R. Avriller and A. Levy Yeyati. “Electron-phonon interaction and full counting statistics in molecular junctions”. In: *Phys. Rev. B* 80 (4 July 2009), p. 041309. DOI: 10.1103/PhysRevB.80.041309. URL: https://link.aps.org/doi/10.1103/PhysRevB.80.041309.

[8] R. Avriller, A. Marché, and G. Jonusauskas. “Stochastic dynamics of resonance electronic energy transfer in bidimensional overexcited molecular ensembles”. In: *Phys. Rev. B* 108 (20 Nov. 2023), p. 205419. DOI: 10.1103/PhysRevB.108.205419. URL: https://link.aps.org/doi/10.1103/PhysRevB.108.205419.

[9] R. Avriller et al. “Photon-emission statistics induced by electron tunneling in plasmonic nanojunctions”. In: *Phys. Rev. B* 104 (24 Dec. 2021), p. L241403. DOI: 10.1103/PhysRevB.104.L241403. URL: https://link.aps.org/doi/10.1103/PhysRevB.104.L241403.

[10] Ruth E. Baker and Matthew J. Simpson. “Correcting mean-field approximations for birth-death-movement processes”. In: *Phys. Rev. E* 82 (4 Oct. 2010), p. 041905. DOI: 10.1103/PhysRevE.82.041905.

[11] Denis G. Baranov, Christian Schäfer, and Maxim V. Gorkunov. “Toward Molecular Chiral Polaritons”. In: *ACS Photonics* 10.8 (Aug. 2023), pp. 2440–2455. DOI: 10.1021/acsphotonics.2c02011. URL: https://doi.org/10.1021/acsphotonics.2c02011 (visited on 06/10/2024).

[12] Nico S. Baßler et al. “Metasurface-Based Hybrid Optical Cavities for Chiral Sensing”. In: *Phys. Rev. Lett.* 132 (4 Jan. 2024), p. 043602. DOI: 10.1103/PhysRevLett.132.043602.

[13] A. Bejarano et al. “Photon blockade in current-driven single-molecule emitters”. In: *In preparation* (2025).

[14] A. Bejarano et al. “Single-molecule electroluminescence: crossover from weak to strong coupling”. In: *In preparation* (2025).

[15] D. Beljonne et al. “Beyond Förster Resonance Energy Transfer in Biological and Nanoscale Systems”. In: *The Journal of Physical Chemistry B* 113.19 (2009), pp. 6583–6599. DOI: 10.1021/jp900708f. URL: https://doi.org/10.1021/jp900708f.

[16] Richard Berndt, James K. Gimzewski, and Peter Johansson. “Inelastic tunneling excitation of tip-induced plasmon modes on noble-metal surfaces”. In: *Phys. Rev. Lett.* 67 (27 Dec. 1991), pp. 3796–3799. DOI: 10.1103/PhysRevLett.67.3796. URL: https://link.aps.org/doi/10.1103/PhysRevLett.67.3796.

[17] Michael Berry. “The Geometric Phase”. In: *Scientific American* 259.6 (1988), pp. 46–55. ISSN: 0036-8733. URL: https://www.jstor.org/stable/24989302 (visited on 06/10/2024).

[18] MV Berry. “Quantum adiabatic anholonomy”. In: *Anomalies, phases, defects* (1990), pp. 125–181.

[19] T. Brandes. “Waiting times and noise in single particle transport”. In: *Annalen der Physik* 17.7 (2008), pp. 477–496. DOI: 10.1002/andp.2008103.

[20] H.J. Carmichael et al. “Photoelectron waiting times and atomic state reduction in resonance fluorescence”. In: *Phys. Rev. A.* 39.3 (1989), p. 1200. DOI: 10.1103/PhysRevA.39.1200.

[21] Tzu-Ling Chen et al. “A 2D chiral microcavity based on apparent circular dichroism”. In: *Nature Communications* 15.1 (2024), p. 3072. DOI: https://doi.org/10.1038/s41467-024-47411-4.

[22] M.-C. Chirio-Lebrun and M. Prats. “Fluorescence resonance energy transfer (FRET): theory and experiments”. In: *Biochemical Education* 26.4 (1998), pp. 320–323. ISSN: 0307-4412. DOI: https://doi.org/10.1016/S0307-4412(98)80010-1. URL: https://www.sciencedirect.com/science/article/pii/S0307441298800101.

[23] Michael C. Chong et al. “Narrow-Line Single-Molecule Transducer between Electronic Circuits and Surface Plasmons”. In: *Phys. Rev. Lett.* 116 (3 Jan. 2016), p. 036802. DOI: 10.1103/PhysRevLett.116.036802. URL: https://link.aps.org/doi/10.1103/PhysRevLett.116.036802.

[24] C. Chuang, J. Knoester, and J. Cao. “Scaling Relations and Optimization of Excitonic Energy Transfer Rates between One-Dimensional Molecular Aggregates”. In: *The Journal of Physical Chemistry B* 118.28 (2014), pp. 7827–7834. DOI: 10.1021/jp4124502. URL: https://doi.org/10.1021/jp4124502.

[25] Cristiano Ciuti, Gérald Bastard, and Iacopo Carusotto. “Quantum vacuum properties of the intersubband cavity polariton field”. en. In: *Phys. Rev. B* 72.11 (Sept. 2005), p. 115303. ISSN: 1098-0121, 1550-235X. DOI: 10.1103/PhysRevB.72.115303. URL: https://link.aps.org/doi/10.1103/PhysRevB.72.115303 (visited on 06/10/2024).

[26] C. Cohen-Tannoudji and S. Reynaud. “Atoms in strong light-fields: Photon antibunching in single atom fluorescence”. In: *Phil. Trans. R. Soc. Lond. A* 293.1402 (1979), pp. 223–237. DOI: 10.1098/rsta.1979.0092.

[27] Claude Cohen-Tannoudji, Jacques Dupont-Roc, and Gilbert Grynberg. *Processus d’interaction entre photons et atomes*. EDP sciences, 1996.

[28] E. U. Condon. “Theories of Optical Rotatory Power”. In: *Rev. Mod. Phys.* 9 (4 Oct. 1937), pp. 432–457. DOI: 10.1103/RevModPhys.9.432. URL: https://link.aps.org/doi/10.1103/RevModPhys.9.432.

[29] A. Cottet, T. Kontos, and B. Dou çot. “Electron-photon coupling in mesoscopic quantum electrodynamics”. In: *Phys. Rev. B* 91 (20 May 2015), p. 205417. DOI: 10.1103/PhysRevB.91.205417. URL: https://link.aps.org/doi/10.1103/PhysRevB.91.205417.

[30] D.P. Craig and T. Thirunamachandran. “An analysis of models for resonant transer of excitation using quantum electrodynamics”. In: *Chemical Physics* 167.3 (1992), pp. 229–240. ISSN: 0301-0104. DOI: https://doi.org/10.1016/0301-0104(92)80198-5. URL: https://www.sciencedirect.com/science/article/pii/0301010492801985.

[31] D.P. Craig and T. Thirunamachandran. “Third-body mediation of resonance coupling between identical molecules”. In: *Chemical Physics* 135.1 (1989), pp. 37–48. ISSN: 0301-0104. DOI: https://doi.org/10.1016/0301-0104(89)87004-1. URL: https://www.sciencedirect.com/science/article/pii/0301010489870041.

[32] Jeanne Crassous. “Chiral transfer in coordination complexes: towards molecular materials”. In: *Chemical Society Reviews* 38.3 (2009), pp. 830–845. DOI: https://doi.org/10.1039/B806203J.

[33] G.J. Daniels et al. “Resonance energy transfer: The unified theory revisited”. In: *The Journal of Chemical Physics* 119.4 (2003), pp. 2264–2274. DOI: 10.1063/1.1579677.

[34] Pierre Delplace and Antoine Venaille. arXiv:2006.08488 [astro-ph, physics:cond-mat, physics:physics]. June 2020. DOI: https://doi.org/10.48550/arXiv.2006.08488. URL: http://arxiv.org/abs/2006.08488 (visited on 06/10/2024).

[35] Courtney A DelPo et al. “Polariton decay in donor–acceptor cavity systems”. In: *The Journal of Physical Chemistry Letters* 12.40 (2021), pp. 9774–9782. DOI: 10.1021/acs.jpclett.1c02644.

[36] R. H. Dicke. “Coherence in Spontaneous Radiation Processes”. In: *Phys. Rev.* 93 (1 Jan. 1954), pp. 99–110. DOI: 10.1103/PhysRev.93.99. URL: https://link.aps.org/doi/10.1103/PhysRev.93.99.

[37] C. Didraga, V. A. Malyshev, and J. Knoester. “Excitation Energy Transfer between Closely Spaced Multichromophoric Systems: Effects of Band Mixing and Intraband Relaxation”. In: *The Journal of Physical Chemistry B* 110.38 (2006), pp. 18818–18827. DOI: 10.1021/jp0569281. URL: https://doi.org/10.1021/jp0569281.

[38] Sérgio R. Domingos, Cristóbal Pérez, and Melanie Schnell. “Sensing Chirality with Rotational Spectroscopy”. In: *Annual Review of Physical Chemistry* 69.Volume 69, 2018 (2018), pp. 499–519. ISSN: 1545-1593. DOI: https://doi.org/10.1146/annurev-physchem-052516-050629. URL: https://www.annualreviews.org/content/journals/10.1146/annurev-physchem-052516-050629.

[39] Benjamin Doppagne et al. “Electrofluorochromism at the single-molecule level”. In: *Science* 361.6399 (2018), pp. 251–255. DOI: 10.1126/science.aat1603.

[40] Benjamin Doppagne et al. “Vibronic Spectroscopy with Submolecular Resolution from STM-Induced Electroluminescence”. In: *Phys. Rev. Lett.* 118 (12 Mar. 2017), p. 127401. DOI: 10.1103/PhysRevLett.118.127401. URL: https://link.aps.org/doi/10.1103/PhysRevLett.118.127401.

[41] M. Du et al. “Theory for polariton-assisted remote energy transfer”. In: *Chem. Sci.* 9 (32 2018), pp. 6659–6669. DOI: 10.1039/C8SC00171E.

[42] Thomas W. Ebbesen. “Hybrid Light–Matter States in a Molecular and Material Science Perspective”. In: *Accounts of Chemical Research* 49.11 (2016), pp. 2403–2412. DOI: 10.1021/acs.accounts.6b00295.

[43] Joshua Feis et al. “Helicity-Preserving Optical Cavity Modes for Enhanced Sensing of Chiral Molecules”. en. In: *Phys. Rev. Lett.* 124.3 (Jan. 2020), p. 033201. ISSN: 0031-9007, 1079-7114. DOI: 10.1103/PhysRevLett.124.033201. URL: https://link.aps.org/doi/10.1103/PhysRevLett.124.033201 (visited on 06/10/2024).

[44] Ivan Fernandez-Corbaton, Martin Fruhnert, and Carsten Rockstuhl. “Objects of Maximum Electromagnetic Chirality”. In: *Phys. Rev. X* 6.3 (July 2016), p. 031013. DOI: 10.1103/PhysRevX.6.031013. URL: https://link.aps.org/doi/10.1103/PhysRevX.6.031013 (visited on 04/01/2022).

[45] Kristen A. Fichthorn and W. H. Weinberg. “Theoretical foundations of dynamical Monte Carlo simulations”. In: *The Journal of Chemical Physics* 95.2 (1991), pp. 1090–1096. DOI: 10.1063/1.461138. URL: https://doi.org/10.1063/1.461138.

[46] Th Förster. “Transfer mechanisms of electronic excitation energy”. In: *Radiation Research Supplement* (1960), pp. 326–339. DOI: 10.2307/3583604.

[47] Francisco J. Garcia-Vidal, Cristiano Ciuti, and Thomas W. Ebbesen. “Manipulating matter by strong coupling to vacuum fields”. In: *Science* 373.6551 (2021), eabd0336. DOI: 10.1126/science.abd0336. URL: https://www.science.org/doi/abs/10.1126/science.abd0336.

[48] Jérôme Gautier et al. “Planar Chirality and Optical Spin–Orbit Coupling for Chiral Fabry–Perot Cavities”. en. In: *ACS Photonics* 9.3 (Mar. 2022), pp. 778–783. ISSN: 2330-4022, 2330-4022. DOI: 10.1021/acsphotonics.1c00780. URL: https://pubs.acs.org/doi/10.1021/acsphotonics.1c00780 (visited on 06/10/2024).

[49] C.D. Geddes and J.R. Lakowicz. *Reviews in fluorescence 2006*. Springer, 2006.

[50] Jino George et al. “Multiple Rabi Splittings under Ultrastrong Vibrational Coupling”. In: *Phys. Rev. Lett.* 117.15 (Oct. 2016), p. 153601. DOI: 10.1103/PhysRevLett.117.153601. URL: https://link.aps.org/doi/10.1103/PhysRevLett.117.153601 (visited on 06/10/2024).

[51] K. Georgiou et al. “Ultralong-Range Polariton-Assisted Energy Transfer in Organic Microcavities”. In: *Angewandte Chemie International Edition* 60.30 (2021), pp. 16661–16667. DOI: https://doi.org/10.1002/anie.202105442.

[52] Daniel T Gillespie. “A general method for numerically simulating the stochastic time evolution of coupled chemical reactions”. In: *Journal of Computational Physics* 22.4 (1976), pp. 403–434. ISSN: 0021-9991. DOI: https://doi.org/10.1016/0021-9991(76)90041-3. URL: https://www.sciencedirect.com/science/article/pii/0021999176900413.

[53] Roy J. Glauber. “The Quantum Theory of Optical Coherence”. In: *Phys. Rev.* 130 (6 June 1963), pp. 2529–2539. DOI: 10.1103/PhysRev.130.2529.

[54] Giovanni Gottarelli et al. “The use of circular dichroism spectroscopy for studying the chiral molecular self-assembly: An overview”. In: *Chirality* 20.3-4 (2008), pp. 471–485. DOI: https://doi.org/10.1002/chir.20459. URL: https://onlinelibrary.wiley.com/doi/abs/10.1002/chir.20459.

[55] A. Grimm et al. “Bright On-Demand Source of Antibunched Microwave Photons Based on Inelastic Cooper Pair Tunneling”. In: *Phys. Rev. X* 9 (2 Apr. 2019), p. 021016. DOI: 10.1103/PhysRevX.9.021016. URL: https://link.aps.org/doi/10.1103/PhysRevX.9.021016.

[56] Leon M Hall. “Trochoids, roses, and thorns—beyond the spirograph”. In: *The College Mathematics Journal* 23.1 (1992), pp. 20–35.

[57] J. H. Hannay. “Angle variable holonomy in adiabatic excursion of an integrable Hamiltonian”. en. In: *Journal of Physics A: Mathematical and General* 18.2 (Feb. 1985), p. 221. ISSN: 0305-4470. DOI: 10.1088/0305-4470/18/2/011. URL: https://dx.doi.org/10.1088/0305-4470/18/2/011 (visited on 06/10/2024).

[58] Serge Haroche and Daniel Kleppner. “Cavity Quantum Electrodynamics”. In: *Physics Today* 42.1 (Jan. 1989), pp. 24–30. ISSN: 0031-9228. DOI: 10.1063/1.881201. URL: https://doi.org/10.1063/1.881201.

[59] E. Hennebicq et al. “Shared-mode assisted resonant energy transfer in the weak coupling regime”. In: *The Journal of Chemical Physics* 130.21 (2009), p. 214505. DOI: 10.1063/1.3140273. URL: https://doi.org/10.1063/1.3140273.

[60] G Hoffmann et al. “Influence of tip geometry in light emission from the scanning tunnelling microscope”. In: *Surface science* 482 (2001), pp. 1159–1162.

[61] T. Holstein. “Theory of transport phenomena in an electron-phonon gas”. In: *Annals of Physics* 29.3 (1964), pp. 410–535. ISSN: 0003-4916. DOI: https://doi.org/10.1016/0003-4916(64)90008-9. URL: https://www.sciencedirect.com/science/article/pii/0003491664900089.

[62] J. J. Hopfield. “Theory of the Contribution of Excitons to the Complex Dielectric Constant of Crystals”. en. In: *Phys. Rev.* 112.5 (Dec. 1958), pp. 1555–1567. ISSN: 0031-899X. DOI: 10.1103/PhysRev.112.1555. URL: https://link.aps.org/doi/10.1103/PhysRev.112.1555 (visited on 06/10/2024).

[63] R. Houdré, R. P. Stanley, and M. Ilegems. “Vacuum-field Rabi splitting in the presence of inhomogeneous broadening: Resolution of a homogeneous linewidth in an inhomogeneously broadened system”. In: *Phys. Rev. A* 53 (4 Apr. 1996), pp. 2711–2715. DOI: 10.1103/PhysRevA.53.2711.

[64] James A. Hutchison et al. “Modifying Chemical Landscapes by Coupling to Vacuum Fields”. In: *Angewandte Chemie International Edition* 51.7 (2012), pp. 1592–1596. DOI: https://doi.org/10.1002/anie.201107033.

[65] Hiroshi Imada et al. “Single-Molecule Investigation of Energy Dynamics in a Coupled Plasmon-Exciton System”. In: *Phys. Rev. Lett.* 119 (1 July 2017), p. 013901. DOI: 10.1103/PhysRevLett.119.013901. URL: https://link.aps.org/doi/10.1103/PhysRevLett.119.013901.

[66] Gert-Ludwig Ingold and Yu V Nazarov. “Charge tunneling rates in ultrasmall junctions”. In: *Single charge tunneling: Coulomb blockade phenomena in nanostructures* (1992), pp. 21–107.

[67] John David Jackson. *Classical electrodynamics*. John Wiley & Sons, 2021.

[68] S. Jang, M. D. Newton, and R. J. Silbey. “Multichromophoric Förster Resonance Energy Transfer”. In: *Phys. Rev. Lett.* 92 (21 May 2004), p. 218301. DOI: 10.1103/PhysRevLett.92.218301. URL: https://link.aps.org/doi/10.1103/PhysRevLett.92.218301.

[69] S. Jang, M.D. Newton, and R.J. Silbey. “Multichromophoric Förster Resonance Energy Transfer from B800 to B850 in the Light Harvesting Complex 2: Evidence for Subtle Energetic Optimization by Purple Bacteria”. In: *The Journal of Physical Chemistry B* 111.24 (2007), pp. 6807–6814. DOI: 10.1021/jp070111l. URL: https://doi.org/10.1021/jp070111l.

[70] S. Jang et al. “Theory of coherent resonance energy transfer”. In: *The Journal of Chemical Physics* 129.10 (2008), p. 101104. DOI: 10.1063/1.2977974. URL: https://doi.org/10.1063/1.2977974.

[71] R.D. Jenkins, G.J. Daniels, and D.L. Andrews. “Quantum pathways for resonance energy transfer”. In: *The Journal of Chemical Physics* 120.24 (2004), pp. 11442–11448. DOI: 10.1063/1.1742697. URL: https://doi.org/10.1063/1.1742697.

[72] Song Jiang et al. “Many-Body Description of STM-Induced Fluorescence of Charged Molecules”. In: *Phys. Rev. Lett.* 130 (12 Mar. 2023), p. 126202. DOI: 10.1103/PhysRevLett.130.126202. URL: https://link.aps.org/doi/10.1103/PhysRevLett.130.126202.

[73] Peter Johansson, R. Monreal, and Peter Apell. “Theory for light emission from a scanning tunneling microscope”. In: *Phys. Rev. B* 42 (14 Nov. 1990), pp. 9210–9213. DOI: 10.1103/PhysRevB.42.9210. URL: https://link.aps.org/doi/10.1103/PhysRevB.42.9210.

[74] Stéphane Kéna-Cohen, Stefan A. Maier, and Donal D. C. Bradley. “Ultrastrongly Coupled Exciton–Polaritons in Metal-Clad Organic Semiconductor Microcavities”. In: *Advanced Optical Materials* 1.11 (2013), pp. 827–833. DOI: https://doi.org/10.1002/adom.201300256.

[75] V. M. Kenkre and R. S. Knox. “Generalized-master-equation theory of excitation transfer”. In: *Phys. Rev. B* 9 (12 June 1974), pp. 5279–5290. DOI: 10.1103/PhysRevB.9.5279. URL: https://link.aps.org/doi/10.1103/PhysRevB.9.5279.

[76] Robert S. Knox. “Förster’s resonance excitation transfer theory: not just a formula”. In: *Journal of Biomedical Optics* 17.1 (2012), p. 011003. DOI: 10.1117/1.JBO.17.1.011003. URL: https://doi.org/10.1117/1.JBO.17.1.011003.

[77] Jens Koch and Felix von Oppen. “Franck-Condon Blockade and Giant Fano Factors in Transport through Single Molecules”. In: *Phys. Rev. Lett.* 94 (20 May 2005), p. 206804. DOI: 10.1103/PhysRevLett.94.206804. URL: https://link.aps.org/doi/10.1103/PhysRevLett.94.206804.

[78] Jens Koch, Felix von Oppen, and A. V. Andreev. “Theory of the Franck-Condon blockade regime”. In: *Phys. Rev. B* 74 (20 Nov. 2006), p. 205438. DOI: 10.1103/PhysRevB.74.205438. URL: https://link.aps.org/doi/10.1103/PhysRevB.74.205438.

[79] Manohar Kumar et al. “Detection of Vibration-Mode Scattering in Electronic Shot Noise”. In: *Phys. Rev. Lett.* 108 (14 Apr. 2012), p. 146602. DOI: 10.1103/PhysRevLett.108.146602. URL: https://link.aps.org/doi/10.1103/PhysRevLett.108.146602.

[80] Lev Davidovich Landau et al. *Electrodynamics of continuous media*. Vol. 8. elsevier, 2013.

[81] Christopher C Leon et al. “Single photon emission from a plasmonic light source driven by a local field-induced coulomb blockade”. In: *ACS nano* 14.4 (2020), pp. 4216–4223.

[82] Ismo Lindell et al. *Electromagnetic waves in chiral and bi-isotropic media*. Artech House, 1994.

[83] M.P.E. Lock, D.L. Andrews, and G.A. Jones. “On the nature of long range electronic coupling in a medium: Distance and orientational dependence for chromophores in molecular aggregates”. In: *The Journal of Chemical Physics* 140.4 (2014), p. 044103. DOI: 10.1063/1.4861695. URL: https://doi.org/10.1063/1.4861695.

[84] A. Marché. “Aspect collectif du transfert d’énergie entre molécules”. In: *Unpublished Master 1 thesis, University of Bordeaux* (2022).

[85] F. Mattiotti et al. “Multifractality in the interacting disordered Tavis-Cummings model”. In: *Phys. Rev. B* 109 (6 Feb. 2024), p. 064202. DOI: 10.1103/PhysRevB.109.064202. URL: https://link.aps.org/doi/10.1103/PhysRevB.109.064202.

[86] L. Mauro et al. “Chiral discrimination in helicity-preserving Fabry-Pérot cavities”. en. In: *Phys. Rev. A* 107.2 (Feb. 2023), p. L021501. ISSN: 2469-9926, 2469-9934. DOI: 10.1103/PhysRevA.107.L021501. URL: https://link.aps.org/doi/10.1103/PhysRevA.107.L021501 (visited on 06/10/2024).

[87] L. Mauro et al. “Classical approaches to chiral polaritonics”. en. In: *Phys. Rev. A* 109.2 (Feb. 2024), p. 023528. ISSN: 2469-9926, 2469-9934. DOI: 10.1103/PhysRevA.109.023528. URL: https://link.aps.org/doi/10.1103/PhysRevA.109.023528 (visited on 06/10/2024).

[88] A. J. Miles, Robert W. Janes, and B. A. Wallace. “Tools and methods for circular dichroism spectroscopy of proteins: a tutorial review”. In: *Chem. Soc. Rev.* 50 (15 2021), pp. 8400–8413. DOI: 10.1039/D0CS00558D. URL: http://dx.doi.org/10.1039/D0CS00558D.

[89] P. Nalbach et al. “Noise-Induced Förster Resonant Energy Transfer between Orthogonal Dipoles in Photoexcited Molecules”. In: *Phys. Rev. Lett.* 108 (21 May 2012), p. 218302. DOI: 10.1103/PhysRevLett.108.218302. URL: https://link.aps.org/doi/10.1103/PhysRevLett.108.218302.

[90] E Orgiu et al. “Conductivity in organic semiconductors hybridized with the vacuum field”. In: *Nature Materials* 14.11 (2015), pp. 1123–1129.

[91] G. Paillotin et al. “Analysis of picosecond laser induced fluorescence phenomena in photosynthetic membranes utilizing a master equation approach”. In: *Biophysical Journal* 25.3 (1979), pp. 513–533. ISSN: 0006-3495. DOI: https://doi.org/10.1016/S0006-3495(79)85320-5. URL: https://www.sciencedirect.com/science/article/pii/S0006349579853205.

[92] Horacio M. Pastawski. “Revisiting the Fermi Golden Rule: Quantum dynamical phase transition as a paradigm shift”. In: *Physica B: Condensed Matter* 398.2 (2007), pp. 278–286. ISSN: 0921-4526. DOI: https://doi.org/10.1016/j.physb.2007.05.024.

[93] B. N. J. Persson and A. Baratoff. “Theory of photon emission in electron tunneling to metallic particles”. In: *Phys. Rev. Lett.* 68 (21 May 1992), pp. 3224–3227. DOI: 10.1103/PhysRevLett.68.3224. URL: https://link.aps.org/doi/10.1103/PhysRevLett.68.3224.

[94] Eric Plum and Nikolay I. Zheludev. “Chiral mirrors”. en. In: *Applied Physics Letters* 106.22 (June 2015), p. 221901. ISSN: 0003-6951, 1077-3118. DOI: 10.1063/1.4921969. URL: https://pubs.aip.org/apl/article/106/22/221901/27626/Chiral-mirrors (visited on 06/10/2024).

[95] E. A. Power and T. Thirunamachandran. “Quantum electrodynamics in a cavity”. In: *Phys. Rev. A* 25 (5 May 1982), pp. 2473–2484. DOI: 10.1103/PhysRevA.25.2473. URL: https://link.aps.org/doi/10.1103/PhysRevA.25.2473.

[96] XH Qiu, GV Nazin, and W Ho. “Vibrationally resolved fluorescence excited with submolecular precision”. In: *Science* 299.5606 (2003), pp. 542–546.

[97] Bijan Ranjbar and Pooria Gill. "Circular Dichroism Techniques: Biomolecular and Nanostructural Analyses- A Review". In: *Chemical Biology & Drug Design* 74.2 (2009), pp. 101–120. DOI: https://doi.org/10.1111/j.1747-0285.2009.00847.x. URL: https://onlinelibrary.wiley.com/doi/abs/10.1111/j.1747-0285.2009.00847.x.

[98] M. Reitz, F. Mineo, and C. Genes. "Energy transfer and correlations in cavity-embedded donor-acceptor configurations". In: *Scientific reports* 8.1 (2018), p. 9050. DOI: 10.1038/s41598-018-27396-z.

[99] S. Reynaud. "La fluorescence de résonance: étude par la méthode de l'atome habillé". In: *Annales de physique*. Vol. 8. EDP Sciences. 1983, pp. 315–370. DOI: 10.1051/anphys/198308080315.

[100] Rosario R. Riso et al. "Strong Coupling in Chiral Cavities: Nonperturbative Framework for Enantiomer Discrimination". en. In: *Phys. Rev. X* 13.3 (July 2023), p. 031002. ISSN: 2160-3308. DOI: 10.1103/PhysRevX.13.031002. URL: https://link.aps.org/doi/10.1103/PhysRevX.13.031002 (visited on 06/10/2024).

[101] Vasil Rokaj et al. "Light–matter interaction in the long-wavelength limit: no ground-state without dipole self-energy". In: *Journal of Physics B: Atomic, Molecular and Optical Physics* 51.3 (2018), p. 034005. DOI: 10.1088/1361-6455/aa9c99.

[102] C. Rolland et al. "Antibunched Photons Emitted by a dc-Biased Josephson Junction". In: *Phys. Rev. Lett.* 122 (18 May 2019), p. 186804. DOI: 10.1103/PhysRevLett.122.186804. URL: https://link.aps.org/doi/10.1103/PhysRevLett.122.186804.

[103] P. Rosenbusch et al. "Critical Rotation of a Harmonically Trapped Bose Gas". In: *Phys. Rev. Lett.* 88 (25 June 2002), p. 250403. DOI: 10.1103/PhysRevLett.88.250403. URL: https://link.aps.org/doi/10.1103/PhysRevLett.88.250403.

[104] R. Sáez-Blázquez et al. "Organic polaritons enable local vibrations to drive long-range energy transfer". In: *Phys. Rev. B* 97 (24 June 2018), 241407(R). DOI: 10.1103/PhysRevB.97.241407. URL: https://link.aps.org/doi/10.1103/PhysRevB.97.241407.

[105] A. Salam. "Resonance energy transfer mediated by a chiral molecule". In: *The Journal of Chemical Physics* 154.7 (2021), p. 074111. DOI: 10.1063/5.0042684. URL: https://doi.org/10.1063/5.0042684.

[106] Andrew H Salij, Randall H Goldsmith, and Roel Tempelaar. "Theory predicts 2D chiral polaritons based on achiral Fabry–Pérot cavities using apparent circular dichroism". In: *Nature communications* 15.1 (2024), p. 340. DOI: https://doi.org/10.1038/s41467-023-44523-1.

[107] Q. Schaeverbeke et al. “Single-Photon Emission Mediated by Single-Electron Tunneling in Plasmonic Nanojunctions”. In: *Phys. Rev. Lett.* 123 (24 Dec. 2019), p. 246601. DOI: 10.1103/PhysRevLett.123.246601.

[108] Quentin Schaeverbeke. “Photon emission and quantum transport in nanoplasmonic cavities”. 2020BORD0097. PhD thesis. 2020. URL: http://www.theses.fr/2020BORD0097/document.

[109] Christian Schäfer et al. “Relevance of the quadratic diamagnetic and self-polarization terms in cavity quantum electrodynamics”. In: *ACS photonics* 7.4 (2020), pp. 975–990. DOI: 10.1021/acsphotonics.9b01649.

[110] Gregory D. Scholes. “Long-Range Resonance Energy Transfer in Molecular Systems”. In: *Annual Review of Physical Chemistry* 54.1 (2003), pp. 57–87. DOI: 10.1146/annurev.physchem.54.011002.103746. URL: https://doi.org/10.1146/annurev.physchem.54.011002.103746.

[111] Gregory D. Scholes, Xanthipe J. Jordanides, and Graham R. Fleming. “Adapting the Förster Theory of Energy Transfer for Modeling Dynamics in Aggregated Molecular Assemblies”. In: *The Journal of Physical Chemistry B* 105.8 (2001), pp. 1640–1651. DOI: 10.1021/jp003571m. URL: https://doi.org/10.1021/jp003571m.

[112] Philip Scott et al. “On enhanced sensing of chiral molecules in optical cavities”. en. In: *Applied Physics Reviews* 7.4 (Dec. 2020), p. 041413. ISSN: 1931-9401. DOI: 10.1063/5.0025006. URL: https://pubs.aip.org/apr/article/7/4/041413/832365/On-enhanced-sensing-of-chiral-molecules-in-optical (visited on 06/10/2024).

[113] Georg Seeber, Bryan E. F. Tiedemann, and Kenneth N. Raymond. “Supramolecular Chirality in Coordination Chemistry”. In: *Supramolecular Chirality*. Ed. by Mercedes Crego-Calama and David N. Reinhoudt. Berlin, Heidelberg: Springer Berlin Heidelberg, 2006, pp. 147–183. ISBN: 978-3-540-32152-1. DOI: 10.1007/128_033. URL: https://doi.org/10.1007/128_033.

[114] H. Sumi. “Theory on Rates of Excitation-Energy Transfer between Molecular Aggregates through Distributed Transition Dipoles with Application to the Antenna System in Bacterial Photosynthesis”. In: *The Journal of Physical Chemistry B* 103.1 (1999), pp. 252–260. DOI: 10.1021/jp983477u. URL: https://doi.org/10.1021/jp983477u.

[115] Michael Tavis and Frederick W Cummings. “Exact solution for an N-molecule—radiation-field Hamiltonian”. In: *Physical Review* 170.2 (1968), p. 379.

[116] T Thirunamachandran and David P Craig. *Molecular quantum electrodynamics: an introduction to radiation-molecule interactions*. Dover Publications, 1998.

[117] Nicolaas Godfried Van Kampen. *Stochastic processes in physics and chemistry*. Vol. 1. Elsevier, 1992.

[118] R. Verberk and M. Orrit. “Photon statistics in the fluorescence of single molecules and nanocrystals: Correlation functions versus distributions of on-and off-times”. In: *J. Chem. Phys.* 119.4 (2003), pp. 2214–2222. DOI: 10.1063/1.1582848.

[119] Kirill Voronin et al. “Single-Handedness Chiral Optical Cavities”. In: *ACS Photonics* 9.8 (Aug. 2022), pp. 2652–2659. DOI: 10.1021/acsphotonics.2c00134. URL: https://doi.org/10.1021/acsphotonics.2c00134 (visited on 06/10/2024).

[120] D. Weeraddana et al. “Controlling resonance energy transfer in nanostructure emitters by positioning near a mirror”. In: *The Journal of Chemical Physics* 147.7 (2017), p. 074117. DOI: 10.1063/1.4998459. URL: https://doi.org/10.1063/1.4998459.

[121] Guochun Yang and Yunjie Xu. “Vibrational Circular Dichroism Spectroscopy of Chiral Molecules”. In: *Electronic and Magnetic Properties of Chiral Molecules and Supramolecular Architectures*. Ed. by Ron Naaman, David N Beratan, and David Waldeck. Berlin, Heidelberg: Springer Berlin Heidelberg, 2011, pp. 189–236. DOI: 10.1007/128_2010_86. URL: https://doi.org/10.1007/128_2010_86.

[122] S. J. Yoo and Q. Han Park. “Chiral Light-Matter Interaction in Optical Resonators”. en. In: *Phys. Rev. Lett.* 114.20 (May 2015), p. 203003. ISSN: 0031-9007, 1079-7114. DOI: 10.1103/PhysRevLett.114.203003. URL: https://link.aps.org/doi/10.1103/PhysRevLett.114.203003 (visited on 06/10/2024).

[123] Xiaolan Zhong et al. “Energy Transfer between Spatially Separated Entangled Molecules”. In: *Angewandte Chemie International Edition* 56.31 (2017), pp. 9034–9038. DOI: https://doi.org/10.1002/anie.201703539.

[124] Yifu Zhu et al. “Vacuum Rabi splitting as a feature of linear-dispersion theory: Analysis and experimental observations”. In: *Phys. Rev. Lett.* 64.21 (May 1990), pp. 2499–2502. DOI: 10.1103/PhysRevLett.64.2499. URL: https://link.aps.org/doi/10.1103/PhysRevLett.64.2499 (visited on 03/08/2022).

[125] X. T. Zou and L. Mandel. “Photon-antibunching and sub-Poissonian photon statistics”. In: *Phys. Rev. A* 41 (1 Jan. 1990), pp. 475–476. DOI: 10.1103/PhysRevA.41.475. URL: https://link.aps.org/doi/10.1103/PhysRevA.41.475.

Bibliography

[1] D. Abramavicius et al. “Coherent Multidimensional Optical Spectroscopy of Excitons in Molecular Aggregates; Quasiparticle versus Supermolecule Perspectives”. In: *Chemical Reviews* 109.6 (2009), pp. 2350–2408. DOI: 10.1021/cr800268n. URL: https://doi.org/10.1021/cr800268n.

[2] Jeeva Anandan. “The geometric phase”. In: *Nature* 360.6402 (1992), pp. 307–313. DOI: https://doi.org/10.1038/360307a0.

[3] D.L. Andrews. “A unified theory of radiative and radiationless molecular energy transfer”. In: *Chemical Physics* 135.2 (1989), pp. 195–201. ISSN: 0301-0104. DOI: https://doi.org/10.1016/0301-0104(89)87019-3.

[4] David L Andrews. “Quantum formulation for nanoscale optical and material chirality: symmetry issues, space and time parity, and observables”. In: *Journal of Optics* 20.3 (2018), p. 033003. DOI: 10.1088/2040-8986/aaaa56.

[5] Vladimir Igorevich Arnol’d. *Mathematical methods of classical mechanics*. Vol. 60. Springer Science & Business Media, 2013.

[6] R Avriller and C Genet. “Chirality and dimensionality in the ultrastrong light-matter coupling regime”. In: *arXiv preprint arXiv:2408.01275* (2024). DOI: https://doi.org/10.48550/arXiv.2408.01275.

[7] R. Avriller and A. Levy Yeyati. “Electron-phonon interaction and full counting statistics in molecular junctions”. In: *Phys. Rev. B* 80 (4 July 2009), p. 041309. DOI: 10.1103/PhysRevB.80.041309. URL: https://link.aps.org/doi/10.1103/PhysRevB.80.041309.

[8] R. Avriller, A. Marché, and G. Jonusauskas. “Stochastic dynamics of resonance electronic energy transfer in bidimensional overexcited molecular ensembles”. In: *Phys. Rev. B* 108 (20 Nov. 2023), p. 205419. DOI: 10.1103/PhysRevB.108.205419. URL: https://link.aps.org/doi/10.1103/PhysRevB.108.205419.

[9] R. Avriller et al. “Photon-emission statistics induced by electron tunneling in plasmonic nanojunctions”. In: *Phys. Rev. B* 104 (24 Dec. 2021), p. L241403. DOI: 10.1103/PhysRevB.104.L241403. URL: https://link.aps.org/doi/10.1103/PhysRevB.104.L241403.

[10] Ruth E. Baker and Matthew J. Simpson. “Correcting mean-field approximations for birth-death-movement processes”. In: *Phys. Rev. E* 82 (4 Oct. 2010), p. 041905. DOI: 10.1103/PhysRevE.82.041905.

[11] Denis G. Baranov, Christian Schäfer, and Maxim V. Gorkunov. “Toward Molecular Chiral Polaritons”. In: *ACS Photonics* 10.8 (Aug. 2023), pp. 2440–2455. DOI: 10.1021/acsphotonics.2c02011. URL: https://doi.org/10.1021/acsphotonics.2c02011 (visited on 06/10/2024).

[12] Nico S. Baßler et al. “Metasurface-Based Hybrid Optical Cavities for Chiral Sensing”. In: *Phys. Rev. Lett.* 132 (4 Jan. 2024), p. 043602. DOI: 10.1103/PhysRevLett.132.043602.

[13] A. Bejarano et al. “Photon blockade in current-driven single-molecule emitters”. In: *In preparation* (2025).

[14] A. Bejarano et al. “Single-molecule electroluminescence: crossover from weak to strong coupling”. In: *In preparation* (2025).

[15] D. Beljonne et al. “Beyond Förster Resonance Energy Transfer in Biological and Nanoscale Systems”. In: *The Journal of Physical Chemistry B* 113.19 (2009), pp. 6583–6599. DOI: 10.1021/jp900708f. URL: https://doi.org/10.1021/jp900708f.

[16] Richard Berndt, James K. Gimzewski, and Peter Johansson. “Inelastic tunneling excitation of tip-induced plasmon modes on noble-metal surfaces”. In: *Phys. Rev. Lett.* 67 (27 Dec. 1991), pp. 3796–3799. DOI: 10.1103/PhysRevLett.67.3796. URL: https://link.aps.org/doi/10.1103/PhysRevLett.67.3796.

[17] Michael Berry. “The Geometric Phase”. In: *Scientific American* 259.6 (1988), pp. 46–55. ISSN: 0036-8733. URL: https://www.jstor.org/stable/24989302 (visited on 06/10/2024).

[18] MV Berry. “Quantum adiabatic anholonomy”. In: *Anomalies, phases, defects* (1990), pp. 125–181.

[19] T. Brandes. “Waiting times and noise in single particle transport”. In: *Annalen der Physik* 17.7 (2008), pp. 477–496. DOI: 10.1002/andp.2008103.

[20] H.J. Carmichael et al. “Photoelectron waiting times and atomic state reduction in resonance fluorescence”. In: *Phys. Rev. A.* 39.3 (1989), p. 1200. DOI: 10.1103/PhysRevA.39.1200.

[21] Tzu-Ling Chen et al. “A 2D chiral microcavity based on apparent circular dichroism”. In: *Nature Communications* 15.1 (2024), p. 3072. DOI: https://doi.org/10.1038/s41467-024-47411-4.

[22] M.-C. Chirio-Lebrun and M. Prats. “Fluorescence resonance energy transfer (FRET): theory and experiments”. In: *Biochemical Education* 26.4 (1998), pp. 320–323. ISSN: 0307-4412. DOI: https://doi.org/10.1016/S0307-4412(98)80010-1. URL: https://www.sciencedirect.com/science/article/pii/S0307441298800101.

[23] Michael C. Chong et al. “Narrow-Line Single-Molecule Transducer between Electronic Circuits and Surface Plasmons”. In: *Phys. Rev. Lett.* 116 (3 Jan. 2016), p. 036802. DOI: 10.1103/PhysRevLett.116.036802. URL: https://link.aps.org/doi/10.1103/PhysRevLett.116.036802.

[24] C. Chuang, J. Knoester, and J. Cao. “Scaling Relations and Optimization of Excitonic Energy Transfer Rates between One-Dimensional Molecular Aggregates”. In: *The Journal of Physical Chemistry B* 118.28 (2014), pp. 7827–7834. DOI: 10.1021/jp4124502. URL: https://doi.org/10.1021/jp4124502.

[25] Cristiano Ciuti, Gérald Bastard, and Iacopo Carusotto. “Quantum vacuum properties of the intersubband cavity polariton field”. en. In: *Phys. Rev. B* 72.11 (Sept. 2005), p. 115303. ISSN: 1098-0121, 1550-235X. DOI: 10.1103/PhysRevB.72.115303. URL: https://link.aps.org/doi/10.1103/PhysRevB.72.115303 (visited on 06/10/2024).

[26] C. Cohen-Tannoudji and S. Reynaud. “Atoms in strong light-fields: Photon antibunching in single atom fluorescence”. In: *Phil. Trans. R. Soc. Lond. A* 293.1402 (1979), pp. 223–237. DOI: 10.1098/rsta.1979.0092.

[27] Claude Cohen-Tannoudji, Jacques Dupont-Roc, and Gilbert Grynberg. *Processus d’interaction entre photons et atomes*. EDP sciences, 1996.

[28] E. U. Condon. “Theories of Optical Rotatory Power”. In: *Rev. Mod. Phys.* 9 (4 Oct. 1937), pp. 432–457. DOI: 10.1103/RevModPhys.9.432. URL: https://link.aps.org/doi/10.1103/RevModPhys.9.432.

[29] A. Cottet, T. Kontos, and B. Dou çot. “Electron-photon coupling in mesoscopic quantum electrodynamics”. In: *Phys. Rev. B* 91 (20 May 2015), p. 205417. DOI: 10.1103/PhysRevB.91.205417. URL: https://link.aps.org/doi/10.1103/PhysRevB.91.205417.

[30] D.P. Craig and T. Thirunamachandran. “An analysis of models for resonant transer of excitation using quantum electrodynamics”. In: *Chemical Physics* 167.3 (1992), pp. 229–240. ISSN: 0301-0104. DOI: https://doi.org/10.1016/0301-0104(92)80198-5. URL: https://www.sciencedirect.com/science/article/pii/0301010492801985.

[31] D.P. Craig and T. Thirunamachandran. “Third-body mediation of resonance coupling between identical molecules”. In: *Chemical Physics* 135.1 (1989), pp. 37–48. ISSN: 0301-0104. DOI: https://doi.org/10.1016/0301-0104(89)87004-1. URL: https://www.sciencedirect.com/science/article/pii/0301010489870041.

[32] Jeanne Crassous. “Chiral transfer in coordination complexes: towards molecular materials”. In: *Chemical Society Reviews* 38.3 (2009), pp. 830–845. DOI: https://doi.org/10.1039/B806203J.

[33] G.J. Daniels et al. “Resonance energy transfer: The unified theory revisited”. In: *The Journal of Chemical Physics* 119.4 (2003), pp. 2264–2274. DOI: 10.1063/1.1579677.

[34] Pierre Delplace and Antoine Venaille. arXiv:2006.08488 [astro-ph, physics:cond-mat, physics:physics]. June 2020. DOI: https://doi.org/10.48550/arXiv.2006.08488. URL: http://arxiv.org/abs/2006.08488 (visited on 06/10/2024).

[35] Courtney A DelPo et al. “Polariton decay in donor–acceptor cavity systems”. In: *The Journal of Physical Chemistry Letters* 12.40 (2021), pp. 9774–9782. DOI: 10.1021/acs.jpclett.1c02644.

[36] R. H. Dicke. “Coherence in Spontaneous Radiation Processes”. In: *Phys. Rev.* 93 (1 Jan. 1954), pp. 99–110. DOI: 10.1103/PhysRev.93.99. URL: https://link.aps.org/doi/10.1103/PhysRev.93.99.

[37] C. Didraga, V. A. Malyshev, and J. Knoester. “Excitation Energy Transfer between Closely Spaced Multichromophoric Systems: Effects of Band Mixing and Intraband Relaxation”. In: *The Journal of Physical Chemistry B* 110.38 (2006), pp. 18818–18827. DOI: 10.1021/jp0569281. URL: https://doi.org/10.1021/jp0569281.

[38] Sérgio R. Domingos, Cristóbal Pérez, and Melanie Schnell. “Sensing Chirality with Rotational Spectroscopy”. In: *Annual Review of Physical Chemistry* 69.Volume 69, 2018 (2018), pp. 499–519. ISSN: 1545-1593. DOI: https://doi.org/10.1146/annurev-physchem-052516-050629. URL: https://www.annualreviews.org/content/journals/10.1146/annurev-physchem-052516-050629.

[39] Benjamin Doppagne et al. “Electrofluorochromism at the single-molecule level”. In: *Science* 361.6399 (2018), pp. 251–255. DOI: 10.1126/science.aat1603.

[40] Benjamin Doppagne et al. “Vibronic Spectroscopy with Submolecular Resolution from STM-Induced Electroluminescence”. In: *Phys. Rev. Lett.* 118 (12 Mar. 2017), p. 127401. DOI: 10.1103/PhysRevLett.118.127401. URL: https://link.aps.org/doi/10.1103/PhysRevLett.118.127401.

[41] M. Du et al. “Theory for polariton-assisted remote energy transfer”. In: *Chem. Sci.* 9 (32 2018), pp. 6659–6669. DOI: 10.1039/C8SC00171E.

[42] Thomas W. Ebbesen. “Hybrid Light–Matter States in a Molecular and Material Science Perspective”. In: *Accounts of Chemical Research* 49.11 (2016), pp. 2403–2412. DOI: 10.1021/acs.accounts.6b00295.

[43] Joshua Feis et al. "Helicity-Preserving Optical Cavity Modes for Enhanced Sensing of Chiral Molecules". en. In: *Phys. Rev. Lett.* 124.3 (Jan. 2020), p. 033201. ISSN: 0031-9007, 1079-7114. DOI: 10.1103/PhysRevLett.124.033201. URL: https://link.aps.org/doi/10.1103/PhysRevLett.124.033201 (visited on 06/10/2024).

[44] Ivan Fernandez-Corbaton, Martin Fruhnert, and Carsten Rockstuhl. "Objects of Maximum Electromagnetic Chirality". In: *Phys. Rev. X* 6.3 (July 2016), p. 031013. DOI: 10.1103/PhysRevX.6.031013. URL: https://link.aps.org/doi/10.1103/PhysRevX.6.031013 (visited on 04/01/2022).

[45] Kristen A. Fichthorn and W. H. Weinberg. "Theoretical foundations of dynamical Monte Carlo simulations". In: *The Journal of Chemical Physics* 95.2 (1991), pp. 1090–1096. DOI: 10.1063/1.461138. URL: https://doi.org/10.1063/1.461138.

[46] Th Förster. "Transfer mechanisms of electronic excitation energy". In: *Radiation Research Supplement* (1960), pp. 326–339. DOI: 10.2307/3583604.

[47] Francisco J. Garcia-Vidal, Cristiano Ciuti, and Thomas W. Ebbesen. "Manipulating matter by strong coupling to vacuum fields". In: *Science* 373.6551 (2021), eabd0336. DOI: 10.1126/science.abd0336. URL: https://www.science.org/doi/abs/10.1126/science.abd0336.

[48] Jérôme Gautier et al. "Planar Chirality and Optical Spin–Orbit Coupling for Chiral Fabry–Perot Cavities". en. In: *ACS Photonics* 9.3 (Mar. 2022), pp. 778–783. ISSN: 2330-4022, 2330-4022. DOI: 10.1021/acsphotonics.1c00780. URL: https://pubs.acs.org/doi/10.1021/acsphotonics.1c00780 (visited on 06/10/2024).

[49] C.D. Geddes and J.R. Lakowicz. *Reviews in fluorescence 2006*. Springer, 2006.

[50] Jino George et al. "Multiple Rabi Splittings under Ultrastrong Vibrational Coupling". In: *Phys. Rev. Lett.* 117.15 (Oct. 2016), p. 153601. DOI: 10.1103/PhysRevLett.117.153601. URL: https://link.aps.org/doi/10.1103/PhysRevLett.117.153601 (visited on 06/10/2024).

[51] K. Georgiou et al. "Ultralong-Range Polariton-Assisted Energy Transfer in Organic Microcavities". In: *Angewandte Chemie International Edition* 60.30 (2021), pp. 16661–16667. DOI: https://doi.org/10.1002/anie.202105442.

[52] Daniel T Gillespie. "A general method for numerically simulating the stochastic time evolution of coupled chemical reactions". In: *Journal of Computational Physics* 22.4 (1976), pp. 403–434. ISSN: 0021-9991. DOI: https://doi.org/10.1016/0021-9991(76)90041-3. URL: https://www.sciencedirect.com/science/article/pii/0021999176900413.

[53] Roy J. Glauber. "The Quantum Theory of Optical Coherence". In: *Phys. Rev.* 130 (6 June 1963), pp. 2529–2539. DOI: 10.1103/PhysRev.130.2529.

[54] Giovanni Gottarelli et al. “The use of circular dichroism spectroscopy for studying the chiral molecular self-assembly: An overview”. In: *Chirality* 20.3-4 (2008), pp. 471–485. DOI: https://doi.org/10.1002/chir.20459. URL: https://onlinelibrary.wiley.com/doi/abs/10.1002/chir.20459.

[55] A. Grimm et al. “Bright On-Demand Source of Antibunched Microwave Photons Based on Inelastic Cooper Pair Tunneling”. In: *Phys. Rev. X* 9 (2 Apr. 2019), p. 021016. DOI: 10.1103/PhysRevX.9.021016. URL: https://link.aps.org/doi/10.1103/PhysRevX.9.021016.

[56] Leon M Hall. “Trochoids, roses, and thorns—beyond the spirograph”. In: *The College Mathematics Journal* 23.1 (1992), pp. 20–35.

[57] J. H. Hannay. “Angle variable holonomy in adiabatic excursion of an integrable Hamiltonian”. en. In: *Journal of Physics A: Mathematical and General* 18.2 (Feb. 1985), p. 221. ISSN: 0305-4470. DOI: 10.1088/0305-4470/18/2/011. URL: https://dx.doi.org/10.1088/0305-4470/18/2/011 (visited on 06/10/2024).

[58] Serge Haroche and Daniel Kleppner. “Cavity Quantum Electrodynamics”. In: *Physics Today* 42.1 (Jan. 1989), pp. 24–30. ISSN: 0031-9228. DOI: 10.1063/1.881201. URL: https://doi.org/10.1063/1.881201.

[59] E. Hennebicq et al. “Shared-mode assisted resonant energy transfer in the weak coupling regime”. In: *The Journal of Chemical Physics* 130.21 (2009), p. 214505. DOI: 10.1063/1.3140273. URL: https://doi.org/10.1063/1.3140273.

[60] G Hoffmann et al. “Influence of tip geometry in light emission from the scanning tunnelling microscope”. In: *Surface science* 482 (2001), pp. 1159–1162.

[61] T. Holstein. “Theory of transport phenomena in an electron-phonon gas”. In: *Annals of Physics* 29.3 (1964), pp. 410–535. ISSN: 0003-4916. DOI: https://doi.org/10.1016/0003-4916(64)90008-9. URL: https://www.sciencedirect.com/science/article/pii/0003491664900089.

[62] J. J. Hopfield. “Theory of the Contribution of Excitons to the Complex Dielectric Constant of Crystals”. en. In: *Phys. Rev.* 112.5 (Dec. 1958), pp. 1555–1567. ISSN: 0031-899X. DOI: 10.1103/PhysRev.112.1555. URL: https://link.aps.org/doi/10.1103/PhysRev.112.1555 (visited on 06/10/2024).

[63] R. Houdré, R. P. Stanley, and M. Ilegems. “Vacuum-field Rabi splitting in the presence of inhomogeneous broadening: Resolution of a homogeneous linewidth in an inhomogeneously broadened system”. In: *Phys. Rev. A* 53 (4 Apr. 1996), pp. 2711–2715. DOI: 10.1103/PhysRevA.53.2711.

[64] James A. Hutchison et al. “Modifying Chemical Landscapes by Coupling to Vacuum Fields”. In: *Angewandte Chemie International Edition* 51.7 (2012), pp. 1592–1596. DOI: https://doi.org/10.1002/anie.201107033.

[65] Hiroshi Imada et al. “Single-Molecule Investigation of Energy Dynamics in a Coupled Plasmon-Exciton System”. In: *Phys. Rev. Lett.* 119 (1 July 2017), p. 013901. DOI: 10.1103/PhysRevLett.119.013901. URL: https://link.aps.org/doi/10.1103/PhysRevLett.119.013901.

[66] Gert-Ludwig Ingold and Yu V Nazarov. “Charge tunneling rates in ultrasmall junctions”. In: *Single charge tunneling: Coulomb blockade phenomena in nanostructures* (1992), pp. 21–107.

[67] John David Jackson. *Classical electrodynamics*. John Wiley & Sons, 2021.

[68] S. Jang, M. D. Newton, and R. J. Silbey. “Multichromophoric Förster Resonance Energy Transfer”. In: *Phys. Rev. Lett.* 92 (21 May 2004), p. 218301. DOI: 10.1103/PhysRevLett.92.218301. URL: https://link.aps.org/doi/10.1103/PhysRevLett.92.218301.

[69] S. Jang, M.D. Newton, and R.J. Silbey. “Multichromophoric Förster Resonance Energy Transfer from B800 to B850 in the Light Harvesting Complex 2: Evidence for Subtle Energetic Optimization by Purple Bacteria”. In: *The Journal of Physical Chemistry B* 111.24 (2007), pp. 6807–6814. DOI: 10.1021/jp070111l. URL: https://doi.org/10.1021/jp070111l.

[70] S. Jang et al. “Theory of coherent resonance energy transfer”. In: *The Journal of Chemical Physics* 129.10 (2008), p. 101104. DOI: 10.1063/1.2977974. URL: https://doi.org/10.1063/1.2977974.

[71] R.D. Jenkins, G.J. Daniels, and D.L. Andrews. “Quantum pathways for resonance energy transfer”. In: *The Journal of Chemical Physics* 120.24 (2004), pp. 11442–11448. DOI: 10.1063/1.1742697. URL: https://doi.org/10.1063/1.1742697.

[72] Song Jiang et al. “Many-Body Description of STM-Induced Fluorescence of Charged Molecules”. In: *Phys. Rev. Lett.* 130 (12 Mar. 2023), p. 126202. DOI: 10.1103/PhysRevLett.130.126202. URL: https://link.aps.org/doi/10.1103/PhysRevLett.130.126202.

[73] Peter Johansson, R. Monreal, and Peter Apell. “Theory for light emission from a scanning tunneling microscope”. In: *Phys. Rev. B* 42 (14 Nov. 1990), pp. 9210–9213. DOI: 10.1103/PhysRevB.42.9210. URL: https://link.aps.org/doi/10.1103/PhysRevB.42.9210.

[74] Stéphane Kéna-Cohen, Stefan A. Maier, and Donal D. C. Bradley. “Ultrastrongly Coupled Exciton–Polaritons in Metal-Clad Organic Semiconductor Microcavities”. In: *Advanced Optical Materials* 1.11 (2013), pp. 827–833. DOI: https://doi.org/10.1002/adom.201300256.

[75] V. M. Kenkre and R. S. Knox. “Generalized-master-equation theory of excitation transfer”. In: *Phys. Rev. B* 9 (12 June 1974), pp. 5279–5290. DOI: 10.1103/PhysRevB.9.5279. URL: https://link.aps.org/doi/10.1103/PhysRevB.9.5279.

[76] Robert S. Knox. “Förster’s resonance excitation transfer theory: not just a formula”. In: *Journal of Biomedical Optics* 17.1 (2012), p. 011003. DOI: 10.1117/1.JBO.17.1.011003. URL: https://doi.org/10.1117/1.JBO.17.1.011003.

[77] Jens Koch and Felix von Oppen. “Franck-Condon Blockade and Giant Fano Factors in Transport through Single Molecules”. In: *Phys. Rev. Lett.* 94 (20 May 2005), p. 206804. DOI: 10.1103/PhysRevLett.94.206804. URL: https://link.aps.org/doi/10.1103/PhysRevLett.94.206804.

[78] Jens Koch, Felix von Oppen, and A. V. Andreev. “Theory of the Franck-Condon blockade regime”. In: *Phys. Rev. B* 74 (20 Nov. 2006), p. 205438. DOI: 10.1103/PhysRevB.74.205438. URL: https://link.aps.org/doi/10.1103/PhysRevB.74.205438.

[79] Manohar Kumar et al. “Detection of Vibration-Mode Scattering in Electronic Shot Noise”. In: *Phys. Rev. Lett.* 108 (14 Apr. 2012), p. 146602. DOI: 10.1103/PhysRevLett.108.146602. URL: https://link.aps.org/doi/10.1103/PhysRevLett.108.146602.

[80] Lev Davidovich Landau et al. *Electrodynamics of continuous media*. Vol. 8. elsevier, 2013.

[81] Christopher C Leon et al. “Single photon emission from a plasmonic light source driven by a local field-induced coulomb blockade”. In: *ACS nano* 14.4 (2020), pp. 4216–4223.

[82] Ismo Lindell et al. *Electromagnetic waves in chiral and bi-isotropic media*. Artech House, 1994.

[83] M.P.E. Lock, D.L. Andrews, and G.A. Jones. “On the nature of long range electronic coupling in a medium: Distance and orientational dependence for chromophores in molecular aggregates”. In: *The Journal of Chemical Physics* 140.4 (2014), p. 044103. DOI: 10.1063/1.4861695. URL: https://doi.org/10.1063/1.4861695.

[84] A. Marché. “Aspect collectif du transfert d’énergie entre molécules”. In: *Unpublished Master 1 thesis, University of Bordeaux* (2022).

[85] F. Mattiotti et al. “Multifractality in the interacting disordered Tavis-Cummings model”. In: *Phys. Rev. B* 109 (6 Feb. 2024), p. 064202. DOI: 10.1103/PhysRevB.109.064202. URL: https://link.aps.org/doi/10.1103/PhysRevB.109.064202.

[86] L. Mauro et al. “Chiral discrimination in helicity-preserving Fabry-Pérot cavities”. en. In: *Phys. Rev. A* 107.2 (Feb. 2023), p. L021501. ISSN: 2469-9926, 2469-9934. DOI: 10.1103/PhysRevA.107.L021501. URL: https://link.aps.org/doi/10.1103/PhysRevA.107.L021501 (visited on 06/10/2024).

[87] L. Mauro et al. “Classical approaches to chiral polaritonics”. en. In: *Phys. Rev. A* 109.2 (Feb. 2024), p. 023528. ISSN: 2469-9926, 2469-9934. DOI: 10.1103/PhysRevA.109.023528. URL: https://link.aps.org/doi/10.1103/PhysRevA.109.023528 (visited on 06/10/2024).

[88] A. J. Miles, Robert W. Janes, and B. A. Wallace. “Tools and methods for circular dichroism spectroscopy of proteins: a tutorial review”. In: *Chem. Soc. Rev.* 50 (15 2021), pp. 8400–8413. DOI: 10.1039/D0CS00558D. URL: http://dx.doi.org/10.1039/D0CS00558D.

[89] P. Nalbach et al. “Noise-Induced Förster Resonant Energy Transfer between Orthogonal Dipoles in Photoexcited Molecules”. In: *Phys. Rev. Lett.* 108 (21 May 2012), p. 218302. DOI: 10.1103/PhysRevLett.108.218302. URL: https://link.aps.org/doi/10.1103/PhysRevLett.108.218302.

[90] E Orgiu et al. “Conductivity in organic semiconductors hybridized with the vacuum field”. In: *Nature Materials* 14.11 (2015), pp. 1123–1129.

[91] G. Paillotin et al. “Analysis of picosecond laser induced fluorescence phenomena in photosynthetic membranes utilizing a master equation approach”. In: *Biophysical Journal* 25.3 (1979), pp. 513–533. ISSN: 0006-3495. DOI: https://doi.org/10.1016/S0006-3495(79)85320-5. URL: https://www.sciencedirect.com/science/article/pii/S0006349579853205.

[92] Horacio M. Pastawski. “Revisiting the Fermi Golden Rule: Quantum dynamical phase transition as a paradigm shift”. In: *Physica B: Condensed Matter* 398.2 (2007), pp. 278–286. ISSN: 0921-4526. DOI: https://doi.org/10.1016/j.physb.2007.05.024.

[93] B. N. J. Persson and A. Baratoff. “Theory of photon emission in electron tunneling to metallic particles”. In: *Phys. Rev. Lett.* 68 (21 May 1992), pp. 3224–3227. DOI: 10.1103/PhysRevLett.68.3224. URL: https://link.aps.org/doi/10.1103/PhysRevLett.68.3224.

[94] Eric Plum and Nikolay I. Zheludev. “Chiral mirrors”. en. In: *Applied Physics Letters* 106.22 (June 2015), p. 221901. ISSN: 0003-6951, 1077-3118. DOI: 10.1063/1.4921969. URL: https://pubs.aip.org/apl/article/106/22/221901/27626/Chiral-mirrors (visited on 06/10/2024).

[95] E. A. Power and T. Thirunamachandran. “Quantum electrodynamics in a cavity”. In: *Phys. Rev. A* 25 (5 May 1982), pp. 2473–2484. DOI: 10.1103/PhysRevA.25.2473. URL: https://link.aps.org/doi/10.1103/PhysRevA.25.2473.

[96] XH Qiu, GV Nazin, and W Ho. “Vibrationally resolved fluorescence excited with submolecular precision”. In: *Science* 299.5606 (2003), pp. 542–546.

[97] Bijan Ranjbar and Pooria Gill. "Circular Dichroism Techniques: Biomolecular and Nanostructural Analyses- A Review". In: *Chemical Biology & Drug Design* 74.2 (2009), pp. 101–120. DOI: https://doi.org/10.1111/j.1747-0285.2009.00847.x. URL: https://onlinelibrary.wiley.com/doi/abs/10.1111/j.1747-0285.2009.00847.x.

[98] M. Reitz, F. Mineo, and C. Genes. "Energy transfer and correlations in cavity-embedded donor-acceptor configurations". In: *Scientific reports* 8.1 (2018), p. 9050. DOI: 10.1038/s41598-018-27396-z.

[99] S. Reynaud. "La fluorescence de résonance: étude par la méthode de l'atome habillé". In: *Annales de physique*. Vol. 8. EDP Sciences. 1983, pp. 315–370. DOI: 10.1051/anphys/198308080315.

[100] Rosario R. Riso et al. "Strong Coupling in Chiral Cavities: Nonperturbative Framework for Enantiomer Discrimination". en. In: *Phys. Rev. X* 13.3 (July 2023), p. 031002. ISSN: 2160-3308. DOI: 10.1103/PhysRevX.13.031002. URL: https://link.aps.org/doi/10.1103/PhysRevX.13.031002 (visited on 06/10/2024).

[101] Vasil Rokaj et al. "Light–matter interaction in the long-wavelength limit: no ground-state without dipole self-energy". In: *Journal of Physics B: Atomic, Molecular and Optical Physics* 51.3 (2018), p. 034005. DOI: 10.1088/1361-6455/aa9c99.

[102] C. Rolland et al. "Antibunched Photons Emitted by a dc-Biased Josephson Junction". In: *Phys. Rev. Lett.* 122 (18 May 2019), p. 186804. DOI: 10.1103/PhysRevLett.122.186804. URL: https://link.aps.org/doi/10.1103/PhysRevLett.122.186804.

[103] P. Rosenbusch et al. "Critical Rotation of a Harmonically Trapped Bose Gas". In: *Phys. Rev. Lett.* 88 (25 June 2002), p. 250403. DOI: 10.1103/PhysRevLett.88.250403. URL: https://link.aps.org/doi/10.1103/PhysRevLett.88.250403.

[104] R. Sáez-Blázquez et al. "Organic polaritons enable local vibrations to drive long-range energy transfer". In: *Phys. Rev. B* 97 (24 June 2018), 241407(R). DOI: 10.1103/PhysRevB.97.241407. URL: https://link.aps.org/doi/10.1103/PhysRevB.97.241407.

[105] A. Salam. "Resonance energy transfer mediated by a chiral molecule". In: *The Journal of Chemical Physics* 154.7 (2021), p. 074111. DOI: 10.1063/5.0042684. URL: https://doi.org/10.1063/5.0042684.

[106] Andrew H Salij, Randall H Goldsmith, and Roel Tempelaar. "Theory predicts 2D chiral polaritons based on achiral Fabry–Pérot cavities using apparent circular dichroism". In: *Nature communications* 15.1 (2024), p. 340. DOI: https://doi.org/10.1038/s41467-023-44523-1.

[107] Q. Schaeverbeke et al. “Single-Photon Emission Mediated by Single-Electron Tunneling in Plasmonic Nanojunctions”. In: *Phys. Rev. Lett.* 123 (24 Dec. 2019), p. 246601. DOI: 10.1103/PhysRevLett.123.246601.

[108] Quentin Schaeverbeke. “Photon emission and quantum transport in nanoplasmonic cavities”. 2020BORD0097. PhD thesis. 2020. URL: http://www.theses.fr/2020BORD0097/document.

[109] Christian Schäfer et al. “Relevance of the quadratic diamagnetic and self-polarization terms in cavity quantum electrodynamics”. In: *ACS photonics* 7.4 (2020), pp. 975–990. DOI: 10.1021/acsphotonics.9b01649.

[110] Gregory D. Scholes. “Long-Range Resonance Energy Transfer in Molecular Systems”. In: *Annual Review of Physical Chemistry* 54.1 (2003), pp. 57–87. DOI: 10.1146/annurev.physchem.54.011002.103746. URL: https://doi.org/10.1146/annurev.physchem.54.011002.103746.

[111] Gregory D. Scholes, Xanthipe J. Jordanides, and Graham R. Fleming. “Adapting the Förster Theory of Energy Transfer for Modeling Dynamics in Aggregated Molecular Assemblies”. In: *The Journal of Physical Chemistry B* 105.8 (2001), pp. 1640–1651. DOI: 10.1021/jp003571m. URL: https://doi.org/10.1021/jp003571m.

[112] Philip Scott et al. “On enhanced sensing of chiral molecules in optical cavities”. en. In: *Applied Physics Reviews* 7.4 (Dec. 2020), p. 041413. ISSN: 1931-9401. DOI: 10.1063/5.0025006. URL: https://pubs.aip.org/apr/article/7/4/041413/832365/On-enhanced-sensing-of-chiral-molecules-in-optical (visited on 06/10/2024).

[113] Georg Seeber, Bryan E. F. Tiedemann, and Kenneth N. Raymond. “Supramolecular Chirality in Coordination Chemistry”. In: *Supramolecular Chirality*. Ed. by Mercedes Crego-Calama and David N. Reinhoudt. Berlin, Heidelberg: Springer Berlin Heidelberg, 2006, pp. 147–183. ISBN: 978-3-540-32152-1. DOI: 10.1007/128_033. URL: https://doi.org/10.1007/128_033.

[114] H. Sumi. “Theory on Rates of Excitation-Energy Transfer between Molecular Aggregates through Distributed Transition Dipoles with Application to the Antenna System in Bacterial Photosynthesis”. In: *The Journal of Physical Chemistry B* 103.1 (1999), pp. 252–260. DOI: 10.1021/jp983477u. URL: https://doi.org/10.1021/jp983477u.

[115] Michael Tavis and Frederick W Cummings. “Exact solution for an N-molecule—radiation-field Hamiltonian”. In: *Physical Review* 170.2 (1968), p. 379.

[116] T Thirunamachandran and David P Craig. *Molecular quantum electrodynamics: an introduction to radiation-molecule interactions*. Dover Publications, 1998.

[117] Nicolaas Godfried Van Kampen. *Stochastic processes in physics and chemistry*. Vol. 1. Elsevier, 1992.

[118] R. Verberk and M. Orrit. “Photon statistics in the fluorescence of single molecules and nanocrystals: Correlation functions versus distributions of on-and off-times”. In: *J. Chem. Phys.* 119.4 (2003), pp. 2214–2222. DOI: 10.1063/1.1582848.

[119] Kirill Voronin et al. “Single-Handedness Chiral Optical Cavities”. In: *ACS Photonics* 9.8 (Aug. 2022), pp. 2652–2659. DOI: 10.1021/acsphotonics.2c00134. URL: https://doi.org/10.1021/acsphotonics.2c00134 (visited on 06/10/2024).

[120] D. Weeraddana et al. “Controlling resonance energy transfer in nanostructure emitters by positioning near a mirror”. In: *The Journal of Chemical Physics* 147.7 (2017), p. 074117. DOI: 10.1063/1.4998459. URL: https://doi.org/10.1063/1.4998459.

[121] Guochun Yang and Yunjie Xu. “Vibrational Circular Dichroism Spectroscopy of Chiral Molecules”. In: *Electronic and Magnetic Properties of Chiral Molecules and Supramolecular Architectures*. Ed. by Ron Naaman, David N Beratan, and David Waldeck. Berlin, Heidelberg: Springer Berlin Heidelberg, 2011, pp. 189–236. DOI: 10.1007/128_2010_86. URL: https://doi.org/10.1007/128_2010_86.

[122] S. J. Yoo and Q. Han Park. “Chiral Light-Matter Interaction in Optical Resonators”. en. In: *Phys. Rev. Lett.* 114.20 (May 2015), p. 203003. ISSN: 0031-9007, 1079-7114. DOI: 10.1103/PhysRevLett.114.203003. URL: https://link.aps.org/doi/10.1103/PhysRevLett.114.203003 (visited on 06/10/2024).

[123] Xiaolan Zhong et al. “Energy Transfer between Spatially Separated Entangled Molecules”. In: *Angewandte Chemie International Edition* 56.31 (2017), pp. 9034–9038. DOI: https://doi.org/10.1002/anie.201703539.

[124] Yifu Zhu et al. “Vacuum Rabi splitting as a feature of linear-dispersion theory: Analysis and experimental observations”. In: *Phys. Rev. Lett.* 64.21 (May 1990), pp. 2499–2502. DOI: 10.1103/PhysRevLett.64.2499. URL: https://link.aps.org/doi/10.1103/PhysRevLett.64.2499 (visited on 03/08/2022).

[125] X. T. Zou and L. Mandel. “Photon-antibunching and sub-Poissonian photon statistics”. In: *Phys. Rev. A* 41 (1 Jan. 1990), pp. 475–476. DOI: 10.1103/PhysRevA.41.475. URL: https://link.aps.org/doi/10.1103/PhysRevA.41.475.